

REACTIVITY AND TOXICITY OF SILICA NANOFORMS FOUND IN COSMETICS

by

PIRUTCHADA MUSIGAPONG

A thesis submitted to The University of Birmingham
for the degree of DOCTOR OF PHILOSOPHY

School of Geography, Earth and Environmental Science
College of Life and Environmental Sciences
The University of Birmingham, UK
February 2020

UNIVERSITY OF
BIRMINGHAM

University of Birmingham Research Archive

e-theses repository

This unpublished thesis/dissertation is copyright of the author and/or third parties. The intellectual property rights of the author or third parties in respect of this work are as defined by The Copyright Designs and Patents Act 1988 or as modified by any successor legislation.

Any use made of information contained in this thesis/dissertation must be in accordance with that legislation and must be properly acknowledged. Further distribution or reproduction in any format is prohibited without the permission of the copyright holder.

Abstract

The use of nanomaterials (NMs) has been rapidly increasing in recent years, and this is reflected in their large-scale use for cosmetic applications. For example, it is expected that silica nanoparticles will reach a global market size of 5 trillion USD by 2025. Amorphous silica nanoparticles (aSiNPs) are widely used to enhance the effectiveness, texture and shelf-life of various commercial cosmetics and act as an anti-caking agent and an absorbent to release active compounds over time in a range of cosmetic formulations (e.g. foundation, lipsticks, and blushes). However, widespread use of cosmetics with aSiNPs increases exposure and may induce effects on human health and the environment that are not yet known.

The EU Cosmetics Regulation (EC Nº 122/2009) requires that NMs present in cosmetics need to be explicitly authorised. Additionally, the physicochemical characterisation of cosmetics is addressed under the International Organisation for Standardization of nanomaterials (ISO/TR13014 (2012)) and the United States Food and Drugs Administration (FDA-2011-D-0489). However, confidence of nanomaterial characterisation is still lacking data because of their unique physical, chemical features, and an inability of instruments to measure and manipulate the nanomaterials. Due to different strengths and limitations of each technique, a combination method is used to increase reliable and reproducible in characterisation of nanomaterials. An interdisciplinary characterisation approach therefore is used to define in aspects ranging from physicochemical to potential biological effects in this study. The main characteristics of eight unmodified

commercial cosmetics were performed by several techniques, such as XRD, XPS, XANES and EXAFS that showed the presence of NMs such as silica, titanium dioxide, iron oxide, and mica. Besides, XRD and XPS can provide both composition and semi-quantitative data. Their complex formulations, aggregation and multimodal particle content limited the evaluation of primary particle size by SAXS. DLS could identify the particle size of the particles contained in these samples, although it was not possible to assess the relative proportion of silica. Also, five standards of Synthetic Amorphous Silica nanomaterials (SASs), requested from Joint Research Centre (JRC) were characterised and compared their properties with the previous data. Most of the standard SASs were in larger size than nanoparticles, one of the critical changes related to the mechanisms of aggregation during a water removal process, a freeze-drying process and thermal process. This is a reason why synthetic amorphous silica nanoparticles were synthesised and then applied on the reconstructed human skin models in order to assess their toxicity.

A sol-gel method was performed to synthesise monodisperse amorphous silica nanoparticles. Subsequently, routine laboratory methods and synchrotron-based techniques were carried out to fully characterise the properties of the synthetic silica. The protocol successfully produced ultrafine (sub-10nm) silica particles with high purity and %yield. Besides, the particles were found to be stable in ultrapure water and their synthesis could be scaled up to allow effective large-scale production. For technique details, various typical nanomaterials, such as colloidal dispersions and powders, leaded to determine the analysis technique uses. DLS (scattering technique) and TEM (diffraction technique) have been

commonly used to determine the particle size and size distribution of nanoparticles. STEM and SAXS are specialized in this context, SAXS, Thailand and Germany have found a much broadened range of information presenting two population of particle sizes and a shape of particles with weak ordering arrangement, but cannot be presented in STEM images. ICP-OES provided information on the concentration of Si. There is the limitation to detect nitrogen which presented in the synthetic procedure. It is desirable to use FT-IR and XPS to extent evaluate the functional group and the surface chemistry. As the further information using FT-IR and XPS methods, the presence of NH group and elemental composition, such as C, N, O and Si can evaluate the purity of final colloidal dispersion of aSiNPs. However, the use of one or many of analytical characterisation methods is enough when providing reliable information of a specific parameter (e.g. size, structure, elemental composition). Their properties are relevant to the assessment of potential environmental and human exposure and risks from the smallest size range of nanoparticles; this work can thus contribute towards future safer product design and development of fate models in nano regulation.

Most cytotoxicity literature to date has focused on inhalation and oral routes of exposure. Skin absorption of such nanoparticles, potential uptake and cellular response, especially in the context of cosmetics, remain poorly investigated. This thesis presents data on (i) skin irritation of lab-synthesised aSiNPs, designed to mimic ultra-small nanoparticles that may be found in commercial cosmetics, (ii) testing of these particles when topically applied to a reconstructed human epidermis (RhE), following OECD guideline no. 439, and (iii) histological

observations of the exposed skin and immune-mediated responses by ELISA-interleukin1-alpha. To understand the integrity of the skin barrier, a full-thickness human skin (Day 11) model was applied to evaluate the penetration ability of aSiNPs. The significance of such potential penetration is that the use of silica nanomaterials in cosmetics may induce a toxic effect if skin penetration occurs and the particles translocate to the bloodstream or internal organs.

The results indicated aSiNPs as a non-irritant and both MTT and ELISA assays were in general agreements. Histological examination showed tissue differentiation and proliferation, with few keratinocytes without a nucleus. XANES and XRF were used to explore the extent of skin penetration in the D11 tissues. The results further showed that the aSiNPs penetrated the outermost skin and reached the deeper skin layer but did not localize underneath the dermis. XANES showed that Ca^{2+} in the epidermis and dermis layers may interact with aSiNPs on the surface and transform their chemical, environment, leading to the reduction of oxidation state from +4 to -2 and potential formation of calcium di-silicide. Additionally, XPS showed the binding energy of silicon was shifted toward lower energy which related to the presence of silanol groups (Si-OH) and alkyl groups (Si-O-C) on the aSiNP surface. The silanol groups induce membrane destabilization and lead to NPs surface interactions with the surrounding-biological environment (e. g. phospholipid, glycoproteins, lipoproteins, electrolytes, ions). XRF showed evidence of the increased capacity of aSiNPs to penetrate skin and gain access to deeper layer of the human skin. Although this may be desirable for more effective action of cosmetics, it might also result in far greater uptake of substances that exert adverse health effects.

To my beloved dad and mum,

Supak & Wanna

Acknowledgements

I wish to express my sincere gratitude to my supervisor Professor Eugenia Valsami-Jones for her invaluable advice, supervision throughout my study and anglicising this thesis. I have greatly benefitted from her knowledge, experience, understanding of nanotechnology and nanomaterials (NMs) and multi-method characterisation. I am also grateful for her positive attitude and encouragement when I faced difficulties with my study and for her patience in helping me. Furthermore, I also wish to express my sincere gratitude to my co-supervisor Professor Iseult Lynch for all her assistance, encouragement and valued discussions throughout my study.

I would like to acknowledge the Office of the Civil Service Commission, Thailand for providing financial support toward the cost of tuition fees and student general maintenance costs during my PhD study and the Office of Educational Affairs, the Royal Thai Embassy, London for taking care of both education and welfare. Scientific and technical support of SLRI, Thailand is gratefully acknowledged.

I would also like to thank for all team spirit of the Environmental Science Group at the University of Birmingham who have been supportive throughout the years; Christine Elgy, Dr Anastasios Papadiamantis, Dr Marie-France Belinga-Desaunay-Nault, and Dr Sophie Marie Briffa for their help in the Laboratory and Dr Indrani Mahapatra for her assistance.

Lastly, I would like to express my endless thanks to my family, especially my father and my mother for their understanding, sincere encouragement and never-ending support all through my life.

Table of Contents

Table of Contents ..... **i**

List of Figures ..... **xi**

List of Abbreviations ..... **xxxii**

Chapter 1 Introduction **1**

1.1 Overview 1

1.2 Nanotechnology and Nanomaterials 6

1.3 Classification of nanomaterials 9

1.4 NM properties relevant to their behaviour, interaction and toxicity 14

1.5 Synthesis methods for amorphous Silica Nanoparticles 17

1.6 NM Regulation 19

1.7 Nanoparticles in cosmetics 21

1.8 Human Skin 22

1.9 Aims and Objectives 40

1.10 Thesis structure 43

1.11 Paper status and author contributions 45

Chapter 2 Methodology **46**

2.1 Introduction 46

2.2 Characterisation 48

2.2.1 Dynamic Light Scattering 48

2.2.2 Transmission Electron Microscopy (TEM) 54

2.2.2.3 Analytical Procedure 55

2.2.3 Scanning Transmission Electron Microscopy (STEM) 56

2.2.3.1 Technique 56

2.2.3.2 Sample Preparation 57

2.2.3.3 Analytical Procedure 57

2.2.4 Scanning Electron Microscopy (SEM) 58

2.2.4.1 Technique 58

2.2.4.2 Sample Preparation 59

2.2.4.3 Analytical Procedure 60

2.2.5 Synchrotron techniques 60

2.2.6 Small Angle X-ray Scattering (SAXS) 62

2.2.6.1 SAXS Technique 62

2.2.6.2 Sample Preparation 67

2.2.6.3 Analytical Procedure 68

2.2.7 X-ray Photoelectron Spectroscopy (XPS) 69

2.2.7.1 Technique 69

2.2.7.2 Sample Preparation 71

2.2.7.3 Analytical Procedure 72

2.2.8 X-ray Absorption Spectroscopy (XAS) 72

2.2.8.1 Technique 72

2.2.8.2 Sample Preparation 76
2.2.8.3 Analytical Procedure 76
2.2.9 Micro X-ray Fluorescence Spectroscopy (μXRF) 77
2.2.9.1 Technique 77
2.2.9.2 Sample Preparation 78
2.2.9.3 Analytical Procedure 78
2.2.10 Fourier Transform-Infrared Spectroscopy (FTIR) 78
2.2.10.1 Technique 78
2.2.10.2 Sample Preparation 79
2.2.10.3 Analytical Procedure 79
2.2.11 X-ray powder Diffraction (XRD) 79
2.2.11.1 Technique 79
2.2.11.2 Sample Preparation 81
2.2.11.3 XRD Analysis 81
2.2.12 Brunauer, Emmett and Teller (BET) surface analysis 82
2.2.12.1 BET Technique 82
2.2.12.2 Sample Preparation 83
2.2.12.3 Analytical Procedure 83
2.2.13 Inductive Coupled Plasma-Optical Emission Spectroscopy (ICP-OES) 84
2.2.13.1 Technique 84

2.2.13.2 Sample Preparation 85

2.2.13.3 Analytical Procedure 86

2.2.14 Summary of analytical approach 86

2.3 Reconstructed Human Skin Models 87

2.3.1 Reconstructed Human Epidermis Model and Reconstructed Human Full-Thickness Skin Model 88

2.4 In Vitro Skin Test 89

2.4.1 *In Vitro* Skin Penetration 90

2.4.2 *In Vitro* Skin Irritation 91

2.4.3 Cytotoxicity 92

2.4.3.1 MTT assay 92

2.4.3.2 ELISA assay 93

2.4.3.3 Histology 94

Chapter 3 Characterisation of NPs from commercial cosmetics and Synthetic Amorphous Silica (SASs) 99

3.1 Introduction 99

3.2 Chemicals and Materials 101

3.3 Sample Storage and Glassware 107

3.4 Method Characterisation of cosmetics and SASs 107

3.5 Sample Preparation 109

3.5.1 Cosmetics 109

3.5.2 SASs 110
3.5.3 XRD 111
3.5.4 XAS-XANES 111
3.5.5 XPS 112
3.5.6 SAXS/WAXS 112
3.5.7 DLS 113
3.5.8 SEM 114
3.5.9 TEM 114
3.5.10 BET 114
3.6 Results 115
3.7 Results of Cosmetic Characterisation 115
3.7.1 Particle size 115
3.7.2 Elemental composition and oxidative state 126
3.7.3 Chemical Composition 135
3.7.4 Surface Charge 141
3.8 Results of SAS Characterisation 143
3.8.1 Particle size and size distribution 143
3.8.2 Morphology (Crystallinity structure) 157
3.8.3 Elemental compositions and oxidative state 159
3.8.4 Shape 168
3.8.5 Surface area 170

3.9 Discussion 171

3.10 Conclusions 176

Chapter 4 Synthesis and Characterisation of Silica Nanoparticles.... 178

4.1 Introduction 178

4.2 Chemical and Materials 180

4.3 Glassware 180

4.4 Synthesis of amorphous silica nanoparticles 180

4.4.1 Sample Preparation 180

4.4.2 Reaction Mechanism 183

4.5 Characterisation 186

4.6 Characterisation of Physicochemical Properties 187

4.6.1 Particle size 188

4.6.2 Shape 203

4.6.3 Morphology (Crystallinity structure) Powder-XRD 204

4.6.4 Surface area 205

4.6.5 Elemental composition 206

4.7 Discussion 215

4.8 Conclusion 220

Chapter 5 Penetration and Distribution Assessment of aSiNPs through a Skin Model 222

5.1 Introduction 222

5.2 Materials and Methods 225

5.2.1 Reagents 225

5.2.2 Colloidal Silica Nanoparticles 225

5.2.3 Reconstructed Human Full Thickness Skin Model: T-skin™ at Day 11 Experiment and Media Preparation 226

5.2.4 *In Vitro* Skin Penetration 227

5.2.4.1 Pre-check 230

5.2.4.2 *In vitro* Skin Penetration Test 230

5.2.4.3 Endpoint 231

5.2.5 XRF Analysis 231

5.2.6 SAXS Analysis 233

5.2.7 XANES Analysis 235

5.2.8 XPS Analysis 235

5.3 Results and Discussions 236

5.3.1 In vitro skin penetration using XRF 236

5.3.2 SAXS 245

5.3.3 XANES 247

5.3.4 XPS 250

5.4 Discussion 257

5.5 Conclusion 259

Chapter 6 Results of the effects of amorphous silica nanoparticles on Episkin™ small/reconstructed human epidermis (RhE) model 260

6.1 Introduction 260

6.2 Chemicals 263

6.2.1 Reagents 263

6.2.2 Colloidal Silica Nanoparticles 263

6.3 Reconstructed Human Epidermis (RhE) Model 264

6.4 MTT assay 265

6.4.1 Assessment of MTT Interference of the Test-Substance 265

6.4.2 Assessment of the Colour Potential of the Test-Substance 267

6.4.3 Treatment 268

6.4.4 Endpoint 268

6.5 Histology 271

6.5.1 Technique 271

6.5.2 Sample Preparation 271

6.5.2.1 Embedding 271

6.5.2.2 Sectioning 273

6.5.2.3 H&E Staining 273

6.5.2.4 Histological Evaluation 274

6.6 ELISA: Human Interleukin-1α (IL-1α) Immunoassay 274

6.6.1 ELISA Technique 274

6.6.2 Preparation of Reagents 275

6.6.3 Calibration Human IL1A Standard Preparation 275

6.7 Statistical Analysis 278

6.8 Results of *In Vitro* Skin Irritation Test 280

6.8.1 Tissue Viability Assessment (MTT assay) 280

6.8.2 Histology Assay 284

6.8.3 ELISA: Human Interleukin-1α (IL-1A) 285

6.9 Discussion 287

6.10 Conclusion 288

Chapter 7 Conclusions and Recommendations for Further Works ... 290

7.1 General Summary of Contents 290

7.1.1 Aim to characterise their physicochemical of commercial cosmetics and synthetic amorphous silica nanomaterials (SASs) using a multi-method approach 291

7.1.2 Aim to synthesise and characterise amorphous silica nanoparticles 293

7.1.3 Aim to study the skin penetration using reconstructed human full thickness skin model T-skin™ at Day 11 294

7.1.4 Aim to investigate the effects of aSiNPs on Episkin™ small/reconstructed human epidermis (RhE) model..... 295

7.2 Future Work..... 296

Appendix 299

References **300**

List of Figures

Figure 1.1: The number of nano-related patents held by the top 10 companies manufacturing cosmetics (Nanocolors, 2009). 1

Figure 1.2: U.S. nanosilica market volume, by product, 2014 – 2025 (kilo-tons); P type, S type, and Type III (Source: Grandview Research, 2017) 4

Figure 1.3: An illustration comparing sizes of various objects found in nature and engineered nanomaterials to give an idea of the nanoscale; adopted from (Saallah and Lenggoro, 2018). 8

Figure 1.4: A simplified representation of MNMs synthesis process (Ealias and Saravanakumar, 2017; Ovais *et al.*, 2017) 11

Figure 1.5: A classification of NMs based on their dimensionality (Poh *et al.*, 2018). 14

Figure 1.6: Schematic representation of skin and routes of penetration of chemicals. Source: (Abd *et al.*, 2016)..... 26

Figure 1.7: Representation of human skin and possible routes of NPs delivery across the skin, Adapted from (Larese Filon *et al.*, 2015; Gubala *et al.*, 2018a) 27

Figure 1.8: An example of the structure of reconstructed human skin models. 30

Figure 1.9: Possible NP transformations influencing potential effects of NP in biological organisms (Sharma *et al.*, 2018) 35

Figure 1.10: Schematic of the thesis structure 43

Figure 2.1: List of experimental techniques used in this study to characterise the aSiNP properties. 47

Figure 2. 2: Schematic illustration of the hydrodynamic diameter (D_h) and hydrodynamic radius (R_h) measured as the size of a hypothetical hard sphere that diffuses in the same fashion as that of a particle for different scenarios – single particle, NP aggregate, and non-spherical particle. 49

Figure 2.3: Schematic diagram of a sample being filtered through a syringe filter into a cuvette. 50

Figure 2.4: A schematic representation of zeta potential (Caputo and Roesslein, 2015). 52

Figure 2. 5: Graph showing the evaluation of the electrostatic stabilization of sample suspensions (Dey, Kumar and Samantaray, 2017). The point of zero charge is where all the surface charges and neutralised..... 53

Figure 2.6: Zeta potential cell (Lázaro García, 2014). 53

Figure 2. 7: Diagram demonstrating the beam path of Transmission Electron Microscopy (Ding, 2011). 55

Figure 2. 8: A schematic of STEM mode of Electron Microscopy (https://en.wikipedia.org/wiki/Scanning_transmission_electron_microscopy)... 57

Figure 2.9: Schematic of the operational features of SEM (Walock, 2012; Shelby, 2019). 58

Figure 2.10: The electron beam-sample interaction in SEM (Walock, 2012)... 59

Figure 2. 11: A schematic of the main components of the Synchrotron Light Source in Thailand (SLRI, 2015). The numbers above correspond to: (1) Electron gun, (2) Linear accelerator, (3) Booster Ring, (4) Storage Ring, (5) Beamline and (6) User workstation area. 61

Figure 2.12: Schematic representation of the scattering vector q; where k_i and k_s are the incident and scattered wave vectors, respectively, at scattering angle θ (Axel, 2017). 63

Figure 2.13: Schematic of 1D SAXS graph with the information that can be indicated at each q region (Bras *et al.*, 2010). 64

Figure 2.14: A simulation of the form factors, $P(q)$, of particles in the scattering pattern, representing the pattern of oscillations representative of the four different shapes/forms of particles (Organolithiums, 2014). 66

Figure 2.15: The sample holder with Kapton® tape for SAXS analysis of liquid samples. 67

Figure 2.16: The basis of photoelectric absorption, relaxation and Auger electron emission. 70

Figure 2.17: A survey spectrum, presenting certain elements on a sample surface and the elemental quantitation of their atomic percentages..... 71

Figure 2.18: Sample preparation for XPS analysis, mounted samples on the carbon tape and attached on the stainless-steel stage. 72

Figure 2.19: The mechanism of X-ray absorption at K-edge (K-edge absorption) 74

Figure 2.20: XAS spectrum of a standard sample shows two parts, namely XANES (in red-dash box) and EXAFS (in the green box), features..... 75

Figure 2.21: A standard powder of sample mounted on an acrylic plastic film for XAS analysis. 76

Figure 2.22: The interaction between incoming X-ray photons and material (Brouwer, 2010)..... 77

Figure 2.23: Standard discs of KBr (left) and sample (right). 79

Figure 2.24: The XRD pattern of a powdered sample is collected at 2θ from 5˚ to 90˚to provide insights into the crystal structure. 80

Figure 2.25: Schematic diagram of an XRD diffractometer system (Toth and Mathworks, 2017). 81

Figure 2.26: Schematic diagram of the ICP-OES technique (Caruso *et al.*, 2017). 85

Figure 3.1: Protocol of cosmetic preparation prior to characterisation, adopted (Lewicka *et al.*, 2011) 110

Figure 3.2: A standard of SiO_2 (quartz) mounted on an acrylic plastic film. ... 112

Figure 3.3: The sample holder with Kapton® tape for liquid sample 113

Figure 3.4: Particle size distributions of sample S1 reported by Z-average, is 156.9 nm. 117

Figure 3.5: Particle size distributions of sample S2 weighted intensity distribution (left) and number distribution (right) 118

Figure 3.6: Particle size distributions of sample S3 weighted intensity, reported the representative average size present in 32.73 nm. 119

Figure 3.7: Particle size distributions of sample S4 reported by Z-average, is 142.3 nm. 120

Figure 3.8: Particle size distributions of sample S5 reported by Z-average, is 87.93 nm. 121

Figure 3.9: Particle size distributions of sample S6 weighted intensity distribution, reported the representative average size present in 152.3 nm. 122

Figure 3.10: Particle size distributions of sample S7 reported by Z-average, is 134.6 nm. 123

Figure 3.11: Particle size distributions of sample S8 reported by Z-average, is 105.4 nm 124

Figure 3.12: The SAXS results of extracted cosmetic particles suspended in ultrapure water for the 8 studied cosmetics; S1-red, S2-dark blue, S3-blue, S4-light blue, S5-pink, S6-yellow, S7-cinnamon brown, S8-green lines..... 125

Figure 3.13: SEM images and EDS elemental atomic compositions (%) of the eight commercial cosmetics: (a) S1, (b) S2, (c) S3, (d) S4, (e) S5, (f) S6, (g) S7, and (h) S8 showing the morphology with low magnification, varying depending on the samples (see scale bars). 127

Figure 3.14: The survey spectra of eight cosmetics (S1-S8) presenting their surface elemental compositions. 129

Figure 3.15: High resolution XPS scans of the Si2p region found in the eight studied cosmetics (S1-S8)..... 130

Figure 3.16: High resolution XPS scans of the Ti2p region found in the eight studied cosmetics (S1 - S8)..... 130

Figure 3.17: The Si*K*-edge XANES spectra of commercial cosmetics (S1 - S8) presented in two groups, black and red lines, corresponding to two types of patterns in the positions of *K*-edge energy. 132

Figure 3.18: The Si*K*-edge XANES spectra of commercial cosmetics (S1 - S8) presenting the energy position of the first shell, and comparing this to the standard of quartz (black line) and silicon metal (red line). The red arrows pointed

the Si*K*-edge energy to identify the oxidative state of substances as well as the black arrows at the first position of spectra..... 133

Figure 3.19: The Ti*K*-edge XANES spectra of commercial cosmetics (S1 - S8), compared to a reference standard of anatase TiO_2..... 134

Figure 3.20: The Ti*K*-edge XANES spectra of commercial cosmetics (S1 - S8), compared to a reference standard of rutile TiO_2..... 134

Figure 3.21: X-ray diffraction pattern of a commercial cosmetic (sample 1 : Powder Foundation). The identified 2θ positions indicate talc- 2M ($Mg_3Si_4O_{10}(OH)_2$), silicon oxide (SiO_2), and potassium titanium vanadium phosphate ($K_2TiV(PO_4)_3$)..... 136

Figure 3.22: X-ray diffraction pattern of a commercial cosmetic (sample 2 : Skin crème oil free photo edition foundation). The identified 2θ positions indicate anatase, syn ($Ti_{0.72}O_2$) and cristobalite (SiO_2)..... 136

Figure 3.23: X-ray diffraction pattern of a commercial cosmetic (sample 3 : Shadow tint for eye). The identified 2θ positions indicate cobalt nickel chromium iron lanthanum oxide ($LaCr_{0.85}Fe_{0.05}Co_{0.05}Ni_{0.05}O_3$), magnesium aluminium silicon oxide ($Mg_6Al_{1.2}Si_{1.8}O_6$), titanium chromium oxide ($Ti_{0.93}Cr_{0.07}O_{1.965}$), and silicon oxide ($SiO_2$)..... 137

Figure 3.24: X-ray diffraction pattern of a commercial cosmetic (sample 4 : Sheertone Shimmer Blush). The identified 2θ positions indicate copper acetate hydroxide hydrate ($Cu_2(OH)_{3.1}(OCOCH_3)_{0.9}\cdot 0.7H_2O$), potassium magnesium gallium fluoride silicate ($KMg_3(GaSi_3O_{10})$), and manganese titanium oxide (Mn_2TiO_4 **α** – Mn_2TiO_4)..... 137

Figure 3.25: X-ray diffraction pattern of a commercial cosmetic (sample 5 : Matte Long Last Lipstick in Pink). The identified 2θ positions indicate anatase, syn ($Ti_{0.72}O_2$), sodium calcium aluminium chromium oxide silicate ($Na_6Al_6Si_6O_{24}(CrO_4)_2$), and n-hexatetracontane ($C_{46}H_{94}$). 138

Figure 3.26: X-ray diffraction pattern of a commercial cosmetic (sample 6 : Shade Eye shadow Palette). The identified 2θ positions indicate mica (K-Mg-Fe-Al-Si-O-H_2O), tris(μ3-hydroxo)-μ3-aceto-biscopper hydrate /copper acetate hydroxide hydrate ($Cu_2(OH)_3(CH_3COO)\cdot H_2O$), 2,6-dichloro-4-nitrophenol ($C_6H_3Cl_2NO_3$), zinc titanium oxide (Zn_2TiO_4 α-Zn_2TiO_4), and dysprosium gallium silver ($Ag_{3.8}Dy_3Ga_{7.2}$). 138

Figure 3.27: X-ray diffraction pattern of a commercial cosmetic (Sample 7 : Loose Face Powder). The identified 2θ positions indicate quartz, low (SiO_2), mica (K-Mg-Fe-Al-Si-O-H_2O), and zinc titanium oxide (Zn_2TiO_4 α-Zn_2TiO_4). 139

Figure 3.28: X-ray diffraction pattern of a commercial cosmetic (sample 8 : Blusher). The identified 2θ positions indicate anatase, syn ($Ti_{0.72}O_2$) and hauyne ($Na_6Ca_2Al_6Si_6O_{24}$)..... 139

Figure 3.29: The size distribution by intensity of SAS2000a**.** 144

Figure 3.30: The size distribution by intensity of SAS2001a**.** 145

Figure 3.31: The size distribution by intensity of SAS2002a**.** 145

Figure 3.32: The size distribution by intensity of SAS2004a**.** 146

Figure 3.33: The size distribution by intensity of SAS10404a**.** 146

Figure 3.34: Representative images of SAS2000a dispersed in UPW. The presence of slightly large aggregates can be observed. The histogram presents mean particle size (d_m) and size distribution..... 147

Figure 3. 35: Representative images of SAS2001a dispersed in UPW. The presence of slightly large aggregates can be observed. The histogram presents mean particle size (d_m) and size distribution..... 148

Figure 3.36: Representative images of SAS2002a dispersed into ultrapure water. The presence of slightly large aggregates can be observed. The histogram presents mean particle size (d_m) and size distribution..... 149

Figure 3. 37: Representative images of SAS2004a dispersed in UPW. The presence of slightly large aggregates can be observed. The histogram presents mean particle size (d_m) and size distribution..... 150

Figure 3. 38: Representative images of SAS10404a dispersed into ultrapure water. The presence of slightly large aggregates can be observed. The histogram presents mean particle size (d_m) and size distribution..... 151

Figure 3.39: The unified exponential-power law describes scattering data based on Beaucage's law. 153

Figure 3.40: The fitted SAXS graph of SAS2000a shows that the diameter (2Rg1) is 19.29 nm, the error ranges of the size distribution (s) is 3.17 and slope (P) is 3.94. 154

Figure 3.41: The fitted SAXS graph of SAS2001a shows that the diameter (2Rg1) is 23.43 nm, the error ranges of the size distribution (s) is 3.67 and slope (P) is 3.83. 155

Figure 3.42: The fitted SAXS graph of SAS2002a shows that the diameter (2Rg1) is 16.74 nm, the error ranges of the size distribution (s) is 2.45 and slope (P) is 3.64. 155

Figure 3.43: The fitted SAXS graph of SAS2004a shows that the diameter (2Rg1) is 18.69 nm, the error ranges of the size distribution (s) is 3.28 and slope (P) is 3.97. 156

Figure 3.44: The fitted SAXS graph of SAS10404a shows that the diameter (2Rg1) is 21.62 nm, the error ranges of the size distribution (s) is 3.65 and slope (P) is 3.93. 156

Figure 3.45: X-ray diffraction patterns of the 5 SAS studied: a) SAS2000a, b) SAS2001a, c) SAS2002a, d) SAS2004a, and e) SAS10404a. 158

Figure 3.46: The diffraction pattern of the five SAS presenting the position and intensity of structural peaks, and indicating amorphous form of silicon dioxide. 159

Figure 3. 47: Survey spectra of the five SAS, presenting the elemental compositions found on the surface. 161

Figure 3.48: High resolution XPS scans for the Si2p region of the five SAS.. 162

Figure 3.49: The EXAFS spectrum of standard quartz presents the pre-edge peak (A), the main transition peak (B), Si*K*-edge peak (C), peak D – G in both K-edge and L-edge corresponds to a crystal structure of quartz (Li *et al.*, 1994). 164

Figure 3.50: The normalized Si*K*-edge EXAFS spectra of five SASs; a) SAS2000a, b) SAS2001a, c) SAS2002a, d) SAS2004a, e) SAS10404a. 165

Figure 3.51: Si*K*-edge XANES (left) and EXAFS (right) spectra of SASs comparing them to silicon metal and quartz. 166

Figure 3. 52: Si*K*- edge XANES spectra of SASs comparing to Si found in cosmetics. 167

Figure 3.53: SEM images of the five SAS; (a) SAS2000a, (b) SAS2001a, (c) SAS2002a, (d) SAS2004a, (e) SAS10404a. 168

Figure 4.1: Depiction of the overall basic reactions in the sol-gel process, forming amorphous silica nanoparticles. 183

Figure 4.2: A picture of the synthesis procedure: the mixture solution is prepared from water and L-lysine to be homogeneous by agitation for 1 hour, then TEOS is added in the system and afterwards the filtration process takes place: the suspension is pumped through a micropore filter (MWCO 1 kDa), placed tangential flow to enable the separation of particles from impurities; the former is retained, whereas the latter goes through the permeable membrane. 184

Figure 4.3: Mechanism of aSiNP nucleation by addition of water and L-lysine as a precursor and catalyst. TEOS was hydrolysed to all possible derivatives and then condensed to form oligomeric precursors and primary seeds. The formation of primary seeds contributes to particle growth (Dixit *et al.*, 2016). 185

Figure 4.4: Particle size distribution of the original aSiNPs, showed some aggregate peaks. 189

Figure 4.5: Particle size distribution of aSiNPs, sonicated the sample 10 minutes to reduce aggregation. 190

Figure 4.6: a), b), and c) Size distribution for aSiNPs batch number 1, 2, and 3, exposed to room temperature (20-24˚C) as various time points..... 192

Figure 4.7: Representative TEM images [(A) - (C)] of the synthesised silica nanoparticles; scale bar 50 nm..... 194

Figure 4.8: Histogram depicting size (nm) versus frequency for aSiNP suspension. 195

Figure 4.9: Examples of STEM micrographs [A-D] for SiNPs, scale bar 10 nm. 196

Figure 4.10: Histogram showing size distribution of 320 aSiNPs measured by STEM. 196

Figure 4.11: SAXS results of aSiNPs suspended in ultrapure water, the 1D pattern showed in the blue line. The fitted curve (red line) composed of two structural levels using SASFit software; the fit was based on a model of a sphere with the lognormal distribution regarding the slope of SAXS pattern (=3.538). 199

Figure 4.12: The fitted SAXS graph of aSiNPs shows the mean radii (X) are 1.64 and 7.18 nm, and the error ranges of the size distributions (s) are 0.53 and 0.57 respectively. 199

Figure 4.13: The SAXS scattering pattern and size distributions from BAM, Germany composed of two structural levels using McSAS 1.3.1; the fitted curve (red line) was a spherical model based on lognormal distribution. Histogram showed bimodal distribution of particles; radius size 3.964 and 8 nm. 201

Figure 4.15: SEM images of amorphous silica nanoparticle powder that were synthesized by a sol-gel process, scale bar 500 nm. 203

Figure 4.14: Scattering profiles of aSiNP suspension; (A) Batch 1, (B) Batch 2, (C) Batch 3 (D) Scattering pattern of Silica sphere (quartz). http://bigbro.biophys.cornell.edu/documents/SAX_Calibrants/kjejan3.png..... 204

Figure 4.16: XRD diffractogram of the powdered aSiNPs..... 205

Figure 4.17: A calibration graph of standard Si..... 207

Figure 4.18:. XPS survey spectra (a) and high resolution XPS spectra in the Si2p (b) and O1s (c) regions. 209

Figure 4.19: The Si*K*-edge XANES spectra of synthesised aSiNP are shown in black, red, and green lines and compared with silica (quartz) (blue line). 210

Figure 4.20: FTIR spectrum of synthesised amorphous silica NPs washed once in ultrapure water..... 211

Figure 4.21: FT-IR spectrum of synthesised amorphous silica nanoparticles obtained from the sol-gel process, following repeated three times purification. 213

Figure 4.22: Comparison between FT-IR spectra of each of the three synthesised amorphous silica nanoparticle batches, which are in good agreement and their peaks corresponded to Figure 4.21. 214

Figure 4.23: FT-IR spectra of synthesised amorphous silica nanoparticles obtained from the sol-gel process after calcination. 215

Figure 5.1: Morphology of the Full Thickness Human Skin Model-T skin Batch No: 18-SKIN-028; reprinted with permission of EpiSkin™..... 226

Figure 5.2: Representative photos of the reconstructed human full thickness skin model at Day 11 attaches in the insert, Batch No: 18-SKIN-028 EpiSkin™; presents a side view (left), a top view (middle), and a bottom view (right). 227

Figure 5.3: Schematic of different layers of the D11 model and its appendages. 227

Figure 5.4: Schematic of protocol for skin penetration testing; Part 1: Inspection (Left) and Part 2: Skin model Preparation (Right)..... 228

Figure 5.5: Schematic of protocol for skin penetration testing; Part 3: Topical Application on D11 models. 229

Figure 5.6: Thermax strip indicator is used to investigate an exposure of temperature during the skin model delivery. 230

Figure 5.7: Representative photo of a cross-sectioned D11 tissue at 70 µm thickness exposure to colloidal aSiNPs at 0.1 mg/mL concentration. The white rectangular is the randomized area for XRF analysis. X axis and Z axis are the width and length, respectively. 232

Figure 5.8: Representative photo of a biopsy punched-off D11 tissue exposure to colloidal aSiNPs at 10 mg/mL concentration. 232

Figure 5.9: Samples of D11 tissues exposed to aSiNPs at 10 mg/mL (left) and 0.1 mg/mL (right) for analysing by SAXS. 234

Figure 5.10: A punch biopsy of D11 tissue (left) exposed to MilliQ water. The rectangular box (black box) scanned, had an area size 0.252 mm^2. µ-XRF reference spectrum (right: black line) is correlated with the specific energy (eV) measured for each element (red line), so the range of elemental compositions found in the D11 tissue was identified. 237

Figure 5.11: Representative image showing the surface area where µ-XRF scanned from the uppermost of D11 to 30 µm depth for the sample exposed to aSiNPs at 0.1 mg/mL concentration, size 0.396 mm^2 (left). The distribution map of Si (right), showing the accumulation amount of aSiNPs. 238

Figure 5.12: Representative image showing the surface area where µ-XRF scanned from the uppermost of skin to 30 µm depth for the sample exposed to

aSiNPs at 10 mg/mL concentration, size 0.27 mm^2 (left). The surface distribution map of Si (right), showing the accumulation amount of aSiNPs. 239

Figure 5.13: Representative image (sample no. 1 exposed to aSiNPs at 10 mg/mL) showing a cross-section of D11 tissue (left) and the presence of Si across the skin model represented by the white box. The colour scale bar is calibrated to show the relative concentration of Si found in the skin from no detection (blue) to high amount (red colour) (right). 242

Figure 5.14: Representative image (sample no. 3 exposed to aSiNPs at 10 mg/mL) showing a cross-section of D11 tissue (left) and the presence of Si across the skin model, represented by the white box. The colour scale bar is calibrated to show the relative concentration of Si found in the skin from no detection (blue colour) to high amount (red colour) (right). 243

Figure 5.15: Representative image (sample no. 1 exposed to aSiNPs at 0.1 mg/mL) showing a cross-section of D11 tissue (left) and the presence of Si across the skin model, represented by the white box. The colour scale bar is calibrated to show the relative concentration of Si found in the skin from no detection (blue colour) to high amount (red colour) (right). 243

Figure 5.16: Representative image (sample no. 3@exposed to aSiNPs at 0.1 mg/mL) showing a cross-section of D11 tissue (left) and the presence of Si across the skin model, represented by the white box. The colour scale bar is calibrated to show the relative concentration of Si found in the skin from no detection (blue colour) to high amount (red colour) (right). 244

Figure 5.17: The SAXS scattering profile results for aSiNPs interspersed into the D11 tissue, fitted using SAXSsPy with a spherical model. The form factors and structure factor were present in the SAXS curve. 246

Figure 5.18: SAXS curve results for the particle sizes of aSiNPs interspersed into the D11 tissue 247

Figure 5.19: Representative Si*K-edge* XANES spectra of Si found in the skin tissue models. The spectra represent the starting suspension and powder compared to referenced standard materials: amorphous silica (SiO_2; 4+) and silicon powder (Si; 0). 249

Figure 5.20: Wide Scan of Comparative Binding Energies from the samples of D11 tissues, Top: Negative Control-UPW (NC_{UPW}), Middle: Si-Low is the D11 skin exposure to 0.1 mg/mL of aSiNPs and Bottom: Si-H is the D11 skin exposure to 10 mg/mL using XPS. 251

Figure 5.21: XPS spectra of the Ca2p, Si2p, Cl2p, N1s, O1s, and C1s signals acquired from the D11 tissue exposure to 0.1 mg/mL of aSiNPs. Black lines are the spectra collected, while the red lines are the result of peak fitting. 252

Figure 5.22: XPS spectra of the Ca2p, Si2p, Cl2p, N1s, O1s, and C1s signals acquired from the D11 tissue exposure to 0.1 mg/mL of aSiNPs. Black lines are the spectra collected, while the red lines are the result of peak fitting. 252

Figure 5.23: The peak fitting of the Ca2p, Si2p, Cl2p, N1s, O1s, and C1s signals acquired from the D11 tissue exposure to 0.1 mg/mL of aSiNPs. 254

Figure 5.24: The peak fitting of the Ca2p, Si2p, Cl2p, N1s, O1s, and C1s signals acquired from the D11 tissue exposure to 10 mg/mL of aSiNPs. 255

Figure 6.1: Morphology of the RhE/S/17 model, Batch No: 18-EKIN-015; reprinted with permission of EpiSkin™. 264

Figure 6.2: Images from experiments investigating potential reaction between the aSiNPs suspensions of this study and the MTT assay. Ultrapure water was used as a control (i.e. no interaction substance/no MTT-reducer); picture (a) shows the solutions' colour before and picture (b) after 3 h incubation. 266

Figure 6.3: Examples of testing the colour potential of the aSiNP suspensions; (a) and (b) the colour of the suspension before and after shaking for 15 minutes. 267

Figure 6.4: Three tissue exposures, each aliquoted in duplicate are shown here with the formazan added, leading to 6 wells per treatment. (a) Blank wells, (b) negative control (NC_{PBS}) wells, (c) positive control (PC_{SDS}) wells, (d) aSiNPs treated wells. 270

Figure 6.5: An example of preserved tissues from skin irritation testing..... 272

Figure 6.6: Embedded RhE tissue in OCT solution on a square sample block. 272

Figure 6.7: Embedded sample in liquid nitrogen until tissue and OCT harden. 272

Figure 6.8: Samples (frozen sections) ready for thin sectioning. 273

Figure 6. 9: The calibration curve provides the relationship between the concentration of Human IL-1α (X-axis) and OD value (Y-axis), demonstrating in the quadratic equation. 276

Figure 6.10: Human IL-1α Standard solutions having acquired blue shading by adding TMB colour-developing reagent..... 277

Figure 6.11: Human IL-1α Standard solutions having acquired yellow shading by adding TMB stop solution 278

Figure 6.12: RhE models were exposed to PBS, SDS, and aSiNPs for 15 minutes and assessed % viability by MTT. Data are shown as the individual results for 3 tissue replicates tested over 3 independent experiments; 1. PBS (1-3), 2. SDS (4-6), and 3. aSiNPs (5-9). 284

Figure 6.13: Histology of REH models stained with H&E following exposure to PBS, SDS and aSiNPs, scale bars 50 µm. SDS treated-tissues showed more keratinocytes without a nucleus than aSiNPs treated-tissues (red arrows). ... 285

Figure 6.14: Immune response, measured as Human IL-1α released from RhE models after exposure to PBS, SDS and aSiNPs. The concentration of human IL-1α was assessed by ELISA, with results were presented in pg/mL. Data are expressed as mean±SE from three independent experiments. *(F(2,6) = 13.369)* 287

List of Tables

Table 1.1 Examples of Nanomaterials (NMs) and where they may be found..... 9

Table 1.2 Examples of Manufactured Nanomaterials (Ju-Nam and Lead, 2008; Keller and Lazareva, 2013; Hochella *et al.*, 2019)..... 11

Table 1.3 Classification of nanomaterials based on chemical composition..... 12

Table 1.4 Physicochemical properties of NMs that influence behaviour and toxicity. 15

Table 1.5 Overview of synthetic aSiNPs, relevant properties and applications 17

Table 1.6 Examples of NP applications in cosmetics and personal care products 22

Table 1.7 Examples of reconstructed skin models available on commercial market (Wever, Petersohn and Mewes, 2013). 29

Table 1.8 Examples of physicochemical properties of NPs affecting or enhancing skin penetration and permeation (Williams and Barry, 2012; Nafisi and Maibach, 2018). 32

Table 1.9 Examples of in vitro studies assessing skin cytotoxicity of SiNPs (Nafisi, Schäfer-Korting and Maibach, 2015). 36

Table 2.1 Methods used for characterising nanoparticles. 95

Table 3.1 Product information as presented in the labels of the eight commercial cosmetics containing silica-based material characterised in this study. 102

Table 3.2 Synthetic Amorphous Silica Nanomaterials (SASs) obtained from the JRC reference test material collection 107

Table 3.3 The details of experimental techniques used for characterisation of SASs and cosmetics. 107

Table 3. 4 The hydrodynamic diameter, Z- average and PdI of materials in nanoscale found in the eight studied cosmetics determined using DLS. 116

Table 3.5 Information on commercial cosmetics (S1 - S8) obtained by XPS, and presented as percentage of atomic composition. 128

Table 3. 6 The information of binding energy of Si2p, O1s and C1s to determine the chemical structure on the surface..... 129

Table 3. 7 Details of the crystalline substances identified by XRD in the studied cosmetics; the substances were identified by matching the diffractogram peaks with those of the reference XRD library. 140

Table 3. 8 The average zeta potential values, standard deviation, mobility, and conductivity of the eight cosmetics. 141

Table 3. 9 The hydrodynamic diameter, Z- average, and PdI measured by using DLS measurements..... 144

Table 3. 10 Details of the fitted parameters obtained from the scattering patterns of the five SAS using unified exponential power law. 153

Table 3. 11 Information of composition obtained from XPS for the five SAS samples and presented in percentage of atomic composition. 161

Table 3.12 Information on the binding energy of Si2p and O1s, used to determine the chemical structure on SASs' surfaces. 162

Table 3. 13 Surface area, C value and correlation coefficient of SASs measured by SA 3100 surface analyser..... 170

Table 3.14 The comparison of the surface areas between the observations in this study and the results of IMC-BAS. 171

Table 3.15 Summary of a set of techniques used for the characterisation of NPs in cosmetics...... 173

Table 4.1 Chemicals and materials used 180

Table 4.2 Amount of chemicals used for the synthesis of aSiNPs 182

Table 4.3 pH and conductivity value of aSiNP suspensions 182

Table 4.4 The experimental techniques used for characterisation of aSiNP.. 186

Table 4.5 The hydrodynamic diameter, Z-average and PDI of aSiNPs using DLS method 189

Table 4.6 The average zeta potential values and standard deviation for the samples of aSiNPs. 192

Table 4.7 SAXS data showing the two distinct populations of particle sizes from different batches of aSiNPs, measured at 10 mg/mL concentration. 198

Table 4.8 Particle size characterisation of aSiNPs..... 202

Table 4.9 The surface area of Synthesized Amorphous Silica Nanomaterials205

Table 4.10 Silicon concentration from synthesis as measured by ICP-OES.. 207

Table 4.11 Surface composition and atomic concentration (%) calculated from the spectra of elements. 208

Table 4.12 Evaluation of analytical methods for physicochemical characterisation of synthesized amorphous silica nanoparticles. 218

Table 5.1 Peak Position for all samples. 256

Table 6.1 Quality controls of RhE/E17 (Batch no. 18-EKIN-015) from EpiSkin™ 265

Table 6.2 Assay acceptance criteria for the Episkin™ Skin Irritation Test 270

Table 6.3 The prediction model of skin irritation potential from the UN GHS and EU CLP classification to hazard communicate in the form of labelling for skin irritation..... 270

Table 6.4 Test of Normality of MTT and ELISA data of treatments (PBS, SDS and aSiNPs) 279

Table 6.5 Test of Homogeneity of Variances 279

Table 6.6 The OD values and %Viability of the tissues used in the test conditions; PBS, SDS and aSiNPs 280

Table 6.7 Reporting results from a one-way *ANOVA* 282

Table 6.8 Pairwise comparisons by post-hoc Tukey's test. 283

Table 6.9 Reporting results from a one-way *ANOVA* 286

Table 6.10 Pairwise comparisons by post-hoc Tukey's test. 286

List of Abbreviations

Term	Explanation / Meaning / Definition
%NSC$_{living}$	Percentage of non-specific colour value of living tissue
%NSMTT	Percentage of non-specific reduction of MTT
˚C	Degrees Celsius
0D	zero dimension
1D	one dimension
2D	two dimensions
3D	three dimensions
ADF	Annular dark field
Ag	Silver
Al_2O_3	Aluminium oxide
ANOVA	Analysis of variance
aSiNPs	amorphous silica nanoparticles
a-SiO2	Amorphous silica
ATR	Attenuated total reflectance
Au	Gold
AuNPs	Gold nanoparticles
B	A pre-factor specific to the type of power-law scattering.
BAM	Bundessanstalt für Materialforchung und-prüfung
BET	Brunauer-Emmett-Teller
BF	Bright field
B$_s$	A pre-factor specific to the type of power-law scattering.
C$_{BET}$	BET constant
C	Carbon
C60	Fullerenes
$C_6H_{14}N_2O_2$	L-lysine monohydrate
Ca	Calcium
CaSi	Calcium Silicide
CdSe	Cadmium selenide
CeO_2	Cerium dioxide

CLP	Classification, labelling and packing regulation
cm^{-1}	Wavenumber
cm^2	square centimetre
CNT	Carbon nanotube
Co	Cobalt
CO_2	Carbon dioxide
Cu	Copper
CV	The coefficient of variation
D	Transitional diffusion coefficient
d	distance between diffracting planes
D11	reconstructed human full thickness skin model/T skin no. Day 11
Da	Dalton
DCM	A double crystal monochromator
Dh	Hydrodynamic Diameter
DLS	Dynamic light scattering
D-PBS	Dulbecco's phosphate buffered saline
DPPH	2,2-diphenyly-1-picrylhydrayl free radical assay
EC	European Commission
ECETOC	European Centre for Ecotoxicology and Toxicology of Chemicals
ECHA	European Chemicals Agency
EDL	Electron double layer
ELISA	Mobil composition of matter no.41
EU	European Union
EUON	European Union Observatory for Nanomaterials
Fe	Iron
Fe_3O_4	Magnetite
FeO	Iron oxide
FT-IR	Fourier-transform infrared spectroscopy
G	Guinier pre-factor of the larger structure
GBP	Great British Pound
$GDA3F^+$	A fresh culture media
GeV	Giga electron volt
G_{gauss}	Gaussian distribution function

GM-CSF	Granulocyte-macrophage colony stimulating factor
G_s	The Guinier pre-factor of the smaller structure
η	Viscosity
h	hour
H&E	Haematoxylin and eosin stain
HAADF	High angle annular dark field
HaCaT	Human keratinocyte line
HCl	Hydrogen chloride
HES	Histology scoring
HNO_3	Nitric acid
hv	photon of X-ray
I(0)	forward scattering intensity
I(q)	scattering intensity
$I_0(E)$	transmitted X-ray intensity
$I_1(E)$	incident X-ray intensity
ICP-OES	Inductively coupled plasma-optical emission spectroscopy
IFNg	Interferon gamma
IL-1α	Interleukin-1 alpha
InP	Indium platinum
ISO	International Organization for Standardization
JRC	(European Commission's) Joint Research Centre
k_{Boltz}	Boltzmann’s constant
K	Potassium
K a	K level
KBr	Potassium bromide
kDa	kilodalton
k_i	incident vector
k_s	scattered wave vector
kV	kilovolt
λ	wavelength
LC	Langerhans cells
LC-SiNP	Lipid-coated silica nanoparticle
LDH	lactate dehydrogenase
LEDs	Light emitting diodes

m^2	square meter
mbar	millibar
MCM-41	Mobil composition of matter no. 41
MEM	Minimum essential medium eagle
MeV	Mega electron volt
mg	milligram
Mg	magnesium
mg/mL	milligram per millitetre
mm	millimetre
mmol/mL	millimole/millilitre
MNMs	Manufactured nanomaterials
mrad	milli radian
mS/cm	milli Siemens per centimetre
MTT	3-(4,5-Dimethylthiazol-2-yl)-2,5-diphenyltetrazolium bromide
mV	millivolt
MWCO	Molecular weight cut-off
n	An integer
N_2	Nitrogen gas
n_a	Adsorbed gas quantity in volume units
NC	Negatively Charged
NC_{UPW}	Negative control of ultrapure water
NC_{PBS}	Negative control of phosphate buffered saline
N-H	Amine group
nm	nanometre
n_m	monolayer capacity
NMs	Nanomaterials
NP	Nanoparticle
NPs	Nanoparticles
NRU	neutral red uptake
O	Oxygen
OCT	Optimal cutting temperature
OD	Optical density
OECD	Organization for Economic Co-operation and Development
p	equilibrium pressure of adsorbates at the temperature of adsorption

P(q)	form factor
p_0	saturation pressure of adsorbates at the temperature of adsorption
PBS	Phosphate buffered saline
PC	Positive control
PC_{SDS}	Positive control of sodium dodecyl sulphate
PdI	Polydispersity index
PES	Polyethersulfone
PSD	Particle size distribution
θ	Theta
q	scattering vector
QDs	Quantum dots
qR	slope of the plot of scattering intensity versus the scattering vector
R	radius of spherical particle
r_e^-	electron density function (distribution)
r	correlation coefficient
ρ_0	Electron density distribution
R^2	coefficient of determination
REACH	Registration, Evaluation, Authorisation& restriction of Chemicals
Rg	Radius of gyration
Rh	Hydrodynamic Radius
RhE	Reconstructed human epidermis skin model
RNA	Ribonucleic acid
rpm	round per minute
Rsub	Surface-fractal cut-off radius of gyration.
s	Standard deviation
S(q)	structure factor
S1	Powder foundation: cosmetic sample number 1
S2	Skin crème oil free photo edition foundation: cosmetic sample number 2
S3	Shadow tint for eye: cosmetic sample number 3
S4	Sheertone shimmer blush: cosmetic sample number 4
S5	Matte long last lipstick in pink: cosmetic sample number 5
S6	PS 9 shade powder eye shadow pallete: cosmetic sample number 6

S7	Loose face powder: cosmetic sample number 7
S8	Blusher: cosmetic sample number 8
SAS10404a	Thermal synthetic amorphous silica nanomaterials number 10404a
SAS2001a	Precipitated synthetic amorphous silica nanomaterials number 2001a
SAS2002a	Thermal synthetic amorphous silica nanomaterials number 2002a
SAS2004a	Precipitated synthetic amorphous silica nanomaterials number 2004a
SAS200a	Precipitated synthetic amorphous silica nanomaterials number 2000a
SASs	Synthetic amorphous silica nanomaterials
SB	Stratum basale
S_{BET}	Specific surface area
SC	Stratum corneum
SCCS	(European Commission) Scientific Committee on Consumer Safety
SD	Standard deviation
SDS	Sodium dodecyl sulphate
SEM-EDS	Scanning electron microscopy-electron density spectroscopy
SG	Stratum granulosum
Si-C	D11 tissue exposed to colloidal aSiNPs at 010 mg/mL
SiK-edge	Silicon K level
Si-Low	D11 tissue exposed to colloidal aSiNPs at 0.1 mg/mL
SiNPs	Silica nanoparticles
SiO_2	Silicon dioxide
Si-O-C	Alkyl group
Si-OH	Silanol group
SL	Stratum lucidum
SLRI	Synchrotron Light Research Institute
SS	Stratum spinosum
STEM	Scanning Transmission electron microscopy
T	Absolute temperature
TEM	Transmission electron microscopy
TEOS	Tetraethyl orthosilicate
TiO_2	Titanium dioxide

TMB	3,3’,5,5’-Tetramethylbenzidine
TNF-a	Tumour necrosis factor alpha
UN GHS	United Nations Globally Harmonized System of Classification and Labelling
UPW	Ultrapure water
USD	United States Dollar(s)
USEPA	United States Environmental Protection Agency
UV	Ultraviolet radiation
UVA	Ultraviolet radiation A
UVB	Ultraviolet radiation B
v/v	volume by volume
WAXS	Wide angle X-ray scattering
WNC	Weakly Negatively Charged
XAS-EXAFS	X-ray absorption spectroscopy-extended X-ray absorption fine structure spectroscopy
XAS-XANES	X-ray absorption spectroscopy-X-ray absorption near edge spectroscopy
XPS	X-ray photoelectron spectroscopy
XRD	X-ray Diffraction
Z-avg	Z average diameter
ZnO	Zinc oxide
ZnSe	Zinc selenium
ZP	Zeta potential
μ	mean (radius)
μ(E)	function of energy
μg/mL	microgram/millilitre
μL	micro Litre
μm	micrometre
Mm/Vs,cm/Vs	micrometre or centimetre/volt second
μ-XRF	Micro-X-ray fluorescent spectroscopy

Chapter 1 Introduction

1.1 Overview

The global cosmetics marketplace was worth approximately GBP 431 billion (USD 532 billion) in 2017 and is expected to reach GBP 651.40 billion (USD 805.61 billion) by 2023 (Orbis Research, 2018). The global market share is highest for Europe and North America but expanding into other global marketplaces also (Grandview Research, 2017). Raj *et al*. (Raj *et al.*, 2012) reported on the top 10 cosmetic manufacturing companies and the number of nano-related patents filed since 2000 throughout 2008 (as shown in **Figure 1.1**).

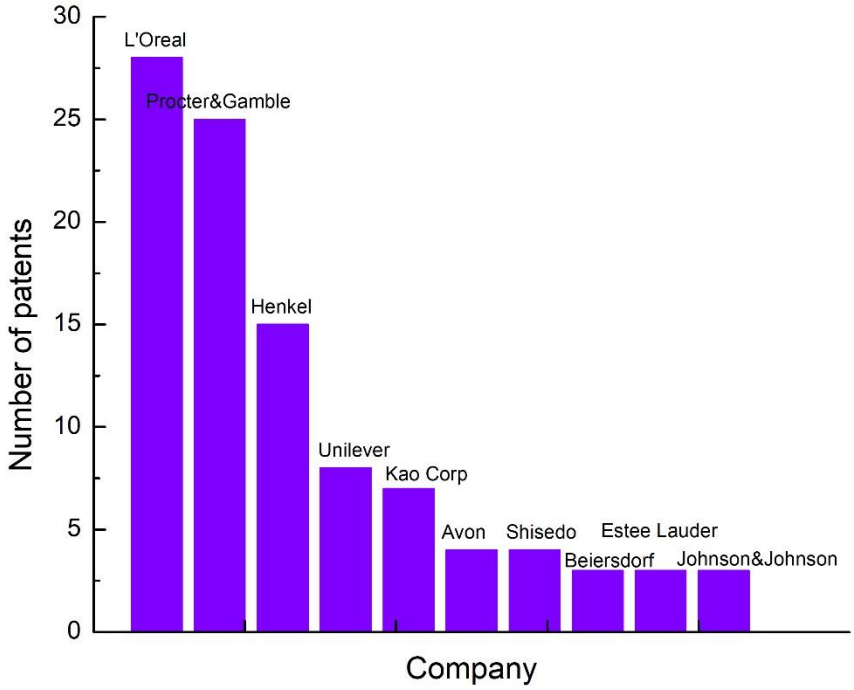


Figure 1.1: The number of nano-related patents held by the top 10 companies manufacturing cosmetics (Nanocolors, 2009).

Nanomaterials (NMs) such as titanium dioxide, carbon black and silicon dioxide are used extensively in a wide range of cosmetic products. While innovations are introduced to activate the unique nanoscale-related properties, there may also be unintended consequences, that need to be considered in parallel. For example, in the case of nanotechnology enabled cosmetics, NMs enhance cosmetics' properties, i.e. appearance, performance, physical stability whereas drawbacks of their use are that they can be (or perceived to be) harmful to humans and the environment. With their increasingly widespread use, human exposure will certainly increase with likely further impact on the environment, necessitating investigation into their potential toxicity (Juliano and Magrini, 2017).

Use of nanomaterials in various products, such as plastics (composites), concrete, electronics, medicines, personal care products and cosmetics is now common, and many such products are already in the market. This fact development is the result of the special properties introduced to the products, or because they enable more efficient use of resources given their increased surface to volume ratio (Borm *et al.*, 2006). However, despite their advantages, NMs have also been reported to show adverse effects on skin, by in vitro, in vivo, and ex vivo studies (Gamer, Leibold and Van Ravenzwaay, 2006; Filipe *et al.*, 2009; Barillet *et al.*, 2010; Labouta, Liu, *et al.*, 2011; Goldstein *et al.*, 2014; Zhu *et al.*, 2014; Adib *et al.*, 2016; Raju *et al.*, 2018). Cosmetics manufacturers are now required to provide specific data relevant not only to the health and safety of cosmetics, but also to the raw materials and to include other technical information in accordance with EU legislation (The European Commission, 2014).

2231 consumer products claim to contain NMs in the European consumer market (Foss Hansen *et al.*, 2016), in particular, cosmetics and personal care products. The principle nanomaterials used in cosmetics are silver, fullerene, gold, alumina, titanium, copper, platinum and silica (Raj *et al.*, 2012; EU, 2016). One of the most abundant NMs in cosmetics manufacturing is amorphous silica nanoparticles (aSiNPs), which are silicon dioxide nanoparticles and its agglomerates where the size of the primary particles are between 1 and 100 nm (Dekkers *et al.*, 2013). Silica in amorphous form existing in nature is generally non-toxic to human, by contrast crystalline forms, such as quartz and cristobalite, are toxic and linked to a human lung cancer, (https://www.cancer.gov/about-cancer/causes-prevention/risk/substances/crystalline-silica).

According to Grandview Research (2017), demand for silica nanoparticles has increased since 2014 and is expected to continue increasing in the U.S. market, (see **Figure 1. 2**). P type silica has been used by the construction and commercial building sectors, while S type can be applied as high content filler material for several applications, such as cosmetics, healthcare and medicine manufacturing. Additionally, Type III has been used in rubber and food manufacturing.

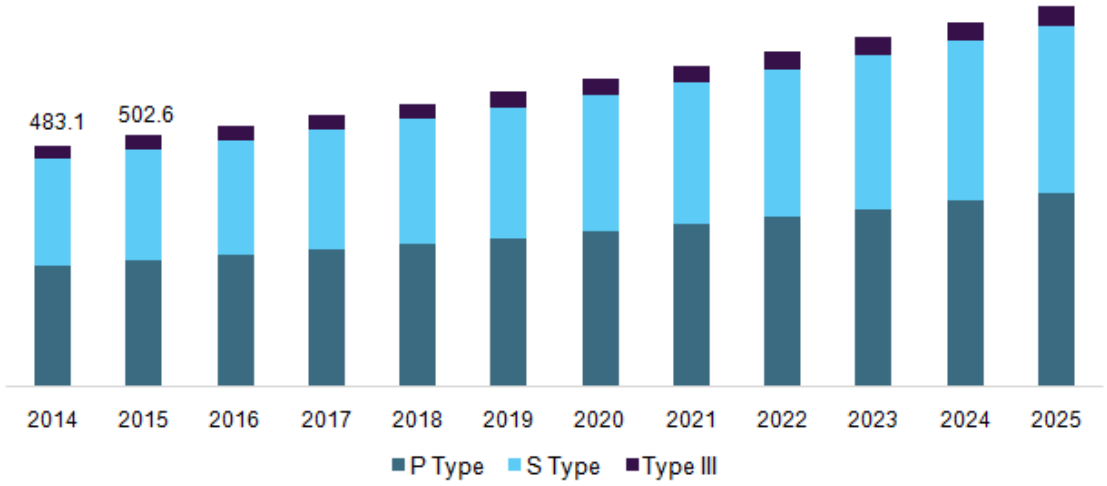


Figure 1.2: U.S. nanosilica market volume, by product, 2014 – 2025 (kilo-tons); P type, S type, and Type III (Source: Grandview Research, 2017)

Synthetic aSiNPs exist in different forms and have been produced by various methods (more information in section 1.5) in several million tons for decades (Vance *et al.*, 2015). For example, it is being used as an emulsifier in cosmetic powders because of its excellent dispersibility and its ability to enhance rheological properties, enhancing cosmetic appearance, texture and shelf life and enabling high pigment levels in cosmetics. Silica nanoparticles are also synergistic and compatible with other ingredients used in cosmetics (Nafisi and Maibach, 2015) allowing ease of formulation.

Only a few studies are currently available that have investigated the safety aspects of silica nanoparticles (SiNPs) despite their widespread use in products (Froggett *et al.*, 2014). For example, size-related cell penetration of SiNPs has been reported along with generation of free radicals and reactive oxygen species (ROS) (Nel *et al.*, 2006; Nabeshi *et al.*, 2010; Krug and Wick, 2011; Park *et al.*, 2013; Liang *et al.*, 2014; Ryu *et al.*, 2014). Additionally, aSiNPs with positive surface charge can enhance the mechanism of skin penetration

(Rancan *et al.*, 2012); similar effects have been seen with gold nanoparticles (Hao *et al.*, 2017). However, SiNPs with strong negative charge have been reported to be more toxic to skin cells than SiNPs with weak negative charge (Quignard *et al.*, 2012; Park *et al.*, 2013; Ryu *et al.*, 2014). It has been found that 20 nm aSiNPs can decrease toxicity of 2,4-dinitrofluorobenzene, which induces contact hypersensitivity (Palmer *et al.*, 2019), whereas 70 nm aSiNPs when topically applied at high doses of 125 µg/ear/day showed minimal effects on the healthy skin of mice (Matsuo *et al.*, 2016).

The relative lack of information on the safety of aSiNPs and the often conflicting evidence in the nanotoxicity literature is a major limitation to the development of cosmetics products containing NPs, and highlights a need for standardised toxicity testing to allow direct comparison of study results. Indeed, the advantages and drawbacks of synthetic aSiNPs are still unknown due to the limited physicochemical characterization provided in most studies of the toxicity or environmental fate and mechanisms of interaction of aSiNPs with cells. Previous research of the physicochemical characteristics of aSiNPs with different properties, i.e. size, shape, surface charge and zeta potential are contradictive, as mentioned above, demonstrating a need for these data to be discussed extensively and for additional work on assessing relevant properties to be carried out, to enable grouping for risk assessment to be performed. Advancements in physicochemical characterisation of nanoparticles enhance knowledge on their reactivity and toxicity variations and support greater accuracy of health risk assessments for cells and organisms (including humans). The cytotoxic effect is often due to NP characteristics, such as morphology, size, shape, surface area and surface charge. The correlation of

cytotoxic effect and particle size has been studied as mentioned above, small size of amorphous silica showed higher cytotoxicity of *in vitro* experiment for nonphagocytic cells (Lin *et al.*, 2006; He *et al.*, 2009; Al-Rawi, Diabaté and Weiss, 2011). On the other hand, in a study of phagocytic cells silica microparticles induce higher cell damage than to NPs (Chong *et al.*, 2005; Morishige *et al.*, 2010). NPs may cause damage or bind to the cell membrane and this may be followed by production of reactive oxygen species (ROS), increase of intracellular Ca^{2+} levels, decrease of cell viability and interference with mitochondria metabolism (Badawy *et al.*, 2011). Surface area (along with roughness and porosity) and surface charge also influence generation of ROS and binding sites for receptors. For example, surface charge-dependent increased toxicity of silver nanomaterials (Ag-NM) to gram positive bacteria has been reported for positively charged Ag-branched polyethyleneimine NMs (10 nm) compared to negatively charged Ag-citrate NMs (10 nm) (Badawy *et al.*, 2011).

1.2 Nanotechnology and Nanomaterials

Nanotechnology deals with nanoscale discoveries, including the development of nanosized-materials and has immense potential in various aspects of life.

The term nanomaterial has been defined by the European Commission since October 2011, as:

"A natural, incidental or manufactured material containing particles, in an unbound state or as an aggregate or as an agglomerate and where, for 50% or more of the particles in the number size distribution, one or more external dimensions is in the size range 1 nm -100 nm."

"In specific cases and where warranted by concerns for the environment, health, safety or competitiveness the number size distribution threshold of the 50% may be replaced by a threshold between 1 and 50%."

*"By derogation from the above, fullerenes, graphene flakes and single wall carbon nanotubes with one or more external dimensions below 1 nm should be considered as nanomaterials." (*The European Commission, 2011*)*

The Joint Research Centre (JRC), which is the research arm of the European Commission, has defined NMs as substances having at least one dimension between 1 and 100 nm in size (JRC, 2010). To illustrate this, the size of flea is 1,000,000 nm wide and viruses are around 100 nm in diameter (**Figure 1.3**). Importantly, NMs can differ greatly in their physicochemical properties when compared to micron-sized particles having identical chemical composition (Gergely and Coroyannakis, 2009). NMs covers all shapes as long as 1 dimension is in the nanoscale, while NPs imply that all three dimensions are nanoscale, i.e. spherical particles typically.

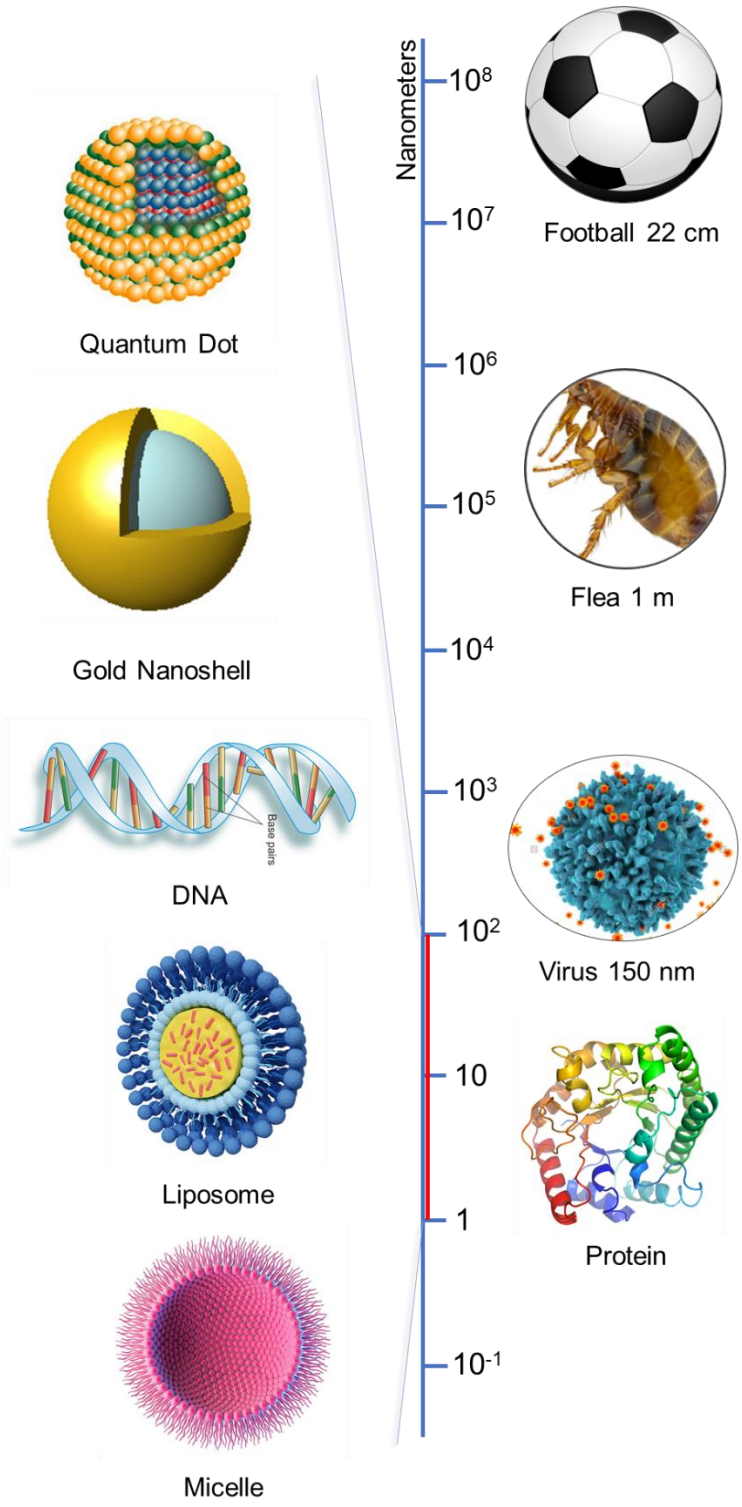


Figure 1.3: An illustration comparing sizes of various objects found in nature and engineered nanomaterials to give an idea of the nanoscale; adopted from (Saallah and Lenggoro, 2018).

The British Standards Institute uses the term nano-object and defines it as "material with one, two or three external dimensions in the nanoscale", i.e., between 1 nm and 100 nm (The British Standards Institute, 2015). The surface area to volume ratio is a significant property of nanomaterials. The smaller nanoparticles have a relative larger surface area (Kattan, 2016). Atoms at surface are more reactive, and for smaller size particles. A greater proportion of their atoms are on the surface - more surface for binding, more surface for catalysis, for carrying fragrance etc.

1.3 Classification of nanomaterials

Nanomaterials (NMs) can be grouped according to their origin, chemical composition, and dimensionality (Dolez, 2015; Hochella *et al.*, 2019).

1.3.1 Origin

NMs can be classified according to their origin as natural, incidental, and engineered, defined more precisely below. Some examples of each type of NM are presented in **Table 1.1**.

Table 1.1 Examples of Nanomaterials (NMs) and where they may be found.

Origin	Formation	Examples	Reference
Natural	Biogenic	Organic colloids: Humic acids, fulvic acids Organism: Viruses Oxides: Magnetite Metal: Ag, Au	(Nowack and Bucheli, 2007)
	Geogenic	Soot: Fullerenes, cristobalite, bismuth oxide Oxides: Fe-oxides Clays: Allophane	

Origin	Formation	Examples	Reference
	Atmospheric	Aerosols: Organic acids, Sea salt	
	Pyrogenic	Soot: carbon nanotubes (CNT), Fullerenes, Nanoglobules, onion-shaped nanosphere	
Incidental	Combustion by-products	CNT, nanoglobules, diesel soot, ultrafine particulates, polymer fumes	(Oberdörster, Oberdörster and Oberdörster, 2005)
Engineered	Considering high production and release estimates as of 2010	TiO_2, SiO_2, Fe, ZnO, Al_2O_3, CeO_2, Cu, Ag, CNT and graphene	(Keller and Lazareva, 2013)

1) Natural nanomaterials

Natural NMs originate from natural processes, for example, volcanic eruptions, forest fires, and sandstorms. Natural processes can form NMs in waters, soils, atmosphere and sediments.

2) Incidental nanomaterials

Incidental NMs are NMs which have been unintentionally released from human activity, e.g. factory emissions, transportation emissions, mining, forest fires. By-products from human activities have been delivered to the atmosphere and sediment to waters and soils.

3) Engineered or manufactured nanomaterials

Manufactured nanomaterials (MNMs) are synthesised either by top-down or bottom-up methods. The simplified processes are presented in **Figure 1.4**. MNMs can be grouped broadly as organic and inorganic compounds, i.e., CNT, polymer, TiO_2, and ZnO (see **Table 1.2**).

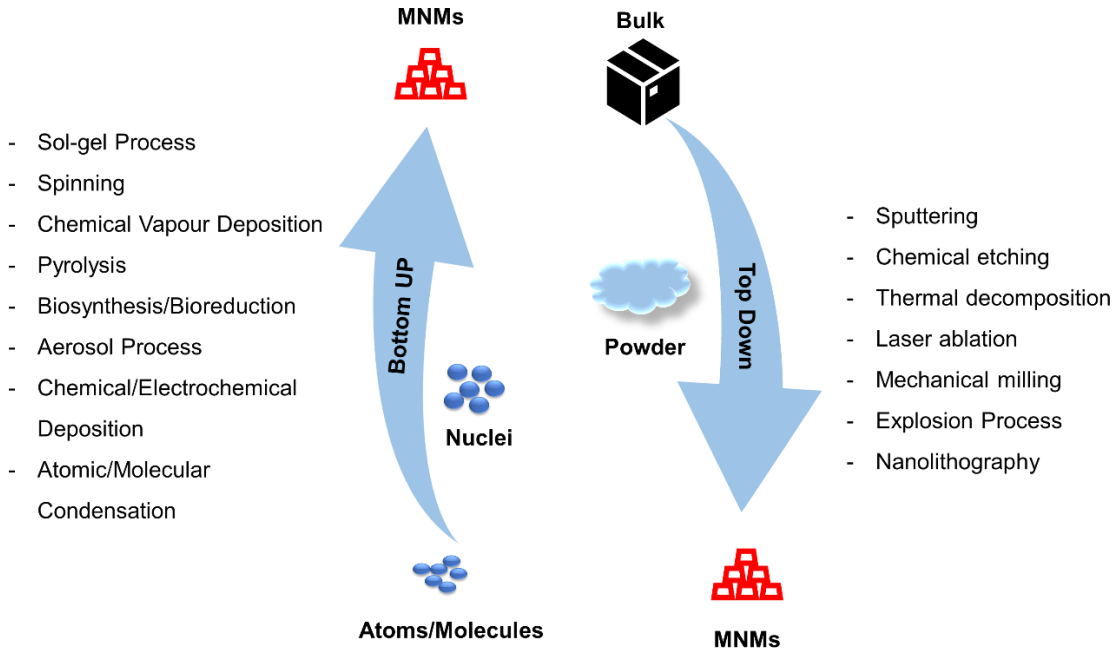


Figure 1.4: A simplified representation of MNMs synthesis process (Ealias and Saravanakumar, 2017; Ovais *et al.*, 2017)

Table 1.2 Examples of Manufactured Nanomaterials (Ju-Nam and Lead, 2008; Keller and Lazareva, 2013; Hochella *et al.*, 2019)

Composition	Group	Example
Organic	Fullerenes	C_{60}, C_{70}, derivatives
	CNTs	Single walled CNTs
		Multi walled CNTs
	Dendrimer	Polymer
Inorganic	Metal Oxides	TiO_2, ZnO, CeO_2, SiO_2
	Metal	Au, Ag
	Quantum dots	CdSe, ZnSe, InP

1.3.2 Chemical Composition

NMs are categorised based on their chemical composition as well as their grouping as organic, inorganic and carbon-based NPs (see **Table 1.3** for examples).

Table 1.3 Classification of nanomaterials based on chemical composition.

Classification	Example	Reference
Organic or Polymers	Dendrimers, micelles, liposomes and ferritin	(Ealias and Saravanakumar, 2017)
Inorganic	**Metal based:** Aluminium, Iron, Silver, Gold, Cobalt, Cadmium, Lead, Copper, Zinc	(Brust *et al.*, 1995; Dhas, Raj and Gedanken, 1998; Yin *et al.*, 1998; Song *et al.*, 2006; Paskevicius *et al.*, 2009; Cumberland, 2010; Khan, Saeed and Khan, 2017; Mörtel *et al.*, 2017)
	Metal Oxide Based: TiO_2, FeO, SiO_2, ZnO, CeO_2, Al_2O_3, Magnetite (Fe_3O_4)	(Pang and Bao, 2002; Tago *et al.*, 2003; Mahshid *et al.*, 2007; Sharma *et al.*, 2011; El Ghandoor *et al.*, 2012; Rahman and Padavettan, 2012; Briffa, 2017; Musigapong *et al.*, 2019)
Carbon Based	Fullerenes (C_{60}), Graphene, Carbon nanotubes (CNTs), Carbon Nanofiber, Carbon black	(Li *et al.*, 2006; Rouse *et al.*, 2007; Ealias and Saravanakumar, 2017; Khan, Saeed and Khan, 2017)

1.3.3 Dimensionality

NMs have been classified into four groups – 0D, 1D, 2D, and 3D - based on the number of dimensions which are outside of the nanometric size range. **Figure 1.5** (Dolez, 2015) shows the examples of NMs under each group.

Zero-dimensional (0D) NMs have all dimensions in the size range of 1-100 nm, such as uniform particles arrays (quantum dots), heterogeneous particles arrays, core-shell quantum dots, and hollow spheres. 0D NMs have been extensively applied in commercial products, i.e. light emitting diodes (LEDs) (Janssen and Stouwdam, 2008), solar cells (Lee *et al.*, 2009), and lasers (Ustinov *et al.*, 2000). However, 0D NMs are unstable and have severe limitations with regard to manufacturing in large quantities. These materials are also strictly NPs, where all others are better termed NMs, as per the ISO terminology for nanotechnology.

One-dimensional (1D) NMs have one external dimensions outside the nanoscale and include nanofibers (TiO_2, SiO_2, Al_2O_3 etc.), nanorods, nanowires (Au, Ag, Co etc.) and carbon nanotubes (CNTs).

Two dimensional (2D) NMs have two external dimensions beyond the nanoscale and comprise of surface coatings, thin films, plates and networks. 2D NMs find widescale use in electronics and other technology-focused applications due to their shape, high surface area, large surface-to-volume ratio and favourable structural stability over 0D and 1D NMs (Tiwari, Tiwari and Kim, 2012).

Finally, three dimensional (3D) NMs have no dimensions in the nanoscale but may be consisting of nanoscale components, e.g. bulk powders, nanocomposite materials (Lin, Shang and Zhang, 2014; Dolez, 2015).

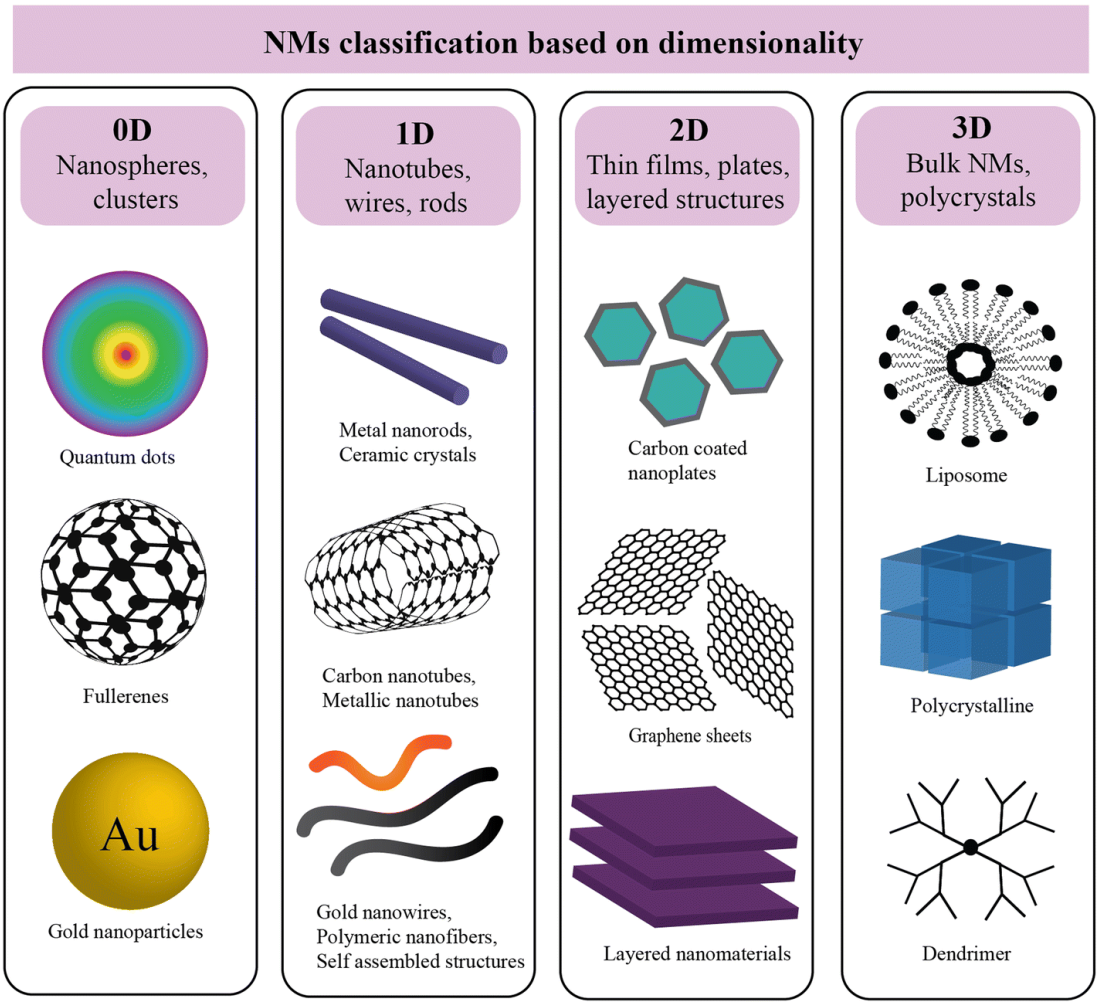


Figure 1.5: A classification of NMs based on their dimensionality (Poh *et al.*, 2018).

1.4 NM properties relevant to their behaviour, interaction and toxicity

The characterisation of physicochemical properties including size, shape, chemical composition, surface charge, solubility, and surface chemistry of NMs is very important to determine their behaviour, interaction and toxicity.

Table 1.4 Physicochemical properties of NMs that influence behaviour and toxicity.

Property	NM effects	Example	Reference
Size/size distribution	Smaller sized NMs can be internalised into an organism, which can potentially lead to its accumulation and induction of toxicity. Size distribution helps to identify what percentage of NMs remain monodispersed rather than agglomerated over time.	80 nm silica NPs more strongly affect cell viability than 500nm.	(Zhang *et al.*, 2010)
Shape	Shape can influence NM uptake and its potential effect.	Spherical-shaped AuNPs can enter HeLa cell more than rod-shaped.	(Chithrani, Ghazani and Chan, 2006)
Solubility	Dissolution of NMs within the cell or its organelles or in media can cause release of ions after internalization of the NM, influencing toxicity.	Trojan horse effect from AgNPs.	(http://pubs.rsc.org/en/content/articlelanding/2018/nr/c7nr05975b#!divAbstract)
Surface charge	Surface charge of NPs helps determine how NPs interact with other chemical species (ions) or in biological fluids. Charged NPs dispersed in water, can interact with the protons and hydroxyl ions of	Negatively charged nanoparticles can interact with the carboxyl or sulfate groups of mucin strands as well as hydrophobic regions of the gastrointestinal tract. Their	(Lai, Wang and Hanes, 2010) (Drescher *et al.*, 2011)

Property	NM effects	Example	Reference
	the water. They may gain or lose protons. Aggregation can occur depending on ionic strength, the Debye length and the effective charge in the electron double layer (EDL), also NPs can be attracted each other by weak van der Waals' forces.	binding can reach the intestinal epithelial surface. Negatively charged silica nanoparticles synthesised using Ludox method increases agglomerations in a cell culture medium containing fetal calf serum.	
Surface coatings/corona	NPs with different surface coatings can induce the absorption of protein and other biomolecules and cause agglomeration, behaviour and can affect fate and toxicity.	Functionalization of silica nanoparticles with positively charged molecules enhances the *in vitro* cellular uptake and decrease the formation of aggregates. The aggregates may decrease the toxicity of NPs to cells.	(Rancan *et al.*, 2012)
Structure/Crystallinity	Physical properties of NPs are affected by the structural orientation of atoms within the particle.	Anatase form of titanium dioxide has been shown to be more photocatalytic, compared to rutile.	(Augustynski, 1993)

1.5 Synthesis methods for amorphous Silica Nanoparticles

Since there are many applications of synthetic aSiNPs, synthesis protocols have been extensively developed to produce different forms of SiNPs as illustrated in **Table 1.5**.

Table 1.5 Overview of synthetic aSiNPs, relevant properties and applications

Silica forms	Synthesis method	Size (nm)[a]	Surface area (m^2/g)	Applications	Reference
Pyrogenic or fumed silica	Thermal process	5-50	50-400	Adsorbents, filler, thickening agents, anti-caking agents, emulsion stabilisers, free-flow agents and carriers in consumer, food and feed products	(ECETOC, 2006; Nafisi, Schäfer-Korting and Maibach, 2015)
Precipitated silica	Wet process	5-100	30-500	Performance additive as filter aid in food production, use as coatings, ink receptive papers, metal casting, refractory products, and catalysts	(ECETOC, 2006; Nafisi, Schäfer-Korting and Maibach, 2015)

Silica forms	Synthesis method	Size (nm)[a]	Surface area (m^2/g)	Applications	Reference
Silica gel	Wet process	1-10	250-1,000	Use in food industry, paints and coatings, pharmaceutical tableting additive, plastics and textiles, and use as anticaking agents, filter aid, emulsifying agents, viscosity control agents, and anti-settling agents	(ECETOC, 2006; Nafisi, Schäfer-Korting and Maibach, 2015)
Nonporous (Stöber) silica	Different methods	50-2000	Variable, with controllable surface properties	Drug delivery, cancer diagnosis and therapy and molecular imaging	(Stöber, Fink and Bohn, 1968; Tang and Cheng, 2013; Nafisi, Schäfer-Korting and Maibach, 2015)
Mesoporous silica	Different methods	2-50	> 1,000	Drug delivery, catalysis and imaging	(Napierska *et al.*, 2010; Nafisi, Schäfer-Korting and Maibach, 2015)

In this study, the major synthesis technique used for aSiNPs preparation was the sol-gel method producing synthetic amorphous silica nanoparticles similar in properties to those in cosmetic products and of ultrasmall; further details are described in Chapter 4.

1.6 NM Regulation

This section discusses the existing regulation dealing with cosmetics containing nanomaterials. In the EU, cosmetic products are regulated under the Regulation on cosmetic products legislation – (EC) No 1223/2009. The recent regulations for risk assessment of cosmetics highlight the information requirements including an estimate of exposure dosage via inhalation, oral and dermal exposure routes. However, guidance provided within this regulation may be insufficient on particular aspects, i.e. cytotoxicity and immune response and about the specific substance property requirements, i.e. physicochemical characterisation and exposure assessment. The European Commission Scientific Committee on Consumer Safety (SCCS) has been requested to revise and develop guidance on the additional nanomaterial characterisation and health risk assessments for the approval of cosmetics containing NMs (Scientific Committee on Consumer Safety, 2012). Cosmetic manufacturers have been required to provide specific data relevant not only to health, safety and awareness of cosmetic applications but also details regarding the raw materials and other technical information in accordance with the EU legislation. The European Chemicals Agency (ECHA) has collected, analysed and reviewed available information from a wide range of sources, and encouraged companies for more information as specified within the legal frameworks. ECHA

launched the first version of the European Union Observatory for Nanomaterials (EUON) in 2017 (The European Commission, 2014), this was set up to provide authoritative information to the public and industry; available at: https://echa.europa.eu/guidance-documents/guidance-on-reach.

The European Commission now requires that products containing nanomaterials have adequate and relevant characterisation data (before they can be marketed) and that sufficient safety assessment (through various exposure routes) is conducted. Cosmetics companies have also been required since 11 July 2013, under EU cosmetic regulation 1223/2009, to add the label "nano" in front of any of nanoscale ingredients, as recommended by the scientific committee on consumer safety (SCCS) and REACH (EcoMundo, 2016; European Commission, 2016). However, currently there is no specific standardized test method to demonstrate the presence (or absence) of nanomaterials in a cosmetics formulation.

From 2013, the cosmetics industry has been required under the EU legislation to strengthen safety requirements for cosmetic products to provide safety assessment data. However, the revised cosmetic regulations also banned the testing of cosmetics on animals from 2013. In Europe, the traditional practice of testing cosmetics on animals has been a topic of controversy for many years, with a strong push towards replacing animal tests with alternative, typically *in vitro* tests. Significant effort has been invested into the development of *in vitro* reconstructed human skin models and *ex vivo* tissue models (pig and human), which have largely replaced animal testing and have been used to study the epidermal and dermal responses to cosmetics.

These *in vitro* three-dimensional epidermal reconstruction models have been used purely for basic research interests since the 1990s. Many different types of 3D human skin models have been developed and were accepted in 2009 by the EU (European Parliament, 2009). For dermal studies on SiNPs, the majority of relevant data on the relationship between size and cytotoxicity are available for large particles (20, 70, 300, 1000 nm) (Nafisi, Schäfer-Korting and Maibach, 2015; Palmer *et al.*, 2019) where the additional information regarding the factors driving skin penetration and permeation, such as chemical transformation and mechanism of localization are lacking and often conflicting.

1.7 Nanoparticles in cosmetics

NPs are being used in almost 600 cosmetic industries (Guix *et al.*, 2008) due to their easy preparation, suitability for carrying active ingredients and availability of a range of emerging technology options. Their unique properties can significantly enhance colour appearance, UV protection, provide long-lasting effects, deeper skin penetration, and extend shelf life of the products including cosmetics and personal care products. Examples of the applications of NPs in cosmetics are given in **Table 1.6**.

Table 1. 6 Examples of NP applications in cosmetics and personal care products

Nanoparticles	Cosmetic products	Properties	Reference
Carbon fullerenes (buckyballs)	Face creams and moisturizers	Against Radical Oxygen Species (anti-aging/ antioxidants)	(Friends of the Earth Australia, 2006)
Titanium dioxide (TiO_2)	Cosmetics, Sunscreens	UV protection including to reflect and scatter UVA and UVB	(Guix *et al.*, 2008)
Zinc oxide (ZnO)	Sunscreen, Make-up remover	Block UV	(Friends of the Earth Australia, 2006; Guix *et al.*, 2008)
Copper	Face colour powder, lipsticks	Antimicrobial agent, colour development	(Camacho-Flores *et al.*, 2015)
Iron oxide (Fe_xO_y)	Brush-on, lipstick	Colour development	(Guix *et al.*, 2008)
Silver (Ag)	Underarm deodorants	Antibacterial activity	(Junevičius *et al.*, 2015)
Gold (Au)	Toothpaste, Acne cream treatment	Antibacterial activity, reduction of pore size, prevention and treatment of acne	(Junevičius *et al.*, 2015; Khezri, Saeedi and Maleki Dizaj, 2018)
Alumina (Al_2O_3)	Gel cosmetics, colour cosmetics	Fillers, waterproof materials, colour development	(Khezri, Saeedi and Maleki Dizaj, 2018)
Silicon dioxide (SiO_2)	Face powder, lipstick, eye shadow, mascara, antiwrinkle products, cosmetic pencils	Preventing re-agglomeration of the pigment, Anti-cake, adsorbent, emulsifier, facelift effect	(Nafisi and Maibach, 2015; Khezri, Saeedi and Maleki Dizaj, 2018)

1.8 Human Skin

Human skin is the largest organ of the body, covering surface area around 1.8 m^2 for an adult. Its complex structure and physicochemical properties facilitate

its role as an outermost barrier against external factors (Nafisi and Maibach, 2018). The skin barrier is involved in preventing human exposure to a range of chemicals, including NPs, through human evolution and, recently, additionally in response to exposure resulting from the expanding cosmetics sector, i.e. body care and skin care products. Nanotechnology used in cosmetic manufacturing is driving additional research into human skin, dermal uptake and consequences of NP exposure via topical application to skin. Detailed information on human skin is provided in the sections below.

1.8.1 Human Skin Structure and Function

Skin is a dynamic organ which changes its structure throughout life, for example, keratinocytes derivation in the inner layers are continuously moving towards the outer layer depending on the stage of cell differentiation. Among the different types of skin cells, keratinocytes are the most represented cells of the epidermis (90%), whereas the Langerhans cells (LCs) represent approximately 3-5% of all epidermis cells (Rancan *et al.*, 2012). Human skin consists of three main layers, namely epidermis, dermis and hypodermis, presenting from the upper layer as represented in **Figure 1.6**.

The epidermis is the outermost layer of the skin, and is divided into parts called the stratum basale (SB), stratum spinosum (SS), stratum granulosum (SG), stratum lucidum (SL), and stratum corneum (SC) as shown in **Figure 1.6**. The epidermis acts as exogenous physical, chemical, and protective waterproof barrier. The SC is a part of an efficient outermost defence, depending on its lipid extracellular matrix, epidermis hydration, transepidermal loss of water, and the pH gradient among the skin (Zhai and Maibach, 2004). The barrier mechanism of the SC arose from its content of corneocytes and lipid-

enrichment regions which impede loss of moisture and solutes. The extracellular lipid component of the SC comprises a bilayer lamella structure of opposite electric charge and with hydrophobic and hydrophilic compartments (Hatta *et al.*, 2006). The long lamellar structure or lipophilic compartment (ceramides, free fatty acids, and cholesterol) maintains the barrier to the translocation of water and electrolytes. In addition, tight junctions underneath the SC seal the topical intercellular spaces between the cells of the viable epidermis. Therefore, if NP is smaller than the gaps between the tight junctions (around 6 nm) or is actively internalized by cells, it may penetrate the skin barrier (Rancan *et al.*, 2012).

The basement membrane is an interface between the epidermis and dermis layers and acts as a supporter for cell attachment. The dermis is an inner layer which is composed of two layers - the papillary and the reticular layers, and contains sweat glands, hair root, nerves, sense organ, lymphatic vessels, and blood vessels within cells and fibrous tissue. In particular, the blood vessels supply nutrients to the living dermis and also remove the cellular waste products. A further skin barrier is represented by fibroblast cells in the reticular layer. Subsets of the fibroblasts corresponding to immune system are specialized in the uptake of pathogens through macrophages and mast cells. The internalisation of proteins and other antigens into cells is carried out through the mechanism of endocytosis, macropinocytosis and phagocytosis as shown in **Figure 1.7**. The primary particle size (Rancan *et al.*, 2012), the degree of aggregation, and the surface charge (Hao *et al.*, 2017) significantly influence particle uptake into cells.

The hypodermis or subcutaneous layer is the innermost layer, which is made up of connective tissue and fat. Fat cells, loose and spongy connective tissues, and blood vessels are the main parts of the hypodermis, and function as protector and insulator of the body.

This complex structure is reproducibly mimicked in the form of reconstructed human skin models, which are widely used in research and industry for evaluation *in vitro* and *in vivo* of local or systemic toxicity, disease, and drugs/delivery system efficacy.

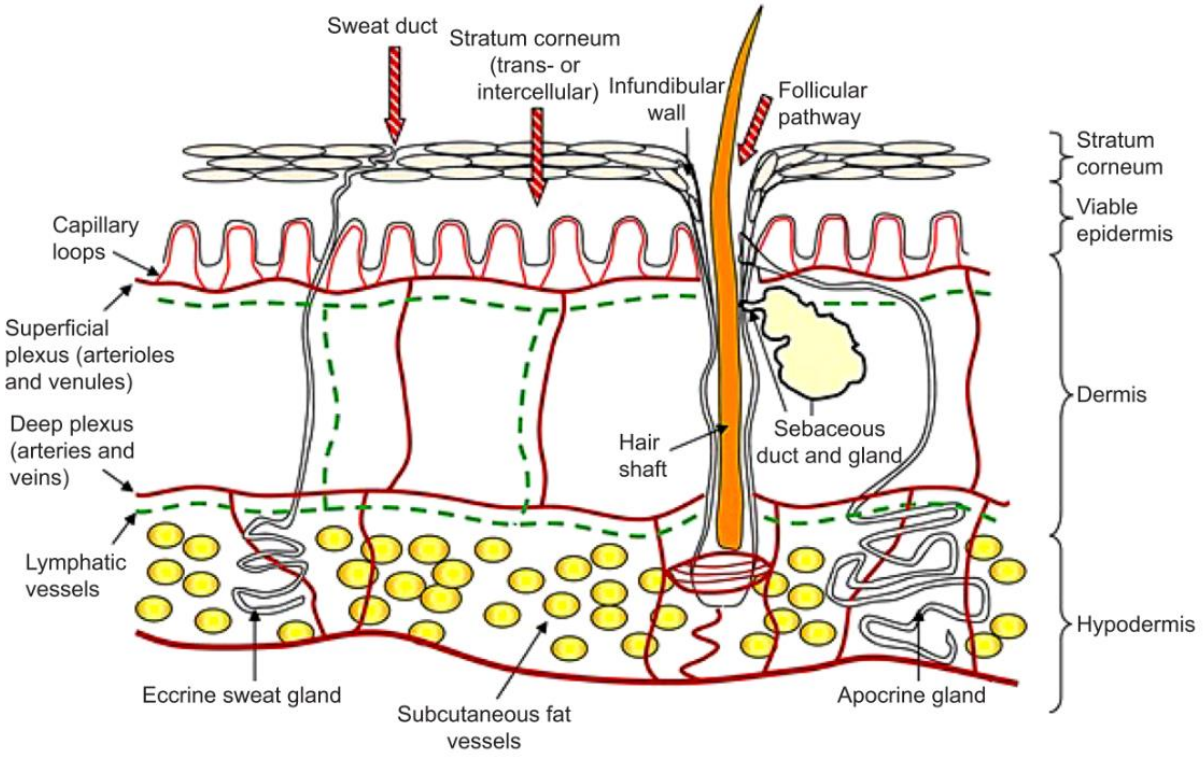


Figure 1.6: Schematic representation of skin and routes of penetration of chemicals. Source: (Abd *et al.*, 2016)

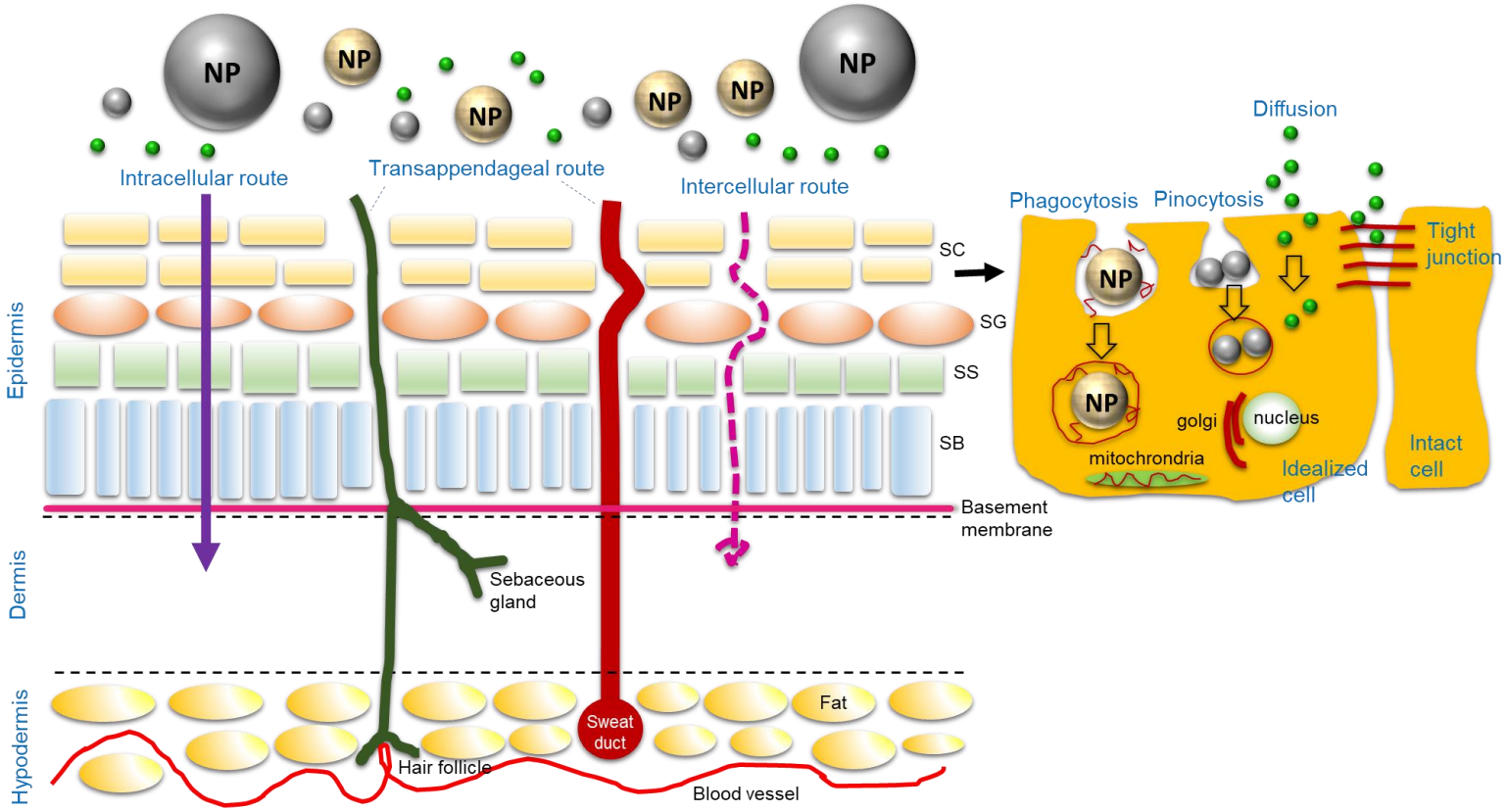


Figure 1.7: Representation of human skin and possible routes of NPs delivery across the skin, Adapted from (Larese Filon *et al.*, 2015; Gubala *et al.*, 2018a)

1.8.2 Reconstructed Human Skin

Initially, new methodologies for using reconstructed human skin models were developed in academic research. The high demand of the cosmetic industries following the global trend to reduce animal testing of cosmetics has driven the use of these skin models in order to replace animal tests. Animal testing of cosmetics has been completely banned since March 2013 (European Union, 2009). The new approach for toxicological testing was implemented based on the Reconstructed human Epidermis (RhE) technology, which showed a promising skin function, physiology, and disease susceptibility, compared with the native human epidermis and has been adapted and validated in terms of the specificity, sensitivity, and accuracy of each batch (OECD, 2015) by the Organization for Economic Co-operation and Development (OECD) and is now available as a standard test guideline. OECD guidelines using the reconstructed human skin models include OECD TG 431 (skin corrosion), OECD TG 439 (skin irritation), OECD 404 (acute dermal irritation/corrosion) and OECD guidance notes on dermal absorption No. 155 (2011) and No. 428 (*in vitro* methods, 2004). Similarly, the United States Environmental Protection Agency (USEPA) Report on Dermal Exposure Assessment (2007) utilises reconstructed human skin models. However, these guidelines suggest two techniques, such as a diffusion cell (or Franz diffusion cell[1]) and the tape stripping methods (Zsikó *et al.*, 2019), which remove the SC and NPs remaining into the skin models. Recently, some skin models have been introduced to the

[1] Franz diffusion cell: an *in vitro* skin permeation assay, consists of two primary chambers separated by an animal skin, i.e. rabbit skin, rat skin, pig skin, or human skin. The test sample is used as an *in vitro* device comprising the top chamber above the skin membrane (into which the test sample is introduced) and the bottom chamber below, which contains the same solution as the test samples are presented in.

commercial market and are available for purchase, as presented in **Table 1.7**.

These models are acceptable as Validated Reference Methods and show a well-differentiated epidermis as well as native human epidermis (Pedrosa *et al.*, 2017).

Table 1.7 Examples of reconstructed skin models available on commercial market (Wever, Petersohn and Mewes, 2013).

Skin models	Manufactures	Country
EpiSkin™	L'Oréal	France
EpiDerm™	MatTek Corporation	USA
Reconstructed Human Epidermis (RhE)	SkinEthic	France
EST1000®	CellSystems	Germany
epiCS	epiCS®	Germany
Phenion® and Open Source Reconstructed Epidermis (OSREp)	Henkel AG&Co. KGaA	Germany
Straticell	Straticell	Belgium
StrataTest	Stratatech	USA
Labcyte	Japan Tissue Engineering Co.,Ltd.	Japan
Vitrolife-Skin™	Gunze Corporation Ltd.	Japan

In general, RhE represents epidermis layers and demonstrates the outermost barrier as SC to protect the skin from environmental factors similar to native skin. In addition, the main layers of epidermis and dermis are presented in the full-thickness skin models, which are placed on an insert and over culture media to feed the skin cells as exemplified in **Figure 1.8**. Both skin models have become reliable tools for preclinical testing, advancing the understanding of biological processes and have apparently achieved the limitation of scientific

inconsistencies. The manifold RhE model has recently been used to evaluate many aspects of cosmetic ingredients including phototoxicity, skin irritation, dermal absorption, skin sensitization, genotoxicity and corrosion testing (Wever, Petersohn and Mewes, 2013).

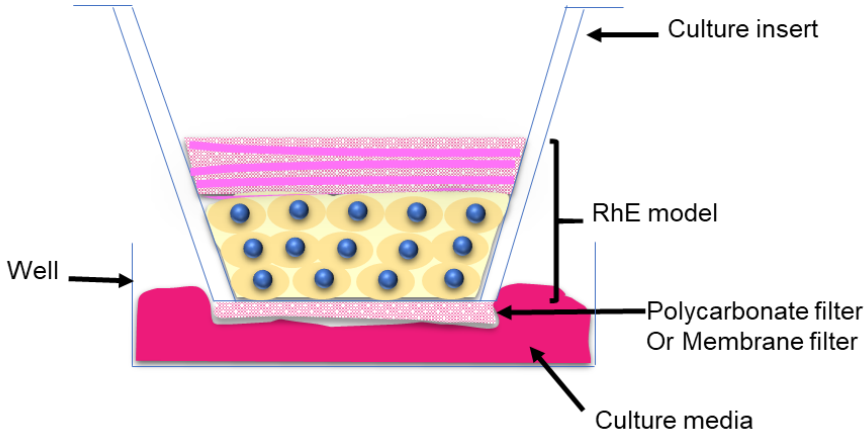


Figure 1.8: An example of the structure of reconstructed human skin models.

1.8.3 Uptake Pathways of NPs across skin barrier and into skin cells

The principle uptake pathways utilised by NPs are determined mainly depending on their physicochemical properties, e.g. size. NPs can cross the skin barrier and enter the systemic circulation by a combination of pathways, such as transepidermal (intercellular and transcellular routes) , or transappendageal routes through hair follicles, sebaceous pores and sweat glands (Nafisi and Maibach, 2018). Using the transepidermal route, NPs being lipophilic and hydrophilic molecules can permeate through the lipophilic membrane of cells, the phospholipid bilayer of the corneocytes or by endocytosis pathways. The transappendageal route covers permeation across the pores of the sweat glands, hair follicles and sebaceous glands. These channels pass over the SC and reach the systemic circulation where there are

transported around the whole body by the lymph and bloodstream. In addition, the cellular internalisation involves macrophages and endothelial cells through the mechanisms of phagocytosis, pinocytosis, diffusion and also unknown pathways as shown in **Figure 1.7**. For example, NPs with diameters ranging between ≤ 4 - 20 nm can potentially absorb into the skin through sebaceous pores and sweat gland pores. Besides, NPs (e.g. polystyrene, solid lipid NPs, titanium dioxide) were detected in the hair follicle infundibulum and even deeper (Lademann *et al.*, 2001; Toll *et al.*, 2004; Münster *et al.*, 2005). Knowledge about skin penetration of NPs is essential for development of cosmetics, particle-core drug delivery systems and toxicology. However, there are few available data on the skin penetration and permeation of SiNPs (Nafisi, Schäfer-Korting and Maibach, 2015). Thus, significant attention in this thesis was focused on determining the potential of skin penetration and work was carried out to explore how deeply aSiNPs could go through the full thickness reconstructed human skin model and the limitations of the experimental approaches.

1.8.4 Skin Penetration Enhancement

Several significant parameters can affect the ability of NPs to translocate across human skin, related to their physicochemical properties. Previous studies revealed that there are some NP parameters that are highly relevant in determining the mechanism and ability of skin penetration; e.g. surface charge, concentration of NPs and ability of NPs to release ions in physiological condition (Larese Filon *et al.*, 2011; Hao *et al.*, 2017). System properties such as exposure time and barrier integrity/function also play a role. Additionally, the

formulation of the NP containing media can affect the behaviour and influence the mechanism of their translocation through the biological tissues.

The intrinsic properties of NPs are prioritized to better understand their influence on skin penetration. The details of skin penetration enhancers were summarized in

Table 1.8.

Table 1. 8 Examples of physicochemical properties of NPs affecting or enhancing skin penetration and permeation (Williams and Barry, 2012; Nafisi and Maibach, 2018).

Physicochemical Properties	Potential Behaviour Effects
Chemical composition and Surface chemistry	NP formulation involves - diffusion coefficient: increasing diffusion coefficient increases diffusion of NPs in skin - partition coefficient represents the distribution of NPs between the SC membrane and the chemical form - oil/water partitioning: NPs having lipophilic parts can permeate across the SC, whereas the hydrophilic part cannot penetrate well as polarity/charge. - Molecular weight (MW) NPs less than 600 Da can pass through the skin. - NP binding with skin components interferes with their penetration into the skin, while NP metabolism induces lower MW molecules that can enhance the permeation.
Size	NPs with diameters ranging between ≤ 4 - 20 nm can potentially diffuse across the skin

Physicochemical Properties	Potential Behaviour Effects
	through sebaceous pores and sweat gland pores.
Shape	Depending on the type of NPs, for example, the spherical carboxylic acid-coated quantum dots can pass through pig skin faster than ellipsoid shape at the same dose (Nafisi and Maibach, 2018).
State	NP stability can influence agglomeration and aggregation, affecting NP penetration.
Surface charge	Positively charged quantum dots (QDs) penetrated deeper into the skin, compared with other QDs. The amount of positively charged gold NPs (AuNPs) that passed through the reconstructed skin model was greater than for neutral and negatively charged AuNPs (Hao *et al.*, 2017).

Furthermore, a high concentration of NPs used during exposure, can reduce the amount of absorption into the skin because of the saturation of loading as a physical skin barrier (Wester, Noonan and Maibach, 1980; Labouta, El-Khordagui, *et al.*, 2011). The exposure time seems to have a linear correlation with the amount of NP penetrating into the skin (Rougier, Lotte and Maibach, 1987; Labouta, El-Khordagui, *et al.*, 2011).

1.8.5 Toxicology of silica nanoparticles through skin – the dermal exposure route

Studies to evaluate potential cellular toxicity using *in vitro* and *in vivo* approaches have highlighted the most successful and reliable methods for cytotoxicity assessment of living organisms. Coupling toxicity experiments with consideration of the mechanisms of NP transformation under the exposure conditions can project the potential toxicity of NPs, defining their health risk and behaviour in biological organisms, as shown in **Figure 1.9**. The transformation of NPs involves intrinsic properties and external factors. For example, ultraviolet radiation can cause the excitation of NPs, corresponding to changes in their energy band gap, oxidation state, surface charge/ coating and leads to formation of free radicals (Nel *et al.*, 2013). Another example is that redox reactions can transfer an electron and generate ions or organic/inorganic matter (Nel *et al.*, 2013). In addition, dissolution correlates with the formation of individual ions and leads to bond splitting of NPs. This transformation can change the surface charge and lead to the formation of agglomerates (Sharma *et al.*, 2018).

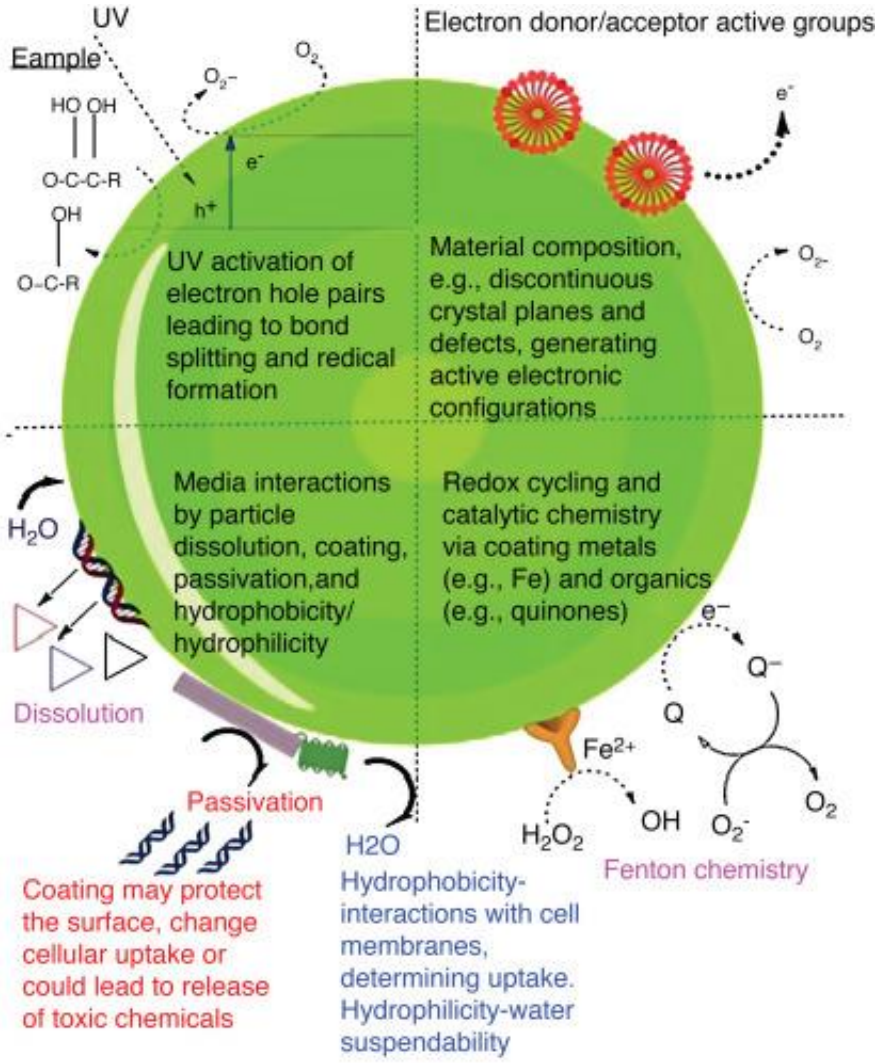


Figure 1.9: Possible NP transformations influencing potential effects of NP in biological organisms (Sharma *et al.*, 2018)

The diversity of NP transformations may induce a variety of potential effects on living organisms. The available information of SiNPs is summarized in **Table 1.9** focusing on cytotoxicity of skin cells.

Table 1.9 Examples of in vitro studies assessing skin cytotoxicity of SiNPs (Nafisi, Schäfer-Korting and Maibach, 2015).

Parameters studied	Treatment/Condition studies	Results	Reference
Size 7, 10-20 nm	*In vitro*: - Human keratinocyte line HaCaT - Human skin equivalent model	SiNPs of 7 and 10-20 nm are relevant to a decrease of cell viabilities of CHKs in a dose-dependent manner	(Park *et al.*, 2010)
Size 20, 100 nm with negatively charged (NC), weakly negatively charged (WNC)	*In vitro*: - Human keratinocyte line HaCaT - Intercellular ROS - EpiDerm skin irritation on human skin equivalent model - 3T3 NRU phototoxicity test in murine 3T3 fibroblast cell	NC-SiNPs 20 nm more toxic than NC 100 nm NC-SiNPs 20 nm more toxic than WNC 20 nm No irritation with EpiDerm No phototoxicity 3T3 NRU fibroblast cell	(Park *et al.*, 2013)
Zeta potentials: Size 70 nm, -21.6±4.5mV Size 300 nm, -31.3±6.5mV Size 1000 nm, -37.7±4.6 mV	*In vitro*: - Human keratinocyte line HaCaT	Endocytosis is relevant SiNP70 nm-mediated cell effects	(Nabeshi, Yoshikawa, Matsuyama, Nakazato, Tochigi, *et al.*, 2011)
Size 42±3 to 291±9 nm; positively and negatively surface charge	*In vitro*: - Human keratinocyte line HaCaT	Positively charged functionalized SiNPs demonstrated the effects on cellular uptake in a size-dependent manner	(Rancan *et al.*, 2012)
Fluorescent non-porous-SiNPs 10-200 nm; different charges	*In vitro*: - Normal Human Dermal Fibroblasts	Smallest particles (10 nm) had a great impact on cell viability.	(Quignard *et al.*, 2012)

Parameters studied	Treatment/Condition studies	Results	Reference
Monodisperse of particle size 80, 500 nm Zeta potentials: Size 80, -5.2±0.2 mV Size 500, -9.8±1.2 mV In culture medium with 10%FBS	*In vitro*: - Normal human dermal fibroblasts	Both particles (80,500 nm) were internalised into fibroblasts within a short time through micropinocytosis and endocytosis SiNPs 80 nm decreased cell viability and affected mitochondrial membrane potential Cell adhesion and migration were involved in SiNP uptake regardless of particle size	(Zhang *et al.*, 2010)
Drug delivery: Quercetin (Q) with plain or octyl-functionalization using Mesoporous silica (MCM-41) as a vehicle	*In vitro*: 2,2-diphenyly-1-picrylhydrazyl free radical (DPPH) assay	Increased efficiency of quercetin encapsulated by MCM-41	(Berlier, Gastaldi, Ugazio, *et al.*, 2013)
Drug delivery: Rutin using NH_2 functionalized MCM-41	*In vitro* DPPH assay	Aminopropyl-functionalized MCM-41 was relevant a stability of a drug substance exposure to light (photostability)	(Berlier, Gastaldi, Sapino, *et al.*, 2013)
SiNPs (70, 300, 1000 nm) Zeta Potentials: SiNP 70: -21.6±4.5 mV SiNP 300: -31.3±6.5 mV SiNP 1000: -37.7±4.6 mV	*In vitro*: Human keratinocyte line HaCaT	Transdermal penetration of SiNP-70 nm through the stratum corneum was related to cellular damage in the skin	(Nabeshi, Yoshikawa, Matsuyama, Nakazato, Matsuo, *et al.*, 2011)
Skin penetration test Bare hydrophilic silica (B-SiNP) size 162±51 nm Lipid-coated silica (LC-SiNP) size 363±74 nm	Volar and dorsal sides of forearm human skin	10% B-SiNPs penetrated the deepest stratum corneum 42% and 18% LC-SiNPs found in volar and dorsal forearm, respectively SiNP surface polarity involved the skin penetration	(Iannuccelli *et al.*, 2014)
aSiNPs size 70 nm	*In vitro* human endothelial cells under physiological cyclic stretch	No significant cytotoxicity to endothelial cells causing by aSiNPs	(Freese *et al.*, 2014)

Parameters studied	Treatment/Condition studies	Results	Reference
aSiNPs (size 40,60, 105 nm) Silica-chitosan composite (size 1-32 nm)	*In vitro* normal fibroblast and tumor cells	SiNPs apparently become slightly toxic to fibroblast cells at high concentrations High dosage of aSiNPs induced more cell membrane damage than Silica-chitosan composite Fibroblasts with long doubling times exhibited more injury from exposure to aSiNPs, compared to tumor cells with short doubling times Silica-chitosan composite induced less inhibition in cell proliferation	(Chang *et al.*, 2007)
aSiNPs generated using different production methods: Lysine-silica (size 2,26,34,36 nm) Stöber (size 18, 60, 104, 335 nm) Ludox (size 11, 14, 15 nm)	*In vitro* human endothelial (EAHY926) cell line	EC50 was lower for smaller particle sizes. At the same number of SiNPs (mmol/mL), the small SiNPs caused less reduction in cell viability than larger SiNPs	(Thomassen *et al.*, 2010)
20nmSiNPs with 2,4-dinitrofluorobenzene (DNFB)	*In vitro* cell line: HaCaT keratinocytes	20nm SiNPs decreased contact hypersensitivity and had a protective effect on the HaCaT calls, by reducing the DNFB induced cytotoxic response at dose above 1 µg/mL	(Palmer *et al.*, 2019)

Nanotechnology advances have been introduced in a wide range of consumer products in our daily life, especially in cosmetics. These may increase the potential consumer exposure to nanoparticles, and thus toxicity studies need much attention for better assessment of nanoparticles and their effects. Skin is the primary exposure route for cosmetics and more studies are needed on its exposure to NPs, hence, in this thesis, this is the primary focus using a human skin model. Although performing the guidance is used for a decade, there is still attempting to norm toxicity evaluation methods. The incentive for this work is realisation that current guidance lacks detail relevant toxicity studies are limited, only a few comprehensive reviews exist on the cytotoxic effects on skin, with limited noteworthy toxicity information on nanotechnology- based consumer products.

The main purpose of this PhD project is to evaluate the reactivity and toxicity of amorphous silica nanoparticles, in the context of their use in cosmetics. To achieve this goal, it was decided to use a sol- gel method to synthesise amorphous silica nanoparticles (aSiNPs), and to characterise the products extensively by using a variety of laboratory techniques, such as Dynamic Light Scattering (DLS), Transmission Electron Microscopy (TEM), Scanning Transmission Electron Microscopy (STEM), Scanning Electron Microscopy (SEM), Brunauer- Emmett- Teller (BET) surface analyser, powder X- ray Diffraction (XRD), Fourier Transmission- Infrared (FT- IR) and Inductively Coupled Plasma- Optical Emission Spectrometry (ICP- OES). Synchrotron based Small angle X-ray Scattering (SAXS), X-ray Photoelectron Spectroscopy (XPS), X-ray Absorption Near-Edge Spectroscopy (XANES), Extended X-ray

absorption fine Structure Spectroscopy (EXAFS) and micro- X- ray Fluorescence analysis (μ- XRF) . Since there are different strengths and limitations of each techniques, several approaches were applied to increase reliability and reproducibility in the characterisation results. This very extensive analytical programme was used for both freshly synthesised products, as well as aged and exposed to tissue, in order to deliver a comprehensive set of quality data. A complete understanding of the mechanism of silica nanoparticles behaviour on skin penetration, interaction and inflammatory response through the secretion of cytokine on skin models has not yet been developed. Hence, in additional to use of *in vitro* reconstructed human skin model, to test toxic effects of aSiNPs (based on the OECD guideline 439, published in 2009) , further examining of histological assays and dermal response assay, and analysis using synchrotron techniques to better understand the fate of aSINPs and their effects were also carried out.

1.9 Aims and Objectives

The main purpose of this thesis is to investigate the use of silica in cosmetics and to assess the dermal toxicity of synthesised aSiNPs in the context of their presence as an ingredient in cosmetics, utilizing the regulatory tests for skin penetration and skin irritation. Since aSiNPs occur in complex formulations in cosmetics, a combination of characterization techniques was applied to elucidate their from and properties. To achieve this overall goal, the specific objectives of the thesis are:

1.9.1 Objective 1: To characterise selected commercial synthetic amorphous silica nanomaterials and nanoparticles extracted from SiNP- containing cosmetics available on the UK high street. A multi- method characterisation

approach was applied to obtain their properties, such as the elemental composition, crystallinity structure, and particle size. This information was used to inform the synthesis of aSiNPs for evaluation in the rest of the thesis and enabled a comparison of the uses, advantages, and limitations of the different characterisation techniques.

1.9.2 Objective 2: To synthesize aSiNP representative of those used commercially in cosmetics, by using a lysine-silica (sol-gel) process which provided ultrasmall nanoparticles, was feasible procedure and controllable NP size, and to extensive characterise their properties by applying multiple techniques including synchrotron-based methods prior to assessing their interactions with, and toxicity to, skin. A comparison of characterisation techniques was given in relation to the property studied. Also, the study of consistency in terms of size, structure and chemistry for uniform evaluation and application as well as purity and stability of aSiNPs were monitored throughout *in vitro* experiments.

1.9.3 Objective 3: To investigate the permeability of the full thickness human skin 3D model (representing the epidermis and dermis layers at Day 11 of its growth) to aSiNPs and investigate their translocation behaviour across the dermal barrier and the underlying mechanism of nanoparticle-cell interaction by conducting *in vitro* skin penetration test. The aSiNP's penetration through the full thickness human skin 3D model was investigated at different concentrations, and its speciation (transformation, i.e. elemental compositions, oxidative state) in the epidermal layer was explored by applying synchrotron-based micro X-ray fluorescent spectroscopy (micro-XRF) and XAS-XANES.

1.9.4 Objective 4: To study the skin irritation potential of the aSiNPs, when topically applied to the reconstructed human epidermis (RhE) skin model in accordance with the UN Globally Harmonized System of Classification and Labelling (GHS). RhE represents the upper layer as well as the epidermis. The protocol chosen for this study was based on the OECD test guideline No. 439 (*in vitro* skin irritation test). The guideline classifies a material/chemical as an irritant if it decreases cell viability to below or equal 50% of the untreated control. Additionally, the RhE histopathology and immune mediated responses interleukin 1-α (IL-1α), measured by ELISA, were used to understand the mechanism of irritation.

Hypotheses

The work presented in this thesis was guided by the following hypotheses:

1. Many high street cosmetics contain silica nanoparticles, often in complex formulations that may require advanced characterisation methods to be able to identify and fully characterise.
2. Physicochemical properties of nanoparticles are dynamic (i.e. may change with time) and have an impact on toxicity.
3. Combining routine-laboratory techniques and synchrotron-based techniques are likely to offer better information of NP properties and enhance understanding of their toxicity.
4. *In vitro* skin experiments can provide mechanistic information of the behaviour of nanoparticles and enable modelling of their fate *in vivo*.

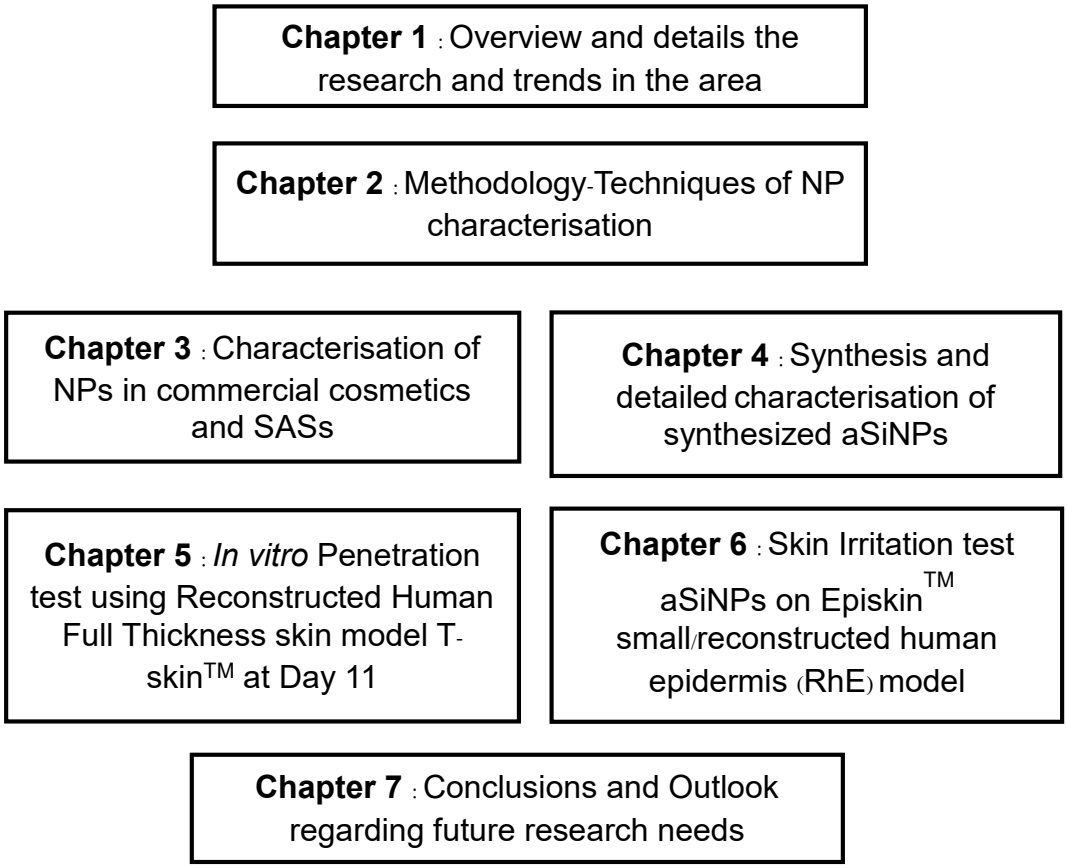


Figure 1.10: Schematic of the thesis structure

1.10 Thesis structure

The thesis consists of 7 chapters the broad content of which is as follows:

Chapter 1 is a general introduction to the research field and a detailed description of the main purposes and objectives of this PhD thesis. This chapter reviews aSiNPs in the context of cosmetic use and it points out the lack of characterization data necessary to understand its behaviour and toxicity. It also includes a synthesis of the current state of knowledge of nanomaterials transformation, fate, behaviour and hazards with focus on the principles of technique use, endpoints related to dermal exposure and relevant literature of skin irritation and penetration by nanomaterials, and identifies knowledge gaps related to aSiNPs.

Chapter 2 provides the experimental details for the research described in the thesis, spanning from the detailed method of synthesis of aSiNPs and their characterization, including theoretical descriptions of the mathematics underpinning the various techniques used, and the practical experimental details and protocols utilised. The chapter details the methods used to characterize the aSiNPs and the protocol adopted for human skin testing of aSiNPs skin penetration and toxicity.

Chapter 3 provides the details of cosmetics containing silica-based materials available on the market and the results of the multi-method characterization of the nanoscale components of samples purchased from the high street for analysis.

Chapter 4 explains the aSiNP synthesis and discusses the results obtained by means of routine characterization methods and synchrotron-based techniques. Sol-gel method is carried out synthesis of bimodal aSiNPs, size 2 and 7 nm.

Chapter 5 focuses on the *in vitro* skin penetration experiments on reconstructed human full thickness skin models at Day 11 from Episkin™ [2] and also provides the results, discussions and conclusion of the *in vitro* skin penetration study using the bimodal (2 and 7 nm) aSiNPs.

Chapter 6 details the *in vitro* skin irritation experiments on reconstructed human epidermis models from Episkin™ [3]. This chapter also provides the results of skin irritation, and describes the histological and inflammatory endpoints,

[2] Reconstructed human full thickness skin model at Day 11, Episkin: " *in vitro* reconstructed human full thickness skin model from normal human keratinocytes cultured on an inert polycarbonate filter at the air-liquid interface for 11 days, in a chemically defined medium. This model exists at different stages of maturity and consists of two layers, i.e., epidermis and dermis"

[3] Episkin: " an *in vitro* reconstructed human epidermis from normal human keratinocytes cultured on an inert polycarbonate filter at the air-liquid interface, in a chemically defined medium. This skin model exists at different stages of maturity and consists of the epidermis layer"

including a discussion of the *in vitro* skin irritation study following OECD TG 439, and conclusions regarding the safety profile of the bimodal (2 and 7 nm) aSiNPs.

Chapter 7 gives an overall summary of the work presented in the thesis and recommendations of possible future work directions.

1.11 Paper status and author contributions

Chapter 4: “Silica Nanoparticle Synthesis and Multi-method Characterisation”, was published in Material Science Forum (March 2019).

P. Musigapong	Principal author; performed all experimental work including collection of SAXS, XRD, TEM and solution data; performed all data analysis.
S. M. Briffa	Aided with STEM data collection and interpretation.
I. Lynch	Co-supervisor, Input to experimental concept; review pre- and post-Submission.
S. Soontaranon	Aided with SAXS data collection and interpretation.
N. Chanlek	Aided with XPS data collection and interpretation.
E. Valsami-Jones	Principal supervisor; input to experimental concept; aided with data interpretation; review pre- and post-submission.

Papers on the *in vitro* penetration and in vitro skin irritation tests are in advances stages of preparation also.

Chapter 2 Methodology

2.1 Introduction

This chapter gives a detailed description of the experimental techniques used in this study. The sample preparation of the synthesized amorphous silica nanoparticles (aSiNPs) and the methods used to characterise their properties are provided in this chapter. The characterisation of aSiNPs is an important step in order to quantify the effects of its properties on its environmental fate, behaviour, and toxicity, and to determine potential transformations of the aSiNPs when transported through the human skin. To what extend the depth information of nanomaterials' properties, a wide range of characterisation techniques was used to determine the particle size, surface charge, shape, structure, specific surface area, surface chemistry, chemical composition and oxidation state, all of which will influence its behaviour, mobility, and potential toxicity, and may be altered as a result of transformation. In this chapter, a description of each experimental technique used, shown in **Figure 2.1**, is given along with the details on the sample preparation and the analytical procedure.

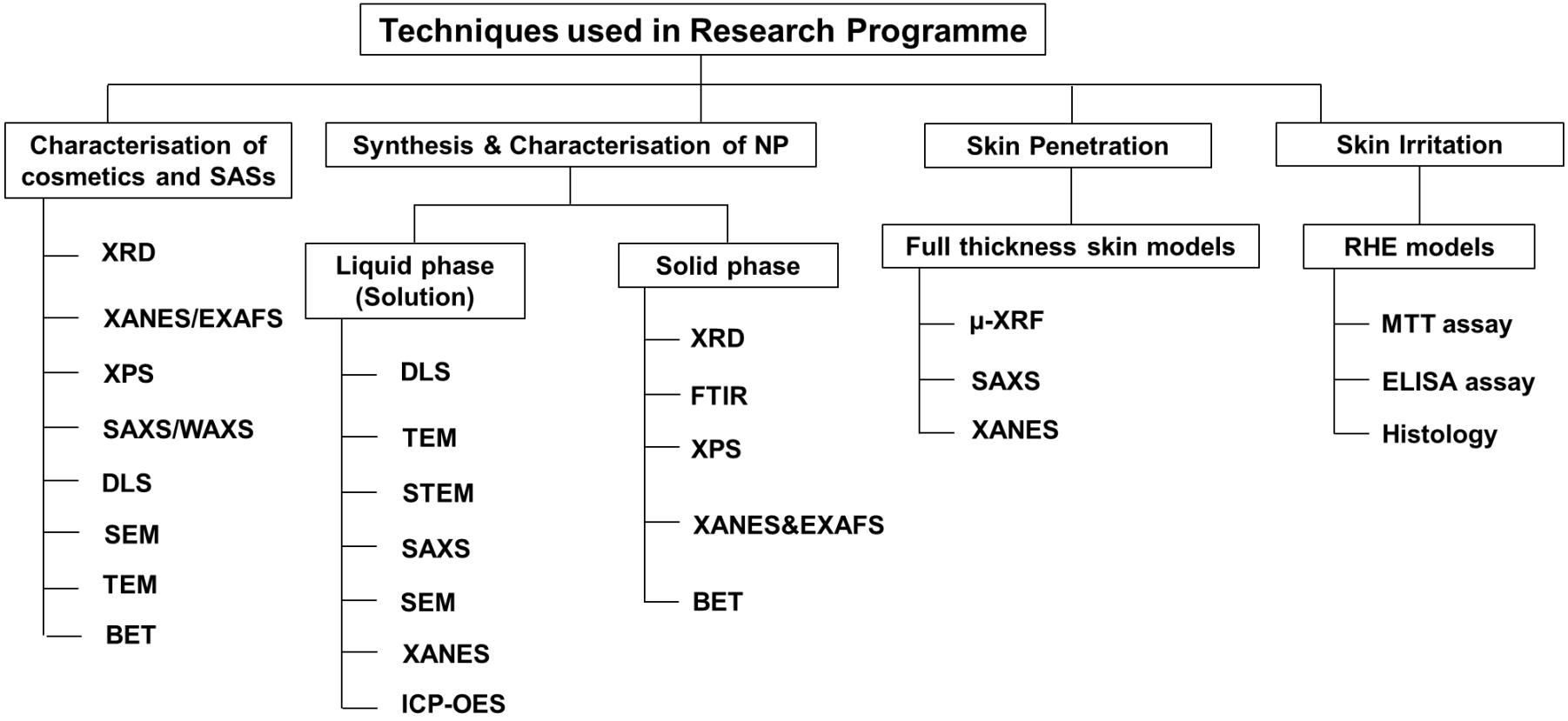


Figure 2.1: List of experimental techniques used in this study to characterise the aSiNP properties.

2.2 Characterisation

Analytical methods are used to identify the characteristics of NPs, such as size, size distribution, structure, shape, concentration, composition, surface area, surface functionality, and surface charge. The instruments and parameters used for these measurements are summarised in **Table 2.1**, and presented in detail below.

2.2.1 Dynamic Light Scattering

2.2.1.1 Size

Dynamic light scattering (DLS) is perhaps the most common method used to measure particle size in 2samples where the particles are dispersed in liquid, i.e. water, solvent or cell culture medium. The technique involves measuring Brownian motion and converting the speed of movement into particle size, the faster the movement, the smaller the particle. DLS uses a laser light, which shines on the sample, undergoing scattering when it hits a particle; a detector placed at a certain angle relative to the incident beam detects the scattered signal. The particle size is determined as the hydrodynamic radius (R_h) and diameter (D_h) as shown in **Figure 2.2**. The hydrodynamic diameter depends on the ionic strength of medium, and the NP surface structure and shape which affect the diffusion speed. For example, an adsorbed polymer layer projecting out into the medium will reduce the diffusion speed more than if the polymer is lying flat on the surface.

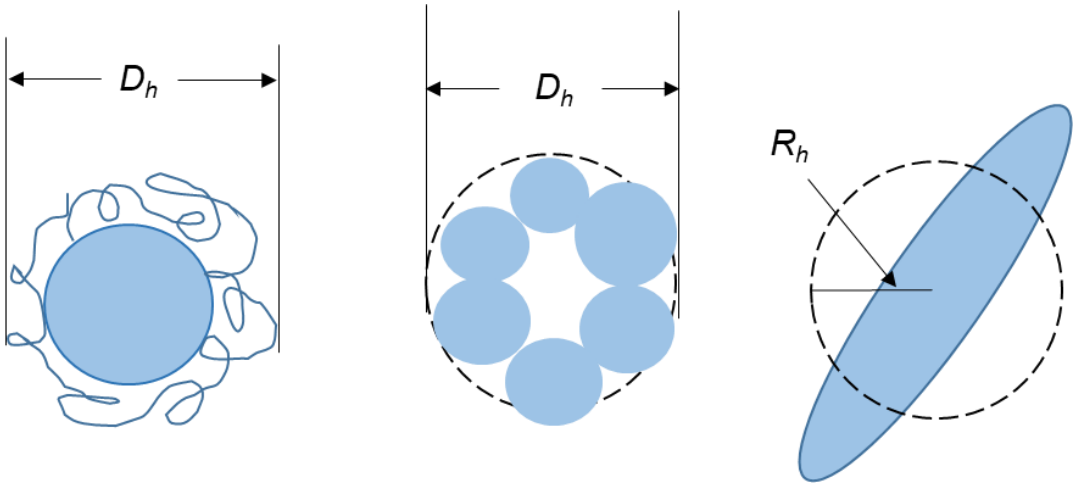


Figure 2.2: Schematic illustration of the hydrodynamic diameter (D_h) and hydrodynamic radius (R_h) measured as the size of a hypothetical hard sphere that diffuses in the same fashion as that of a particle for different scenarios – single particle, NP aggregate, and non-spherical particle.

DLS is based on the Brownian motion, which is the random movement of particles resulting from their bombardment by the solvent molecules that surround them. DLS measures the speed of particle diffusion which depends on the particle size and dispersant viscosity. The velocity of the Brownian motion is defined by the translational diffusion coefficient (D), which can be converted into a particle size using the Strokes- Einstein equation as seen below:

$$D_h = \frac{kT}{3\pi\eta D} \qquad \textbf{(2.1)}$$

where:- D_h = hydrodynamic diameter

k_{Boltz} = Boltzmann's constant

T = absolute temperature

η = viscosity

D = transitional diffusion coefficient.

2.2.1.2 Sample Preparation for DLS Size Analysis

The sample suspension is filtered to remove any large particles and impurities by using a 0.2 μm syringe filter or through a filter series, such as 0.2 μm and 0.1 μm as shown in **Figure 2.3**. If the sample is too concentrated or contaminated with any large particles and contaminants, multiple scattering will interfere the average measured size of the particles.

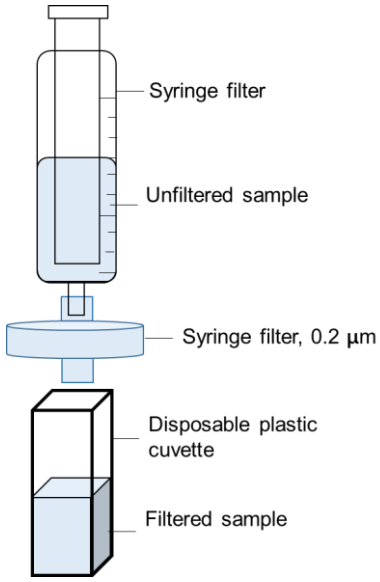


Figure 2.3: Schematic diagram of a sample being filtered through a syringe filter into a cuvette.

2.2.1.3 Size Analysis Procedure

The Malvern Zetasizer (nano ZS) with Zetasizer Software Version 7.11 (Malvern Instruments Ltd, 2014) is used to measure the hydrodynamic diameter and surface zeta potential. A standard operating procedure is set up as a measurement file which involves introduction of values for the refractive index and absorptivity of the material being measured (e.g. SiO_2 in this thesis), an absorption for the dispersant, the measurement temperature (i.e. 20˚C, 25 ˚C) and the number of measurements to be taken for each sample (typically 10 scans). The filtered sample is placed into the sample holder of the apparatus.

The size measurements are collected as a minimum of six consecutive measurements to ensure repeatability and to obtain the Z-average. The particle size obtained from DLS measurements represents the particle size in terms of the intensity, volume and number distributions-weighted Z-average, with the polydispersity index (PdI) being the standard deviation. In general, diameter weighted intensity has the highest value compared to the other representations. The PdI measures the broadness of the particle size distribution which is calculated using equation **(2.2)** shown below.

$$PdI = \frac{\text{Weight average molecular weight}}{\text{Number average molecular weight}} \quad \textbf{(2.2)}$$

A PdI value below 0.3 indicates a homogeneous sample, whereas a PDI value greater than 0.7 indicates a broad distribution of particle size, and that the sample is not suitable for analysis based on the DLS technique (Stetefeld, McKenna and Patel, 2016). The optimal particle concentration range for reproducibility should be not too dilute but not too concentrated, suggesting around 10^8 -10^{12} particles/mL based on 30 nm gold (Malvern Instruments Ltd). If the sample is too dilute that is not too scattering, the data refers to quality report being an improper concentration. Whereas too scattering not enough light reaches the detector, the data is not reproducibility and cannot interpretation.

2.2.1.4 Zeta Potential

Zeta potential is an important parameter that provides information about electrostatic particle stability, as indicated by the magnitude of charge on the particle surfaces. When NPs are suspended in a liquid, depending on the ionic

strength of the dispersing medium, some of the surface changes dissociate to form a layer of oppositely charged ions surrounding the NP surface known as the "Stern Layer". The Stern layer induces the presence of the electric double layer where an ion potential at this boundary represents the zeta potential (**Figure 2.4**). Zeta potential values beyond ±30 mV indicate that the particle is electrostatically stable as seen in **Figure 2.5**.

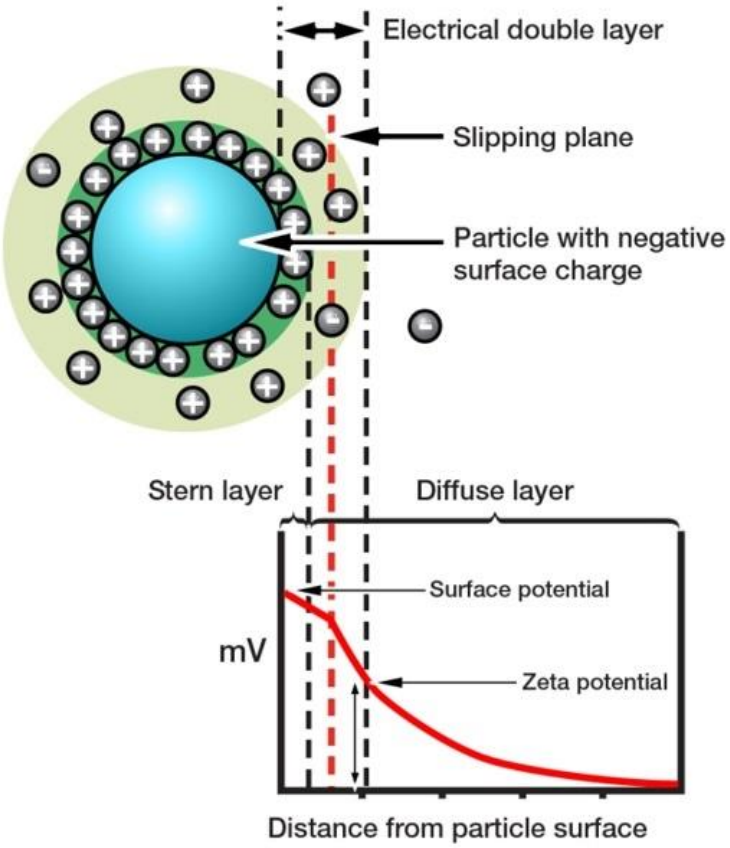


Figure 2.4: A schematic representation of zeta potential (Caputo and Roesslein, 2015).

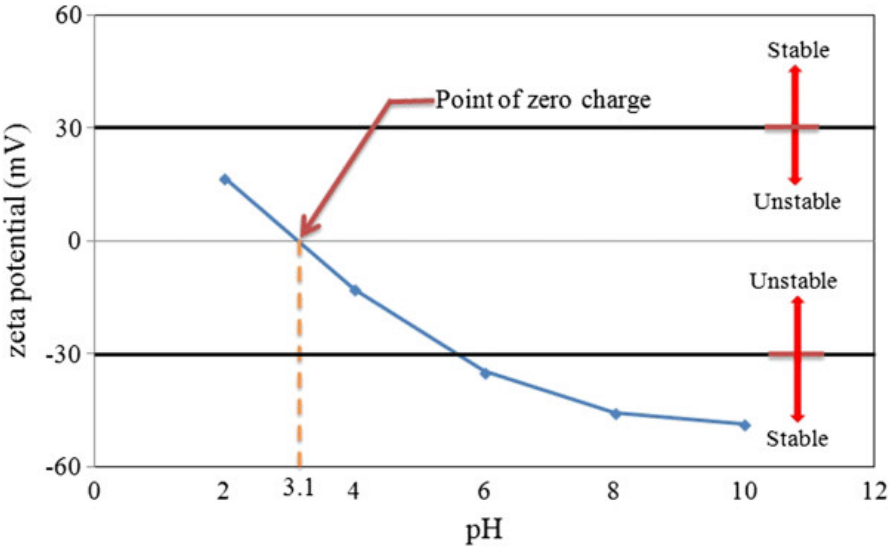


Figure 2.5: Graph showing the evaluation of the electrostatic stabilization of sample suspensions (Dey, Kumar and Samantaray, 2017). The point of zero charge is where all the surface charges and neutralised.

2.2.1.5 Zeta Potential Analysis

A standard operating procedure for zeta potential measurements involves introducing values for the refractive index, absorption of the material and of the dispersant and the temperature (20˚C) on a Malvern Zetasizer (nano ZS) using Zetasizer Software Version 7.11 (2014). A standard material, i.e. polystyrene, should be measured before the sample test. For a zeta potential measurement, 1 mL of a dispersion is injected into the zeta potential cell (**Figure 2.6**) and then placed in the sample holder. Three repeated measurements are obtained and averaged to generate the zeta potential value.

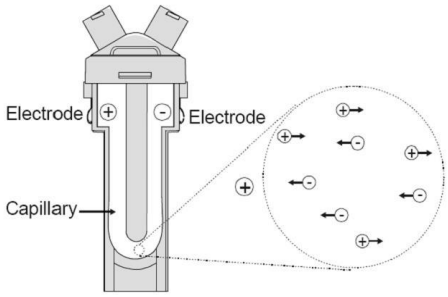


Figure 2.6: Zeta potential cell (Lázaro García, 2014).

2.2.2 Transmission Electron Microscopy (TEM)

2.2.2.1 Technique

TEM is a powerful analytical tool involving microscopic analysis of nanomaterials. TEM generates a high energy electron beam transmitted through a very thin sample deposited on a copper grid. An image is provided from the interaction of the electrons emitted through a very thin sample with varying magnification. The shape, size, density, and distribution of particles can be characterised using TEM analysis.

A side-view diagram of TEM showing the operating system is shown in **Figure 2.7**. A beam of high energy electrons is generated from the gun at the top of the first condenser lens. The electron beam is modified into a thin and small beam by passing through the condenser lenses which have apertures that focussed the small electrons. The electrons are transmitted through the sample to create a diffraction pattern as an image on the screen. The beam is magnified by the intermediate lens and projector lens to imprint and magnify the image.

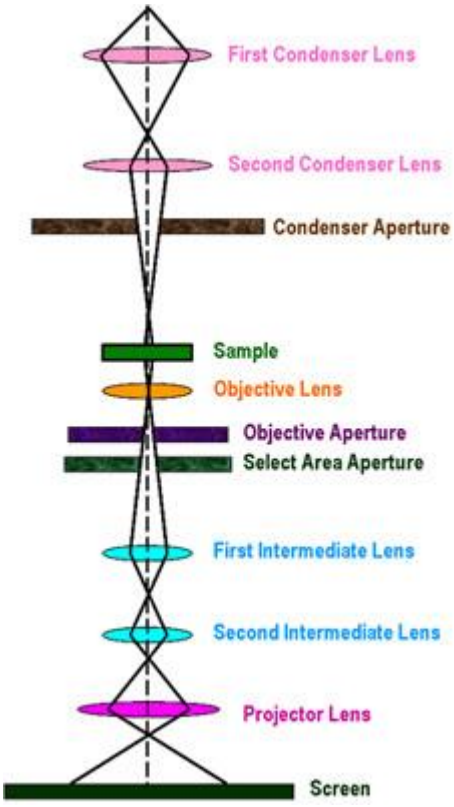


Figure 2.7: Diagram demonstrating the beam path of Transmission Electron Microscopy (Ding, 2011).

2.2.2.2 Sample Preparation

A few droplets of a sample dispersion are spread over the surface of a copper TEM grid coated with a thin film of holey carbon (Carbon film on 300 mesh Copper grid 3.05 mm). The drops of the sample are left to dry at room temperature for half an hour in order for the sample particles to become attached to the copper grid. The grid is then gently rinsed repeatedly using ultrapure water to remove any excess salts and loose particles, and then placed at room temperature until they have dried thoroughly before analysis.

2.2.2.3 Analytical Procedure

In this thesis, images were obtained using a Jeol 1200EX TEM (accelerating voltage 80 kV) and were analysed using Image J to assess particle size. At

least 100 particles of the sample were measured from the images and the individual measurements of particle size were used to calculate an average size and to plot a histogram of the particle size distribution of each sample.

2.2.3 Scanning Transmission Electron Microscopy (STEM)

2.2.3.1 Technique

The first scanning transmission electron microscope (STEM) was built by Manfred von Ardenne in 1937 – 1938 (Pennycook and Nellist, 2011). STEM combines the principle techniques of TEM and SEM, which provide information about elemental composition and electronic structure using the incident electron beam to excite the emission of characteristic X-rays from a sample at the ultimate resolution, that of a single atom (Pennycook *et al.*, 2010). The backscattered or secondary electrons passing through a sufficiently thin sample can form scanning images giving the details of structure and composition. STEM is equipped with multiple detectors, including a bright field (BF) and annular dark field (ADF) detectors operating simultaneously to collect the maximum information from different and complementary views of the sample from each scan. Z-contrast or high angle annular dark field (HAADF) is an imaging technique used for enhancing and complementing STEM results. A schematic of STEM configuration is shown in **Figure 2.8**.

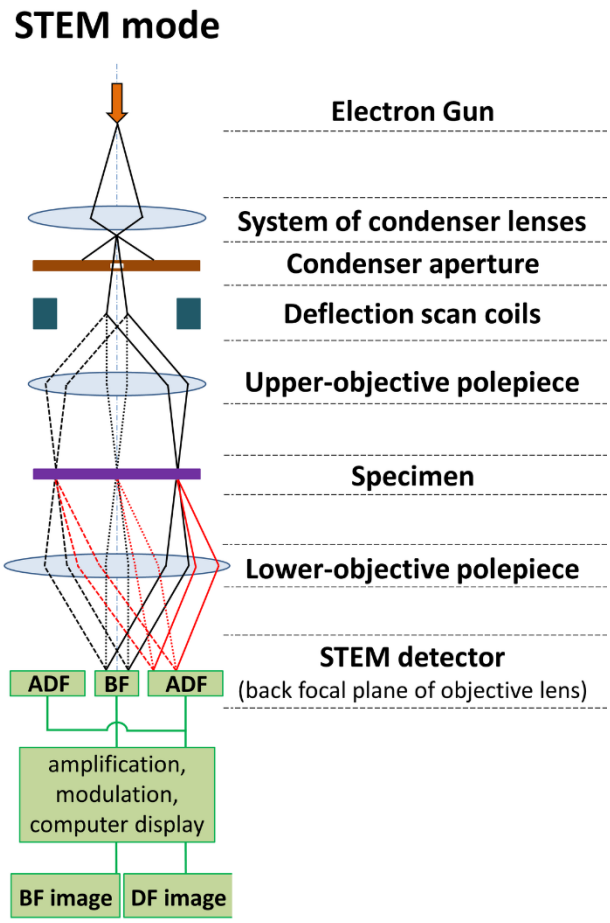


Figure 2.8: A schematic of STEM mode of Electron Microscopy (https://en.wikipedia.org/wiki/Scanning_transmission_electron_microscopy).

2.2.3.2 Sample Preparation

The samples for STEM analysis were prepared as for TEM described in section 2.2.2.2.

2.2.3.3 Analytical Procedure

STEM imaging was carried out at the Physics Department of the University of Birmingham by Dr Sophie Briffa. The HAADF was performed in a 200 kV JEM2100F STEM (JEOL) with a spherical aberration corrector. HAADF images were taken at the inner and outer angles of 62 and 164 at a probe convergence semi-angle of 19 mrad and camera length of 10 cm.

2.2.4 Scanning Electron Microscopy (SEM)

2.2.4.1 Technique

A scanning electron microscope (SEM) is a powerful and versatile tool for characterization of materials. SEM uses the specific coils above the objective lens to scan over the surface of a sample in order to create a 2-dimensional image (as shown in **Figure 2.9**). The electrons in the beam, the position of which is controlled by the scan coils, interact with the sample and produce various signals. These signals can be used to obtain information about the surface morphology, chemical composition, and crystalline structure of the sample (Susan Swapp, 2017).

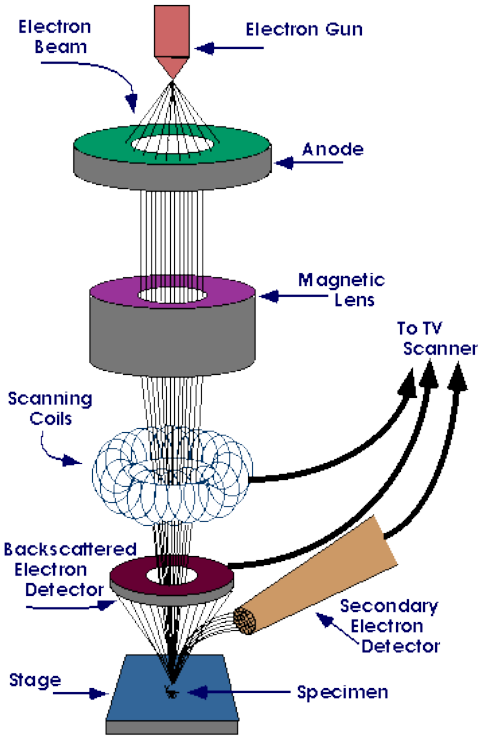


Figure 2.9: Schematic of the operational features of SEM (Walock, 2012; Shelby, 2019).

The incident electrons are produced at the top of the column under vacuum, decelerated in the sample and passed through a combination of lenses and

apertures within a special chamber that protects the electrons from contaminants, i.e. vibrations or noise. Secondary electrons, backscattered electrons, diffracted backscattered electrons, photons, visible light and heat arise when the focused beam of electrons hits the surface of the sample mounted on a stage (see **Figure 2.10**). Generally, the secondary electrons of the sample and the backscattered electrons are used to create an image of the sample showing the morphology and surface topology, while photons (characteristic X-ray) can be used to determine the elemental composition of the sample.

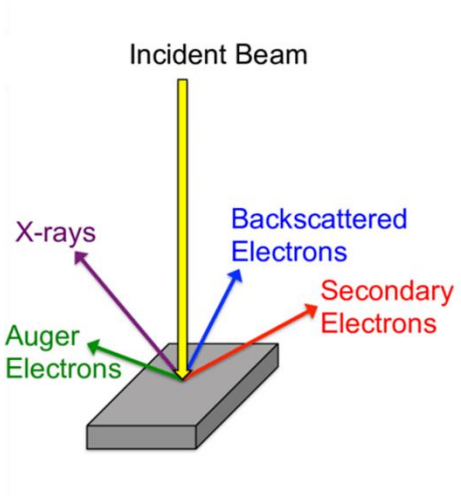


Figure 2.10: The electron beam-sample interaction in SEM (Walock, 2012).

2.2.4.2 Sample Preparation

The powdered aSiNPs produced by using low-temperature dehydration process, also known as lyophilisation. The powdered samples are mounted on a stage, then coated with a thin layer of gold to be electrically insulating material and placed in the chamber area. The microscope is designed to operate at low vacuums, both the column and the chamber are evacuated by a combination of pumps. The level of the vacuum will depend on the design of the microscope.

2.2.4.3 Analytical Procedure

SEM imaging was carried out on Zeiss AURIGA Field Emission Scanning Electron Microscope at the Suranaree University of Technology, Thailand. The focused electron beam was produced to hit the surface of the sample, then penetrated a few microns through the sample depending on the accelerating voltage and the density of the sample. The various signals, such as secondary electrons, backscattered electrons, photons were collected to form images and displayed on the computer screen.

The resolution of images obtained from SEM analysis depends on the electron spot size and interaction volume of the electron beam with the sample. Typically, SEM can provide resolution 1- 20 nm or below 1 nm as atomic resolution, whereas desktop systems can provide a resolution of 20 nm or more.

2.2.5 Synchrotron techniques

Synchrotron radiation is an electromagnetic radiation produced from charged particles moving at velocities very close to the speed of light. The radiation is forced to change direction by actions of electrons coming from a magnetic field and then loses a certain amount of energy, which is discharged in the form of electromagnetic waves called “synchrotron light”. Synchrotron radiation allows probing material properties with far greater resolution than lab-based techniques and has thus been used in recent years to address many fundamental research questions.

The synchrotron light source at the Synchrotron Light Research Institute (SLRI) in Thailand has been accessed for this study. A schematic of the structure of

SLRI, showing its main parts, can be seen in **Figure 2.11**; SLRI is a medium energy synchrotron at 3 GeV. The electron gun is the first component, producing a large number of electrons by using thermal ionic emission from the cathode of the electron gun until the electrons are released and then high positive voltage is applied to pull the electrons into the linear accelerator. In the booster ring, the electrons are divided into electron bunches and then accelerated at a linear speed by microwaves to attain 40 MeV. The booster ring increases the electron energy reaching to values around 1 GeV. The electrons pass through the bending magnets and transfer into the storage ring at the final stage. The desired range of synchrotron radiation is selected to create optimized conditions for applications in the specific fields of spectroscopy, scattering, and imaging. In this study, synchrotron-based techniques, such as Small Angle X-ray Scattering (SAXS), X-ray Photoelectric Spectroscopy (XPS), X-ray Absorption Spectroscopy (XAS), and micro-X-ray Fluorescence spectroscopy (μ-XRF) were used for characterization of the synthesized nanomaterials.

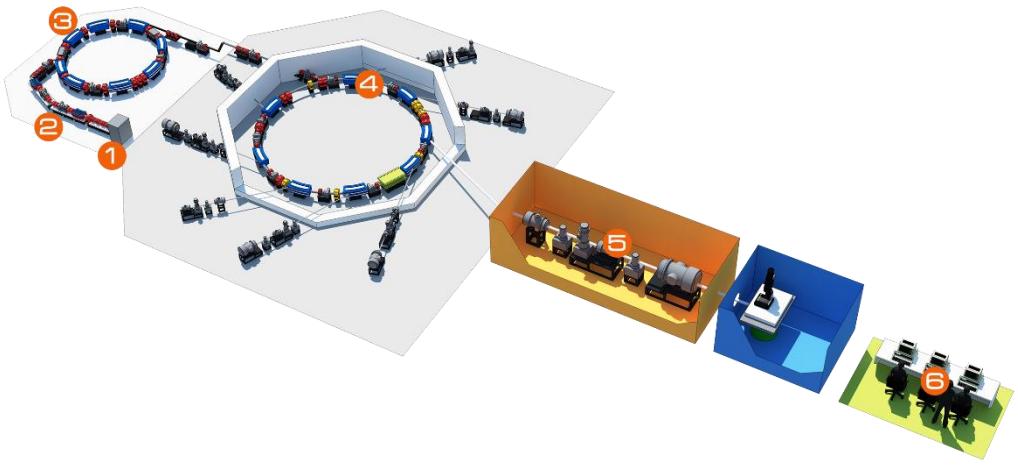


Figure 2.11: A schematic of the main components of the Synchrotron Light Source in Thailand (SLRI, 2015). The numbers above correspond to: (1)

Electron gun, (2) Linear accelerator, (3) Booster Ring, (4) Storage Ring, (5) Beamline and (6) User workstation area.

2.2.6 Small Angle X-ray Scattering (SAXS)

2.2.6.1 SAXS Technique

SAXS is a non-destructive method, requiring a small sample either in solid or liquid form or a combination of the two (Schnablegger and Singh, 2013). SAXS is used to determine the structure of particles at the smallest angles ($5^{\circ} < 2\theta < 50^{\circ}$, where θ is the angle between the incident beam and a crystallographic reflecting plane). In principle, when X-rays hit a material, there are two interactions: absorption and scattering. Absorption can occur at any wavelength depending on the atomic species of the material and the wavelength. The absorption should be small to attain high-quality SAXS data. Compton or inelastic scattering can occur when the incident photon collides with an electron and is scattered to lower energy, which is part of the featureless background radiation and provides no structural information. Rayleigh or Thomson scattering, which is the elastic scattering of electromagnetic radiation, happens when the incident photons collide with strongly bound electrons at the same frequency. Then the electrons are scattered resulting in an oscillating electric field. These patterns provide information about the particle structure of samples (Beaucage, 1995; Schnablegger and Singh, 2013).

Scattering patterns (as seen in **Figure 2.12**) are usually relative to the length of the scattering vector (q), which represents the wavelength (λ) of the incident radiation and the scattering angle (θ) (also known as Bragg's law).

$$q = \frac{4\pi \sin\theta}{\lambda}, [1/nm] \quad \textbf{(2.3)}$$

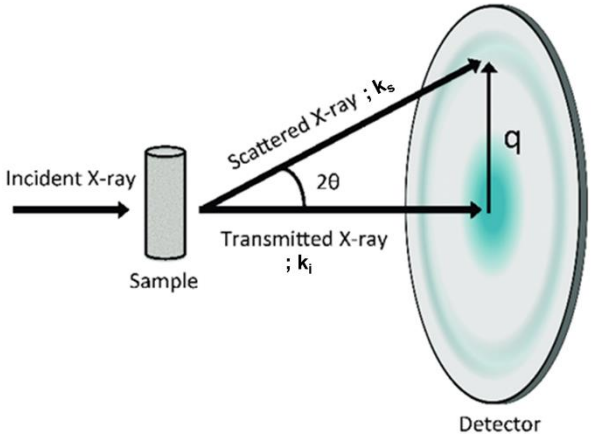


Figure 2.12: Schematic representation of the scattering vector q; where k_i and k_s are the incident and scattered wave vectors, respectively, at scattering angle θ (Axel, 2017).

Scattering patterns or the structure in reciprocal space are reduced into one-dimensional (1D) scans normally using the Guinier and Porod approximation (Schnablegger and Singh, 2013). Each ring of scattering patterns corresponds to one data point in the reduced 1D graph. The various regions of q in the 1D graph contain information about the sample as indicated in **Figure 2.13**. The scattering intensity is plotted as a function of scattering vector q.

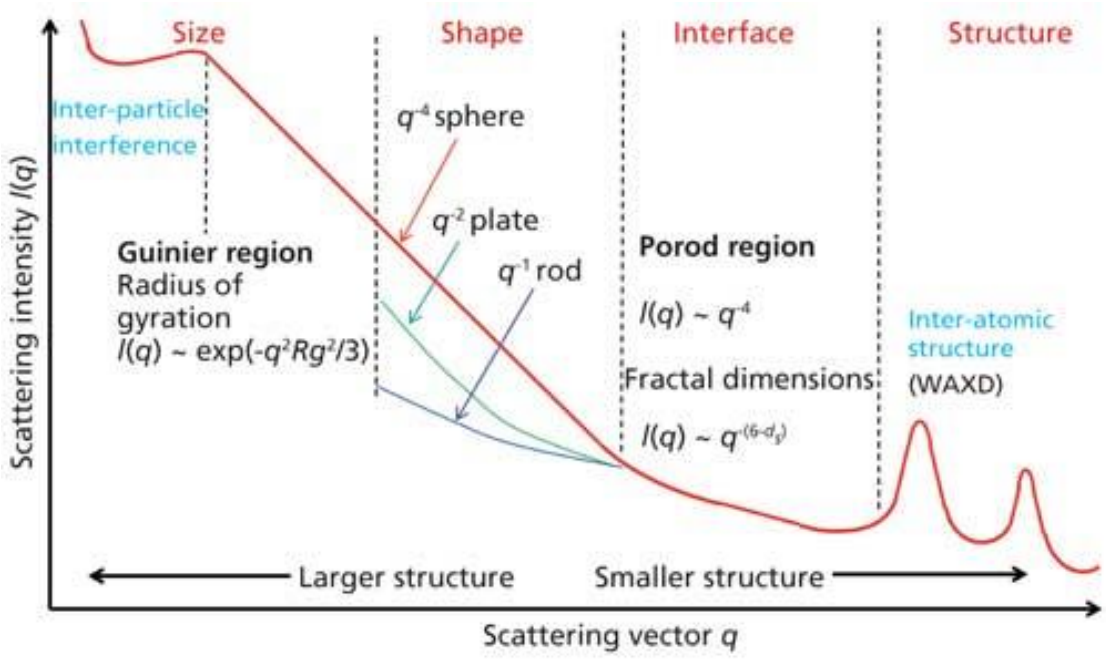


Figure 2.13: Schematic of 1D SAXS graph with the information that can be indicated at each q region (Bras *et al.*, 2010).

The scattering pattern at small values of q, called the Guinier region, contain information about whole particles, if they are small, as well as internal structure information for large- scale particles. The radius of a spherical particle, presented in term of the radius of gyration (R_g), is calculated as described in Equation **(2.4)**.

$$I(q) = I(0)\exp[\frac{-R_{g^2}q^2}{3}] \quad \textbf{(2.4)}$$

where:

I(q) is the scattering intensity and I(0) is the forward scattering intensity and q is the scattering vector magnitude.

R_g is model independent and is used to define the particle dimensions. In this thesis, the particles are assumed to be spherical with homogeneous density, and thus R_g can be calculated from equation **(2.5)**.

$$R = \sqrt{\frac{5}{3}R_g} \quad \textbf{(2.5)}$$

The scattering pattern in the Porod region at high q calculated from the Fourier transform of the real-space density distribution (also known as form factor) can provide information on particle shape.

The form factor

The oscillating pattern can describe the shape or the form of the particle as shown in **Figure 2.14**. Therefore, it is called the form factor, P(q). When the particles are all identical in size and shape (i.e. monodisperse sample) and distribute without particle interaction (i.e. dilute sample, freely floating), the form factor can provide entirely the description of the scattering pattern. In contrast, if the sample is polydisperse, the form factors from each particle size are summed up to give an average scattering pattern of the whole sample. Therefore, the form factor is the Fourier transformation of the scattering length density distribution of the particles.

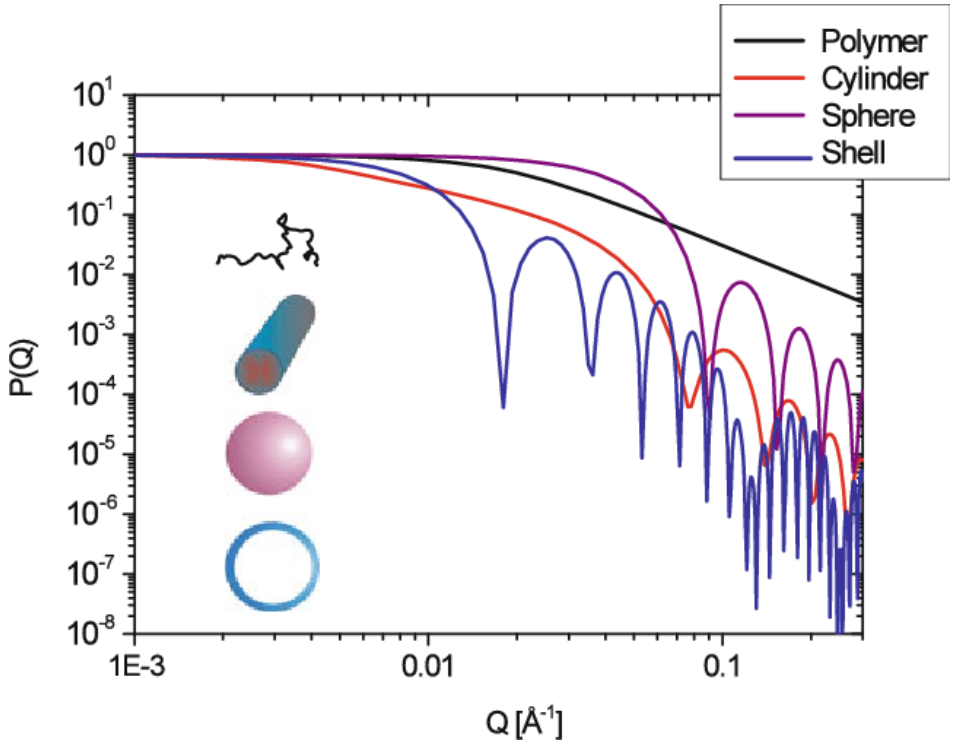


Figure 2.14: A simulation of the form factors, P(q), of particles in the scattering pattern, representing the pattern of oscillations representative of the four different shapes/forms of particles (Organolithiums, 2014).

In the case of spherical monodisperse particles, the form factor can describe the scattering pattern as follows:

$$P(q) = 4\pi\rho_{0^3}3\frac{\sin(qR) - qR\cos(qR)}{(qR)^3} \qquad \textbf{(2.6)}$$

where:

P(q) = the particle form factor

ρ_0 = electron density distribution

qR = the slope of the plot of scattering intensity versus the scattering vector (equal to -4)

The structure factor

SAXS experiments can describe the information of complex systems, such as densely packed particles, particle interaction potentials, electrostatic, and concentration effects. The structure factor S(q) is related to the probability distribution function of the distances between particles coming into the same order of magnitude as distances within particles. S(q) thus contains information about the position of the particle arrangements.

2.2.6.2 Sample Preparation

Synthesised aSiNPs were stored at 4°C before analysis. Colloidal aSiNP dispersions were prepared at three concentrations from low to high concentration (i.e. the stock or original concentration) equivalent to 2.5, 5 and 11 mg/mL with and without filtering. 2-5 mL of the aSiNPs dispersions were injected into the sample holder (as shown in **Figure 2.15**). The sample holder has been removed to show the window which is transparent to X-rays. The material used to as the window should be non-scattering, resistant to chemical attack and to elevated temperatures. Kapton® tape (i.e. polyimide film) was used as a window material in this study.



Figure 2.15: The sample holder with Kapton® tape for SAXS analysis of liquid samples.

2.2.6.3 Analytical Procedure

All SAXS data were collected on beamline 1.3W at the Synchrotron Research Institute using a double multilayer monochromatic (W/B4C) X-ray beam at 9 keV, with Rayonix SX165 detector to collect the SAXS patterns. As well as SAXS measurement of ageing of aSiNPs was carried out at Bundessanstalt für Materialforchung und-prüfung (BAM), Berlin, Germany analyzing the stock solution and original concentration. The scattering patterns were reduced to one-dimensional curves of intensity (I) and q by the integrated beam intensity. For the simulation, the SAXSIT version 3.66 software, developed by SLRI was used to normalize and align data from SLRI, Thailand. For the fitting data, the SASFit and MacSAS analyses were carried out on the normalized scattering data using a spherical model with 1D SAXS curves from SLRI and BAM, respectively.

The scattering curves were fit in SASFit using a model that describes the scattering as arising from a population of spherical primary particles (spherical form factor as seen in Equation 2.5), which are monodisperse. The full equation describing scattering model was as follows:

$$I(q) = |P(q)|^2 = (4\pi)^2 \rho_{0^3} [3 \frac{\sin(qR) - qR\cos(qR)}{(qR)^3}]^2 \qquad \textbf{(2.7)}$$

where:

I(q)	=	Intensity of X-ray
P(q)	=	the particle form factor
ρ_0	=	electron density distribution
qR	=	the slope of the plot of scattering intensity versus the scattering vector (equal to -4)

A more detailed description of this fitted model can be found in Chapter 3 and 4.

2.2.7 X-ray Photoelectron Spectroscopy (XPS)

2.2.7.1 Technique

XPS is an analytical technique providing both elemental and chemical state information of solid nanomaterials at the outer surface around 5-10 nm depth (Murphy, 1967; Biesinger, 2009). The technique involves exposing the nanomaterials to soft X-rays and measuring the kinetic energy of the emitted photoelectrons. Due to the low energy of these electrons, they can only escape from the surface (top few atomic layers, or a few nanometers) of the particles and thus XPS is a surface characterization technique.

Figure 2.16 shows the photon of X-ray (hv) at levels of Al or Mg at *K* level (*K*α) which is transmitted through the samples within the ultrahigh vacuum; the electron in the first shell of the atom can absorb the energy. The incident of photoelectric effects or photoemission will occur when the electron absorbs energy at least at that energy level. The photoelectric effect induces an energy compensation by transitioning energy from the outermost electron inwards, namely relaxation. The outermost electron can escape from the excited state by losing energy in the form of X-ray fluorescence or Auger electron emission.

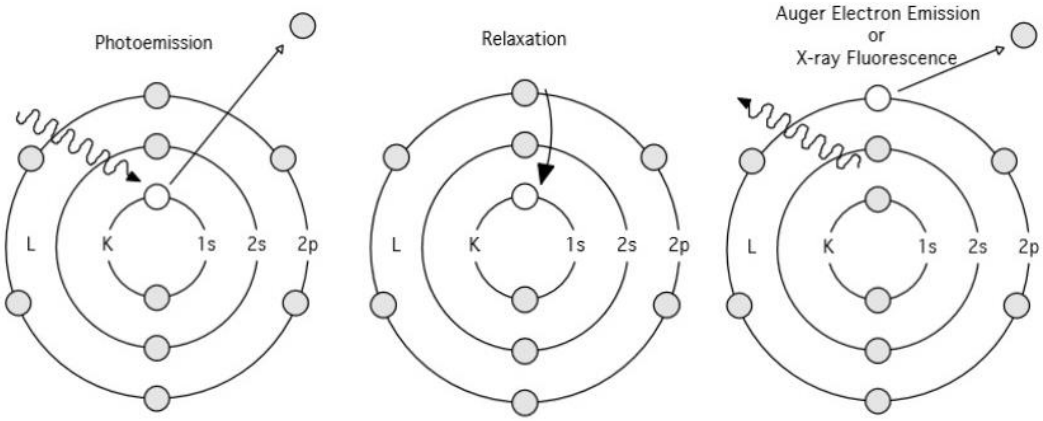


Figure 2.16: The basis of photoelectric absorption, relaxation and Auger electron emission.

The survey spectrum represents the kinetic energy of the peak positions at a sequence of energies that can be used to indicate the elemental composition while the peak intensities measure the quantity of a material on the sample surface (see **Figure 2.17**). Heide (2011) explained the limitations of the XPS technique, why hydrogen and helium are not detectable, but beyond these smallest elements, all other elements can be observed. In 2018, Zhong *et al.* (2018) demonstrated that the gas phase spectra of H and He can be observed using synchrotron-based ambient pressure-XPS technique if the X-ray source is bright enough.

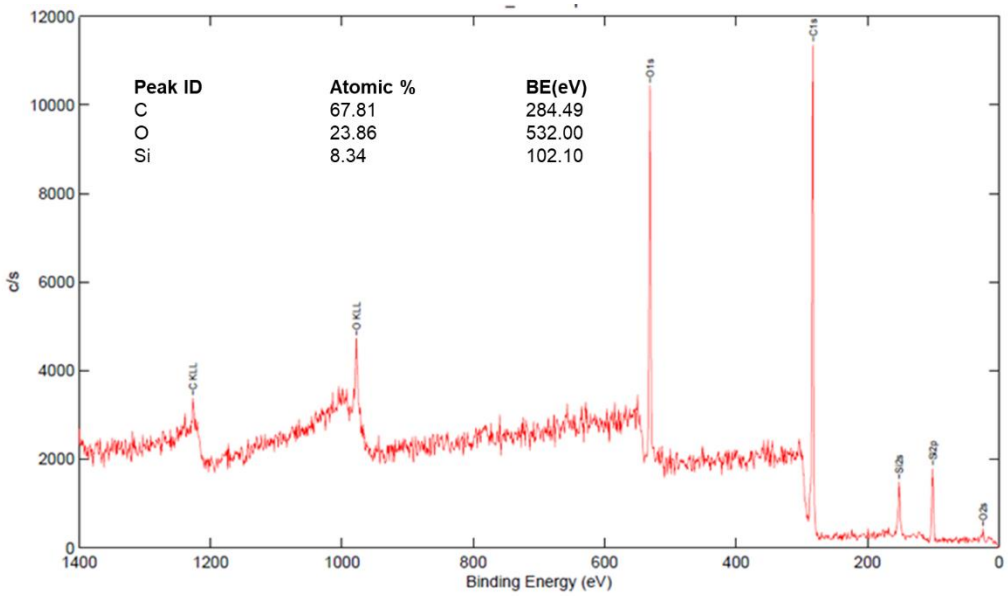


Figure 2.17: A survey spectrum, presenting certain elements on a sample surface and the elemental quantitation of their atomic percentages.

2.2.7.2 Sample Preparation

Powdered samples are mounted on carbon tape, then labelled and attached on the stainless-steel stage as shown in **Figure 2.18**. The stage is placed in the high vacuum chamber and is illuminated by using X-rays at the energy levels of Al *K*α or Mg *K*α. The kinetic energy of the emitted electron causes the photoelectric effect which is detected and then converted to the binding energy. This information provided the characteristic and quantitative information regarding the elements at the sample surface.

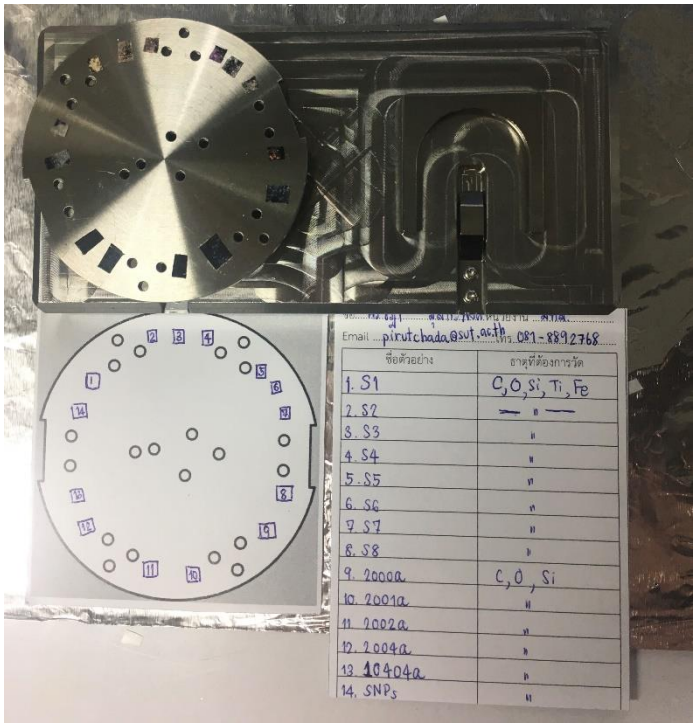


Figure 2.18: Sample preparation for XPS analysis, mounted samples on the carbon tape and attached on the stainless-steel stage.

2.2.7.3 Analytical Procedure

The XPS data presented in this thesis was generated using a PHI5000 Versa Probe II, ULVAC- PHI, Japan to identify the elemental composition of the sample surface. The XPS source was equipped with monochromatic Al*K*α X-ray at beam energy 1486. 6 eV. The experiments were carried out under ultrahigh vacuum conditions - pressure below 10^{-8} mbar. The surface area at 100x100 μm^2 and 5-10 nm depth were observed for each sample.

2.2.8 X-ray Absorption Spectroscopy (XAS)

2.2.8.1 Technique

XAS is a widely utilized method applied to determine the local structure of materials. When high-energy X-rays strike a core electron from the ground state

to an unoccupied state or continuum level, as seen in **Figure 2.19**, then an X-ray photon is absorbed by the core electron. After that the excited atom returns to the ground state by emitting fluorescence or an Auger electron.

In XAS, the absorbing element in the sample is characterized by the absorption changes in X-ray photon energy. All forms of sample, i.e. solid, gas, or liquid can be measured by the XAS technique. This technique involves a tunable monochromatic X-ray passing through the sample and absorbing enough energy to excite an electron as a function of it' s binding energy. XAS data are collected by measuring a function of energy (μ(E)) as the X-ray absorption coefficient. XAS signal can be detected in three modes, such as transmission, fluorescent yield and electron yield. Beamline 5.2 at SLRI applies the transmission mode. In the experiment, the electrons being absorbed are measured by the difference in X-ray intensity before and after passing through the sample. This involves Beer-Lambert's Law as described in equation **(2.8)**.

$$I_1(E) = I_0\, e^{-\mu(E)x} \qquad \textbf{(2.8)}$$

Where $I_1(E)$ and $I_0(E)$ are the incident and transmitted X-ray intensities, μ(E) is the X-ray absorption coefficient and x is the sample thickness. Then, to obtain the absorption coefficient, this equation is rearranged as shown in equation **(2.9)** to obtain the absorption coefficient (μ(E)).

$$\mu(E)x = ln(I_0/\, I_1) \qquad \textbf{(2.9)}$$

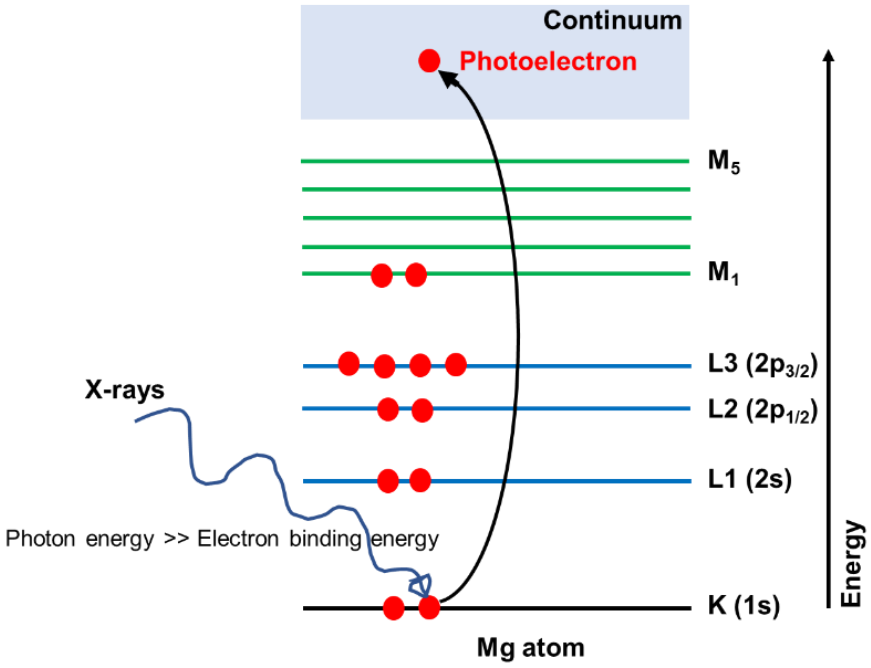


Figure 2.19: The mechanism of X-ray absorption at K-edge (K-edge absorption)

The XAS spectra of virtually all elements contain two parts, namely XANES and EXAFS features. XANES refers to the absorption fine structure close to an absorption edge which is dominated by electronic transitions from a core level to unoccupied states for photoelectrons, thus it measures a local electronic structure and reflects local density of states (LDOS) above the Fermi level. The K-edge is a sudden increased in X-ray absorption occurring when the energy of the X-rays is just above the binding energy of the innermost electron shell of the atoms interacting with the photons. This region (as shown in **Figure 2.19**) usually shows the largest variations in μ(E) and is important for indicating the specific structural information of materials. Edge position can determine the oxidation state by comparing with the fingerprint of standard material and XANES feature can indicate the structural morphology, i.e. crystalline and amorphous structures.

Further from the sample edge, EXAFS reveals the local atomic environment, i.e. the number of neighbouring atoms, type of neighbouring atoms, and bond length to the element (see **Figure 2.20**). More specifically, the oscillations are observed in the EXAFS feature at energies above the absorption edge. The wave interactions between the ejected photoelectron and the electrons of other surrounding atoms arise from constructive and destructive interactions, and give information on the location and identify of the surrounding atoms and the local bonding environment present in the sample.

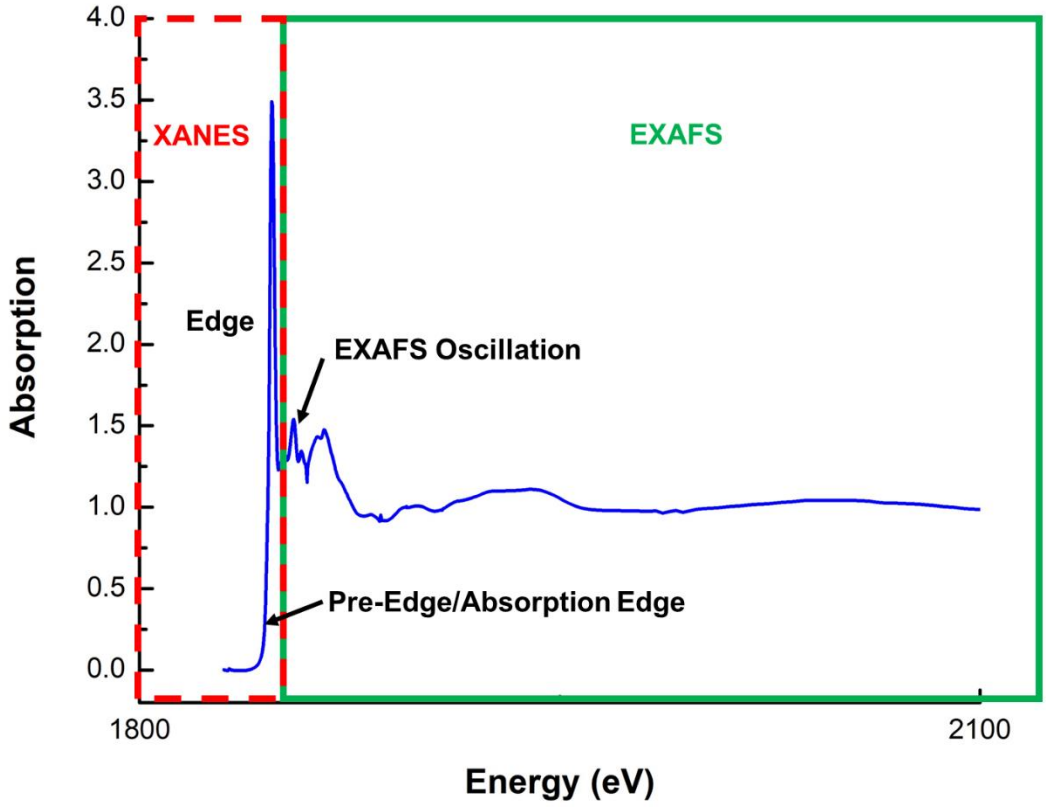


Figure 2.20: XAS spectrum of a standard sample shows two parts, namely XANES (in red-dash box) and EXAFS (in the green box), features.

2.2.8.2 Sample Preparation

Prior to analysis, the powder standard has to be prepared and compared to reference XAS spectra as the fingerprint spectra for comparative purposes. The standards are well-ground and mounted on acrylic plastic film to form the X-ray transparent windows (shown in **Figure 2.21**). Then, the sample solutions were injected into an acrylic plastic cell with each side sealed with Kapton® tape.

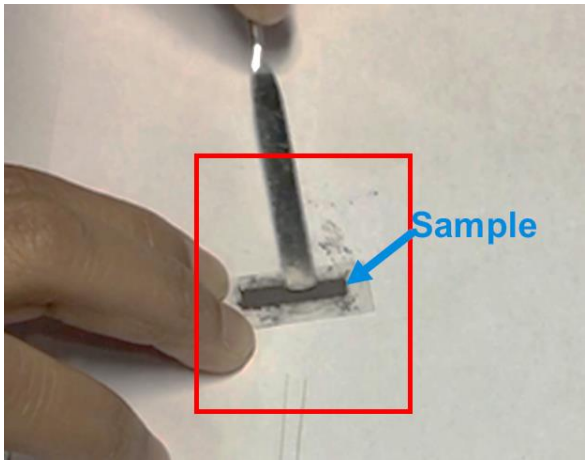


Figure 2.21: A standard powder of sample mounted on an acrylic plastic film for XAS analysis.

2.2.8.3 Analytical Procedure

A range of XAS techniques including XANES and EXAFS are available at the SLRI, Nakhon Ratchasima, Thailand. XAS monochromatizes synchrotron light from a bending magnet to obtain an X-ray beam with photon energy ranging from 12.5 keV to 10 keV. Photon energy is scanned by a double crystal monochromator (DCM). Si K-edge spectra were collected in fluorescence mode at Beamlines 5.2 and 8 at the SLRI at a total step of 93 times for 3-6 hours, with three repeated scans collected for each sample. Spectra were averaged and normalized in Athena, followed by fitting in Artemis (Bruce Ravel, 2009).

2.2.9 Micro X-ray Fluorescence Spectroscopy (μXRF)

2.2.9.1 Technique

μ- XRF is used to determine the chemical composition of materials and sometimes can be used to assess the thickness and composition of layers and coatings. Fluorescence, Compton scatter and Rayleigh scatter (see **Figure 2.22**) occur when incoming X-ray photons strike a material. As seen previously in **Figure 2.16**, the secondary X-ray or fluorescence is emitted from a material when exposed to energy greater than its ionization energy. XRF technique measures discrete energies equivalent to a different colour and the intensity of emitted fluorescence radiation. These measurements provide information about a specific element and its concentration in the sample. Furthermore, a tunable beam size of the X-ray (in micrometres) can be used to examine the distribution of elements in the sample. This technique is called micro-X-ray fluorescence spectroscopy/imaging.

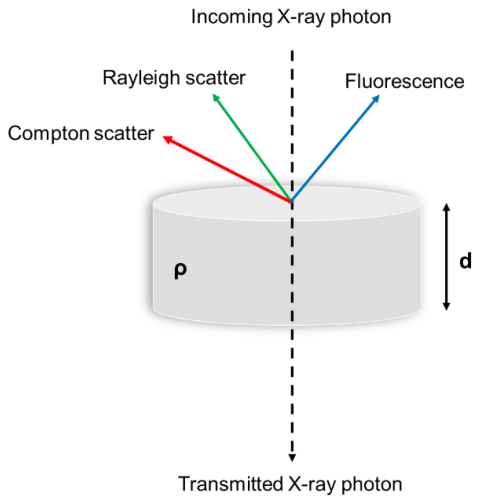


Figure 2.22: The interaction between incoming X-ray photons and material (Brouwer, 2010).

2.2.9.2 Sample Preparation

μ-XRF technique is applied to determine the elemental distribution through the samples which are attached to an acrylic plastic film and placed on the sample stage (as shown in section 5.2.5, Chapter 5).

2.2.9.3 Analytical Procedure

μ-XRF technique (beam size 30 μm) with energy ranging from 2-10 keV is available at beamline 6b, SLRI (Thailand). The analysis procedure involves using a wire-scan method to collect a total number of points around 900 at time steps of 30 seconds for 6 hours per sample. The spectra are collected and analyzed by fitting in PyMca version 5.4.1(Solé *et al.*, 2007).

2.2.10 Fourier Transform-Infrared Spectroscopy (FTIR)

2.2.10.1 Technique

FT-IR is a characterization technique which aims to identify the chemical structure of organic and inorganic molecules. Infrared light passes through the sample that is being irradiated with the infrared part of the electromagnetic radiation spectrum. The IR spectrum records the molecular absorption and transmission, thus making a fingerprint of the sample. This fingerprint contains a variation of vibrations, rotations and translations of the bonds within the molecule. The IR spectrum including vibrations, rotations and translations is unique to a particular substance showing a unique combination of specific bonds and functional groups.

2.2.10.2 Sample Preparation

2 mg of powdered samples from each batch was blended with 198 mg of potassium boron (KBr) and then made a pellet (see in Fig. 2.21) by using a hydraulic pressure gauge.



Figure 2.23: Standard discs of KBr (left) and sample (right).

2.2.10.3 Analytical Procedure

FT-IR technique was carried out using a Varian 660-IR FT-IR Spectrophotometer at the School of Chemical Engineering of the University of Birmingham. “Agilent resolutions pro” software was used to run the spectrometer. FT-IR analysis involved the characterization of a reference KBr pellet as a background scan, followed by subsequent powdered samples, placed on the Attenuated Total Reflectance (ATR) attachment of the instrument. The sample spectra were obtained between 400 and 4000 cm^{-1} wave number.

2.2.11 X-ray powder Diffraction (XRD)

2.2.11.1 Technique

XRD is a characterisation technique that uses X-rays to identify a material’s crystal structure, and infer chemical composition and potentially particle size (for small enough particles) (Barbara L Dutrow, 2019)). XRD examines materials using the diffraction of X-rays at different angles. An X-ray diffraction

pattern (see **Figure 2.24**) is plotted between the diffracted X-ray intensity and the angle 2theta (2θ) obtained at different angles from each set of lattice planes in a sample. The intensities and the position of the peaks are used to identify the structure (or phase) of the material. The experimental XRD pattern can be compared to reference patterns of standard materials to enable identification of the material.

During the measurement, an incident X-ray beam interacts with planes of atoms while the detector moves in a circle around the sample (**Figure 2.25**). Then, part of the beam is relatively transmitted, absorbed, reflected, scattered or diffracted during the measurement. If the interactions between an X-ray beam and the sample is a diffracted X-ray, then the distance between the planes of atoms can be measured by using Bragg's Law as shown in equation **(2.10)**

where *n* is an integer, λ is the wavelength of the X-rays, *d* is the distance between diffracting planes, and θ is the angle between the incident ray and the diffracting planes (Bragg and Bragg, 1913).

$$n\lambda = 2d\sin\theta \qquad \textbf{(2.10)}$$

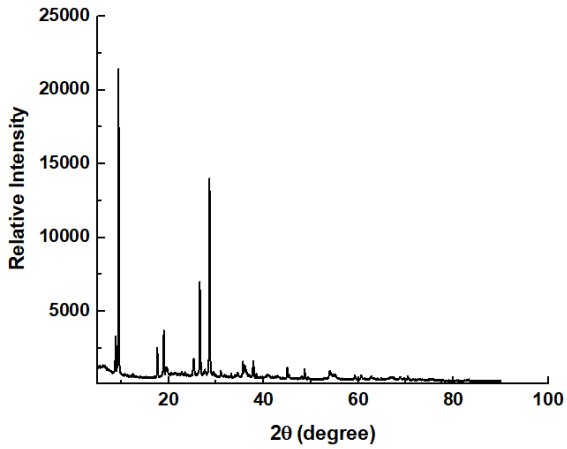


Figure 2.24: The XRD pattern of a powdered sample is collected at 2θ from 5˚ to 90˚to provide insights into the crystal structure.

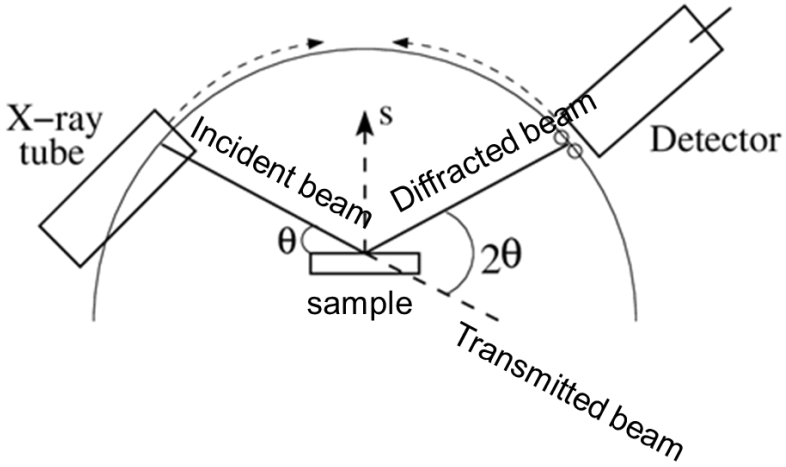


Figure 2.25: Schematic diagram of an XRD diffractometer system (Toth and Mathworks, 2017).

2.2.11.2 Sample Preparation

Only solid samples (powder) can be characterised by XRD, but sample preparation is quick and rapid. Samples were stored in the desiccator for at least 24 hours prior to measurement to ensure complete drying. Dried samples were then ground to obtain a fine powder to be used for analysis. The powdered samples are smeared onto a flat surface of a sample slide.

2.2.11.3 XRD Analysis

XRD analysis was carried out in the School of Chemistry at the University of Birmingham using a Bruker D8 Advance diffractometer. Powdered samples were sprinkled on 1 cm^2 disk holders and loaded into the diffractometer. Diffraction patterns were obtained by scanning with Cu Kα radiation over a range of Bragg angles (5 to 90˚) at room temperature over a period of 30 minutes. The resultant patterns are depicted as obtained and then analyzed by

comparing to reference spectra (fingerprints) using Eva software (Ocean and Program, 2013).

2.2.12 Brunauer, Emmett and Teller (BET) surface analysis

2.2.12.1 BET Technique

BET is one of a few techniques available to measure surface area. Surface area measurement involves characterization of the adsorption process of a gas, commonly N_2 gas, on the surface of the sample at liquid nitrogen temperature. Nitrogen gas is assumed not to interact with the particle's surface. The Brunauer, Emmett and Teller (BET) equation (Equation **Error! Reference source not found.**) is used to calculate the surface area of a sample, where p is the equilibrium (p) and p_0 is the saturation pressure of adsorbates at the temperature of adsorption, n_a is the adsorbed gas quantity in volume units, n_m is the monolayer capacity, and C_{BET} is the BET constant.

$$\frac{p}{n_a(p_0 - p)} = \frac{1}{n_m C_{BET}} + \frac{(C_{BET} - 1)}{n_m C_{BET}} \cdot \frac{p}{p_0} \quad \textbf{(2.11)}$$

where; $n_m = \frac{1}{gradient - intercept}$

$$C_{BET} = 1 + \frac{gradient}{intercept}$$

$$S_{total} = \frac{n_m N_s}{V}$$

Eventually, the change in volume of gas absorbed to the surface is calculated and given as the specific surface area in grams per meter squared (m^2g^{-1}). The sample must be in powder form and dried.

2.2.12.2 Sample Preparation

The powdered samples are kept in the desiccator for at least 24 hours to ensure complete drying. Prior to the surface area analysis, the samples must be outgassed to remove water and contaminants. The outgas process is under a vacuum at high temperature. Samples are gently compacted into the glass cell with a glass rod to minimize the dead space in the cell. The cell is placed into the heating mantle and cooled down before it is ready to adsorb nitrogen gas; this is then followed by desorption of the gas.

2.2.12.3 Analytical Procedure

BET was carried out to estimate the surface area of dry powdered samples on SA 3100 Surface Area Analyzer. The samples of amorphous silica materials were heated under vacuum at 300˚C for several hours to remove surface adsorbed moisture and contaminants. aSiNPs were repeatedly tested for surface area from all batches. The powdered aSiNPs are weighed before and after outgassing, then the net weight is used to set up and calculate the specific surface area. At liquid nitrogen temperature, nitrogen is adsorbed onto the sample surface by a physical force such as a weak Van der Waals attraction. Data are collected in the form of a BET isotherm. The isotherm is plotted between the amount of gas adsorbed onto the surface of the sample and the relative pressure. The specific surface area is calculated using the sample mass as shown in Equation **(2.12)**.

$$S_{BET} = \frac{S_{BET}}{Sample\ mass} \qquad \textbf{(2.12)}$$

2.2.13 Inductive Coupled Plasma-Optical Emission Spectroscopy (ICP-OES)

2.2.13.1 Technique

The detection of elemental concentration with high sensitivity involves using a mass spectroscopy technique. ICP-OES is a type of emission spectroscopy which determines elemental composition. This technique uses a flame temperature in the range from 8000 to 1000 Kelvin. The inductively coupled plasma generates excited atoms and ions that emit the electromagnetic radiation when they return to their ground state. The electromagnetic radiation has specific emission wavelengths to enable identification of which element is present and its relative proportion within a sample. The schematic diagram of ICP-OES mechanism is shown in **Figure 2.26**. There are two main parts that consist of a light source unit and an optical spectrometer. The liquid sample is pumped into the system passing a nebulizer that turns the sample into an aerosol and is then injected into the plasma. The aerosol is exposed to high temperature in the plasma that excites the atoms leading to release of the emission wavelengths. The emitted radiation from the plasma is used to identify the type and intensity of elements present in the sample. For the quantification of intensity, there are two methods, namely radial and axial viewings for analyzing the proportion of elements. The radial viewing has an excellent tolerance to dissolved solids and torch lifetimes but has lower sensitivity than the axial viewing. The axial viewing can provide 5-20x improvement in detection limits by enhancing the signal-to-noise ratio.

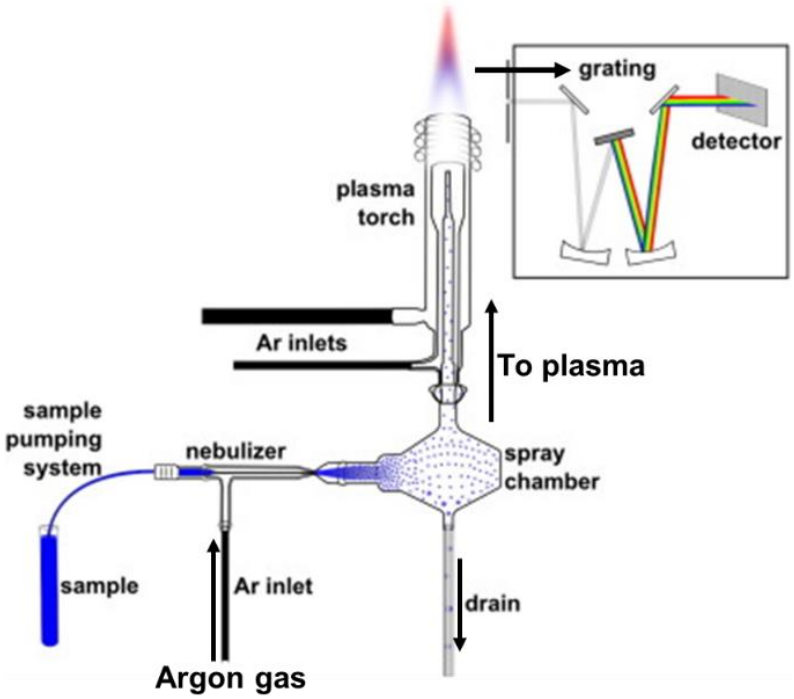


Figure 2.26: Schematic diagram of the ICP-OES technique (Caruso *et al.*, 2017).

Calibration curves are introduced and verified using a series of standard reference solutions for the analyte (s) of interest prior to sample. It is recommended to prepare a blank and internal standard if expecting to encounter in the matrix or digestion interferences for correction and calculation of %recovery.

2.2.13.2 Sample Preparation

Prior to the analysis of elemental concentration, sample solutions need to be filtered through a 0.22 m polyethersulfone (PES) filter. Powders are normally firstly digested overnight. For non-refractive materials, digestion can be carried out in 20% nitric acid (HNO_3), and then diluted to a final concentration of 2% HNO_3.

2.2.13.3 Analytical Procedure

ICP-OES analyses were conducted using an Optima 8000 spectrometer. Elemental concentrations were measured by comparison to calibration standards. Analysis took place using a radial detection system, which was used for analysis with a 70 second delay time. Three separate dispersions from each batch were measured in order to obtain an average of three measurements for each sample. The standard samples were interposed at every 10 measurements of the samples including blanks.

2.2.14 Summary of analytical approach

Table 2. 1 summarises all methods considered/ used in this thesis, their strengths and weaknesses, the type of information they provide and, where appropriate, their particle size resolution. Given the diversity in the physicochemical characteristics of nanomaterials, their small size and the complexity of the matrix they are found in, there are challenges in delivering a reliable and comprehensive evaluation of their properties. In some occasions a single method is used for the study of a particular property, e.g. surface area, surface charge, while in other cases they are combined in order to complement each other.

For example, DLS evaluates a particle size and size distribution of a sample using light scattering, while SAXS provides higher resolution through X-ray scattering and thus allows more precise size information. Other complementary information comes from XRD, which provides the atomic structure of an unknown material. Using XAS (XANES/ EXAFS) extensively demonstrates oxidation state and bonding environment similar to surface chemical analysis

of XPS. XPS is a quantitative technique to analyse the elemental composition, surface functionalization as FTIR technique and oxidation state in materials under ultra-high vacuum.

TEM is a common technique to offer an image of NP size, shape, and uniform structure relative to the advantage of STEM assessing the size, fine clusters, and elemental composition. TEM imaging is typically ideal for clean sub-100 nm particles and very low sample loading, whereas SEM is a widely used method for imaging that is employed to determine NP morphology of larger >100 nm particles.

ICP-OES is ideal for the quantification of elemental concentration in chemically digested samples, whereas μXRF provides equivalent but higher resolution, solid state elemental analysis, with the additional benefit of providing elemental composition maps. Combining all these techniques together in the characterisation of nanomaterials in complex matrices thus enables optimal interpretation of their state and behaviour.

2.3 Reconstructed Human Skin Models

Tissue/organ transplantations of bone, tendon, heart valve, and skin, are the most significant treatments being developed in research stage of clinical tests for solving human health problems and saving lives. New methodologies for generating reconstructed human skin models have been developed in academic research. The new approach of toxicological testing that avoids animal testing of cosmetics ingredients, e.g. *in vitro* skin irritation, corrosion, and UV exposure assessment, are implemented based on the reconstructed human epidermis (RhE) technology and have proven to be a promising method of assessing skin function, physiology, and disease, compared with the native

human epidermis. These tests are now standardised by the Organization for Economic Co-operation and Development (OECD) guideline.

In general, the RhE model contains the living skin cells equivalent to the human skin, and is prepared by seeding keratinocytes in the collagen matrix. RhE shows a well-differentiated epidermis as well as native human epidermis (Pedrosa *et al.*, 2017). The RhE represents epidermis layers and demonstrates the outermost barrier as stratum corneum (SC) to protect the skin from environmental factors similar to native skin. In addition, the main layers of epidermis and dermis are presented in the full-thickness skin models, which are placed on an insert and over a culture medium containing nutrient factor to feed the skin cells as exemplified in **Figure 1.8** (section 1.7.2).

2.3.1 Reconstructed Human Epidermis Model and Reconstructed Human Full-Thickness Skin Model

In principle, the RhE model is cultured by seeding keratinocytes in a collagen matrix. The keratinocytes proliferate in the stratum basale layer and then grow to a daughter cell. The daughter cells migrate to the stratum spinosum and differentiate to granular cells in the stratum granulosum layer. The Langerhans cells are also in stratum granulosum contributing to the immunological responses of the skin. The upper next layer, namely the stratum lucidum contains a thin layer of dead cells and the stratum corneum is the outermost layer and plays the functional role of a skin barrier containing corneocytes and dead cells. Therefore, the RhE models, such as Episkin, Epiderm, and Epidermal Skin Test 1000 models, have an epidermis layer and a basement

membrane that lies on the collagen matrix which acts as the artificial nutrients. On the other hand, the reconstructed human full-thickness skin model consists of a dermal equivalent embedded fibroblasts and epidermal layer, for example, Epiderm^{FT}, StrataTest, and Advanced Skin Test 2000 models. The skin models are not only functional in terms of protecting against the access of exogenous substances into the body, but can also be used to measure transport of the exogenous substances into the skin.

2.4 In Vitro Skin Test

In vitro testing is a biological method that uses organs, tissue sections, tissue cultures and cell lines to understand processes in organisms and animals. *In vitro* methods have been used to examine the potential toxicity of chemicals, e.g. the chemical interaction studies, receptor binding studies, etc. To prevent human health effects and understand potential human toxicity contributed by accidental and intentional exposure of materials including nanomaterials, the intensive investigation of the perspective toxicities has been widely assessed using *in vitro* tests, which are especially useful for teasing out mechanisms of action, determination of sites of accumulation of toxicants and for assessing degradation of toxicants in cells. For dermal toxicity testing, *in vitro* skin tests are well established.

For this thesis, two in vitro skin models have been used; the reconstructed human epidermis models, and the reconstructed human full-thickness skin model/T skin no. D11 (including the fresh and maintenance media) were purchased from EPISKIN^{TM} (Lyon, France). The models were used to quantify the cell viability and cytotoxicity effects following exposure to the aSiNPs, using a range of well-established cellular toxicity assays such as the MTT assay (cell

death), histology (to measure changes in cellular structures) and an ELISA assay (release of cytokines, as part of an inflammatory responses). These assays are described in detail below, and the results are presented in Chapter 6.

2.4.1 *In Vitro* Skin Penetration

Many studies of skin penetration have used Franz diffusion cells (Gysler *et al.*, 1999; Ashtikar *et al.*, 2013; Crosera *et al.*, 2015; Salamanca *et al.*, 2018). The diffusion area of skin tissue is around 2.5-3.5 cm^2 and toxicants that are able to penetrate the skin collect in the lower compartment containing the aqueous solution from which they can be quantified, but no assessment can be made as to what happens beyond the epidermis layer. Most tissues are obtained from volunteers who were subjected to surgical operations. The main purpose of Franz diffusion cell is to calculate the permeation rate of drugs for controlled delivery (Salamanca *et al.*, 2018).

In this thesis, the natural mechanism of human skin permeation and diffusion is applied to determine the skin penetration potential of the aSiNPs. The skin penetration test is conducted in an *in vitro* reconstructed human full thickness skin model T-skin TM at Day 11 (D11 model) with a diffusion area of 1 cm^2 under a biological fume hood. Three independent D11 models are exposed to 10 µL of each liquid substance; the negative control and the test substance (aSiNPs) for 2 hours and conducted in triplicate, incubated at 37˚C for 22-24 hours. The negative control was performed using ultrapure water (Milli Q water). At the end of the exposure period, the D11 models have been eliminated the rest of the substance by using 25 mL PBS for five times. The media in the bottom chamber is collected first, as is the wash PBS to determine the aSiNPs

across the outermost layer to the polycarbonate filter. To ensure that PBS, which is used to remove the remaining of aSiNPs attached on the skin (including on an uppermost stratum corneum and lower collagen matrix) is directly quantified the amount of aSiNPs that came through the tissues by ICP-OES. The synchrotron-based techniques are employed to characterise aSiNP properties post *in vitro* skin penetration testing. For example, XRF is used to extensively identify for mechanisms of skin penetration, determinations of sites of accumulation of aSiNPs, and SAXS, XANES, and XPS are used to assess the degradations of aSiNPs in cells, i. e. size, oxidation state, elemental composition at the sample surface. The details of synchrotron work and analysis are described in section 5.2 and 5.3 in Chapter 5.

2.4.2 *In Vitro* Skin Irritation

An assessment of skin irritation is mostly required as a means of evaluating biological safety, as an alternative method to other commonly used in vivo and in vitro models. The OECD offers the guideline for *in vitro* skin irritation; OECD TG 439 performance standard using reconstructed human skin models (OECD, 2010). Reconstructed human epidermis (RhE) models, small size (0.5 cm^2), day 17 (RhE/S/17) contain epidermis layers which were purchased from EpiSkin™ (Lyon, France). The experimental procedures consist of the RhE preparation, the topical application of test substances; the positive (SDS) and negative (PBS) controls and aSiNP dispersion on the RhE models, which were described in detail in section 6.4 in Chapter 6.

2.4.3 Cytotoxicity

In general, cytotoxicity is used to evaluate the cellular viability on exposure to a substance and the degree of being toxicity of a substance to living organisms, cells and tissues. Cytotoxicity assays are widely used in biological applications and in drug delivery development (Prow *et al.*, 2011; Rancan *et al.*, 2012; Di Cristo *et al.*, 2016; Gupta and Rai, 2016).

Cytotoxicity assays are important to identify the response and activity of the target organ relevant to the exposure using the quantitative and qualitative assays. There are many techniques used to monitor the cytotoxic action of chemicals in cell. For example, the lactate dehydrogenase (LDH) assay assesses the release of protease biomarkers following administration of the test substance to quantify the numbers of living and dead cells. Cytotoxicity can also be determined using MTT assay, ELISA assay, MEM elution assay, and direct contact test (Kasper *et al.*, 2011; Uboldi *et al.*, 2012).

The *in vitro* determination of the value of cell metabolic activity, intrinsic cytotoxicity, mechanism of toxicity, and mode of action of substances is an early detection of cellular damage leading to the prevention of an unpleasant outcome. However, the correlation of cytotoxicity results remains to be further compared with other biological evaluation and with outcomes *in vivo*.

2.4.3.1 MTT assay

MTT assay is a sensitive method to determine mitochondrial activity (Mosmann, 2005) by using a colourimetric assay technique. The colour dye of yellow water-soluble tetrazolium salt [3-(4,5-Dimethylthiazol-2-yl)-2,5-diphenyltetrazolium bromide, a tetrazole]-MTT and an insoluble purple formazan is used to measure the reduction of enzyme activity. If the activity of enzyme declines, the yellow

colour will turn into an insoluble purple colour in aqueous solution. Acidic isopropanol is used to extract the insoluble purple formazan and then measures changes in the colour which corresponds to the number of metabolically active (live) cells. The absorbance of the purple solution is measured by a spectrophotometer at a wavelength of 570 nm. The changes in metabolic activity of treated cells are generally compared with the amount of insoluble purple formazan produced by untreated control cells. The full description of the MTT assay is detailed in section 6.4, Chapter 6.

2.4.3.2 ELISA assay

Enzyme-linked immunosorbent assay (ELISA) is an immunoassay method allowing detection of secretory cytokines in the biological samples and quantification of peptide, protein, antibody and hormone levels. ELISA correlates the specific antibodies binding the target antigen using various techniques, i.e. direct, indirect, sandwich, and competitive ELISAs. In ELISA, antigen-antibody combination is used to indicate the presence of antigen binding and quantify the colourimetric response from enzyme activity.

Numerous aspects of ELISA assays are associated with cellular communication about the regulation of immunity, inflammation, cell activation, cell migration, cell proliferation, apoptosis, and hematopoiesis. ELISA is important to determine the expression of immune responses. The inflammatory of proinflammatory cytokines are signalling molecules excreted from immune cells, such as interleukin-1, interleukin-12, interleukine-18, tumour necrosis factor alpha (TNF-α), interferon gamma (IFNγ) and granulocyte-macrophage colony stimulating factor (GM-CSF). Interleukin-1α (IL-1α) is an important cytokine released from keratinocytes in the outermost layer of the skin. IL-1α

level positively correlates with the skin irritation, which is in turn contributes to inflammatory response (Perkins *et al.*, 2001; Bou-Dargham *et al.*, 2017). In this thesis, Human interleukin-1α (IL-1α) protein levels are determined using an ELISA PicoKine Kit (Boster Biological Technology) as per the manufacturer's instruction as an indicator for skin inflammation.

2.4.3.3 Histology

Histology is the study of the microanatomy of cells, tissues, and organs which involves visualising their structure using a microscope. It provides the correlation between structure and function, correlating possible causes of differentiation or proliferation and treatments. Haematoxylin and eosin (H&E) stain is commonly used to colour cells and tissues for histological study. Eosin stain is an acidic dye, which reacts with the basic components in cells, such as cytoplasmic proteins, intracellular membranes, extracellular fibres and epithelial keratinocytes in red or pink. Haematoxylin stain is a compound of a basic dye (base part: Cl^-) and aluminium ions (acid part: Al^{3+}) to form the active dye-metal complex. When the acidic structures, i.e. nucleus, and parts of the cytoplasm containing RNA combines with acid part of haematoxylin it turns into a purplish-blue. Histological assessments were carried out at the Institute of Cardiovascular Sciences, the University of Birmingham. The full description of the histological study is given in section 6.5 in Chapter 6.

.

Table 2.1 Methods used for characterising nanoparticles.

Technique	Parameter measured	Main Advantages	Main Limitations	Resolution (for particle size)
DLS	Hydrodynamic diameter and zeta potential	Rapid and simple to operate Straightforward to obtain the particle size (for monodisperse particles) Monitor the formation of aggregation and agglomeration from size distribution and PdI Provides the surface charge of NPs	Overestimates size toward the large particle sizes, multimodal distribution and high concentration of sample may interfere with the results Requires a minimum of three measurement	0.3nm-10μm
TEM	Shape and size, composition	Samples are stable for long periods after preparation. Direct observation of morphology, aggregates and agglomerates	Gives randomised details of the sample on parts of the TEM grid Using imageJ particle size can be measured but requires at least 200 particles Images a very small sub-sample	Sub-nm
STEM	Shape and size, atomic	As for TEM, but higher resolution. High structural precision.	Difficult to operate. May get damage NPs when keeping the beam too long at one position	Sub-nm

Technique	Parameter measured	Main Advantages	Main Limitations	Resolution (for particle size)
	structure, composition			
SAXS	Size, shape and surface topography	Easy sample preparation, quick measurement per sample Provides primary particle size, shape, and surface topography	Difficult to interpret High cost of examination per sample Sample with high dispersion (high PDI) might affect the fitting and interpretation steps Must measure both test solution and air for background subtraction for each sample	1nm to 100 nm
XRD	Crystalline structure	Gives atomic structure of samples that can be linked to composition. Identification of unknown materials	Powder samples only Heterogeneous and multiphase material is difficult to identify in unknown samples	Sub-nm
SEM	Size, shape, composition	Quick and rapid sample preparation	Examination under high vacuum is difficult if the sample is wet.	~20 nm

Technique	Parameter measured	Main Advantages	Main Limitations	Resolution (for particle size)
		Obtains 3D image of morphology and identify elemental composition	Sample must be prepared appropriately.	
XPS	Surface chemistry and %atom composition	Gives qualitative and quantitative information on the surface chemistry of sample Provides the chemical structure at the surface	Sample must be powder form and is analysed under vacuum Spectra difficult to interpret High cost of examination per sample	n/a
XAS-XANES/EXAFS	Element, oxidation number and structure	Variety of sample forms are measurable, e.g. powder, liquid, gel Gives further information on particle structure, elemental composition, and oxidation state	Spectra difficult to interpret High cost of examination per sample	n/a
FT-IR	Functional group	Quick measurement to achieve a standard quality spectrum. Variety of sample forms are measurable, e.g. powder, liquid	Difficult to interpret if no reference spectrum	n/a

Technique	Parameter measured	Main Advantages	Main Limitations	Resolution (for particle size)
BET	Surface area	Ease of measurement, unique method for surface area.	Powder samples only. Requires high amount of sample. Requires a minimum of three measurements per sample	No minimum, maximum ~10 μm
ICP-OES	Elemental concentration	Can examine at low concentration limit in ppb (quantitative data). Broad range of elements and concentrations.	Liquid samples only Digestion of solids using an appropriate acid and correlate to the recovery rate of substances. Not suitable for some elements (e.g. carbon)	Particle size resolution not relevant.
μ-XRF	Elemental mapping	Gives a qualitative (elemental) and semi-quantitative information Can give particle distribution mapping	Difficult to analyse and interpret data	n/a

Chapter 3 Characterisation of NPs from commercial cosmetics and Synthetic Amorphous Silica (SASs)

3.1 Introduction

The application of nanotechnology-related innovations has recently become common in a variety of consumer products, including sunscreens, cosmetics, and personal care products. 2231 consumer products available on the European consumer market claim to contain nanomaterials (NMs). In particular, the principle NMs used in cosmetics are silver, fullerene, gold, alumina, zinc oxide, mica, titanium, copper, platinum and silica (Foss Hansen *et al.*, 2016). The justification to use NMs in cosmetics is in order to increase effectiveness of UV protection, enhanced cosmetic appearance, e.g. texture, shelf life and to enable high pigment levels (Wiesenthal *et al.*, 2011; Nafisi and Maibach, 2015). Notably, a previous study by the Consumer Union tested 19 sunscreens containing zinc oxide and titanium oxide nanoparticles, but only one of the sunscreens declared the use of nanoparticles on its label (Chatterjee, 2008). This finding shows that manufacturers have not always provided information about the use of nanomaterials in their products in the past, and thus that consumers may not always be fully informed. An increasing number of requests for safety assessment of commercial products have been published (Nel *et al.*, 2006; Bijker *et al.*, 2007; Chatterjee, 2008; Foss Hansen *et al.*, 2008). Legislation regarding nanomaterial-

containing cosmetics, which came to force in 2013 explicitly requires any nanoscale ingredients to be listed to reassure consumers and comply with EU Cosmetics Regulation (EC No 1223/2009) (https://eur-lex.europa.eu/legal-content/en/TXT/?uri=CELEX:02009R1223-20160812).

The scientific committee on consumer safety has provided opinions of health and safety risks in their guidance on the safety assessment of nanomaterials in cosmetics (Scientific Committee on Consumer Safety, 2012). Recently, the European Chemicals Agency (ECHA) provided guidance to help the registrants preparing dossiers for nanoform registration in December 2019 (https://echa.europa.eu/documents/10162/13655/how_to_register_nano_en.pdf/f8c046ec-f60b-4349-492b-e915fd9e3ca0). Thereof, cosmetics containing NMs need to address potential risks due to their compositions and forms. Additionally, full characterisation should be carried out and information regarding the presence and form of nanomaterials in the product should be declared on their labels.

Using appropriate analytical techniques is essential to achieve reliable characterisation of NMs-containing cosmetics products. The International Organization for Standardization (ISO) established a guidance on physicochemical characterization of NMs (ISO/TR13014:2012(E)) and technical measurement methods in 2012 that is a prerequisite prior to toxicological assessment (The International Organization for Standardization, 2012). In fact, the characterisation of nanomaterials in commercial products can be quite challenging due to the complexity of the matrix, the potential presence of other particulate components and, often, the limited information provided by

manufacturers in order to maintain trade benefits. The use of a wide range of characterisation techniques is therefore a necessary approach. In this context, previous studies have identified only NPs in simple formulations (Chang *et al.*, 2007; Becheri *et al.*, 2008; Hao *et al.*, 2017), but few studies have discussed or evaluated unmodified commercial products (Chatterjee, 2008; Tyner *et al.*, 2009; Lewicka *et al.*, 2011). Furthermore, there is still a lack of studies addressing the NPs in complex materials.

In order to address this gap, the aim of this chapter is to identify nanoparticles found in commercial cosmetic products that list silicon/silica as ingredients and compare them to synthetic amorphous silica (SAS) nanomaterials established as standards. However, due to the absence of appropriate reference standards for this purpose, the application of characterisation techniques is also used to develop better fundamental understanding of their properties in complex matrices. The most suitable methods will be discussed in this chapter. Detailed description of SASs is compared to data from the European Commission's Joint Research Centre (JRC), Institute for Health and Consumer Protection (Rasmussen *et al.*, 2013) (http://publications.jrc.ec.europa.eu/repository/bitstream/111111111/29367/1/lbna26046enn-nm_repository_sio2.pdf). JRC repository provides the physicochemical characterisation of SASs to support European Union policy.

3.2 Chemicals and Materials

Ethanol (analytical grade) was prepared at 70% v/v and ultrapure water was steam sterilized in the oven at 121°C, 15 min before use.

Eight different cosmetics containing silica- based materials on their product description were purchased from a local convenient superstore in Birmingham, UK and the ingredients as listed by the suppliers are shown in **Table 3.1**. Five different standards of SASs were obtained from the JRC, listed in **Table 3.2**.

Table 3.1 Product information as presented in the labels of the eight commercial cosmetics containing silica-based material characterised in this study.

Sample code	Type	Form	Ingredients
Sample 1 (S1)	Powder foundation	Fluffy powder	Talc, Nylon-12, Mica, Dimethicone, **Silica**, Magnesium Myristate, Ethylene/Acrylic Acid, Copolymer, Zinc Stearate, Dimethyiconal, Sorbic Acid, Dehydroacetic Acid, Lauroyl Lysine. [+/- (May contain): CI 77891 (Titanium Dioxide), CI 77491/77492/77499 (Iron Oxides)]
Sample 2 (S2)	Skin crème oil free photo edition foundation	Powder	Cyclopentasiloxane, Aqua/Water/EAU, Phenyl Trimethicone, Ethyl Palmitate, PEG-12 Dimethicone Crosspolymer, **Silica Dimethicone Silylate**, Butylene Glycol, Glycerin, Isononyl isononanoate, Polysilicone-11, Hydroxystearate, C30-45 Alkyl Cetearyl Dimethicone Crosspolymer, Sorbitan Sesquioleate, Caprylohydroxamic acid, Glyceryl Acrylate/Acrylic Acid Copolymer, Ascorbyl Palmitate, Retinyl Palmitate, Tocopheryl Acetate, Serica/silk powder/Poudre De Soie, Saccharomyces/Xylinum/Black Tea

Sample code	Type	Form	Ingredients
			Ferment, Hydroxyethylcellulose. May contain (+/-): CI 77891 (Titanium Dioxide), CI 77491/77492/77499 (Iron Oxides)
Sample 3 (S3)	Shadow tint for eye	Dense Creme	C11-12 Isoparaffin, Polyethylene, Ethylhexyl Isononanoate, Copernicia Cerifera (Carnauba), Wax/Cera Carnauba/Cire De Carnauba, Isohexadecane, **Hydrated Silica**, Octyldodecanal, Cetyl Dimethicone, Tocopheryl Acetate, Synthetic Fluorphlogopite, Disteardimonium Hectorite, Stearic Acid, Propylene Carbonate, **Silica**, Tin Oxide, [+/- Mica, Titanium Dioxide (CI 77891), Iron Oxides (CI 77491/77492/77499)], Bismuth Oxychloride (CI 77163), Manganese Violet (CI 77742), Yellow 5 Lake (CI 19140), Chromium Oxide Greens (CI 77288), Carmine (CI 75470) [LIN39367]
Sample 4 (S4)	Sheertone Shimmer Blush	Fluffy powder	Talc, Octyldodecyl Stearate, Dimethicone, Nylon-12, Zinc Stearate, **Silica**, Octyldodeanol, Tetrasodium EDTA, Potassium Sorbate, Chlorphenesin, [+/- Mica, Titanium Dioxide (CI 77891), Iron Oxides (CI 77491/77492/77499)], Bismuth Oxychloride (CI 77163), Blue 1 Lake (CI 42090), Carmine (CI 75470),

Sample code	Type	Form	Ingredients
			Chromium Hydroxide Greens (CI 77289), Chromium Oxide Greens (CI 77288), Ferric Ferrocyanide (CI 77510), Manganese Violet (CI 77742), Red 6 (CI 15850), Red 7 (CI 15850), Red 7 Lake (CI 15850), Yellow 5 Lake (CI 19140), Yellow 6 Lake (CI 15985), [LIN32529]
Sample 5 (S5)	Matte Long Last Lipstick in Pink	Dense Creme	Isododecane, Paraffin, Dimethicone, Ethylhexyl, Palmitate, Mineral Oil, Polybutene, Cyclohexasiloxane, Bees Wax, Microcrystalline Wax, Fragrance, **Silica Dimethyl Silicate**, Glycol Montanate, Hydrogenated Styrene/Isoprene Copolymer, Phenoxyethanol, Copernicia Cerifera Wax, Tocopheryl Acetate, Benzyl Benzoate, May contain: Mica CI 15850 (Red6/Red 6 Lake/ Red 7 Lake), CI 15985 (Yellow 5 Lake), Red 40 Lake), CI 19140 (Yellow 5 Lake), CI 45410 (Red 27 Lake/ Red 28 Lake), CI 47005 (Yellow 10 Lake), CI 73360 (Red 30 Lake), CI 77491/CI 77492/ CI 77499/ (Iron Oxides), CI 77742 (Manganese Violet), CI 77891 (Titanium Dioxide)
Sample 6 (S6)	PS 9 Shade Eye shadow Palette	Powder	Mica, Talc, Caprylic Triglyceride, Hydrogenated Polybutene, Synthetic Fluorphlogopite, Polymethyl Methacrylate, Magnesium Stearate,

Sample code	Type	Form	Ingredients
			Synthetic Fluorphlogopite, Polymethyl Methacrylate, Magnesium Stearate, Diisostearyl Malate, Zinc Stearate, **Silica**, Aluminium Starch Octenyl Succinate, Methylparaben, Propylparaben, Tocopheryl Acetate, Tin Oxide Dipentaerythrityl Hexahydroxystearate, Methylparaben, Propylparaben, Tocopheryl Acetate, Tin Oxide, [+/-] Red 40 Lake (CI 16035), Yellow 5 Lake (CI 19140), Blue 1 Lake (CI 42090), Ultramarines (CI 77007), Black 2 (CI 77266), Chromium Oxide Greens (CI 77288), Chromium Hydroxide Green (CI 77289), Iron Oxides (CI 77491/77492/77499), Ferric Ammonium Ferrocyanide (CI 77510), Manganese Violet (CI 77742), Titanium Dioxide (CI 77891)
Sample 7 (S7)	Loose Face Powder	Fluffy Powder	Mica, Talc, Dimethicone, Caprylic Triglyceride, Magnesium Stearate, Polymethyl Methacrylate, Hydrogenated Polybutene, Synthetic Fluorphlogopite, **Silica**, Ethylhexyl Palmitate, Methylparaben, Propylparaben, Tocopheryl acetate, [+/-] Red 6, Red 7 Lake (CI 15850), Yellow 6 Lake (CI 15985), Red 40 Lake (CI 16035), Yellow 5 Lake (CI 19140), Blue 1 Lake (CI 42090), Red 21

Sample code	Type	Form	Ingredients
			Lake/Red 22 Lake (CI 45380), Red 27 Lake/Red 28 Lake (CI 45410), Ultramarines (CI 77007), Black 2 (CI 77266), Chromium Oxide Greens (CI 77288), Chromium Hydroxide Green (CI 77289), Iron Oxides (CI 77491/77492/77499), Ferric Ammonium Ferrocyanide (CI 77510), Manganese Violet (CI 77742), Titanium Dioxide (CI 77891)
Sample 8 (S8)	Blusher	Dense creme	Isododecane, Talc, Synthetic Fluorphlogopite, Mica, Cyclopentasiloxane, Ethylhexyl Palmitate, Trimethylsiloxysilicate, Paraffin, Polybutene, Cyclohexasiloxane, Bees Wax, Synthetic wax, Glycol Montanate, **Silica Dimethyl Silicate**, Tin Oxide, Copernicia Cerifera Wax, Phenoxyethanol, Tocopheryl Acetate, May contain: Mica CI 15850 (Red6/Red 6 Lake/ Red 7 Lake), Ultramarines (CI 77007), Black 2 (CI 77266), Chromium Oxide Greens (CI 77288), Iron Oxides (CI 77491/CI 77492/ CI 77499/), Ferric Ammonium Ferrocyanide (CI 77510), Manganese Violet (CI 77742), Titanium Dioxide (CI 77891)

Table 3.2 Synthetic Amorphous Silica Nanomaterials (SASs) obtained from the JRC reference test material collection

No.	Sample code name	Type of SAS	Form
1	SAS 2000a	Precipitated SAS	White powder
2	SAS 2001a	Precipitated SAS	White powder
3	SAS 2002a	Thermal SAS	White powder
4	SAS 2004a	Precipitated SAS	White powder
5	SAS 10404a	Thermal SAS	White powder

3.3 Sample Storage and Glassware

Polystyrene tubes and Eppendorf® tubes were obtained from Eppendorf® UK Limited. Ultrapure water (UPW) with 10% nitric acid (HNO_3) was used to wash the glassware and to remove any particles. The glassware was then rinsed three times with UPW to ensure no traces of acid remained. Then, all glassware was steam sterilized at 121˚C.

3.4 Method Characterisation of cosmetics and SASs

Eight cosmetics and five SASs, as described in Table 3.1 and Table 3.2, were extensively characterised using various physical and chemical techniques. The techniques used, the parameters measured and sample forms for analysis are shown in

Table 3.3. The details of techniques were described in Chapter 2.

Table 3.3 The details of experimental techniques used for characterisation of SASs and cosmetics.

Technique	Parameters assessed	Sample form
Powder X-ray Diffraction (XRD)	Structural and chemical composition	Powder
X-ray Absorption Spectroscopy-X-ray absorption Near Edge Spectroscopy (XAS-XANES)	Elemental composition, Atomic structure	Powder
X-ray Photoelectron Spectroscopy (XPS)	Atomic composition, atomic percentage values and element ratios	Powder
Small angle X-ray Scattering (SAXS/WAXS)	Size, shape, structure and surface texture	NM is suspended in UPW
Scanning Electron Microscopy (SEM)	Shape and elemental composition	Powder
Transmission Electron Microscopy (TEM)	Size and shape	NM suspended in UPW
Dynamic Light Scattering (DLS)	Size and zeta potential	NM suspended in UPW
BET surface area analyser	Surface area	Powder

3.5 Sample Preparation

3.5.1 Cosmetics

Prior to cosmetic characterisation, all samples were prepared following the protocol shown in **Figure 3.1**. The samples were extracted as emulsion using 8 mL absolute ethanol which was added in 5 mg of the cosmetics. The suspension thus produced was then homogenized by shaker for 10 minutes and subsequently centrifuged at 4500 rpm for 15 minutes (Lewicka *et al.*, 2011). The top solution was discarded and the residue at the bottom was left to air dry for 24 hours. The process was repeated three times.

In order to produce a suspension sample for characterization, 0.5 mg of the dried solid sample was diluted in 1 mL UPW and ultrasonicated for 20 minutes whereupon the physicochemical properties of samples were measured by DLS, TEM, SEM-EDS, and SAXS. Ultrapure water without nanoparticles is used as a blank. For SAXS measurements, a range of concentrations of three blind samples and three analysed samples were examined to ensure that results are precise and reliable.

Solid samples of extracted particles from cosmetics were 109haracterized by XRD, XPS, and XAS-XANES/EXAFS. By means of synchrotron technique, which is a powerful tool have been used for characterizing ingredients and products in an efficient manner. In relation to the quality control of cosmetics, combining tools can make possible to determine the quality of cosmetics with a wide range of data and obtain a deep characterisation leading to a precise information.

3.5.2 SASs

SASs were obtained from JRC in powder form. The samples of SASs were prepared appropriately for the technique, conditions during measurement (i.e. wet or dry) and protocol used. More specifically to suspend the NMs in UPW, 5mg SASs were added into 1 mL UPW and then ultrasonicated for 20 minutes. These samples were then analysed by XRD, XAS- XANES/ EXAFS, XPS, SAXS/WAXS, DLS, and BET.

The sample preparation for all techniques was described below.

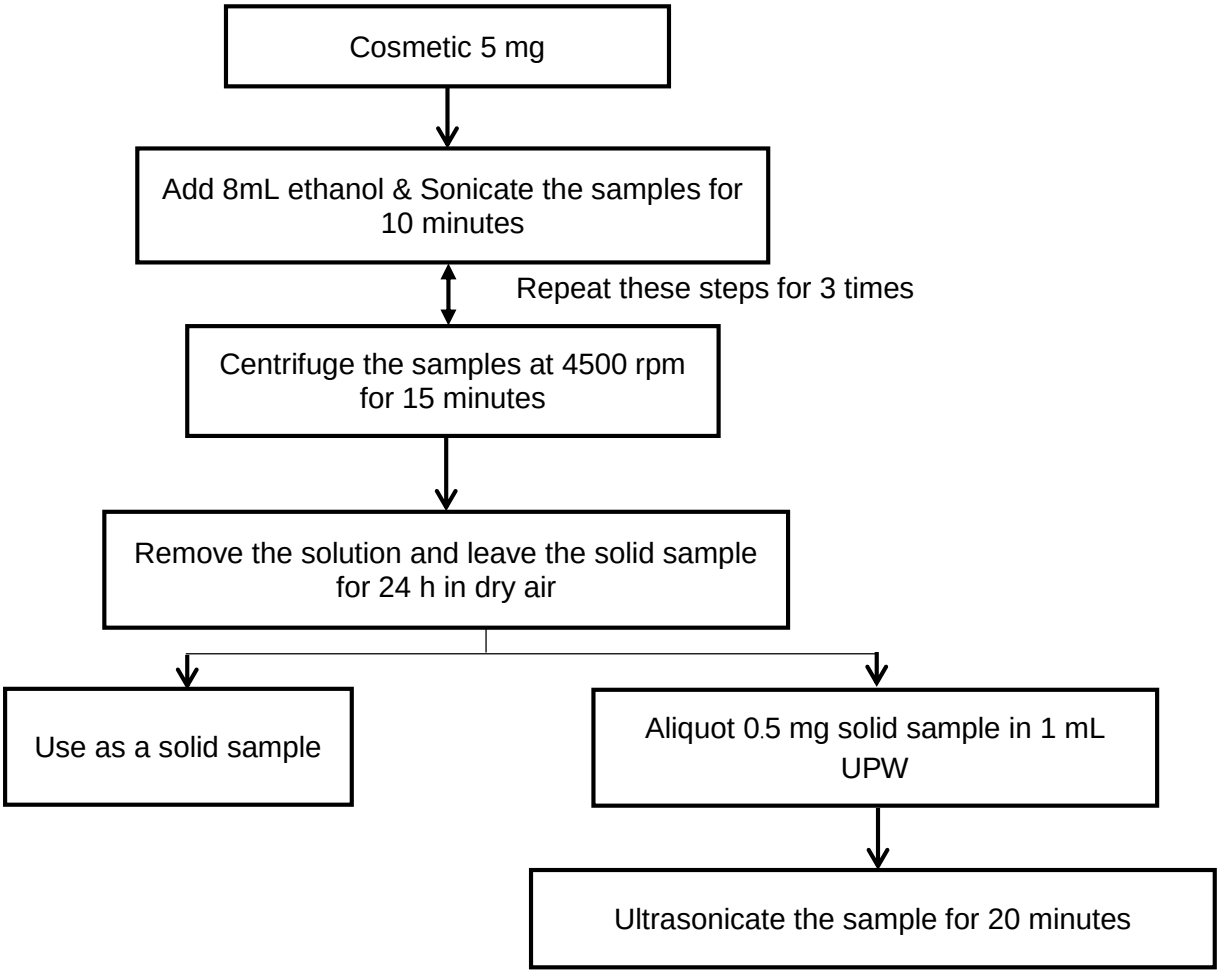


Figure 3.1: Protocol of cosmetic preparation prior to characterisation, adopted (Lewicka *et al.*, 2011)

3.5.3 XRD

Only solid samples (powders) can be characterised by XRD. The sample preparation is quick and involves mounting the sample on the flat surface of a sample slide. Prior to sample preparation, samples were stored in a desiccator for at least 24 hours to ensure moisture removal. Dried samples were then grounded to obtain a fine powder to be used for analysis. The finely powdered samples were smeared onto the sample slides or masking tape and subsequently placed into the slot. Powder Diffractometer Bruker D8 for XRD at the School of Chemistry, the University of Birmingham was applied to scan over a 2θ range from 5-90˚. EVA software was employed to identify the components present in the cosmetics and SASs.

3.5.4 XAS-XANES

Prior to analysis, standards for quartz and silicon metal had to be prepared and examined to establish reference XAS spectra as the fingerprint spectra for comparative purposes. Standard silicon dioxide (quartz, SiO_2) and silicon metal (Si) were well-ground and mounted on acrylic plastic film, providing an X-ray transparent window (shown in **Figure 3.2**). As a sample preparation, XANES technique requires minimal amount regarding the concentration, composition, and the thickness of a sample. The thickness of sample should be appropriate for the analysis (to account for the concentration of analyte element present, to minimize photon absorption) to ensure an appropriate edge jump of the K-edge energy. In the case of a dilute sample, the fluorescence mode must be employed to investigate the sample. All XANES spectra of cosmetics and SASs were

obtained using XAS beamline 5.2, at Synchrotron Light Research Institute (SLRI), Nakhon Ratchasima, Thailand.

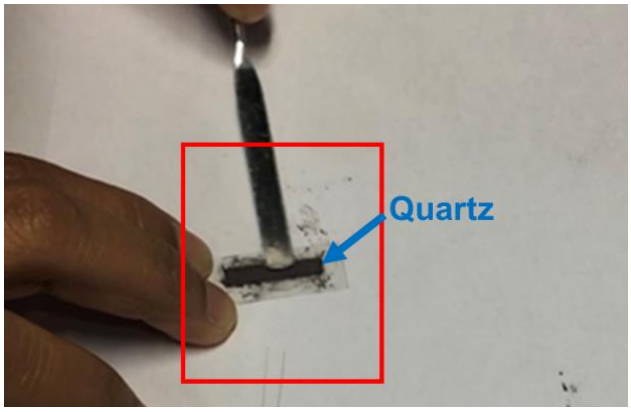


Figure 3.2: A standard of SiO_2 (quartz) mounted on an acrylic plastic film.

3.5.5 XPS

Powdered samples were mounted on carbon tape, then labelled and attached on the stage as shown in **Figure 2.18** (Chapter 2). The stage was placed in a high vacuum and was illuminated by X-rays at the energy levels of Al *K*α or Mg *K*α. The kinetic energy of emitted electrons caused a photoelectric effect to be detected and then converted to binding energy. This information was then used to assign the characteristics and quantities of elements at the sample surface. XPS measurements were carried out at beamline 3.2b SLRI, Thailand.

3.5.6 SAXS/WAXS

The extracted cosmetics were suspended in ultrapure water at the concentration of 5 mg/mL with filtering with a syringe filtered 0.2 μm. Each sample was injected in the sample holder around 2 – 5 mL (as seen in **Figure 3.3**). The sample holder window has to be transparent to X-rays. Kapton® tape was used as a window

material in this study. The material used for a window should scatters less, be resistant to chemical attack and elevated temperatures.



Figure 3.3: The sample holder with Kapton® tape for liquid sample

3.5.7 DLS

Freshly produced colloidal suspension of the studied cosmetics (extracted) were prepared by adding 1 mL of UPW on 0.5 mg of extracted cosmetics vortexing and then removing any large particles and impurities with a syringe filtered 0.2 µm as shown in **Figure 2.3** (Chapter 2) and then ultrasonicated for 15 minutes prior to size measurement. DLS measurements were performed to determine the particle size and size distribution using a Malvern Zetasizer Nano ZS **(** Malvern, Herrenberg, Germany**)** equipped with a 633 He**-**Ne laser and operating at an angle of 173 degrees**.** Zetasizer software version 7**.**12 created by Malvern, was used to manipulate the data**.**

For SASs, DLS measurements were performed to determine the particle size and size distribution using a Malvern Zetasizer Nano ZS **(** Malvern, Herrenberg, Germany**)** equipped with a 633 He**-**Ne lase and operating at an angle of 173 degrees**.** Zetasizer software version 7**.**12 was used to manipulate the data, created by Malvern**.** The powdered samples were suspended in UPW and ultrasonicated at 80**%** amplitude for 20 minutes prior to measurements**.** The measurement was made under thermostat conditions at 20 °C**.** The intensity size

distribution, the Z-average diameter (Z-avg), and the polydispersity index (PdI) were obtained from the autocorrelation function using the general-purpose mode.

3.5.8 SEM

The solid samples were mounted on a stage, then coated with a thin layer of gold which acts as an electrically insulating material and placed in the chamber area. FIB- SEM Carl Zeiss Model Auriga at Suranaree University of Technology, Nakhon Ratchasima, Thailand was used to investigate both the cosmetics and SASs The microscope was designed to operate at low vacuums, both the column and the chamber were evacuated by a combination of pumps.

3.5.9 TEM

A few droplets of the SAS suspension were spread over the surface of a TEM copper grid coated with a thin film of holey carbon (Carbon film on 300 mesh Copper grid 3.05 mm). The droplets of the sample were left to dry at room temperature for half an hour in order for the sample particles to become attached to the copper grid. The grid is then gently rinsed repeatedly by using ultrapure water to remove any excess salts and loose particles and then placed in room temperature for 24 hours until completely dried. TEM FEI model TECNAI G^2 20S-TWIN, at Suranaree University of Technology, Nakhon Ratchasima, Thailand was used to identify the morphology of SASs.

3.5.10 BET

The powdered samples were kept in a desiccator at least 24 hours to ensure complete dryness. Prior to the surface area analysis, the samples were

outgassed to remove water and other surface contaminants. The outgas process was carried out under a vacuum at high temperatures (300˚C). Samples were gently compacted into the glass cell with a glass rod to minimize the dead space in the cell. The cell was placed into the heating mantle and cooled down. Then, the outgassed samples were ready to absorb nitrogen gas, which was in a Dewar flask and to follow by desorption of the gas. The changes in volume of gas absorption were calculated to provide the specific surface area. SA 3100 surface area analyzer at WG01, the School of Geography, Earth and Environmental Sciences, the University of Birmingham was employed to measure the surface area of SASs.

3.6 Results

This section describes the results of commercial cosmetics and synthetic amorphous silica nanomaterials (SASs) characterisation. A multi-method approach was used to characterise eight cosmetics (focusing on the inorganic particle content) and five different SASs. XRD, XAS-XANES, XPS, SEM and WAXS were applied to measure elemental composition and structural morphology. DLS and SAXS provided particle size and size distribution, whereas zeta potential was obtained from DLS. BET analysis provided the specific surface area of samples.

3.7 Results of Cosmetic Characterisation

3.7.1 Particle size

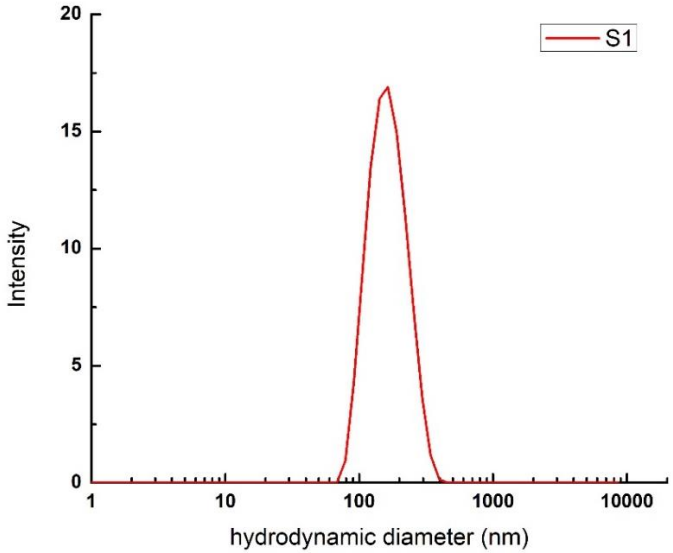
DLS

Cosmetics are complex substances that may contain multimodal size distribution and components, therefore, DLS provides an average of multiple measurements **(**10 scans**)** for intensity distribution of silica and other nanoscale particles found in the eight studied cosmetics**.** DLS provides the particle size and size distribution for each cosmetic, as shown in **Figure 3.4 - Figure 3.11.**

Table 3. 4 summarises Z**-** average, and PdI values, and the hydrodynamic diameter**.** According to the DLS results, the cosmetic samples had a relatively narrow size distribution, with peaks in the nanoscale range and PdI showed a good range indicating that the cosmetic samples contained a substantial nanoparticulate component in their formulation**.**

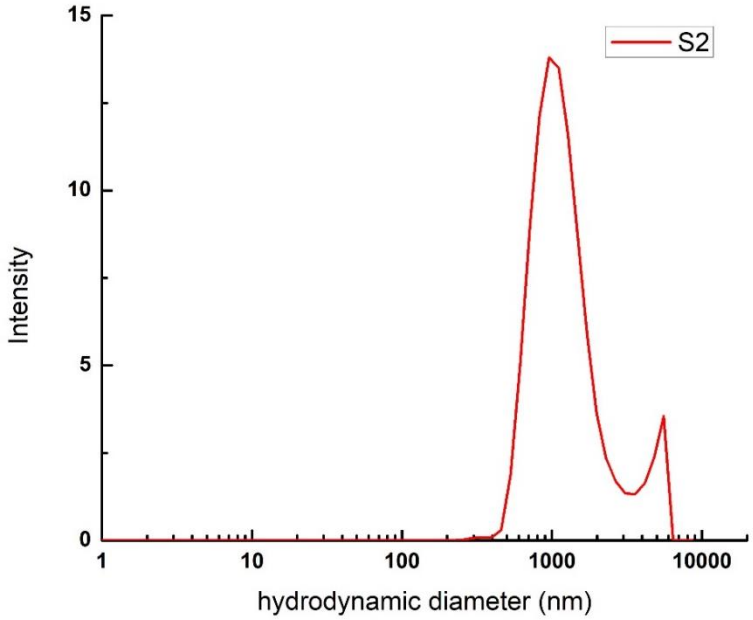
Table 3. 4 The hydrodynamic diameter, Z- average and PdI of materials in nanoscale found in the eight studied cosmetics determined using DLS.

Sample no.	Z-average (d.nm)	PdI	Intensity PSD, nm (%Intensity)
S1	155.1	0.178	161.5±45.54 **(**100**%)**
S2	1568	0.772	984.2±263.8 **(**84.3**%)**
S3	130.0	0.175	160.8±75.09 **(**100**%)**
S4	142.3	0.174	151.2±46.78 **(**100**%)**
S5	87.93	0.120	101.5±40.40 **(**100**%)**
S6	139.5	0.22	152.3±55.28 **(**97.5**%)**
S7	134.6	0.137	153.7±56.56 **(**100**%)**
S8	105.4	0.132	123.7±50.61 **(**100**%)**



			Diam. (nm)	%Intensity	Width (nm)
Z-Average (d.nm):	155.1	Peak 1	161.5	100	45.54
PdI:	0.178	Peak 2	-	-	-
Intercept:	0.933	Peak 2	-	-	-
Result quality:	Good				

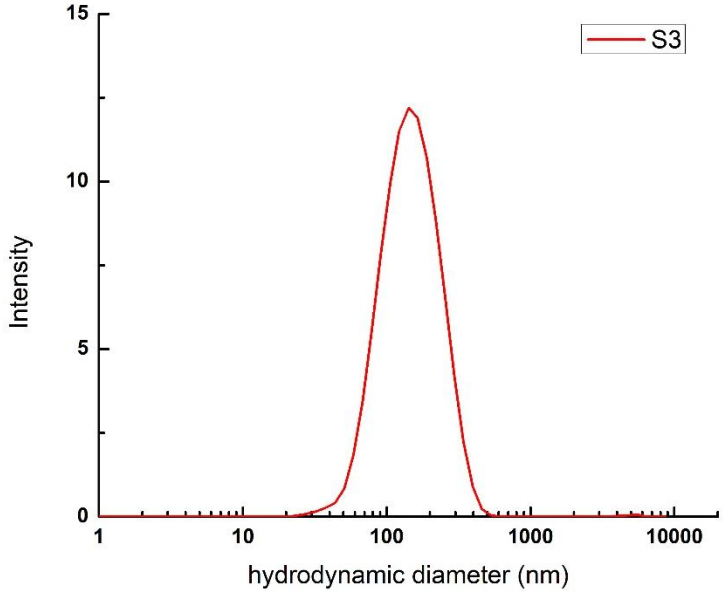
Figure 3.4: Particle size distributions of sample S1 reported by Z-average, is 156.9 nm.



.

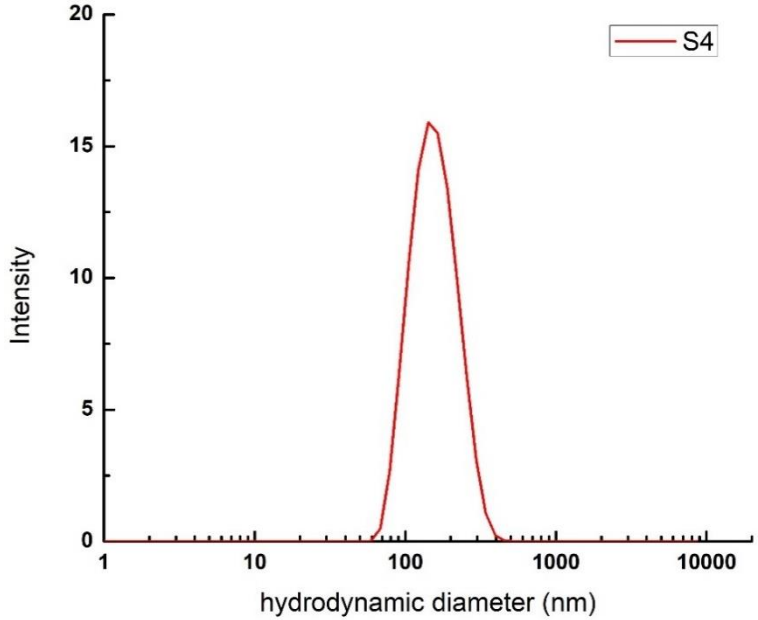
			Diam. (nm)	%Intensity	Width (nm)	Volume	Number
Z-Average (d.nm):	1568	**Peak 1**	984.2	84.3	263.8	93.2	76.9
PdI:	0.772	**Peak 2**	5590	13.8	579.8	3	23.1
Intercept:	0.956	**Peak 3**	**-**	**-**	**-**	**-**	**-**
Result quality:	**-**						

Figure 3.5: Particle size distributions of sample S2 weighted intensity distribution **(**left**)** and number distribution **(**right**)**



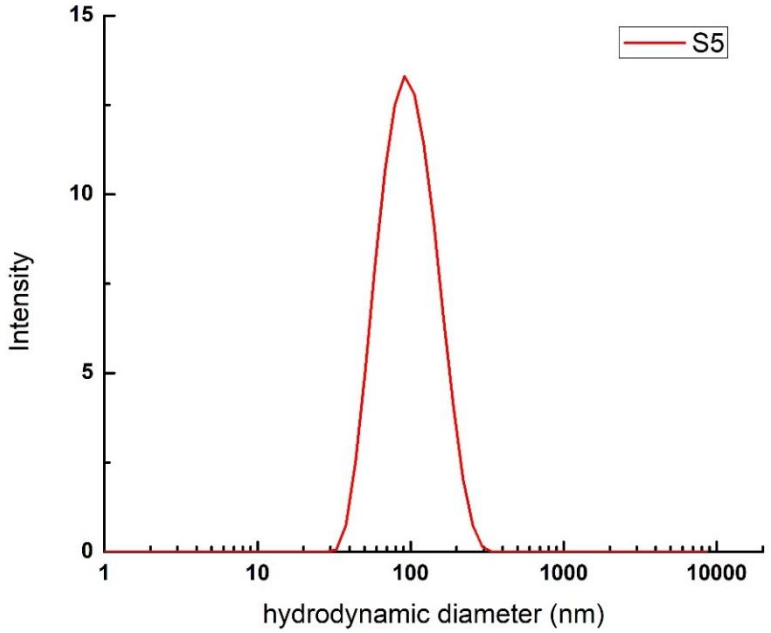
			Diam. (nm)	%Intensity	Width (nm)
Z-Average (d.nm):	130.0	**Peak 1**	160.8	100	75.09
PdI:	0.175	**Peak 2**	-	-	-
Intercept:	0.955	**Peak 3**	-	-	-
Result quality:	Good				

Figure 3.6: Particle size distributions of sample S3 weighted intensity, reported the representative average size present in 32.73 nm.



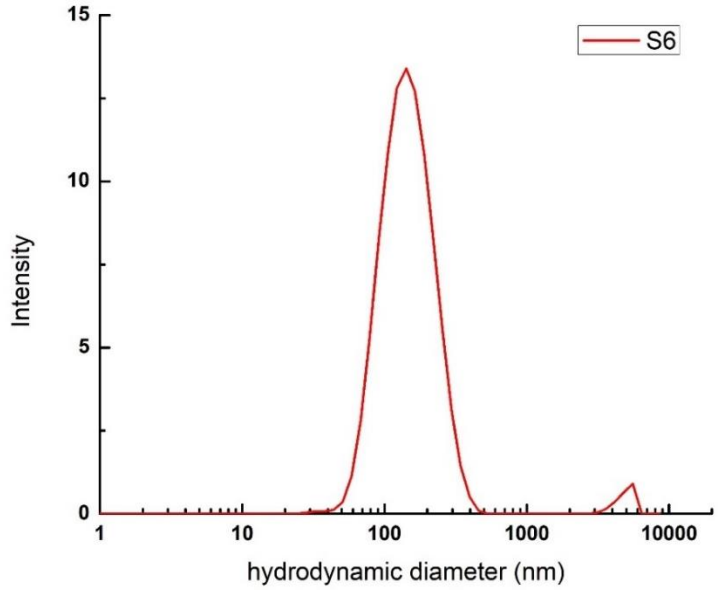
			Diam. (nm)	%Intensity	Width (nm)
Z-Average (d.nm):	142.3	**Peak 1**	151.2	100	46.78
PdI:	0.174	**Peak 2**	-	-	-
Intercept:	0.927	**Peak 3**	-	-	-
Result quality:	Good				

Figure 3.7: Particle size distributions of sample S4 reported by Z-average, is 142.3 nm.



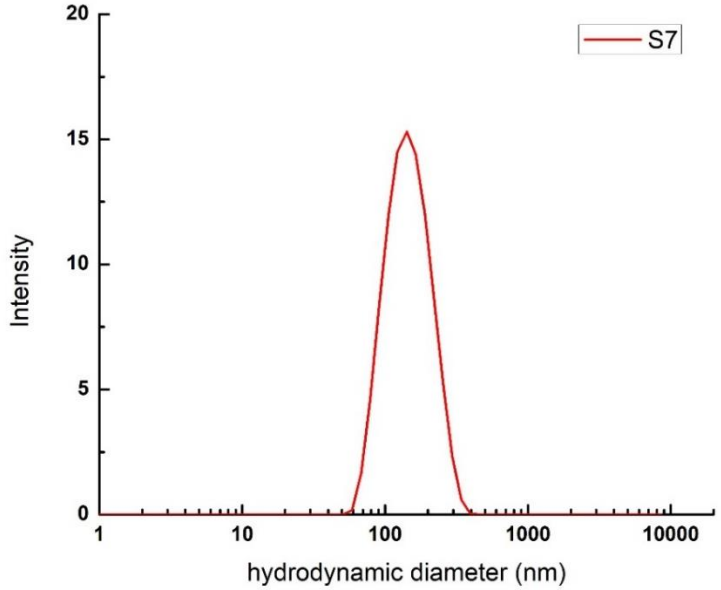
			Diam. (nm)	%Intensity	Width (nm)
Z-Average (d.nm):	87.93	**Peak 1**	101.5	100	40.40
PdI:	0.120	**Peak 2**	-	-	-
Intercept:	0.952	**Peak 3**	-	-	-
Result quality:	Good				

Figure 3.8: Particle size distributions of sample S5 reported by Z-average, is 87.93 nm.



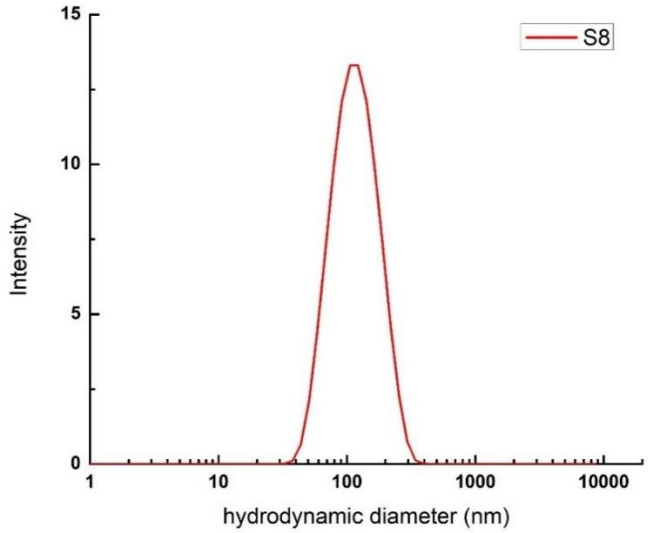
			Diam. (nm)	%Intensity	Width (nm)	Volume	Number
Z-Average (d.nm):	139.5	**Peak 1**	152.3	97.5	55.28	80.6	100
PdI:	0.220	**Peak 2**	5018	2.5	598.0	19.4	**-**
Intercept:	0.944	**Peak 3**	**-**	**-**	**-**	**-**	**-**
Result quality:	Good						

Figure 3.9: Particle size distributions of sample S6 weighted intensity distribution, reported the representative average size present in 152.3 nm.



			Diam. (nm)	%Intensity	Width (nm)
Z-Average (d.nm):	134.6	**Peak 1**	153.7	100	56.56
PdI:	0.137	**Peak 2**	**-**	**-**	**-**
Intercept:	0.954	**Peak 3**	**-**	**-**	**-**
Result quality:	Good				

Figure 3.10: Particle size distributions of sample S7 reported by Z-average, is 134.6 nm.



			Diam. (nm)	%Intensity	Width (nm)
Z-Average (d.nm):	105.4	**Peak 1**	123.7	100	50.61
PdI:	0.132	**Peak 2**	**-**	**-**	**-**
Intercept:	0.951	**Peak 3**	**-**	**-**	**-**
Result quality:	Good				

Figure 3.11: Particle size distributions of sample S8 reported by Z-average, is 105.4 nm

SAXS

The cosmetics were further characterised for primary particle size and size distribution using SAXS beamline 1.3, at SLRI. The scattering patterns of the eight samples appear as straight lines, as shown in **Figure 3.12**, therefore, the form factor and structural level cannot be fitted to the appropriate models**.** This finding is likely a result of the complex characteristics of the cosmetics, more specifically, inter**-**particle features, presence of multimodal complex components, and**/**or the formation of agglomerates, or densely packed aggregates of samples and their intrinsic components**.**

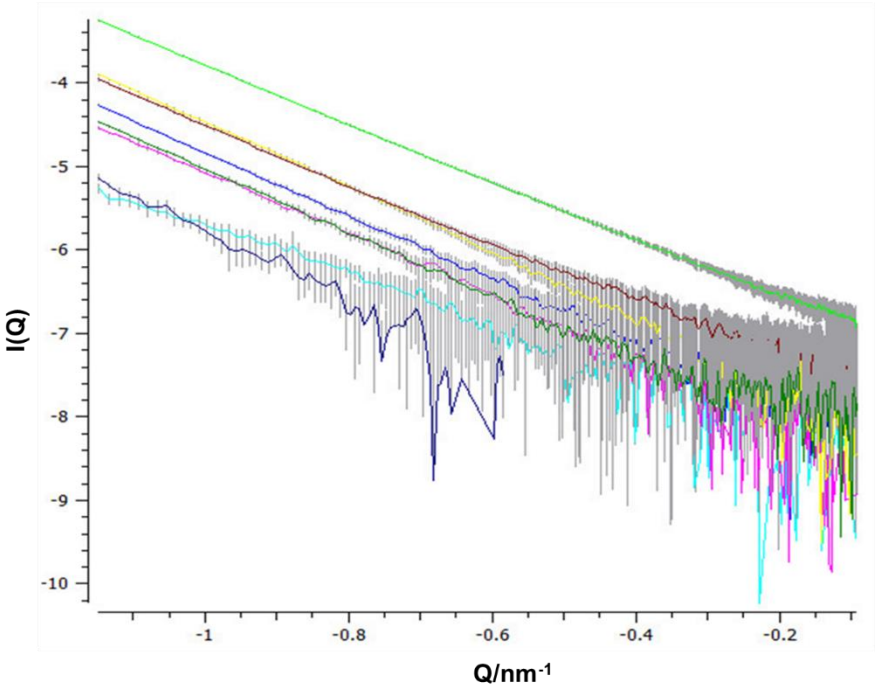


Figure 3.12: The SAXS results of extracted cosmetic particles suspended in ultrapure water for the 8 studied cosmetics; S1-red, S2-dark blue, S3-blue, S4-light blue, S5-pink, S6-yellow, S7-cinnamon brown, S8-green lines.

3.7.2 Elemental composition and oxidative state

SEM

Extracted solid samples, coated by gold, were examined using SEM and EDS techniques. The SEM images and EDS results at the marked spots for the eight commercial cosmetics studied are shown along with compositional details are shown in **Figure 3.13**. Most of the samples were found to contain some Si and Ti.

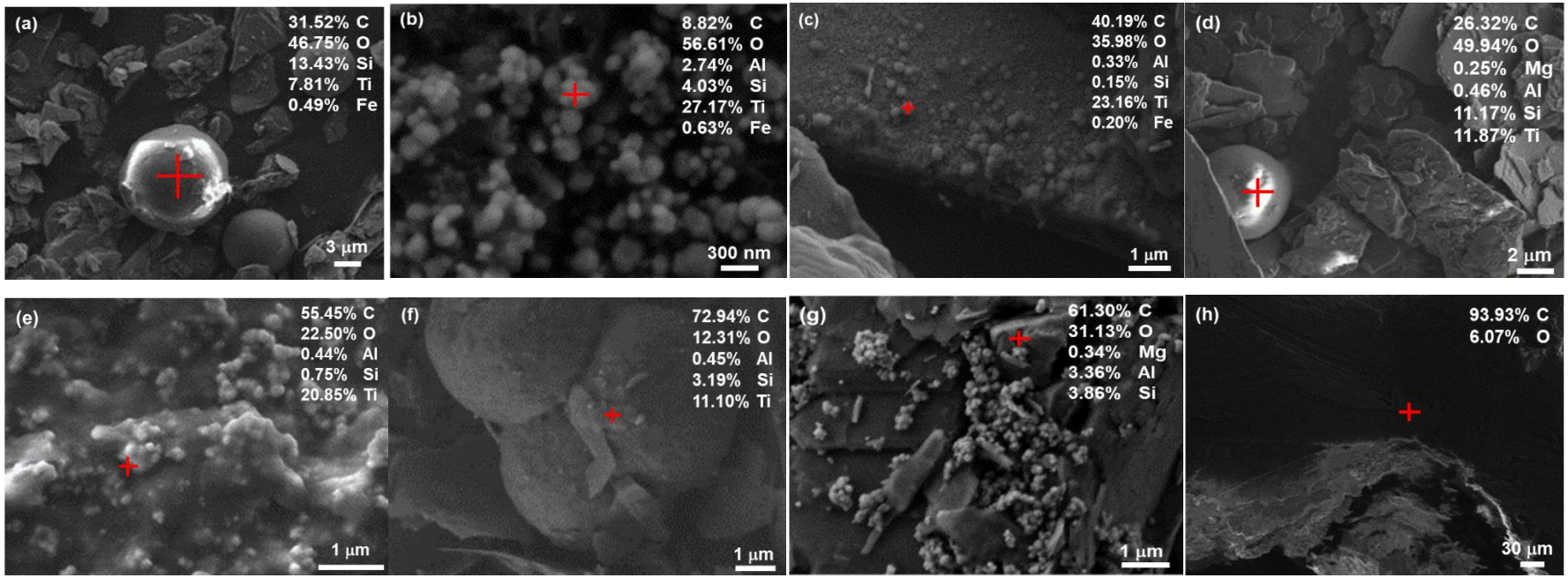


Figure 3.13: SEM images and EDS elemental atomic compositions (%) of the eight commercial cosmetics: (a) S1, (b) S2, (c) S3, (d) S4, (e) S5, (f) S6, (g) S7, and (h) S8 showing the morphology with low magnification, varying depending on the samples (see scale bars).

XPS

XPS analysis was used to explore the surface chemistry of the eight cosmetics. The survey spectra in **Figure 3.14** indicate the presence of Si, O, C, Ca, Mg, K and Ti in the samples. The percentages of atomic concentration are shown in **Table 3.5**. The high resolution XPS scans in the Si2p and Ti2p regions are shown in **Figure 3.15** and **Figure 3.16**, respectively. To determine the chemical structure of the Si atom, the binding energy of Si2p, O1s and C1s are observed and the details presented in **Table 3.6** to identify functional groups, such as silanol and alkyl groups. The binding energy of Si2p and O1s are shifted lower to 103 eV and ~532 eV, respectively, indicating the presence of silicon oxide in a few cosmetics (Thermo Scientific XPS, 2013). The high resolution XPS scans in the Ti2p peak position at 458.8 eV indicate the presence of TiO_2 in the cosmetic as shown in **Figure 3.16**, compared to the library reference of NIST X-ray Photoelectron Spectroscopy Database.

Table 3.5 Information on commercial cosmetics (S1 - S8) obtained by XPS, and presented as percentage of atomic composition.

Sample No.	C	O	Si	Ti	Fe	Mg	Ca	K
	Atomic composition (%)							
S1	13.99	42.18	14.59	0.10	0.90	8.05	3.72	16.47
S2	28.25	47.94	14.85	4.76	2.90	0.00	0.13	1.18
S3	84.77	10.51	2.11	0.78	0.12	0.05	0.16	1.50
S4	31.58	38.40	9.82	2.49	0.17	2.59	2.73	12.23
S5	91.64	3.52	1.17	0.31	0.44	0.00	0.33	2.59
S6	41.90	36.76	14.73	0.37	0.11	1.49	0.95	3.69
S7	25.00	43.26	13.88	0.36	1.62	3.23	2.69	9.96
S8	66.40	23.50	8.74	0.17	0.00	0.00	0.08	1.10

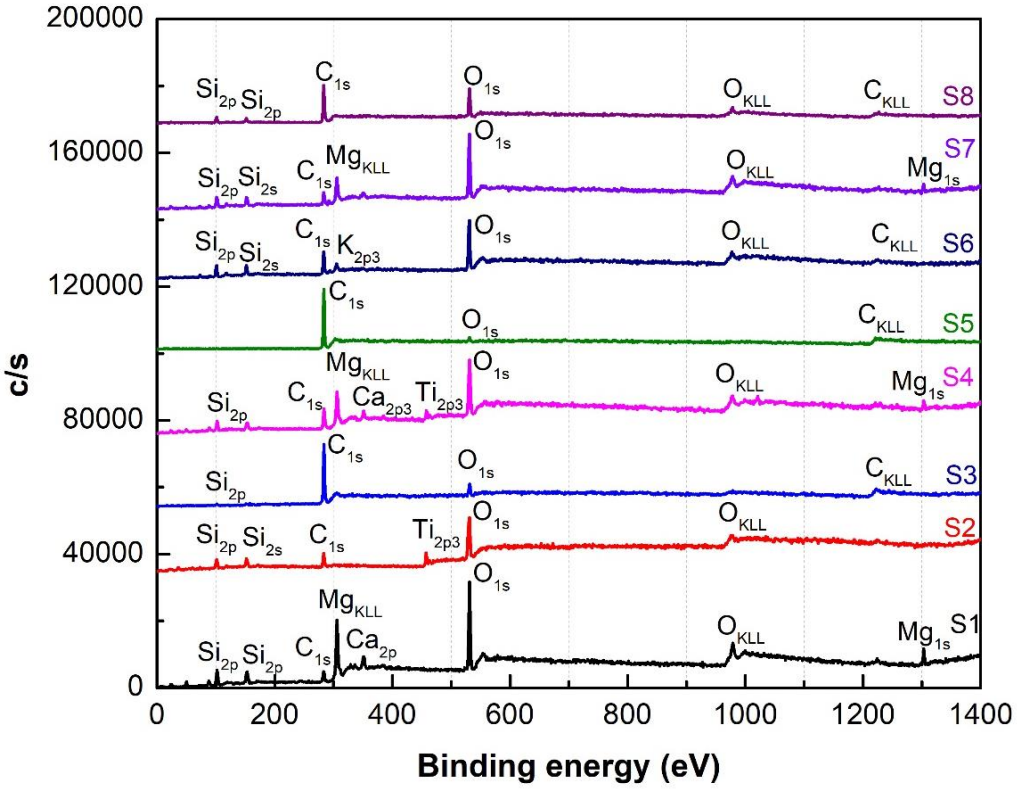


Figure 3.14: The survey spectra of eight cosmetics (S1-S8) presenting their surface elemental compositions.

Table 3.6 The information of binding energy of Si2p, O1s and C1s to determine the chemical structure on the surface.

Sample no.	Binding Energy (eV)		
	Si2p	O1s	C1s
S1	103.05	532.34	284.49
S2	102.50	531.97	284.49
S3	103.70	531.77	284.49
S4	103.15	531.77	284.49
S5	101.73	531.77	284.53
S6	102.18	529.43	284.52
S7	102.24	531.81	284.49
S8	102.00	532.00	284.49

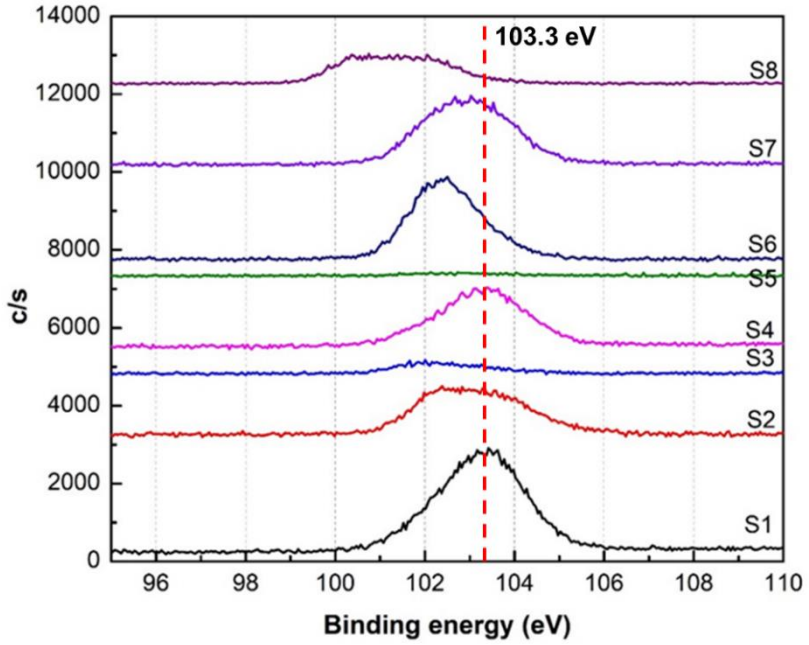


Figure 3.15: High resolution XPS scans of the Si2p region found in the eight studied cosmetics (S1-S8).

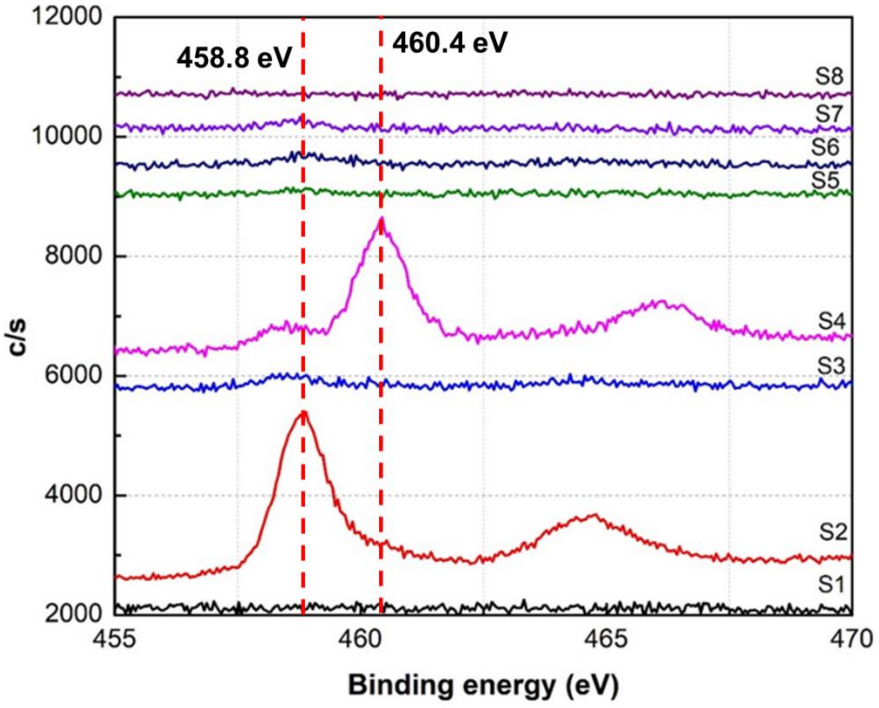


Figure 3.16: High resolution XPS scans of the Ti2p region found in the eight studied cosmetics (S1 - S8).

XAS-XANES

The oxidation state and structure of silicon found in the eight commercial cosmetics studied was resolved using XANES in fluorescence mode. The XANES spectra of Si*K*-edge for the eight cosmetics are shown in **Figure 3.17**. The features of Si*K*-edge spectra were divided into 2 types. The first shell of Si*K*-edge from the eight spectra displays quite different features, compared to the standard quartz and silicon metal as shown in **Figure 3.18**. It is apparent that the peak Si*K*-edge has shifted to lower energy from quartz at between 1844 and 1848 eV, suggesting the oxidation state of Si found in the cosmetics is between 2+ and 3+. The shift for peak Si is related to the local structure of Si atom that may represent different groups, such as silanol group (Si-OH) and alkyl group (Si-O-C) (Li *et al.*, 1994).

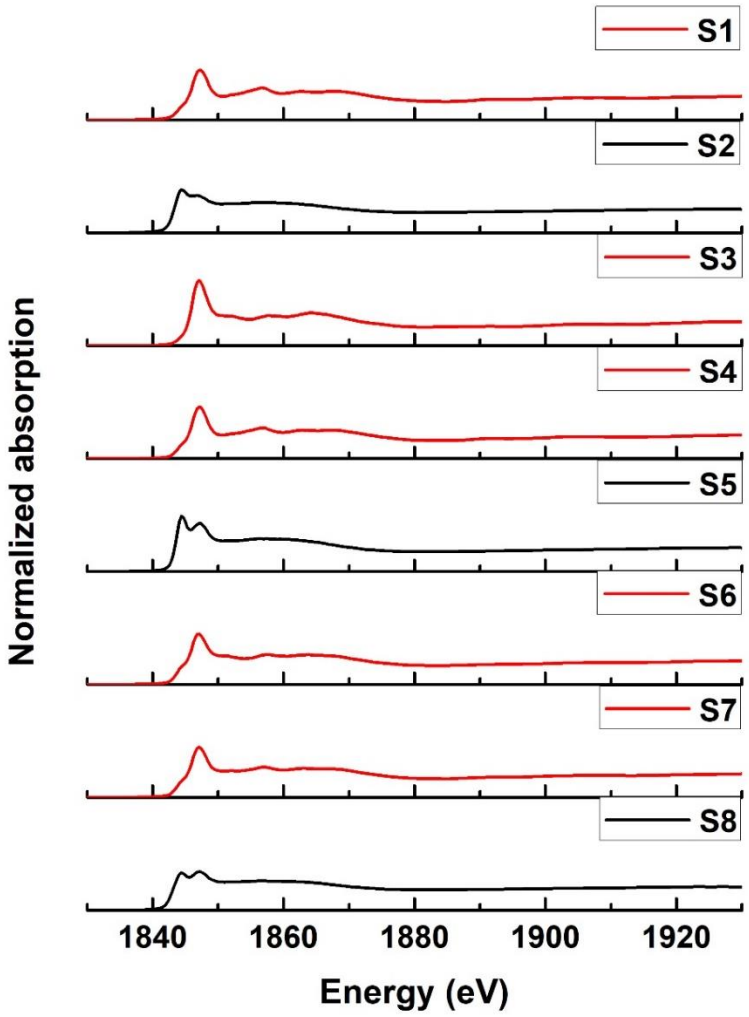


Figure 3.17: The Si*K*-edge XANES spectra of commercial cosmetics (S1 - S8) presented in two groups, black and red lines, corresponding to two types of patterns in the positions of *K*-edge energy.

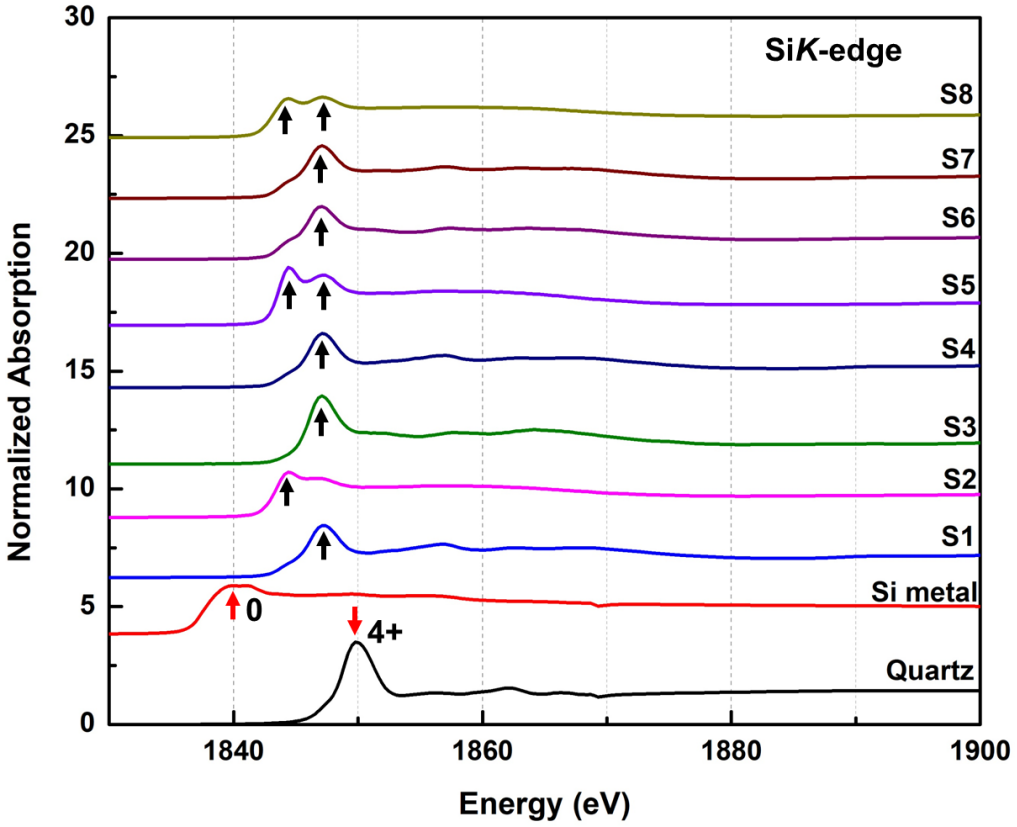


Figure 3.18: The Si*K*-edge XANES spectra of commercial cosmetics (S1 - S8) presenting the energy position of the first shell, and comparing this to the standard of quartz (black line) and silicon metal (red line). The red arrows pointed the Si*K*-edge energy to identify the oxidative state of substances as well as the black arrows at the first position of spectra.

In addition, the spectra of a titanium peak were observed and compared to a standard for anatase and rutile TiO_2 reference patterns shown in **Figure 3.19** and **Figure 3.20**, respectively. In most part, the spectra are similar to anatase TiO_2, indicating that this form of TiO_2 was incorporated in the commercial cosmetics.

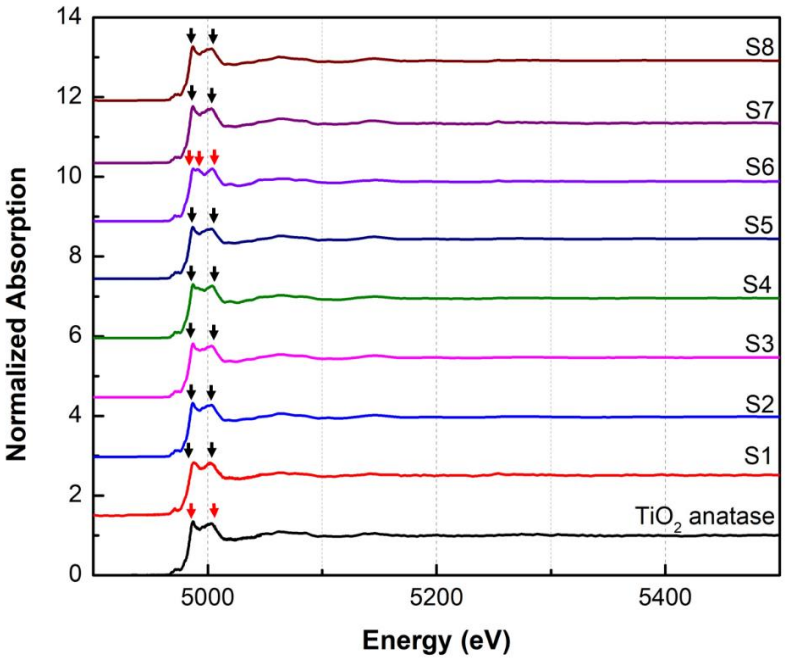


Figure 3.19: The Ti*K*-edge XANES spectra of commercial cosmetics (S1 - S8), compared to a reference standard of anatase TiO_2.

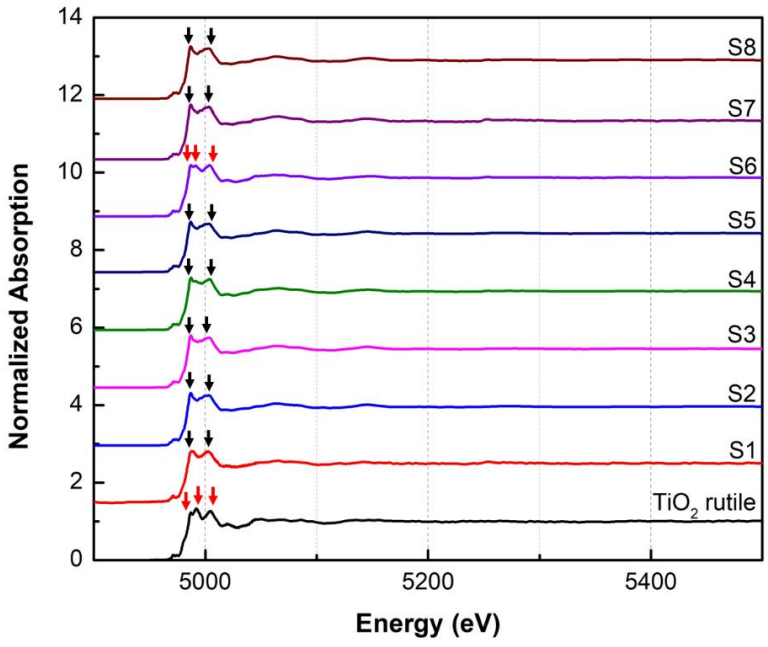


Figure 3.20: The Ti*K*-edge XANES spectra of commercial cosmetics (S1 - S8), compared to a reference standard of rutile TiO_2.

3.7.3 Chemical Composition

XRD

All cosmetics were characterised without any pre-treatment using powder XRD to identify any components with crystalline structure. XRD spectra of a number of the cosmetic samples exhibited peaks at $2\partial = 22^{o}$ representing silicon dioxide in sample number 1, 2, 3, and 7 (Rasmussen *et al.*, 2013; Nandawar, Singh and Fozia Z. Haque, 2015). This finding was expected as silicon or silicon dioxide is contained in many commercial cosmetics. The full X-ray diffraction patterns of sample S1-S8 are shown in **Figure 3.21 - Figure 3.28**. A number of peaks representing titanium dioxide were also identified in the XRD spectra from eight samples, then the structure of titanium dioxide was further characterised using XAS-XANES in the next section. Moreover, several other crystalline substances were identified in the studied cosmetics as shown in **Table 3.7**, in accordance with the compositions listed on their labels **Table 3.1**. EVA software was useful to provide the results for cosmetics that were used in this preliminary study, but the results were difficult to interpret due to overlapping peaks or materials present in low concentration. However, the full characterisation of cosmetics needs to resolve these limits and to consider an appropriate method for identification.

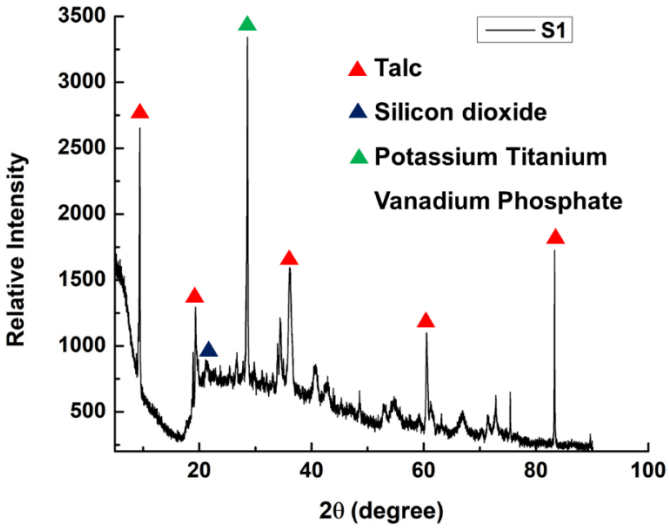


Figure 3.21: X-ray diffraction pattern of a commercial cosmetic (sample 1 : Powder Foundation). The identified 2θ positions indicate talc-2M ($Mg_3Si_4O_{10}(OH)_2$), silicon oxide (SiO_2), and potassium titanium vanadium phosphate ($K_2TiV(PO_4)_3$).

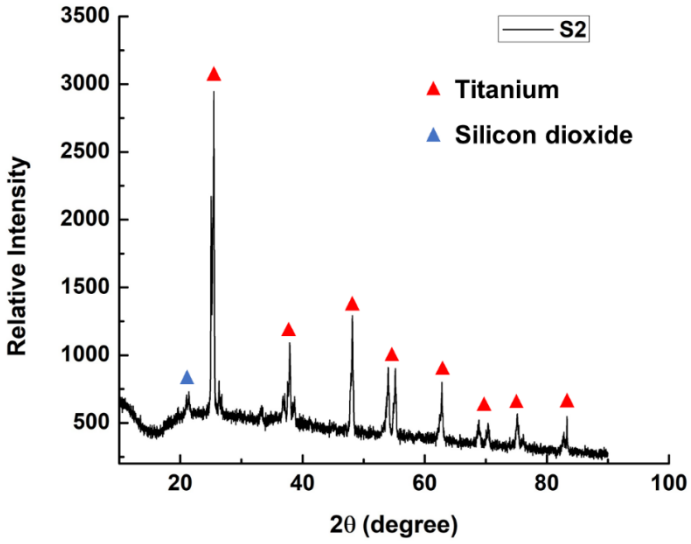


Figure 3.22: X-ray diffraction pattern of a commercial cosmetic (sample 2 : Skin crème oil free photo edition foundation). The identified 2θ positions indicate anatase, syn ($Ti_{0.72}O_2$) and cristobalite (SiO_2).

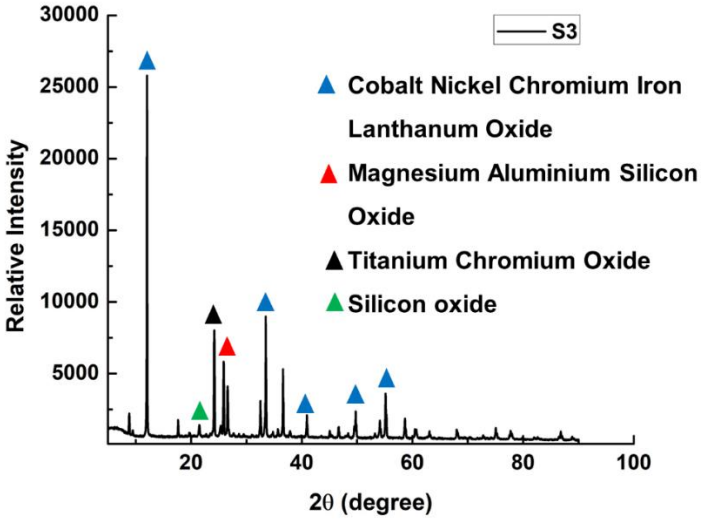


Figure 3.23: X-ray diffraction pattern of a commercial cosmetic (sample 3 : Shadow tint for eye). The identified 2θ positions indicate cobalt nickel chromium iron lanthanum oxide ($LaCr_{0.85}Fe_{0.05}Co_{0.05}Ni_{0.05}O_3$), magnesium aluminium silicon oxide ($Mg_6Al_{1.2}Si_{1.8}O_6$), titanium chromium oxide ($Ti_{0.93}Cr_{0.07}O_{1.965}$), and silicon oxide ($SiO_2$).

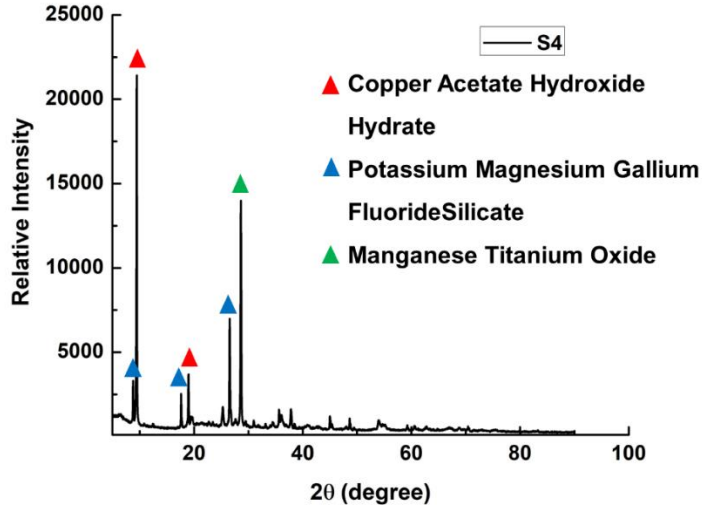


Figure 3.24: X-ray diffraction pattern of a commercial cosmetic (sample 4 : Sheertone Shimmer Blush). The identified 2θ positions indicate copper acetate hydroxide hydrate ($Cu_2(OH)_{3.1}(OCOCH_3)_{0.9}\cdot 0.7H_2O$), potassium magnesium gallium fluoride silicate ($KMg_3(GaSi_3O_{10})$), and manganese titanium oxide (Mn_2TiO_4 **α** – Mn_2TiO_4).

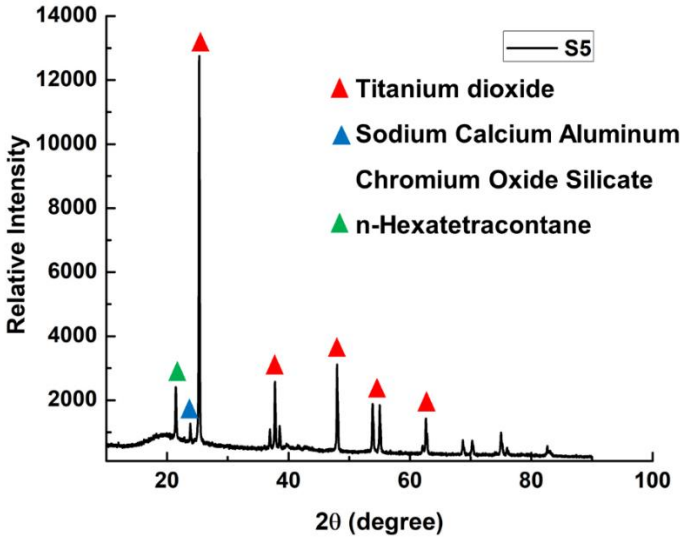


Figure 3.25: X-ray diffraction pattern of a commercial cosmetic (sample 5 : Matte Long Last Lipstick in Pink). The identified 2θ positions indicate anatase, syn ($Ti_{0.72}$ O_2), sodium calcium aluminium chromium oxide silicate ($Na_6Al_6Si_6O_{24}(CrO_4)_2$), and n-hexatetracontane ($C_{46}H_{94}$).

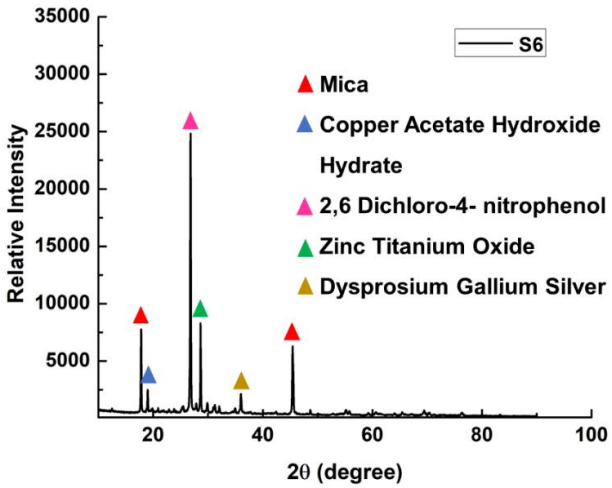


Figure 3.26: X-ray diffraction pattern of a commercial cosmetic (sample 6 : Shade Eye shadow Palette). The identified 2θ positions indicate mica (K-Mg-Fe-Al-Si-O-H_2O), tris(μ3-hydroxo)-μ3-aceto-biscopper hydrate /copper acetate hydroxide hydrate ($Cu_2(OH)_3(CH_3COO)\cdot H_2O$), 2,6-dichloro-4-nitrophenol ($C_6H_3Cl_2NO_3$), zinc titanium oxide (Zn_2TiO_4 α-Zn_2TiO_4), and dysprosium gallium silver ($Ag_{3.8}Dy_3Ga_{7.2}$).

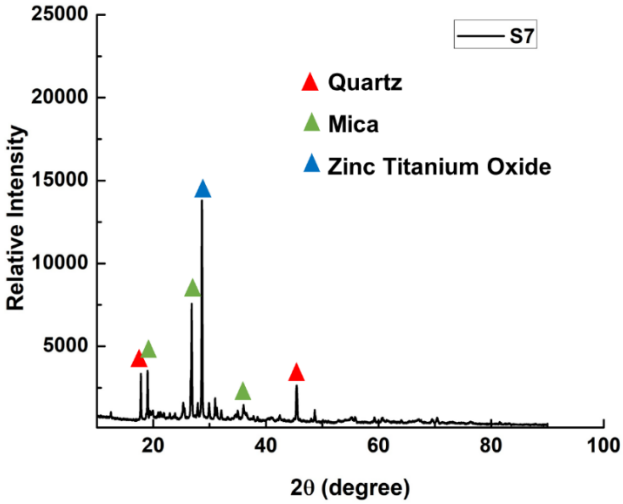


Figure 3.27: X-ray diffraction pattern of a commercial cosmetic (Sample 7 : Loose Face Powder). The identified 2θ positions indicate quartz, low (SiO_2), mica (K-Mg-Fe-Al-Si-O-H_2O), and zinc titanium oxide (Zn_2TiO_4 α-Zn_2TiO_4).

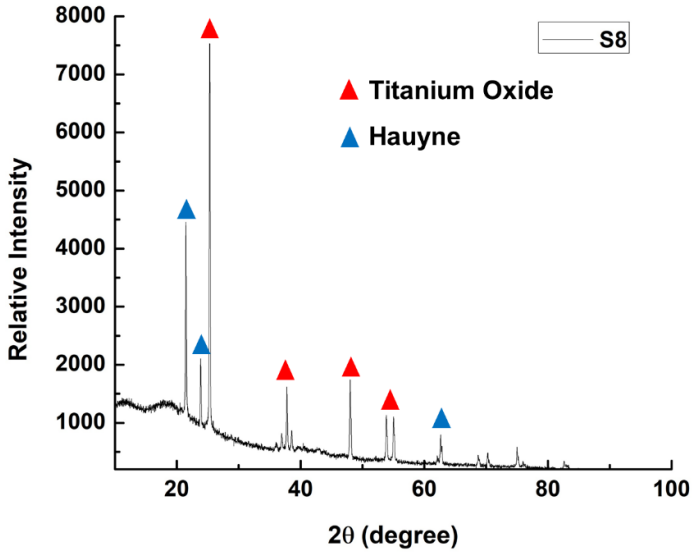


Figure 3.28: X-ray diffraction pattern of a commercial cosmetic (sample 8 : Blusher). The identified 2θ positions indicate anatase, syn ($Ti_{0.72}O_2$) and hauyne ($Na_6Ca_2Al_6Si_6O_{24}$).

Table 3.7 Details of the crystalline substances identified by XRD in the studied cosmetics; the substances were identified by matching the diffractogram peaks with those of the reference XRD library.

Sample No.	Chemical composition
S1	Talc-2M ($Mg_3Si_4O_{10}(OH)_2$), silicon oxide (SiO_2), and potassium titanium vanadium phosphate ($K_2TiV(PO_4)_3$)
S2	Anatase, syn ($Ti_{0.72}O_2$) and cristobalite (SiO_2)
S3	Cobalt nickel chromium iron lanthanum oxide ($LaCr_{0.85}Fe_{0.05}Co_{0.05}Ni_{0.05}O_3$), magnesium aluminium silicon oxide ($Mg_6Al_{1.2}Si_{1.8}O_6$), titanium chromium oxide ($Ti_{0.93}Cr_{0.07}O_{1.965}$), silicon oxide ($SiO_2$)
S4	Copper acetate hydroxide hydrate ($Cu_2(OH)_{3.1}(OCOCH_3)_{0.9}\cdot 0.7H_2O$), potassium magnesium gallium fluoride silicate ($KMg_3(GaSi_3O_{10})$), and manganese titanium oxide (Mn_2TiO_4 α – Mn_2TiO_4)
S5	Anatase, syn ($Ti_{0.72}$ O_2), sodium calcium aluminium chromium oxide silicate ($Na_6Al_6Si_6O_{24}(CrO_4)_2$), n-hexatetracontane ($C_{46}H_{94}$)
S6	Mica (K-Mg-Fe-Al-Si-O-H_2O) , tris(μ3-hydroxo)-μ3-aceto-biscopper hydrate/copper acetate hydroxide hydrate ($Cu_2(OH)_3(CH_3COO)\cdot H_2O$), 2,6-dichloro-4-nitrophenol ($C_6H_3Cl_2NO_3$), zinc titanium oxide (Zn_2TiO_4 α-Zn_2TiO_4), dysprosium gallium silver ($Ag_{3.8}Dy_3Ga_{7.2}$), glycolated (K,H_{30}) $Al_2(Si_3Al)O_{10}(OH)\cdot xH_2O$)

Sample No.	Chemical composition
S7	Quartz, low (SiO_2), mica (K-Mg-Fe-Al-Si-O-H_2O), and zinc titanium oxide (Zn_2TiO_4 α-Zn_2TiO_4)
S8	Anatase, syn ($Ti_{0.72}O_2$), hauyne ($Na_6Ca_2Al_6Si_6O_{24}$)

3.7.4 Surface Charge

Zeta-potential measurement

Surface charge of the nanoparticulate component found in the eight cosmetic samples studied, was determined using DLS**.** The measurements were conducted in triplicate for each sample**. Table 3.8** shows the zeta**-**potential, mobility and conductivity of the eight cosmetics**.** The zeta**-**potential values of the cosmetics are closed to zero, indicating instability of the cosmetic suspensions**.** This finding suggests a tendency towards coagulation or flocculation of the suspensions resulting in sedimentation for the particles (Yoon and Deng, 2004), unless they are sterically stabilised.

Table 3.8 The average zeta potential values, standard deviation, mobility, and conductivity of the eight cosmetics.

Sample no.	Zeta Potential (average±SD, mV)	Mob (μmcm/Vs)	Conductivity (mS/cm)
S1	0.263±0.436	0.01869	0.0485
S2	-3.2 ±3.14	-0.2268	0.016
S3	-15.7±4.01	-1.11377	0.0105
S4	-7.34±1.02	-0.5205	0.0167

Sample no.	Zeta Potential (average±SD, mV)	Mob (μmcm/Vs)	Conductivity (mS/cm)
S5	-23.1±0.681	-1.638	0.00283
S6	-3.58±2.63	-0.25357	0.005
S7	-4.07±1.71	-0.00823	0.00478
S8	10.7±1.15	0.7562	0.00792

3.8 Results of SAS Characterisation

This section describes the results of SASs characterisation. A multi-method approach was used to characterise SASs. XRD, XAS-EXAFS/XANES, XPS, WAXS/SAXS, SEM were applied to measure elemental composition and structural morphology. DLS, TEM and SAXS provided particle size and size distribution, whereas zeta potential was obtained from DLS. BET analysis provided the specific surface area of samples.

3.8.1 Particle size and size distribution

DLS

The powdered samples were suspended in UPW and ultrasonicated at 80% amplitude for 20 minutes prior to measurements. The measurement was made under thermostat conditions at 20 °C. The intensity size distribution, the Z-average diameter (Z-avg), and the polydispersity index (PdI) were obtained from the autocorrelation function using the general-purpose mode. DLS results including hydrodynamic diameter, Z-average and PdI illustrated in

Table 3.9, and compared to the previous measurements by the JRC (ECETOC, 2006). The size distribution graphs obtained from three different samples as shown in **Figure 3.29** - **Figure 3.33**. According to the DLS results, the SASs have a narrow size distribution peak and polydispersity (PDI) showed a good range indicating that the samples are suitable for analysis by this technique.

Table 3.9 The hydrodynamic diameter, Z-average, and PdI measured by using DLS measurements.

Sample name	Z-average (d.nm)	PdI	Size (nm)	Z-average by JRC (d.nm)
SAS 2000a	217.7	0.199	243.6	234.9±18.6
SAS 2001a	217.2	0.257	222.1	224.2±79
SAS 2002a	225	0.277	223.4	159.9±1.8
SAS 2004a	249	0.262	258.1	-
SAS 10404a	122.4	0.262	118.9	-

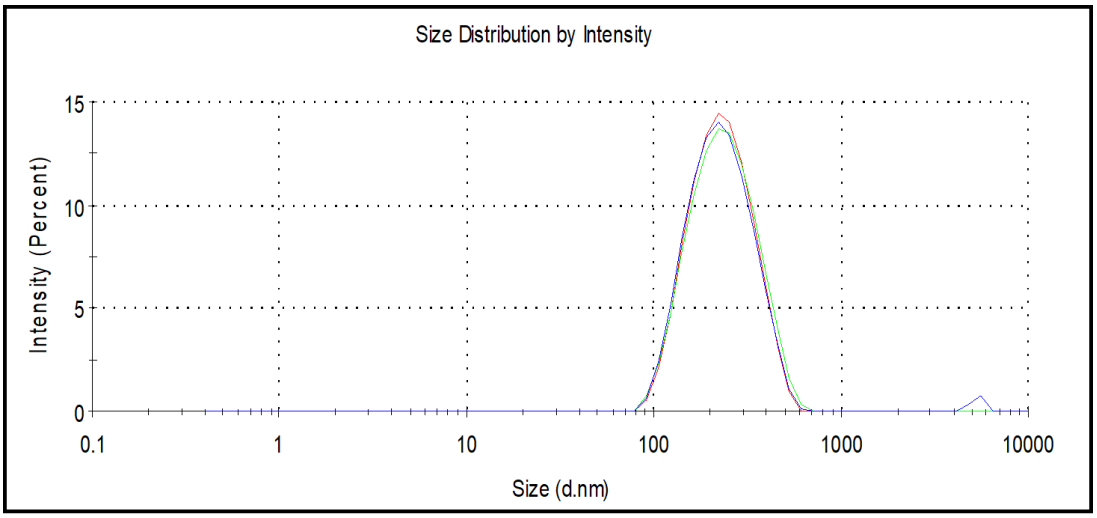


Figure 3.29: The size distribution by intensity of SAS2000a.

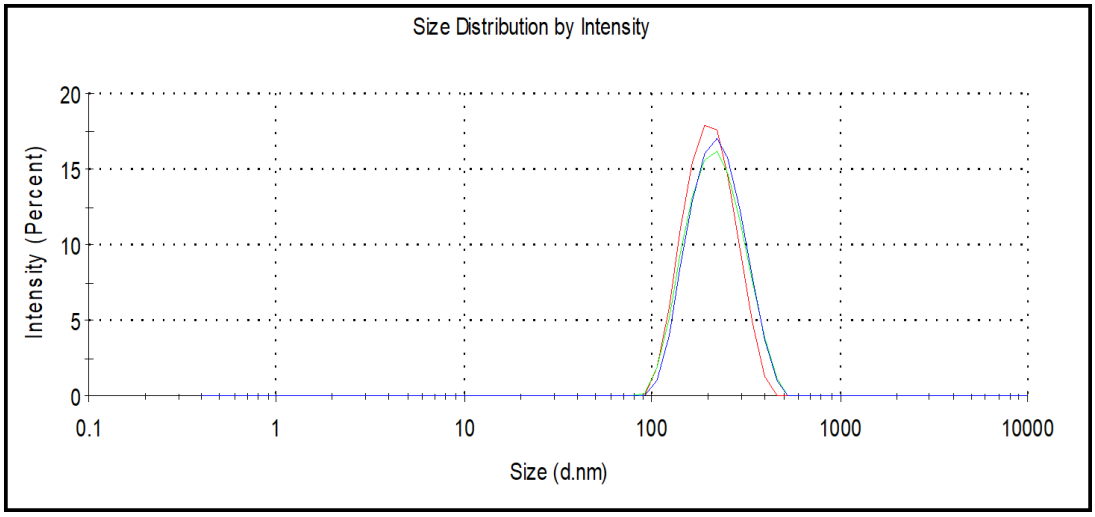


Figure 3.30: The size distribution by intensity of SAS2001a**.**

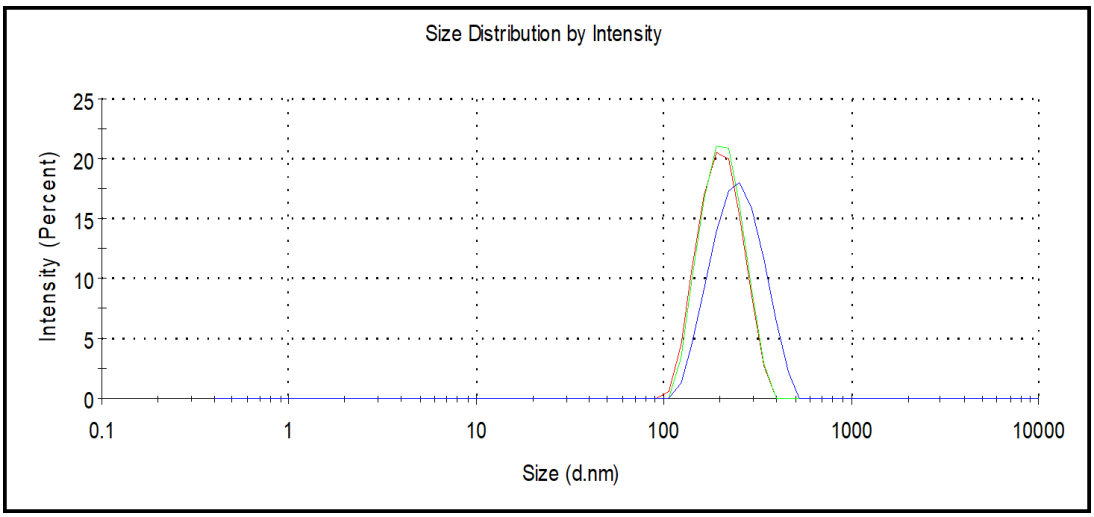


Figure 3.31: The size distribution by intensity of SAS2002a**.**

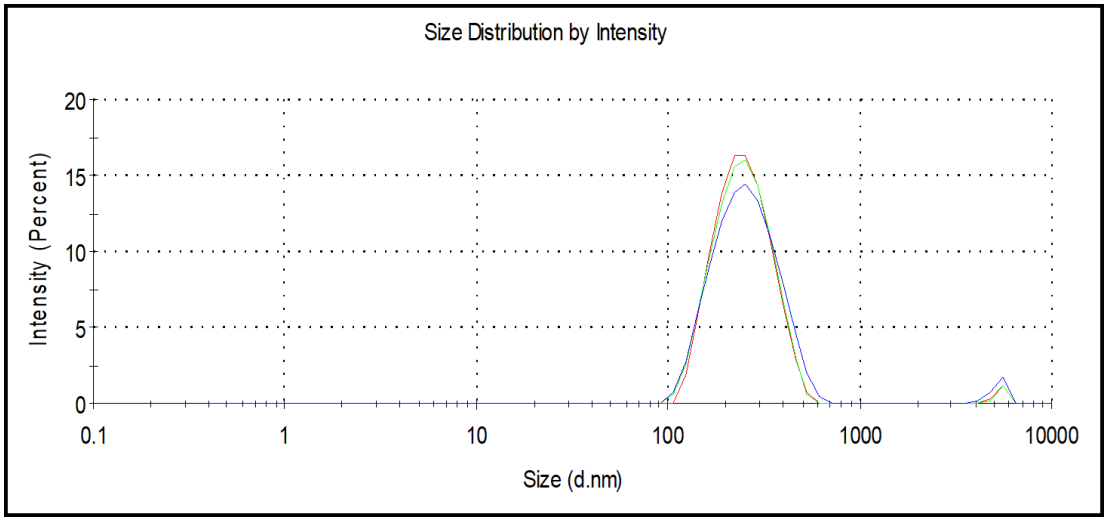


Figure 3.32: The size distribution by intensity of SAS2004a**.**

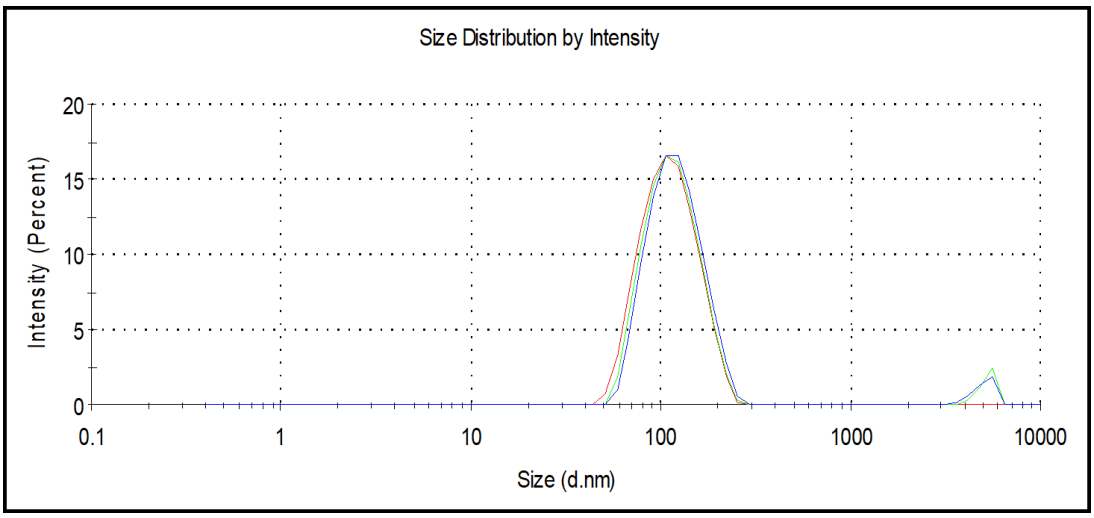


Figure 3.33: The size distribution by intensity of SAS10404a**.**

TEM

The representative TEM images of the five SAS showing the complex structure of SAS aggregates are given in **Figure 3. 34 - Figure 3. 38**. The general morphology of the primary sub-units of the five SAS is slightly rounded. The morphology of particle aggregates is dense and complex in structure. It is noted that the image resolution does not allow identification of individual particle edges therefore it is difficult to estimate particle size accurately.

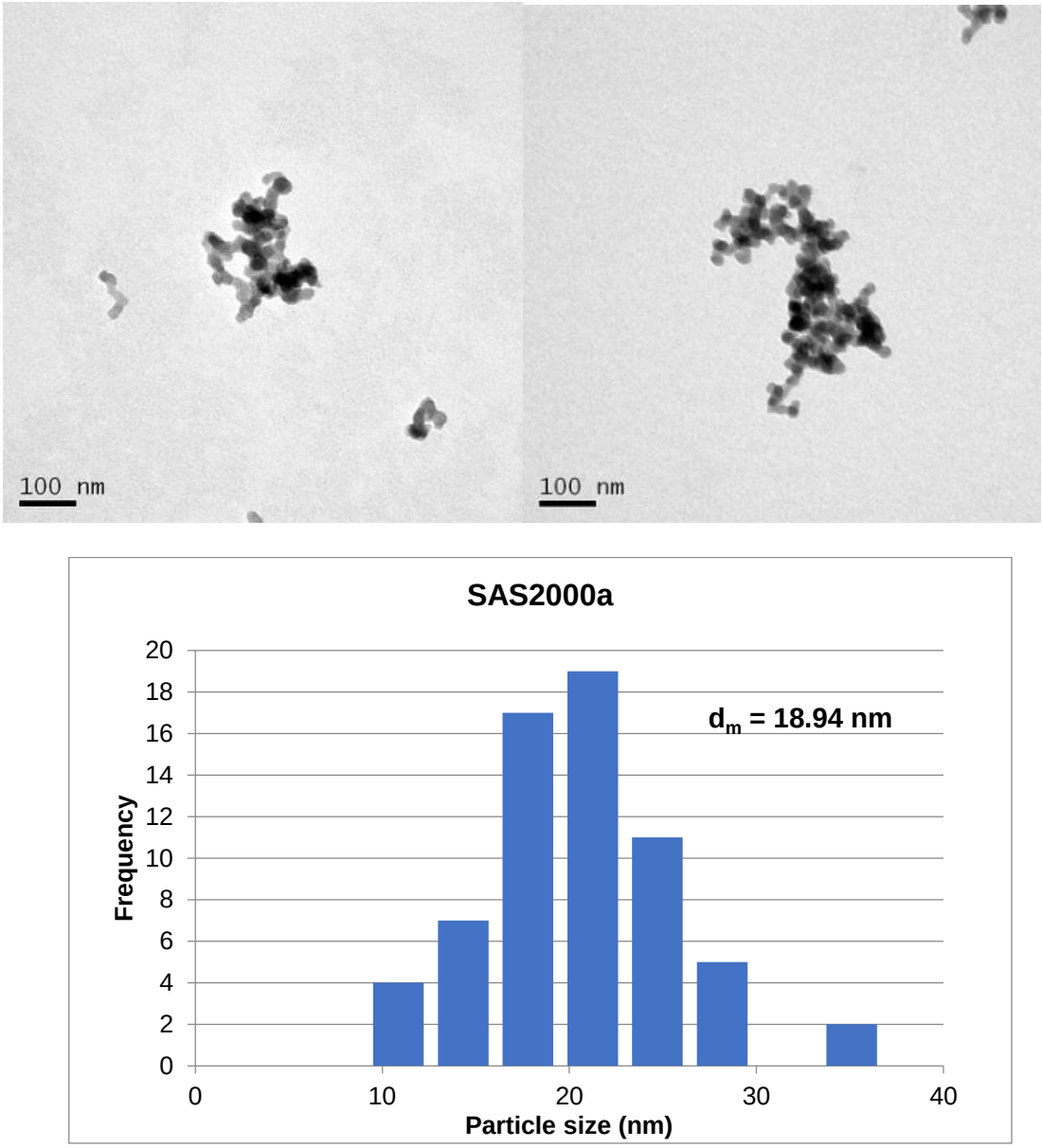


Figure 3.34: Representative images of SAS2000a dispersed in UPW. The presence of slightly large aggregates can be observed. The histogram presents mean particle size (d_m) and size distribution.

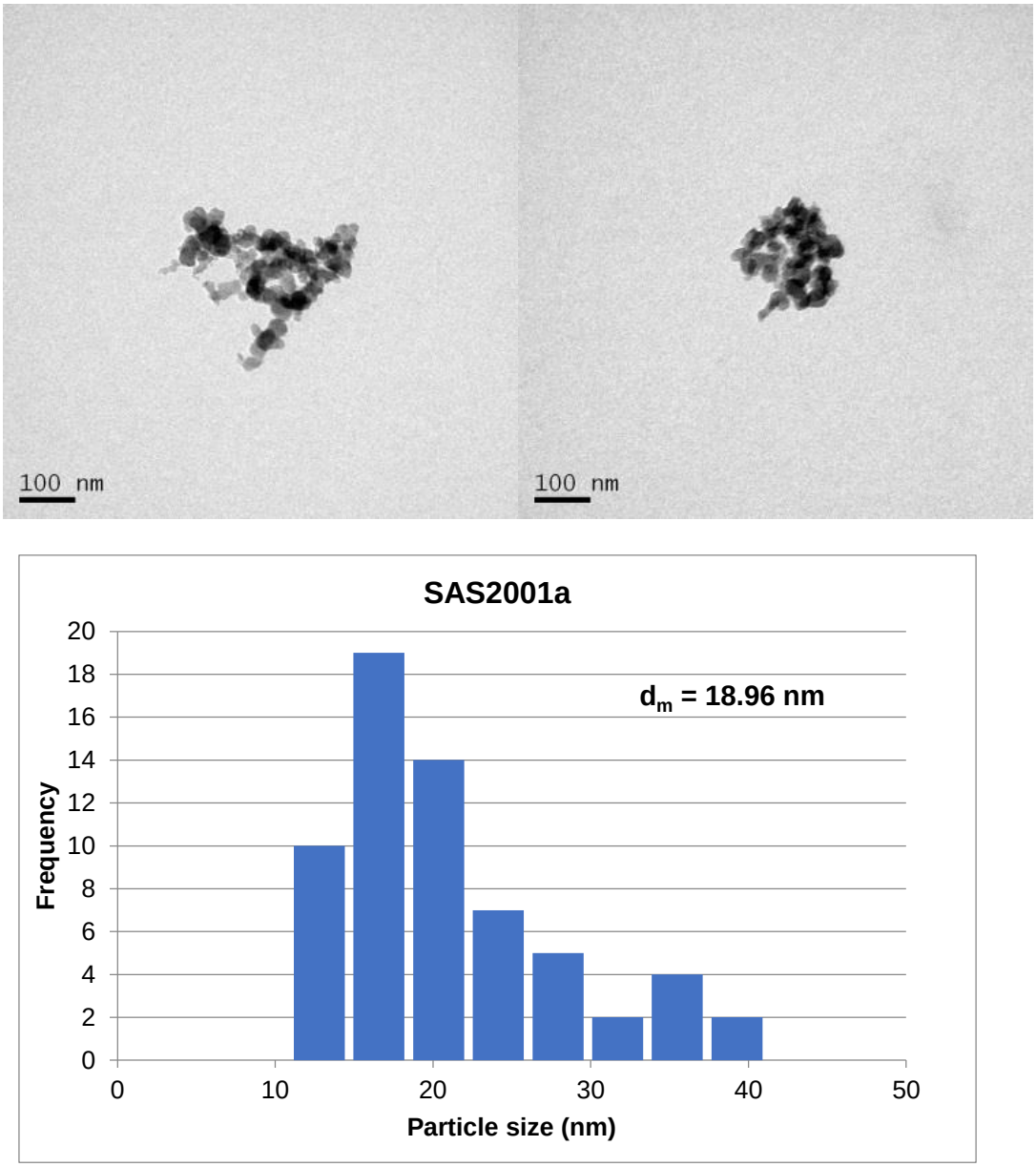
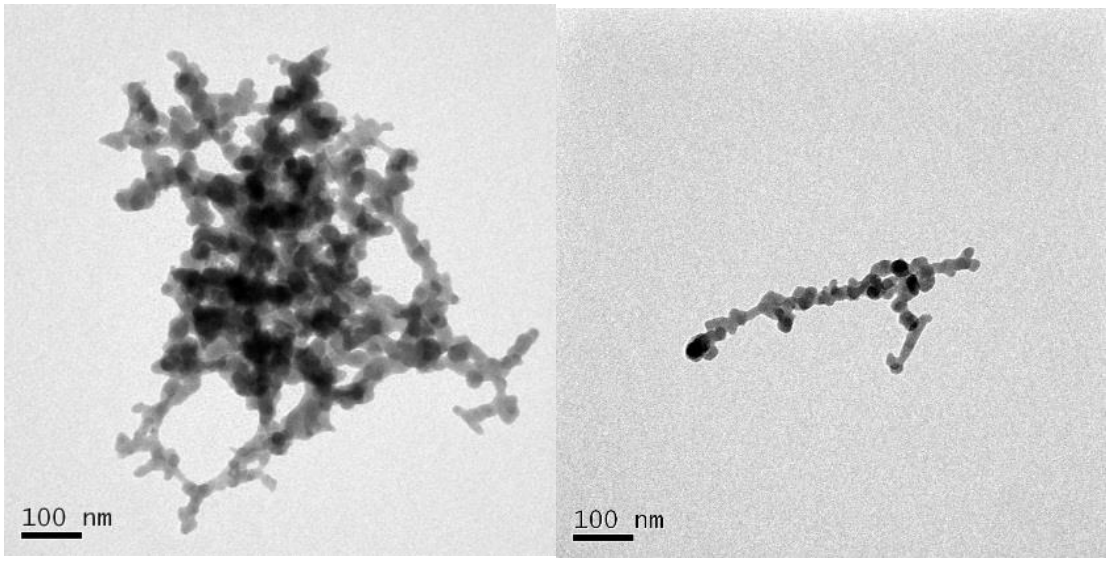


Figure 3.35: Representative images of SAS2001a dispersed in UPW. The presence of slightly large aggregates can be observed. The histogram presents mean particle size (d_m) and size distribution.



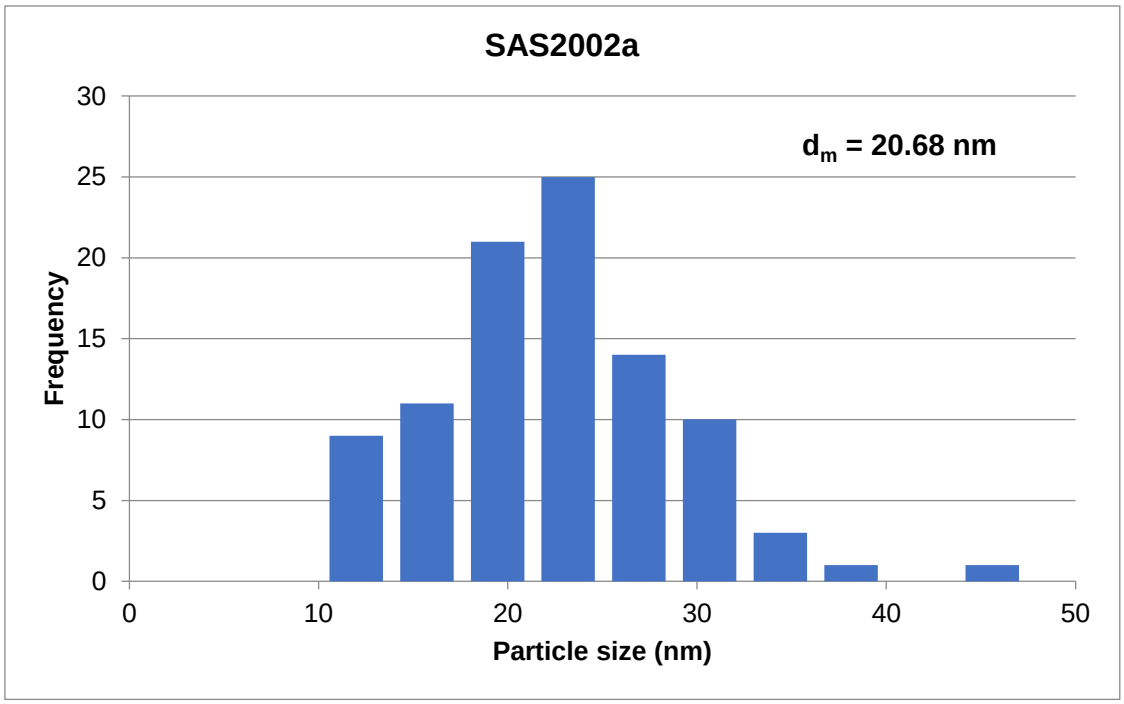
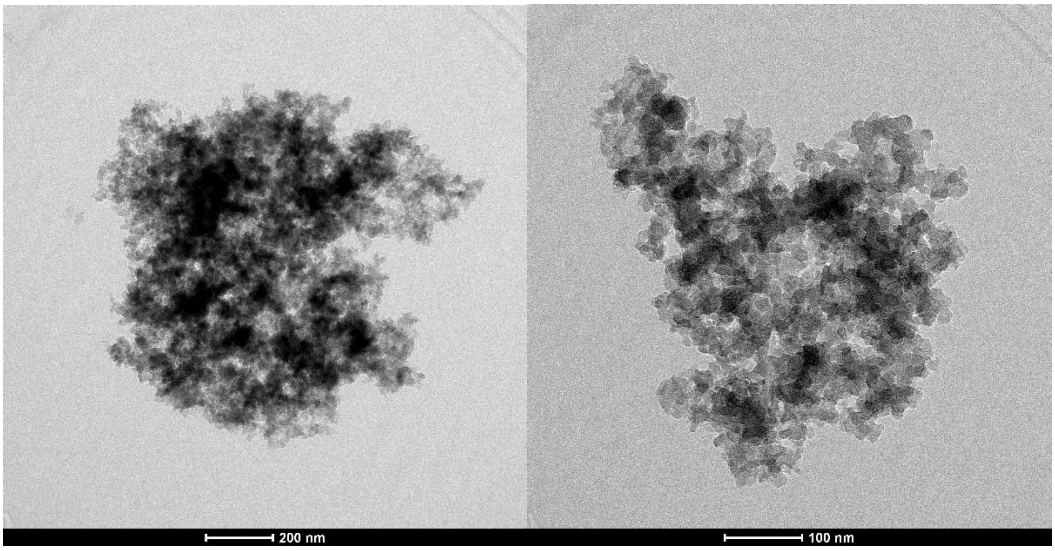


Figure 3.36: Representative images of SAS2002a dispersed into ultrapure water. The presence of slightly large aggregates can be observed. The histogram presents mean particle size (d_m) and size distribution.



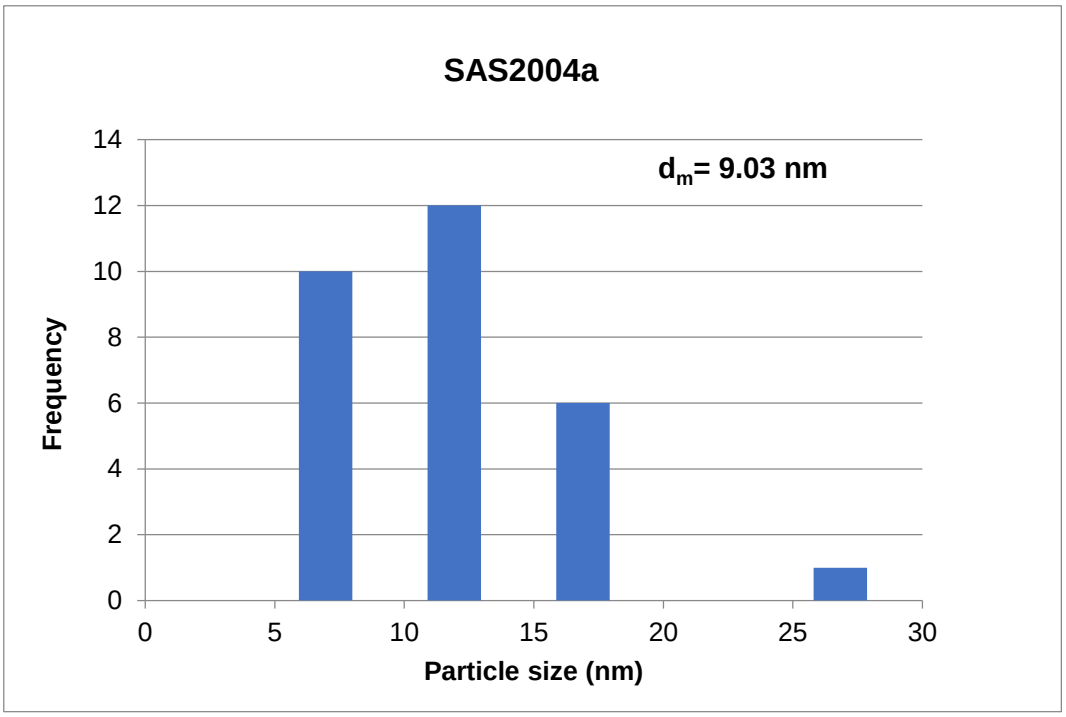
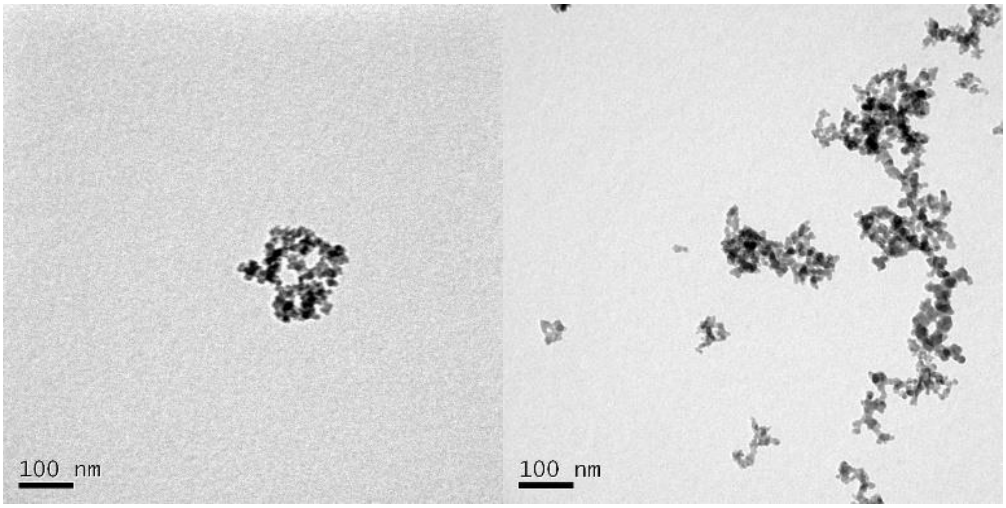


Figure 3.37: Representative images of SAS2004a dispersed in UPW. The presence of slightly large aggregates can be observed. The histogram presents mean particle size (d_m) and size distribution.



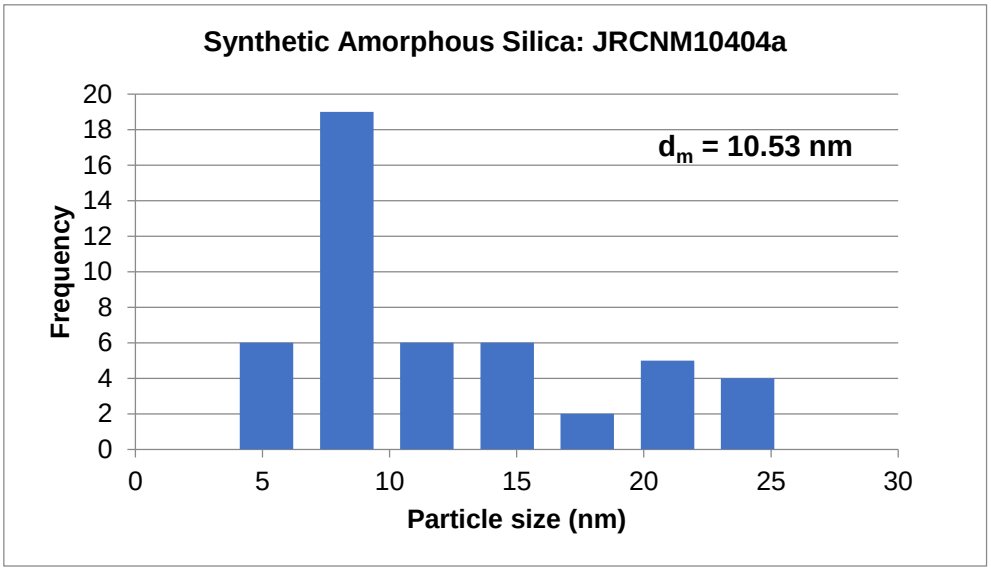


Figure 3.38: Representative images of SAS10404a dispersed into ultrapure water. The presence of slightly large aggregates can be observed. The histogram presents mean particle size (d_m) and size distribution.

SAXS

SAXS was employed to determine the primary particle size and size distribution of the five SAS. The scattering patterns (as shown in **Figure 3.40** - **Figure 3.44**) were fitted using unified exponential-power law based on the Beaucage model as shown in equation **(3.1)** and the scattering patterns in **Figure 3.39**.

Unified Exponential Power Law

$$I(q) = G\exp\left(-\frac{q^2{R_g}^2}{3}\right) + B\,exp\left(-\frac{q^2{R_{sub}}^2}{3}\right)\left\{\frac{\left[\frac{qR_g}{\sqrt{6}}\right]^3}{q}\right\}^P \quad \textbf{(3.1)}$$

$$+\ G_s\exp\left(-\frac{q^2{R_g}^2}{3}\right) + B_s\left\{\frac{\left[\frac{qR_g}{\sqrt{6}}\right]^3}{q}\right\}^{P_s}$$

$$\mu = \sqrt{\frac{5{R_g}^2}{3\exp(14\sigma^2)}}$$

$$\sigma = \sqrt{\frac{ln\left[\frac{B{R_g}^4}{1.62G}\right]}{12}}$$

$$\langle R\rangle = \mu\exp\left(\frac{\sigma^2}{2}\right)$$

$$SD = \mu\sqrt{\omega(\omega-1)}$$

Note: $\omega = \exp(\sigma^2)$

Input Parameters for Beaucage model:

1. [G] *G* is the Guinier pre-factor of the larger structure
2. [B] *B* is a pre-factor specific to the type of power-law scattering. *B* is defined according to the regime in which the exponent *P* falls.
3. [Gs] G_s is the Guinier pre-factor of the smaller structure
4. [Bs] B_s is a pre-factor specific to the type of power-law scattering. B_s is defined according to the regime in which the exponent P_s falls.
5. [Rg] large-scale structure
6. [Rsub] surface-fractal cut-off radius of gyration, R_{sub} defines the high-*Q* cut off for the intermediate power law

7. [Rs] size R_s of small subunits
8. [P] scaling exponent of the power law assigned to the larger structure R_g
9. [Ps] scaling exponent of the power law assigned to the smaller structure R_s

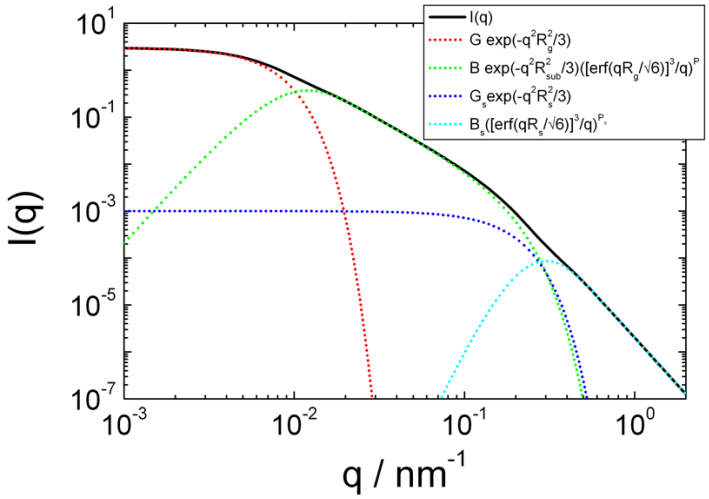


Figure 3.39: The unified exponential-power law describes scattering data based on Beaucage's law.

Table 3.10 Details of the fitted parameters obtained from the scattering patterns of the five SAS using unified exponential power law.

Sample no.	Main size and structure parameters from SAXS unified fit model			
	2 Rg_1 (nm)	**<R>/(nm)**	**SD**	**Slope (P)**
SAS2000a	19.2958	6.7256	3.1772	3.9373
SAS2001a	23.4292	7.4896	3.6657	3.8270
SAS2002a	16.7442	4.8019	2.4505	3.6391
SAS2004a	18.6863	7.2942	3.2787	3.9668
SAS10404a	21.6159	7.8751	3.6504	3.9259

Note: Rg is the radius of gyration from primary particle, while <R> is the mean particle radius that can be found from the first moment of the distribution.

The 1-dimensional (1D) SAXS graphs of the five SAS are fitted by using the unified exponential power law and subtracted the incoherent background from the experimental data. As the fitted graphs below, the 1D SAXS graphs of the five SAS show 3 power-law regimes; at high q, a power-law of -4 is observed for the surface of the primary particle. At intermediate q, a weak slope corresponds of a mass fractal regime. At low q, a power-law of -4 is observed for mass-fractal aggregates. The slop (p) around 3-4 (as shown in **Table 3.10**) means that the shape of the five SAS samples is spherical form factor (Guinier, André and Fournet, 1955; Schnablegger and Singh, 2013).

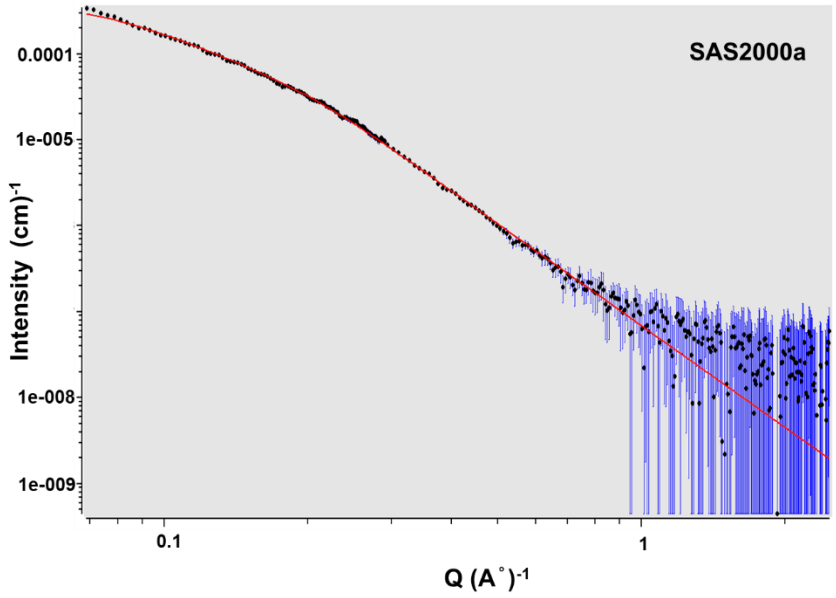


Figure 3.40: The fitted SAXS graph of SAS2000a shows that the diameter (2Rg1) is 19.29 nm, the error ranges of the size distribution (s) is 3.17 and slope (P) is 3.94.

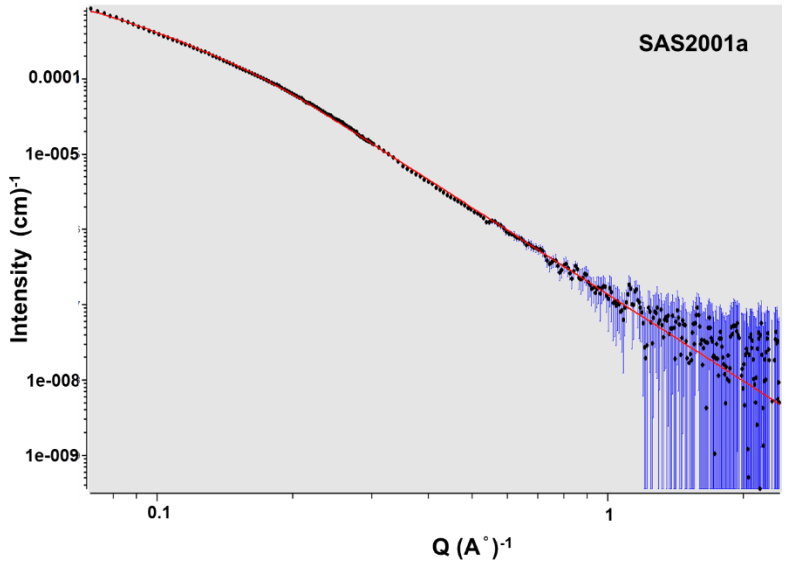


Figure 3.41: The fitted SAXS graph of SAS2001a shows that the diameter (2Rg1) is 23.43 nm, the error ranges of the size distribution (s) is 3.67 and slope (P) is 3.83.

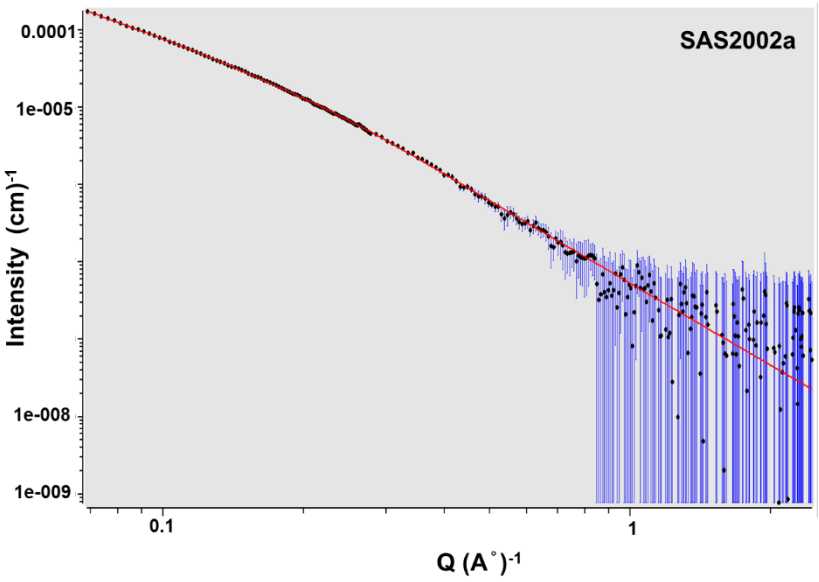


Figure 3.42: The fitted SAXS graph of SAS2002a shows that the diameter (2Rg1) is 16.74 nm, the error ranges of the size distribution (s) is 2.45 and slope (P) is 3.64.

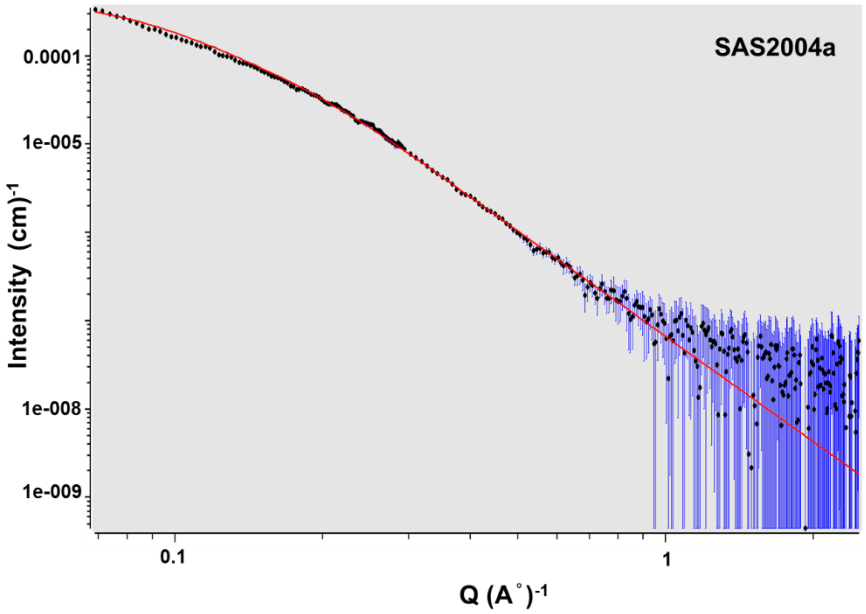


Figure 3.43: The fitted SAXS graph of SAS2004a shows that the diameter (2Rg1) is 18.69 nm, the error ranges of the size distribution (s) is 3.28 and slope (P) is 3.97.

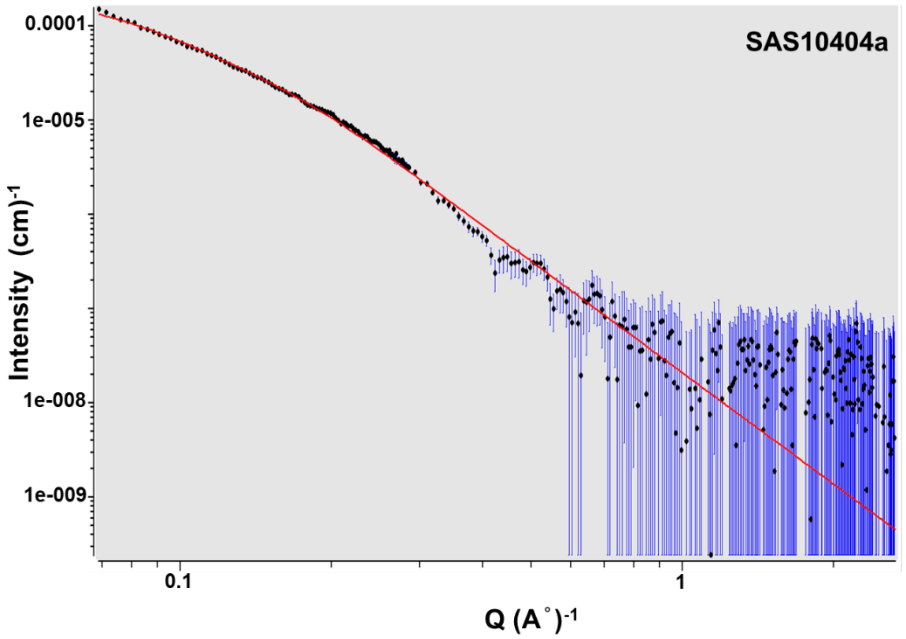


Figure 3.44: The fitted SAXS graph of SAS10404a shows that the diameter (2Rg1) is 21.62 nm, the error ranges of the size distribution (s) is 3.65 and slope (P) is 3.93.

3.8.2 Morphology (Crystallinity structure)

XRD

Five powdered SASs were investigated to identify the element and crystallinity using powder X-ray diffraction (XRD). The XRD diffractograms illustrated broad peaks at ~22º2∂ (**Figure 3.45**), which indicated amorphous form of silicon dioxide. This finding is good agreement with the study of ECETOC, (2006), Rasmussen *et al.* (2013) and Nandawar, Singh and Fozia Z. Haque (2015). The identification on the other peaks in the SASs was matched using EVA software, which represented a mineral polymorph of silicon dioxide, namely cristobalite. Cristobalite is crystalline silica, showed sharp peaks in the four SAS samples (as shown in **Figure 3.45** a) - d)) that may contaminate a small amount in the samples.

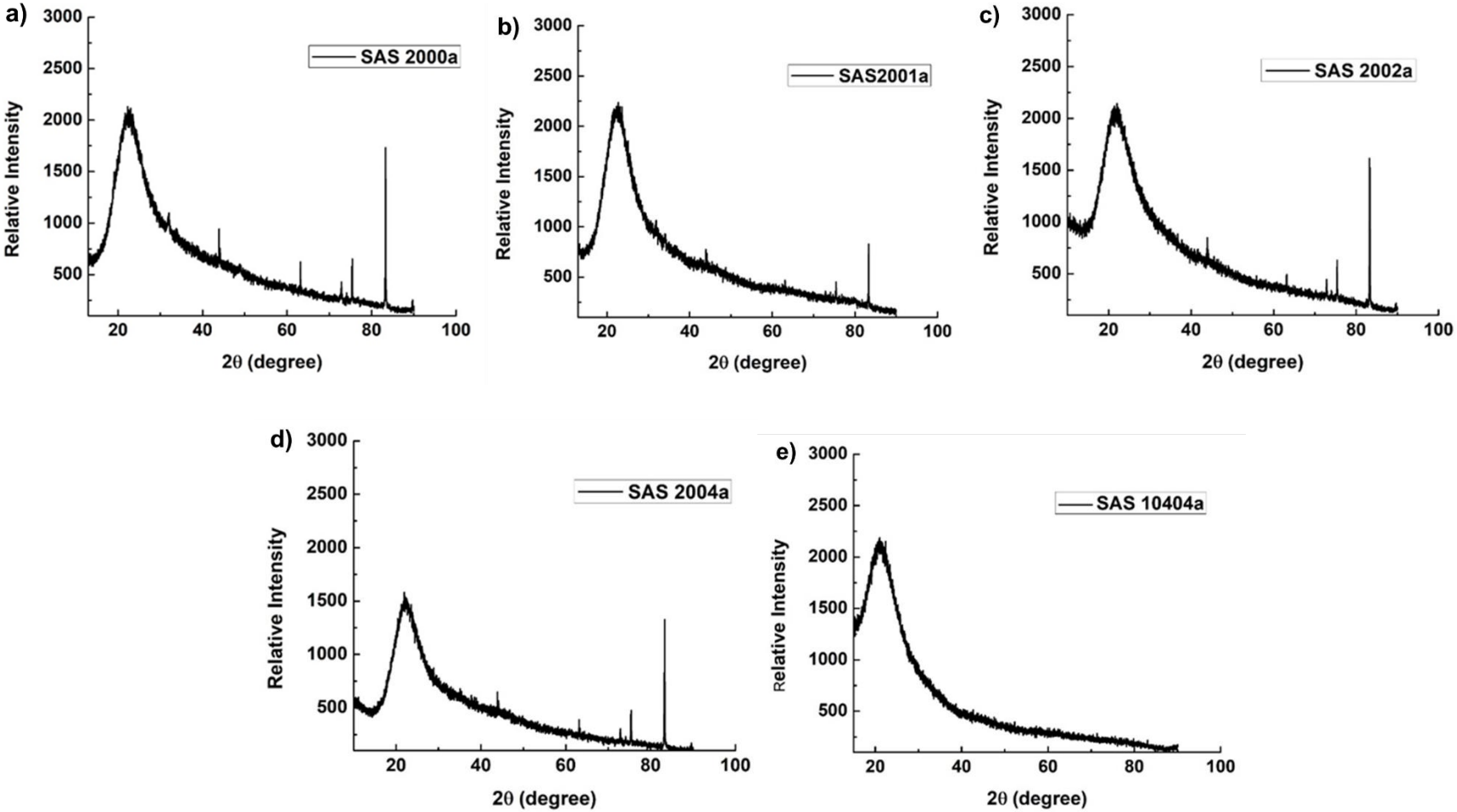


Figure 3.45: X-ray diffraction patterns of the 5 SAS studied: a) SAS2000a, b) SAS2001a, c) SAS2002a, d) SAS2004a, and e) SAS10404a.

WAXS

In WAXS, short length scale measurements enable the description of the crystallographic order, therefore, the level of crystallinity of SASs was determined using WAXS. The position and intensity of peaks in the diffraction patterns from the five SAS are shown in **Figure 3.46**.

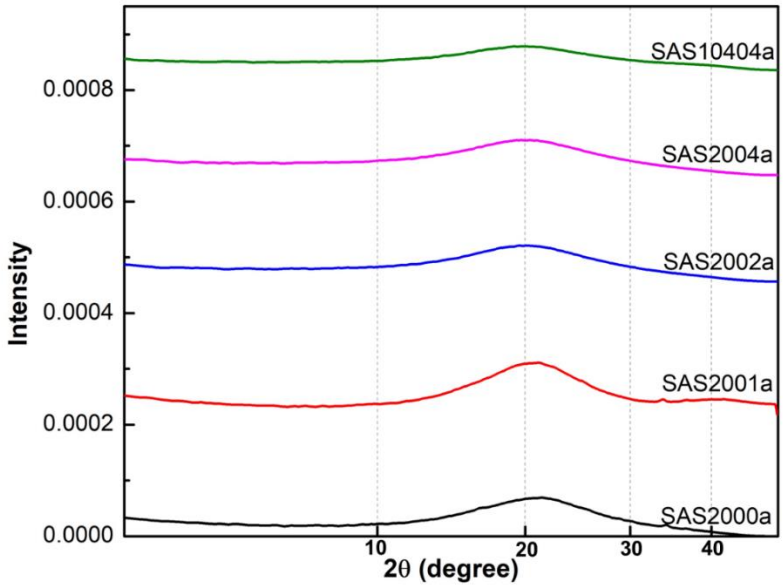


Figure 3.46: The diffraction pattern of the five SAS presenting the position and intensity of structural peaks, and indicating amorphous form of silicon dioxide.

3.8.3 Elemental compositions and oxidative state

XPS

XPS spectra of the five SASs are presented in **Figure 3.47** and **Table 3.11** provides the elemental composition in percentage for C1s, O1s, and Si2p at the surface of the samples. High resolution XPS scans in the Si2p region are shown in **Figure 3.48**. To determine the chemical structure of the Si atom, the binding energy of Si2p and O1s is measured and the details presented in **Table 3.12**.

The binding energies of Si2p and O1s are observed at 103.7 eV and 533 eV, respectively, indicating the presence of SiO_2 (silicon (IV) dioxide) in SASs (Thermo Scientific XPS, 2013) and comparing to the library reference of NIST X-ray Photoelectron Spectroscopy Database.

Table 3. 11 Information of composition obtained from XPS for the five SAS samples and presented in percentage of atomic composition.

Sample No.	Atomic Composition (%)		
	C	O	Si
SAS2000a	6.31	66.70	26.99
SAS2001a	26.49	53.83	19.68
SAS2002a	4.73	67.08	28.19
SAS2004a	23.34	56.16	20.50
SAS10404a	35.19	47.71	17.10

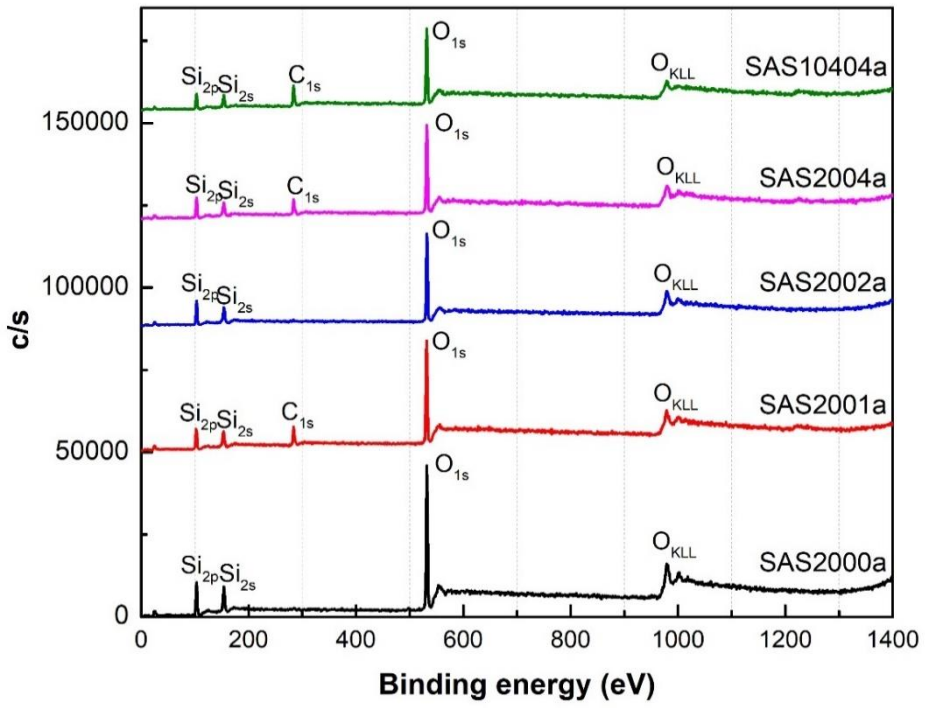


Figure 3.47: Survey spectra of the five SAS, presenting the elemental compositions found on the surface.

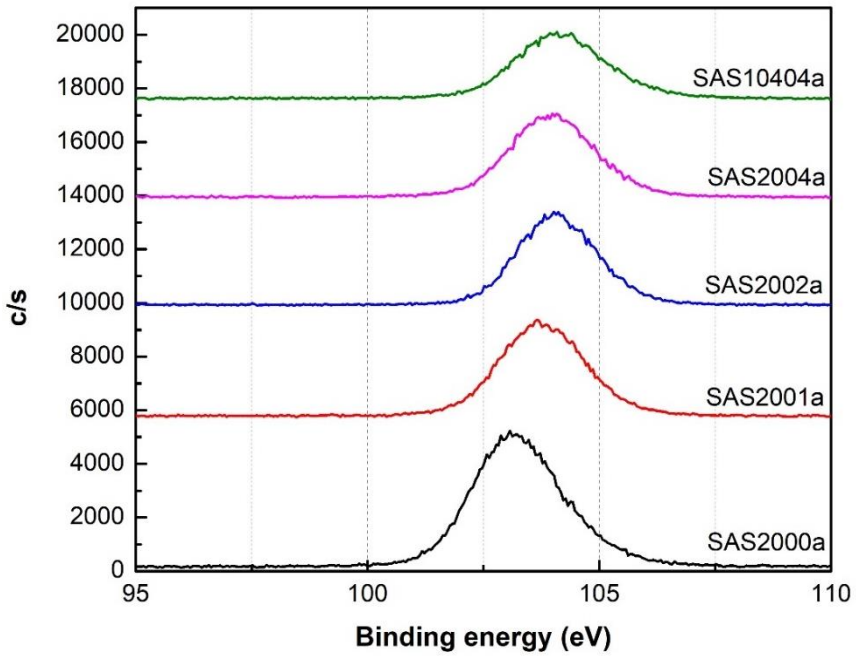


Figure 3.48: High resolution XPS scans for the Si2p region of the five SAS.

Table 3.12 Information on the binding energy of Si2p and O1s, used to determine the chemical structure on SASs' surfaces.

Sample no.	Binding Energy (eV)	
	Si2p	**O1s**
SAS2000a	103.19	532.5
SAS2001a	103.45	532.5
SAS2002a	103.77	533.18
SAS2004a	103.76	533.25
SAS10404a	103.70	533.2

XAS-EXAFS

The EXAFS spectra for the Si K-edge were normalised and compared to the standard quartz (shown in **Figure 3.49**) to determine the structure of SASs. The experiments were performed in a fluorescence mode and in transmission mode and the signals were collected by using the 13-component Ge-detector. The data were processed using the ATHENA program. As presented in **Figure 3.50**, the normalized Si*K*-edge EXAFS spectra of SASs showed the structure and oxidation state of the five samples, comparing to silicon metal and quartz. The feature of Si*K*-edge XANES and EXAFS spectra of the five SASs are similar at a relatively sharp absorption peak (1847±0.1 eV) but still have minor differences in their features, specifically. at the region of peaks D-G. The region of peaks D-G represents the distance between an atom and neighbouring atom, which use to identify elemental composition surrounding the atom and crystalline structure of materials. For example, the features of EXAFS spectra for SAS2001a and SAS2004a have a hump at the region D (see **Figure 3.50**), which is likely crystalline morphology. High thermal (>1300˚C) and rapid thermal quenching for synthesis of amorphous silica nanomaterial can induce crystalline morphology (Nel *et al.*, 2013).

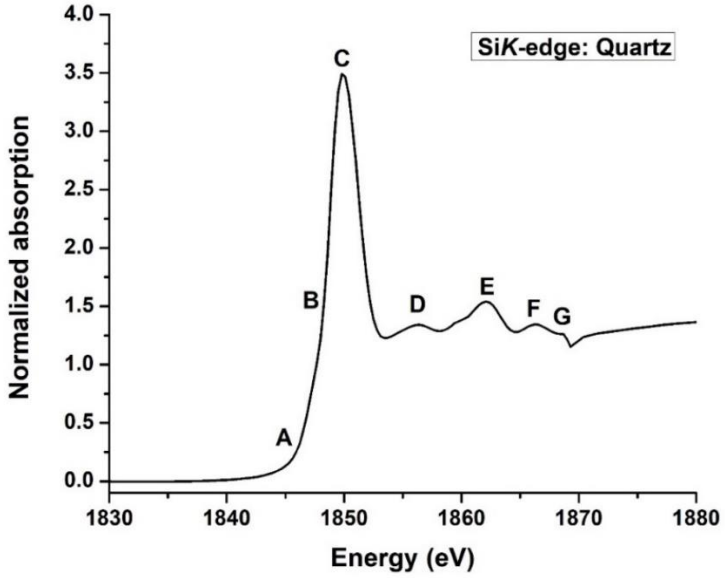


Figure 3.49: The EXAFS spectrum of standard quartz presents the pre-edge peak (A), the main transition peak (B), Si*K*-edge peak (C), peak D – G in both K-edge and L-edge corresponds to a crystal structure of quartz (Li *et al.*, 1994).

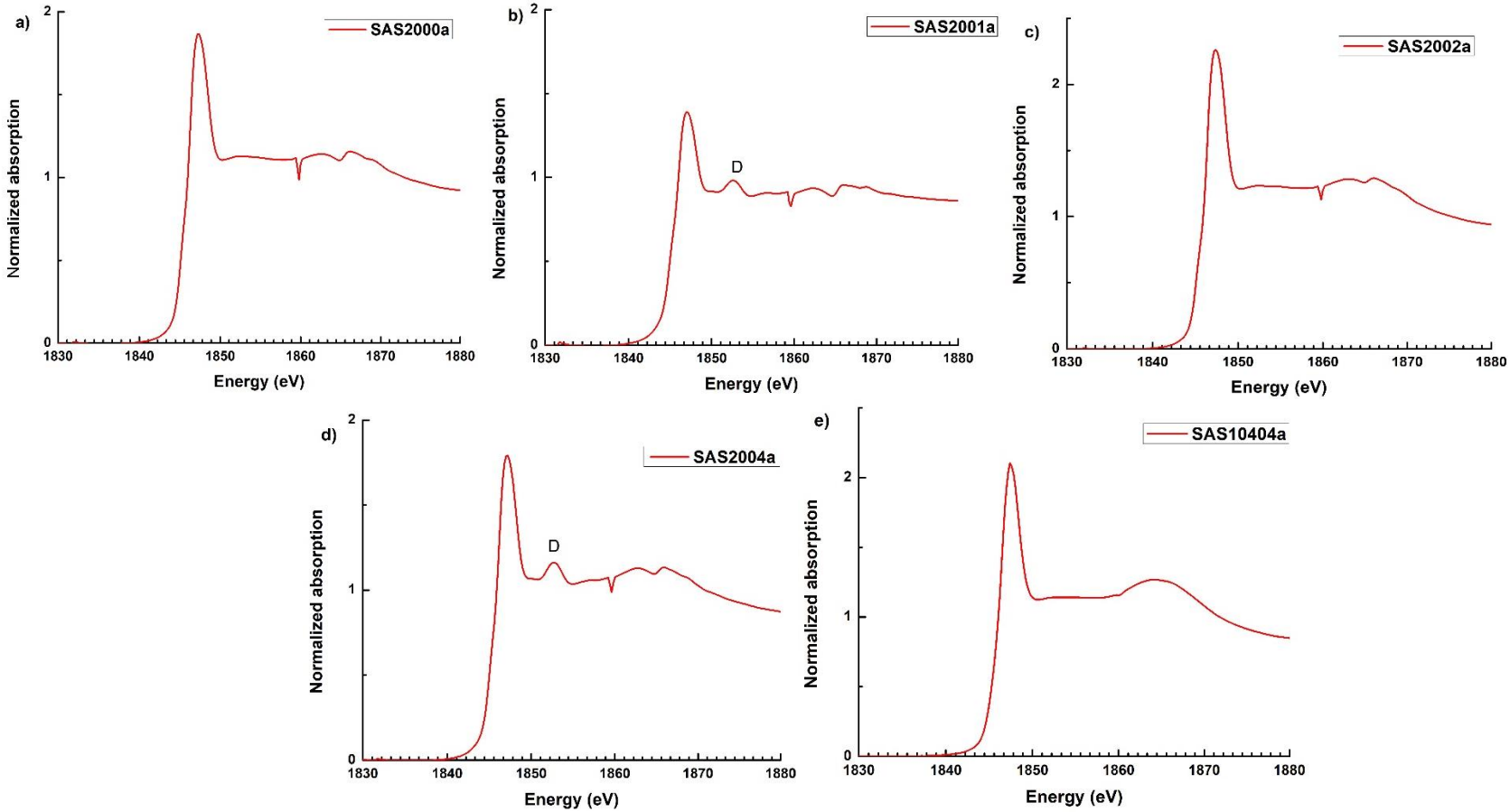


Figure 3.50: The normalized Si*K*-edge EXAFS spectra of five SASs; a) SAS2000a, b) SAS2001a, c) SAS2002a, d) SAS2004a, e) SAS10404a.

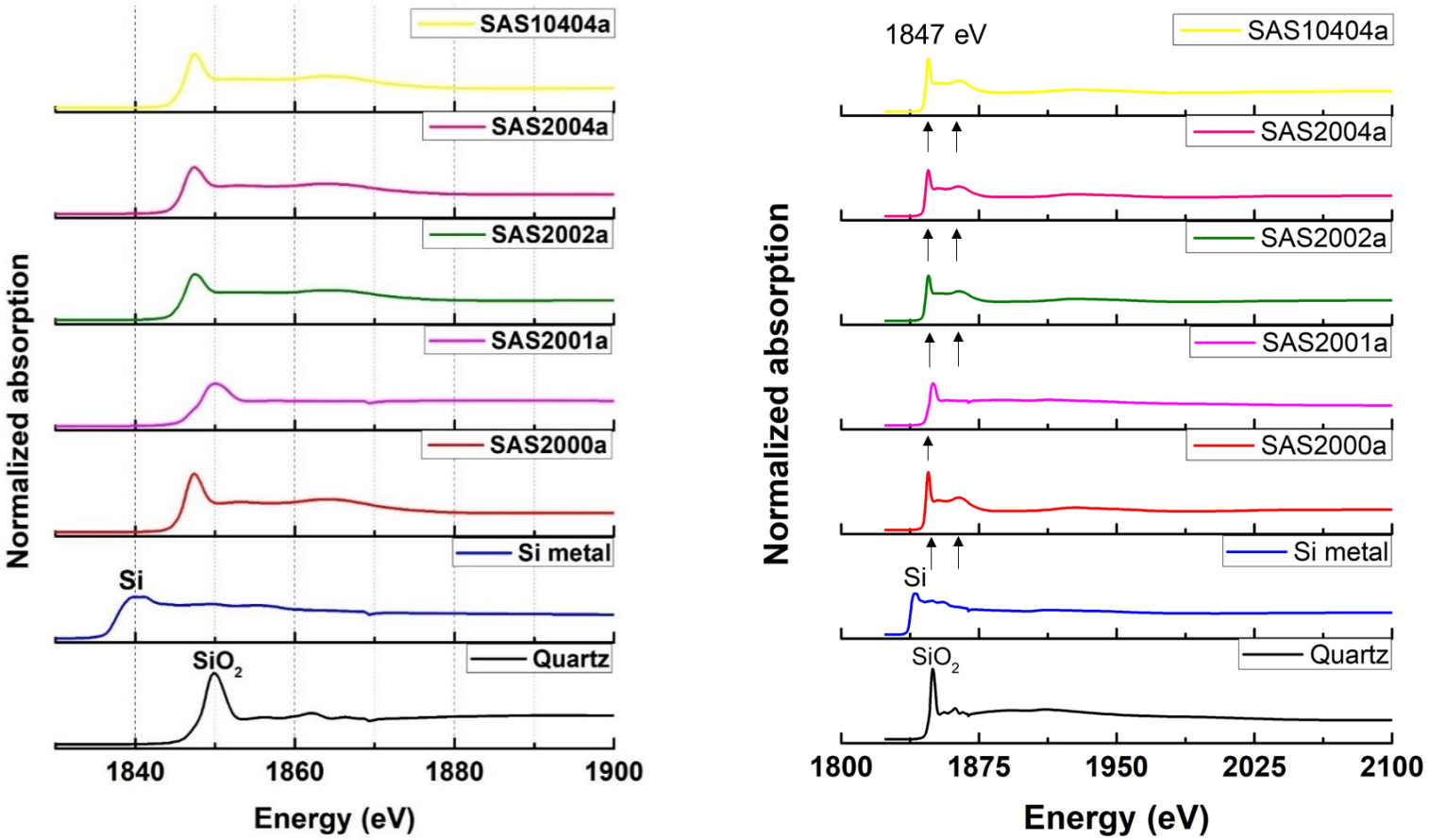


Figure 3.51: Si*K*-edge XANES (left) and EXAFS (right) spectra of SASs comparing them to silicon metal and quartz.

XAS-XANES

Si*K*-edge XANES spectra were acquired to evaluate the chemical state of the silicon found in the five SASs samples and compared with the eight cosmetic samples studied. As seen in Figure 3.52, the Si*K*-edge position (1847 eV) and the spectrum features of SAS2000a, SAS2002a, SAS2004a, SAS10404a are likely of the studied cosmetics; S1, S3, S4, S6, and S7. These results can assume that the four SASs (SAS2000a, SAS2002a, SAS2004a, SAS10404a) are possibly components contained in the studied cosmetics (S1, S3, S4, S6, and S7).

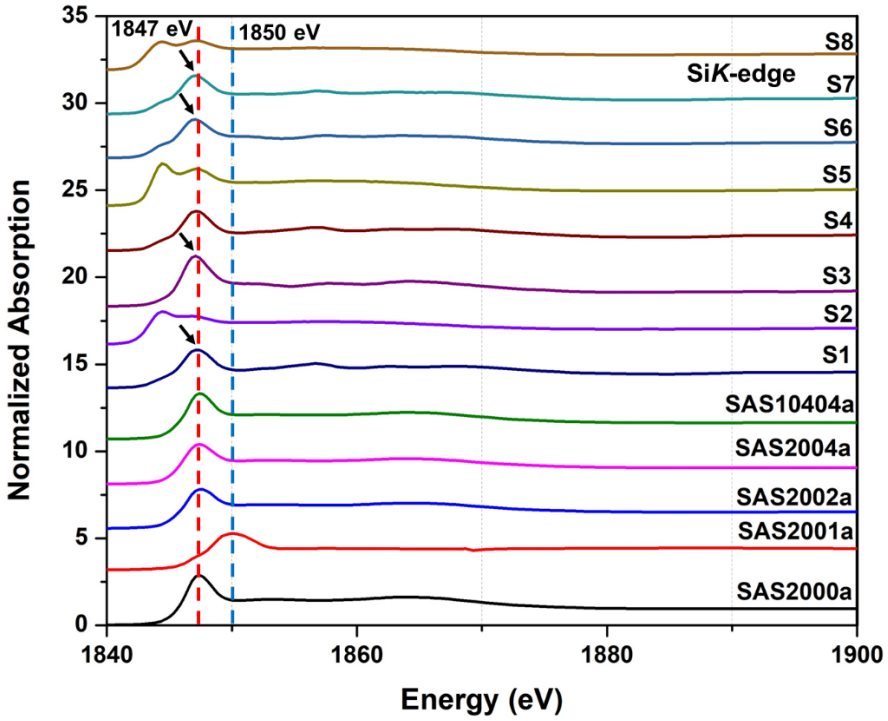


Figure 3.52: Si*K*-edge XANES spectra of SASs comparing to Si found in cosmetics.

3.8.4 Shape

SEM

SEM analysis was performed to understand the morphology of the powdered SASs. The particles were observed to be spherical in shape and organised as densely packed aggregates, as displayed in **Figure 3.53**.

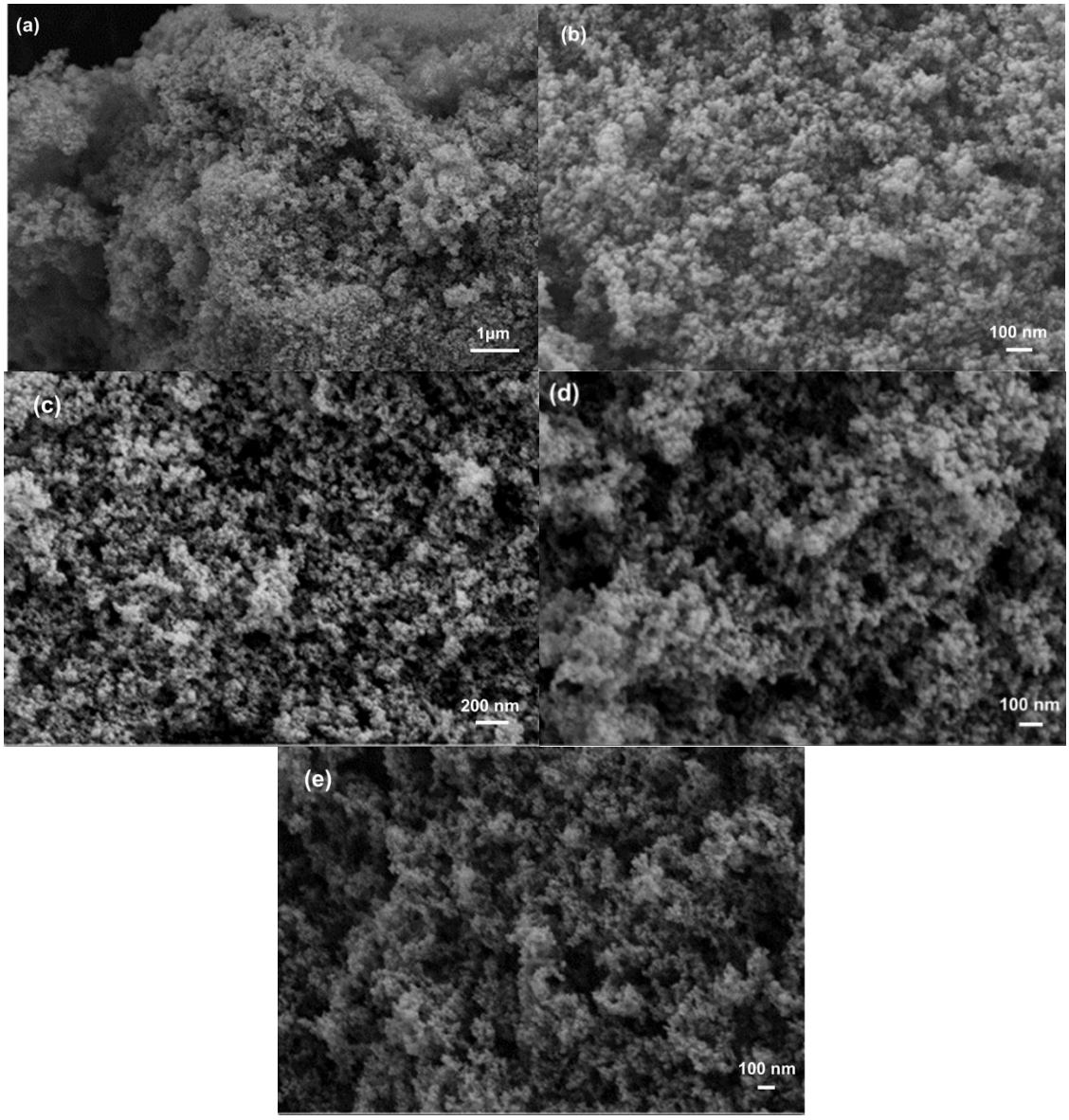


Figure 3.53: SEM images of the five SAS; (a) SAS2000a, (b) SAS2001a, (c) SAS2002a, (d) SAS2004a, (e) SAS10404a.

TEM

Representative TEM images of the five SAS showing the complex structure of SAS aggregates are given in **Figure 3.34** - **Figure 3.38**. The general morphology of the primary sub-units of the five SAS is slightly rounded. The morphology of particle aggregates is dense and complex in structure. It is noted that the image resolution does not allow identification of individual particle edges therefore it is difficult to estimate particle size accurately.

3.8.5 Surface area

BET

BET was carried out to estimate the specific surface area of dry powdered SASs on a SA 3100 Surface Area Analyzer. The samples of SASs were heated under vacuum at 300˚C for several hours to remove moisture and contaminants. SAS NMs were repeatedly measured, and the results are exhibited in **Table 3.13**. BET technique is an accurate and simple method for the surface area characterisation. The resultant particles have a similar surface area to the previous data from IMC-BAS.

Table 3.13 Surface area, C value and correlation coefficient of SASs measured by SA 3100 surface analyser.

Sample No.	Test no.	2000a	2001a	2002a	2004a	10404a
Surface area m^2/g	1	185.42	238.21	201.86	128.04	203.77
	2	185.65	240.38	203.05	129.93	203.00
	3	186.09	241.28	203.01	130.08	206.68
C value	1	116.70	112.42	81.93	68.42	91.89
	2	112.25	109.44	81.39	65.12	96.93
	3	111.75	110.07	81.53	64.29	89.33
Correlation coefficient	1	0.9999	0.9999	0.9999	0.9999	0.9999
	2	0.9999	0.9999	0.9999	0.9999	0.9999
	3	0.9999	0.9999	0.9999	0.9999	0.9999

Table 3.14 provides the mean surface areas of SASs, compared to the previous measurements by IMC- BAS. The data from the observation show small deviations from the IMC-BAS study.

Table 3.14 The comparison of the surface areas between the observations in this study and the results of IMC-BAS.

Sample no.	Surface area (m^2/g)	
	Observed	**IMC-BAS***
2000a	185.72±0.34	189.16*
2001a	239.96±1.58	140.46*
2002a	202.64±0.68	191.9871
2004a	129.35±1.14	134.3128
10404a	204.48±1.94	-

* Previous specific surface area data obtained from IMC- BAS measurement (European Centre for Ecotoxicology and Toxicology of Chemicals, 2006).

3.9 Discussion

The main properties were explored in the characterisation of NPs found in cosmetics are size, shape and chemical composition. The technique approaches can also extent evaluate size distribution, crystalline structure, atomic energy level and surface chemistry. As mentioned above, the possibility to measure the size of NPs was demonstrated using DLS. A major hurdle with DLS is the improvement of the specific NP detection or ingredient NPs in complex matrices. Besides, the extracted commercial cosmetics cannot be carried out by SAXS which may be sensitive to complex matrices. As cosmetic compositions are diverse and complex relative to the difficulties of the sample preparation, analysis, and data interpretation. The extraction procedure to ensemble of samples needs

to be addressed for successful SAXS measurement. However, SEM-EDS, XRD, XPS and XAS (XANES-EXAFS) techniques were not only provided results in a good agreement but obtained a wide range of their properties. A systematic measurement method in complex materials would be especially credible and robust, therefore combining tools at least two techniques should be applied to characterise the properties. In this case, XRD is a suitable tool for unknown materials combining to XPS that probes quantitative and qualitative compositions whilst XAS possible contributes the abundance of these properties at once. The evaluation of available characteristic methods was described about the uses, advantage, and limitation in **Table 3.15**.

Table 3.15 Summary of a set of techniques used for the characterisation of NPs in cosmetics.

Technique	Methods	Main information	Advantage	Limitation/Problem
Light scattering	**DLS**	Hydrodynamic diameter Particle size distribution PDI of colloidal suspension Zeta potential	Simple and fast size measurement. Accurate results are influenced by dispersibility including size distribution and zeta potential.	- Limited ratio quantitative elemental composition of colloidal suspension - Inability to distinguish mixtures or complex matrices, sensitive to large sizes.
Electron microscopy	**SEM-EDX**	Quantitative and qualitative elemental composition Single particle resolution	Information on elemental composition and 2D image.	Limited penetration depth into dried sample
X-ray (synchrotron source)	**SAXS**	- Primary particle - Agglomeration/Aggregation	SAXS can provide all these information at once.	- Difficult to interpret. Must know background of sample before analysis..

Technique	Methods	Main information	Advantage	Limitation/Problem
		- Surface topology (size, shape, roughness)		- Nanomaterials from complex matrices should be required to treatment properly before quantification.
	XPS	- Elemental composition - The oxidation state identification - The binding energy of electronic states	- Qualitative and quantitative elemental composition on surface (1-10 nm).	- High energy beams can destruct sample during analysis - Considerable errors in analysing chemically heterogeneous
	XAS (EXAFS/XANES)	- Atomic energy level and electronic structure of materials	- All data can be obtained at once.	- Time consuming - Sensitivity to the thickness of samples

Technique	Methods	Main information	Advantage	Limitation/Problem
		- The oxidative state of identification and structure	- Determine solids, liquids, and very dilute samples	which relates to the absorption energy. - Difficult to proceed and interpret data
	XRD	Crystallographic information	Rapid, provides information on crystal structure	Results in peak overlaps leading to mismatch interpretation

3.10 Conclusions

The analysis using XRD, XAS-XANES/EXAFS, XPS and SEM-EDS techniques provided significant information of elemental composition, crystalline phases and structural material of the eight cosmetics and the five SASs. Multiple analytical methods highlighted the correlation and complementary support with each technique to complete the interpretation and to give a better understanding of the materials used. The presence of elemental components, i.e., silica, titanium dioxide, and other materials was successfully confirmed using XRD, XAS, XPS and SEM-EDS. Additionally, the proportion of the material components can be exhibited in the percentage of atom composition by XPS measurement, hence confirming the presence of C, O, Fe, Mg, Ca, K, Ti, and Si in the eight cosmetics relevant to their ingredients on labels. However, some were not appropriate for the detection of NPs in the complex formulations of commercial cosmetics. Especially, SAXS has limited suitability for characterising primary particle size in multimodal and complex samples. By contrast, DLS can identify the particle size of the particles contained in these samples but cannot confirm what proportion is silica. Some limits may arise from an unsuitable treatment procedure prior to the measurement.

The commercial cosmetic characterisation was achieved by means of various techniques included DLS, SEM-EDX, XRD, XPS and XAS. DLS results confirmed the presence of NP in the matrices whilst SAXS was limitations to examine a primary particle and other properties. Furthermore, using SEM-EDX, XRD, XPS, and XAS showed reliable and repeatable results of their elemental compositions

and semi-quantitative data. The multi-technique uses can attribute to increasing the quality of information.

For the SAS analysis, SAXS data of primary particles showed quite large particles and some aggregates, and the SEM and TEM images also provided evidence of the aggregation in the SAS dispersions. Through the XRD method, the diffraction patterns of the four SAS samples (SAS2000a, SAS2001a, SAS2002a, SAS2004a) showed some sharp peaks, indicating a crystalline phase, along with amorphous silica in the four SASs and matching with the crystal planes of cristobalite. Notably, crystalline silica (quartz or cristobalite) is apparently a human carcinogen.

The characterisation results for the five SAS emphasise the need for testing of silica that may be found in cosmetics as their properties may enable them to undergo skin penetration and induce toxicity to human skin.

Having characterised the SASs in cosmetics, it was decided that for the rest of the thesis, lab synthesised aSiNPs would be used. aSiNPs were synthesised using the sol- gel process with L- lysine in order to obtain small particles for assessment of *in vitro* skin penetration and skin irritation. The synthesis and characterisation are presented in Chapter 4, and the interactions with the skin models are presented in Chapter 5 and 6.

Chapter 4 Synthesis and Characterisation of Silica Nanoparticles

4.1 Introduction

Nowadays there are many of amorphous silica nanoparticles (aSiNPs) that can be produced and launched in the global market. aSiNPs are produced directly in the powder form by removing the solvents, i.e., water, ethanol from the gel structure. The common procedure can keep NPs in the same state. In fact, this step leads NPs to aggregate in a few seconds through a solid bridging mechanism. Aggregates may affect entire properties of NMs. A particle size-tuneable for the large-scale synthesis of nanoparticles, therefore, has been uncontrollable involving their interactions determine nanoparticle formation and characteristics. This problem mainly exists in the commercial standards of silica nanomaterials that used in this study. As a result, a considerable application of synthesis techniques is desired to produce in the laboratory. Numerous techniques have been published on the synthesis of silica nanoparticles, which can be grouped under two main processes, which are based on hydrolysis and condensation, namely the *Stöber* method and the sol-gel process (Stöber, Fink and Bohn, 1968; Bogush, Tracy and Zukoski IV, 1988; Bowan and Peppas, 1991; Davis *et al.*, 2006; Lin, Abadeer and Haynes, 2011). Moreover, siloxane (Si-O-Si) bonds are formed by polymerisation during a water-producing condensation reaction. Interestingly, amorphous silica nanoparticles (aSiNPs) are prepared by the sol-gel process have hydrophilic surfaces which makes them biocompatible with proteins; they also have tuneable particle size under

various temperatures; hence, this synthesis method has attracted significant interest in biological research. In addition, synthetic aSiNPs in the form of dispersion can prevent inter-particle interaction to form agglomeration.

This approach has been challenged to achieve amorphous silica nanoparticle using sol-gel process that provides consistency in terms of size, structure, stability and chemistry for uniform evaluation and application. These is essential to ensure obtaining the high quality of NPs, repeatable and meaningful results for research purposes.

This chapter presents the method of synthesis of aSiNPs, and details the techniques and methods used for physicochemical characterisation of aSiNPs. Routine analytical methods and synchrotron-based techniques provide the extensive description of the NMs. This physicochemical information will be further discussed in Chapters 5 and 6.

aSiNPs were synthesized using tetraethyl orthosilicate (TEOS) and L-lysine as a precursor and catalytic agent, respectively. This synthesis process yielded stable, monodisperse nanoparticles, and physicochemical characterisation were done by using multiple techniques: DLS, TEM, STEM, SAXS, XRD, FT-IR, XAS, and XPS. The manuscript describing the results has been published (Musigapong *et al.*, 2019). The finding from other techniques and details of characterisation by SAXS (ageing aSiNPs), DLS (particle stability), SEM, XANES, BET and ICP-OES are extended beyond what was presented in the paper we completed (as shown in the following section).

4.2 Chemical and Materials

The chemicals and materials purchased from suppliers are shown in **Table 4.1**. Ultrapure water (UPW) was steam sterilized in the oven at 121°C, 15 min before use in the synthesis process, following a literature study (Thomassen *et al.*, 2010).

Table 4.1 Chemicals and materials used

Chemical/Material	Details	Brand
Tetraethyl Orthosilicate	Reagent grade, 98%w/w	Fisher
L**(+)-**Lysine monohydrate	Reagent grade, 99%	Sigma Aldrich
Nitrogen gas	High purity grade	BOC
EMD Millipore ultracel™ Ultrafiltration DiscGSA/ VA	Diameter 76 mm, filtration area 41.8 cm^2, MWCO 1kDa	Fisher
EMD Millipore Amicon™ Bioseparations Stirred Cells	Size 400 mL	Fisher

4.3 Glassware

UPW with 10% nitric acid (HNO_3) was used to wash the glassware and to remove any particles. The glassware was then rinsed three times with only UPW to ensure no traces of acid remained. Then, all glassware was steam sterilized at 121˚C.

4.4 Synthesis of amorphous silica nanoparticles

4.4.1 Sample Preparation

aSiNPs were synthesised according to the studies of Davis *et al.* (2006) and Thomassen *et al.* (2010). In general, the synthesis of aSiNPs involved the use

of standard reactants as in Stöber, Fink and Bohn. (1968). More specifically, three components were mixed in precise proportions: water, tetraethyl orthosilicate (TEOS; $Si(OC_2H_5)_4$) and L-Lysine monohydrate ($C_6H_{14}N_2O_2$). The mass ratio of the three components was: 205:29.67:1.02 g. Quantities and volumes of the reactants used are shown in

Table 4.2. The process involves hydrolysis and condensation of a metal precursor (TEOS). L-lysine acts as a catalyst leading to the formation of organic complex (RO-Si-OH) bonding (refers to equation **(4.1)**) and plays the role of a capping agent for limiting particle growth. 205 mL of ultrapure water was poured in a round bottom flask (**Figure 4.2**) and 1.02 g of L-lysine monohydrate was added during constant magnetic stirring of the solution, at 400 rpm for 1 hour or until a clear solution without bubbles was obtained. The entire experiment was carried in a laminar flow hood. After equilibration was achieved, the prescribed amount of TEOS (31.9 mL) was added in the former solution and then stirring was carried on for 5 days in order to complete the reaction. At the end of the experiment, ultrafiltration was used to purify and remove any impurities and low molecular weight substance, e.g., L-lysine, through a permeable membrane while colloids (particles) are retained. This synthesis and ultrafiltration procedure with 300 mL of UPW at low pressures of N_2 gas was carried out three times. The pH values of the final solution were measured and were found to be in the range of 9-10 as shown in

Table 4.3 (Davis, 2007; Thomassen *et al.*, 2010).

Table 4.2 Amount of chemicals used for the synthesis of aSiNPs

Amorphous silica nanoparticle		
List of chemicals	**Amount used**	**Unit**
Ultrapure water	205	mL
TEOS **(**98**%)**	31**.**9	mL
L**-**Lysine monohydrate	1**.**02	G

Table 4.3 pH and conductivity value of aSiNP suspensions

Process	**pH value**	**Conductivity (µS/cm)**
Hydrolysis reaction	9.14±0.01	3.83±0.21
After purification	9.06±0.05	4.63±0.31

4.4.2 Reaction Mechanism

The overall reactions of TEOS and L-lysine via the sol-gel process (Powers *et al.*, 2006) can be seen in **Figure 4.1**, and are described in three reactions as shown in the equation series of reaction **(4.1)**:

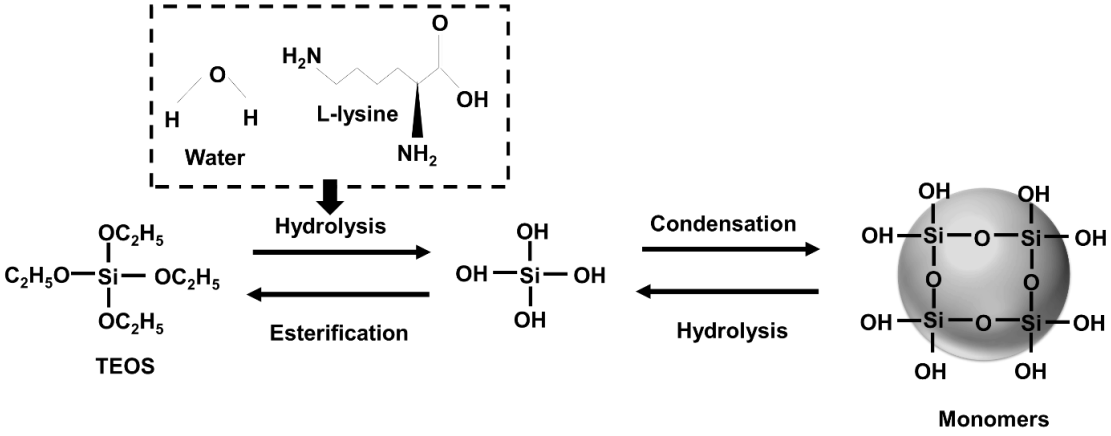


Figure 4.1: Depiction of the overall basic reactions in the sol-gel process, forming amorphous silica nanoparticles**.**

Equation series of the reaction

$$\equiv Si - (OC_2H_5)_4 + H_2O \underset{\text{esterification}}{\overset{\text{hydrolysis}}{\rightleftharpoons}} \equiv Si - OH + C_2H_5OH \qquad (4.1)$$

$$\equiv Si - OC_2H_5 + HO - Si \equiv \underset{\text{alcoholysis}}{\overset{\text{alcohol condensation}}{\rightleftharpoons}} \equiv Si - O - Si \equiv + C_2H_5OH$$

$$\equiv Si - OH + HO - Si \equiv \underset{\text{hydrolysis}}{\overset{\text{water condensation}}{\rightleftharpoons}} \equiv Si - O - Si \equiv + H_2O$$

The hydrolysis reaction leads to the formation of TEOS monomer [$Si(OC_2H_5)_3OH$] and a condensed intermediate to eventually form silica. The final solution is colourless. The preparation steps for the synthesis is depicted in **Figure 4.2** and **Figure 4.3**.

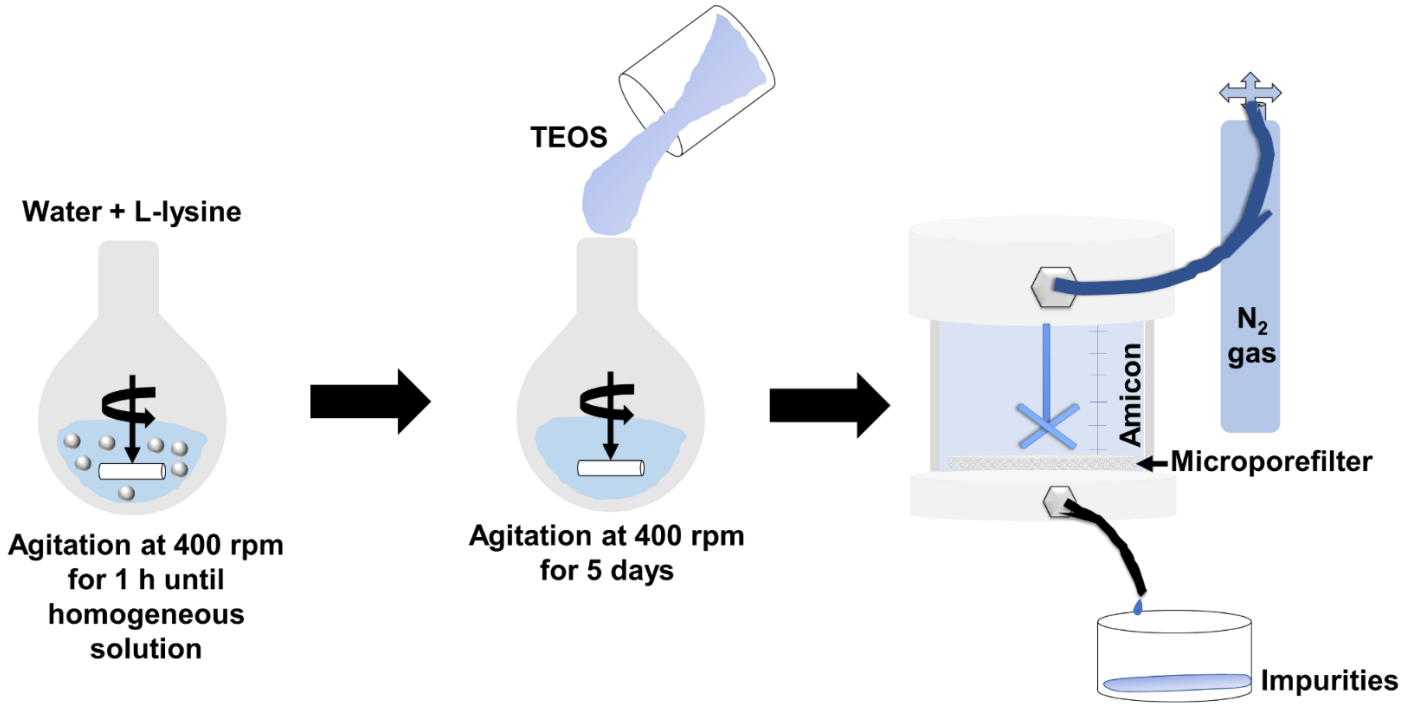


Figure 4.2: A picture of the synthesis procedure**:** the mixture solution is prepared from water and L**-**lysine to be homogeneous by agitation for 1 hour, then TEOS is added in the system and afterwards the filtration process takes place**:** the suspension is pumped through a micropore filter **(**MWCO 1 kDa**)**, placed tangential flow to enable the separation of particles from impurities; the former is retained, whereas the latter goes through the permeable membrane**.**

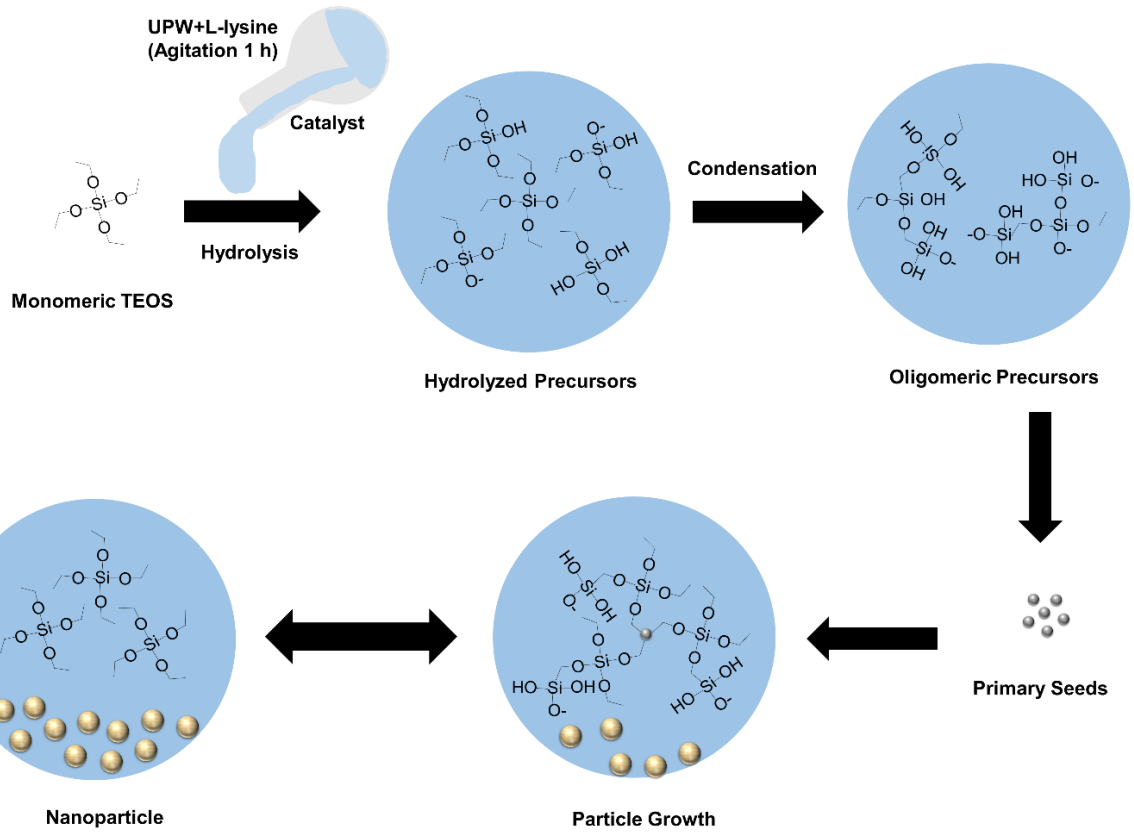


Figure 4.3: Mechanism of aSiNP nucleation by addition of water and L-lysine as a precursor and catalyst. TEOS was hydrolysed to all possible derivatives and then condensed to form oligomeric precursors and primary seeds. The formation of primary seeds contributes to particle growth (Dixit *et al.*, 2016).

4.5 Characterisation

The synthesised aSiNPs, as described in section 4. 4, were extensively characterised using various physical and chemical techniques. The techniques used and the parameters measured are shown in **Table 4. 4**. The work presented here has provided highly advanced characterisation details of synthesised silica (size 2 nm) using L-lysine as a precursor, which was not available in the literature. Information, such as functional groups, element, oxidation states and structure have been published previously (Musigapong *et al.*, 2019). Here, in addition to standard laboratory characterisation, work is also presented on advanced characterisation information involving synchrotron radiation, and specifically SAXS, XPS and XAS-EXAFS and XANES, which were conducted for the synthesised aSiNPs.

Table 4.4 The experimental techniques used for characterisation of aSiNP.

No.	Technique	Parameters assessed section show
1	Dynamic Light Scattering (DLS)	Size and zeta potential
2	Transmission Electron Microscopy (TEM)	Size and shape
3	Scanning Transmission Electron Microscopy (STEM)	Size and shape
4	Small angle X-ray Scattering (SAXS)	Size, shape and surface texture
5	Scanning Electron Microscopy (SEM)	Shape
6	Powder X-ray Diffraction (XRD)	Structure
7	BET surface area analyser	Surface area

No.	Technique	Parameters assessed section show
8	X-ray Photoelectron Spectroscopy (XPS)	Atomic composition, atomic percentage values and element ratios
9	X-ray Absorption Near-Edge Spectroscopy (XANES)	Elemental composition and oxidation state
10	Extended X-ray absorption fine Structure Spectroscopy (EXAFS)	Local atomic structure
11	Inductively Coupled Plasma-Optical Emission Spectroscopy (ICP-OES)	Elemental concentration

4.6 Characterisation of Physicochemical Properties

In order to investigate an achievement of NP synthesis, the properties of aSiNPs, such as particle size, zeta potential, shape, crystalline structure, elemental surface composition, oxidation state, and concentration were carried out in this section. Regarding particle size, it is important for explaining the fate, behaviour, toxicological properties and some changes from the bulk material. The particle size also influences the kinetics of internalisation and biodistribution in the organism and the environment as highlighted in Chapter 1. Furthermore, nanoparticles can cross body's natural defence barriers (e.g. skin barrier) resulting in prolonged circulation in blood. Synthesising homogeneous NPs; especially in size is essential to improve sample quality, and to ensure consistency in biological experiments. Shape and structure of nanoparticles influence the fate in biological systems, i.e. uptake mechanism and uptake by cell types and their interactions (Albanese, Tang and Chan, 2012; Truong *et al.*, 2015). The shape of aSiNPs was determined from images

obtained by using TEM, STEM, SEM, and the scattering patterns by means of SAXS technique. Moreover, SAXS and XRD were used to examine the structure, surface topography, and crystallinity of synthesised aSiNPs. The zeta potential is used for determining the overall charge of aSiNPs on surface and helps to deduce the stability of aSiNP dispersions.

The aSiNPs were analysed for elemental composition using XPS and XAS-EXAFS. FT-IR was implemented to determine the presence of functional bonding. The chemical composition of the synthesised aSiNP was helped establish sample purity. Additionally, ICP-OES was used to obtain the concentration of synthesised aSiNP dispersion and its result was used to calculate the percentage yield.

For this work, it was therefore decided to provide the comprehensive characterisation list of **Table 4.4**. The following sections describe the results from each technique.

4.6.1 Particle size

DLS

DLS measurements were performed to evaluate the particle size and size distribution of aSiNP dispersion produced following the procedure described earlier and without any further processing (i.e. no sonication). The hydrodynamic diameter and size distribution were obtained from six measurements of the same sample of aSiNP dispersions. **Table 4.5** shows the hydrodynamic diameter, Z-average and PDI values. **Figure 4.4** shows the particle size distribution graphs obtained from the original three different synthesis batches, which were not sonicated. To break some aggregates, the

sonication was employed 10 minutes prior to measurement, the particle size distribution graph was shown in **Figure 4.5**. According to DLS results, aSiNPs had a narrow size distribution peak and polydispersity (PDI) showed a good range indicating that the samples are suitable for analysis by this technique. The presence of particle size range of the samples (2.2-2.679 nm) is similar to Thomassen *et al.* (2010) that showed 2 nm using DLS measurements. Although DLS results indicate a size range between 2 and 10 nm, it is possible that more than one size populations exist in this narrow size range that cannot be resolved by DLS.

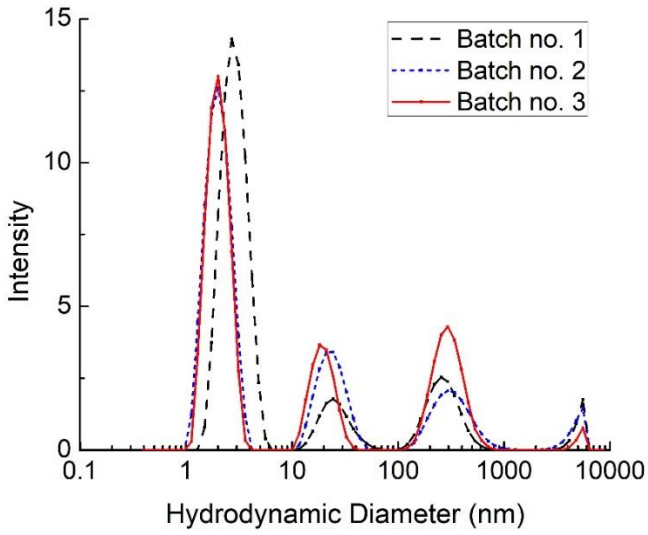


Figure 4.4: Particle size distribution of the original aSiNPs, showed some aggregate peaks.

Table 4.5 The hydrodynamic diameter, Z-average and PDI of aSiNPs using DLS method

Batch no.	Size (nm)	Z-average (d.nm)	PdI
1	2.679±0.869	3.814	0.251
2	2.616±0.856	4.233	0.273
3	2.200±0.643	5.523	0.346

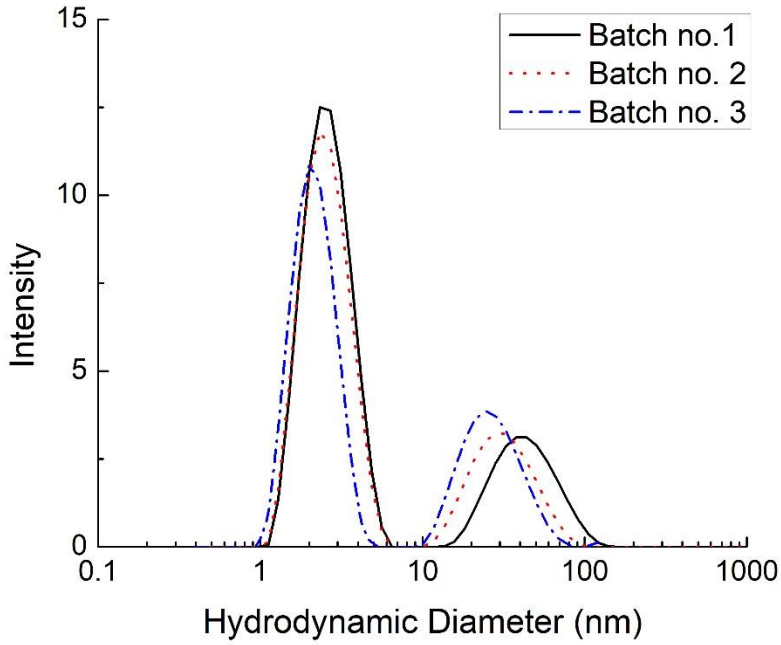
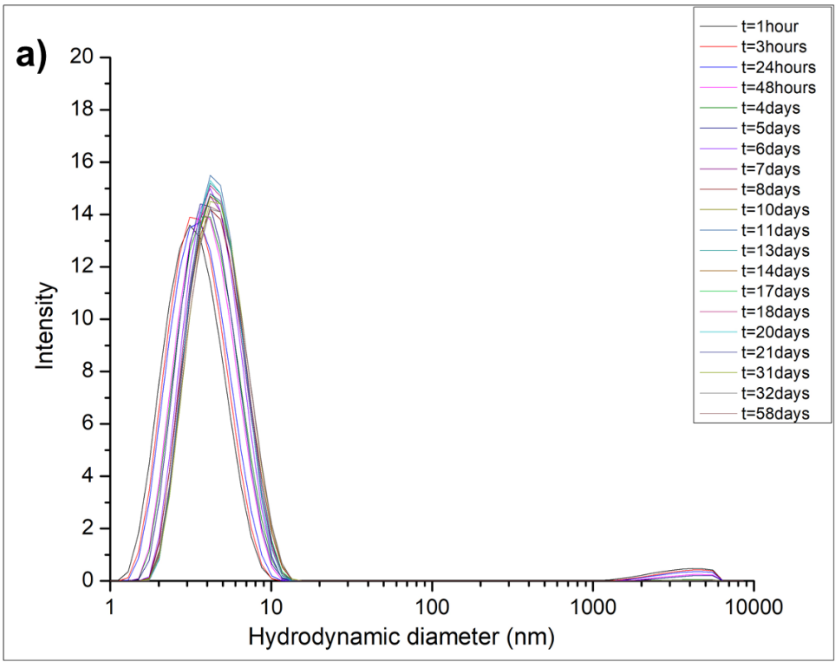


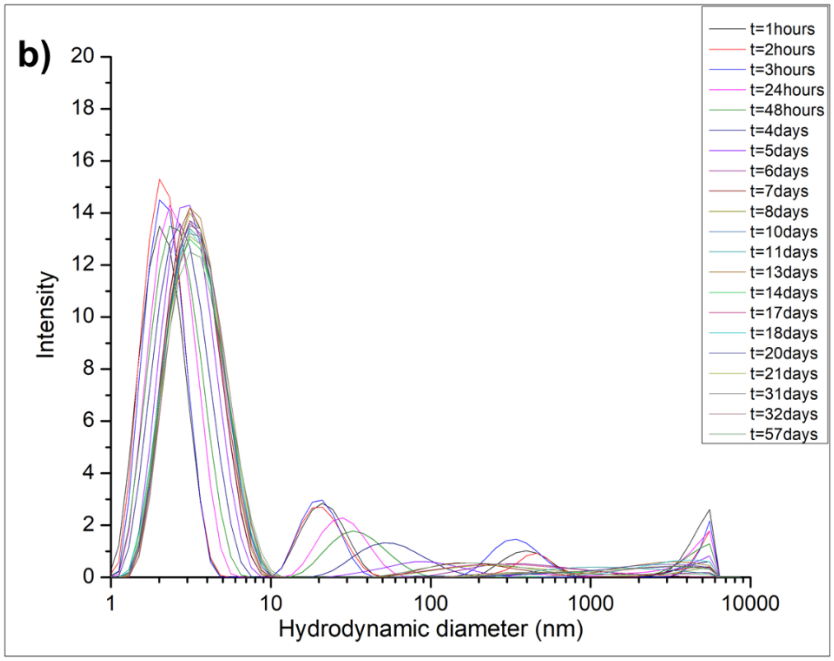
Figure 4.5: Particle size distribution of aSiNPs, sonicated the sample 10 minutes to reduce aggregation.

Monitoring of particle size change

Bare aSiNPs were prepared through hydrolysis and condensation reactions. The stability of the aSiNP suspension in ultrapure water at room temperature was checked for 1hr, 3 hrs and 24 hrs and thereafter till 58 days and the particle size and size distribution was measured using DLS. **Figure 4.6** a) - c) showed a slight increase in average hydrodynamic diameter between 0 hr and 58 days. The data presented in **Figure 4.6** (a) showed the bimodal distribution and the average size represented aSiNP batch no.1 was 3.536 (96.6%) with PdI 0.194. Whereas graph (b) showed the multiple distributions and the average size represented aSiNP batch no. 2 was 3.569 (93.9%) with PdI 0.218, and graph (c) showed the trimodal distribution with the average size of 3.461 (96.3%) and PdI 0.198. The observed small size change of all batches suggested that aSiNPs were stable over the time points. Regarding the larger size peaks,

aSiNPs are likely to have undergone some aggregations, since they were not sonicated prior to the measurements, with hydrogen bonding stabilising the larger aggregates.





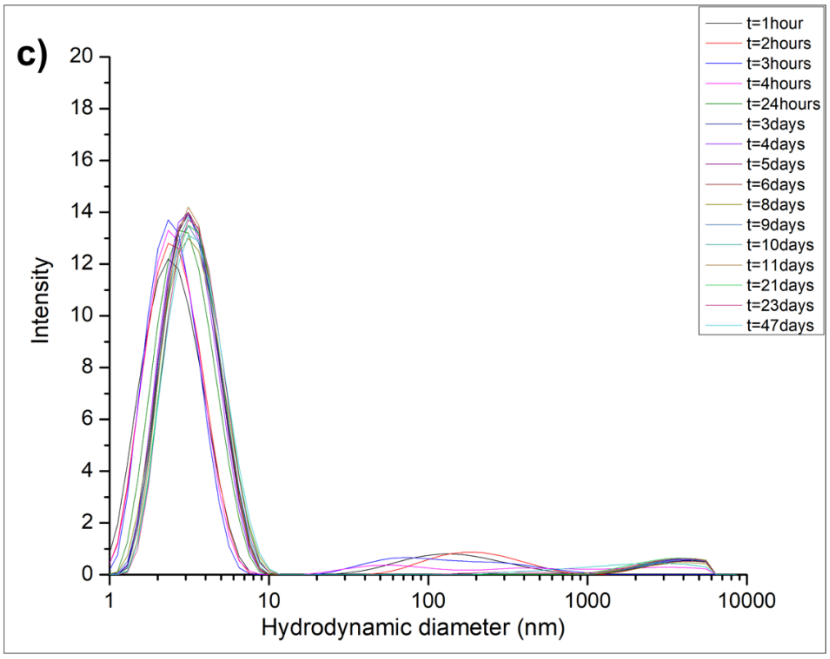


Figure 4.6: a), b), and c) Size distribution for aSiNPs batch number 1, 2, and 3, exposed to room temperature (20-24˚C) as various time points.

The zeta potential is used for determining the overall charge of aSiNPs and helps to deduce the stability of aSiNP dispersions. The results of the average zeta potential values, standard deviation (SD) and other relevant parameters are detailed in **Table 4.6**.

Table 4.6 The average zeta potential values and standard deviation for the samples of aSiNPs.

Samples of aSiNP dispersion	Average Zeta Potential ± SD (mV)	Mobility (μmcm/Vs)	Conductivity mS/cm
Batch 1	-31.8±2.45	-2.259±0.17	0.313±0.01
Batch 2	-33.0±1.11	-2.342±0.08	0.316±0.01
Batch 3	-43.5±9.52	-3.083±0.67	0.324±0.002

The average zeta potential values obtained for all batches of aSiNPs were over -30 mV indicating that aSiNPs were stable (higher charge, higher stability) (Dey, Kumar and Samantaray, 2017). Additionally, the presence of amine group (N-H) associated with the charged silica species in the aSiNPs suspension and can lead to larger particle stabilization.

TEM

Size and size distribution of aSiNPs were determined by using TEM. TEM grids were prepared by precipitation technique. TEM images showed a monodisperse of aSiNPs with the average particle size 16.43±4.21nm (as shown in **Figure 4.7** (A-C)). The aggregation seen on TEM images could have occurred during sample preparation as the samples were left to air dry on grids. It is noted that the image resolution does not allow identification of individual particle edges and therefore it is difficult to estimate particle size accurately. The TEM data are therefore only shown for completeness and are not considered as reliable as some of the other methods discussed next.

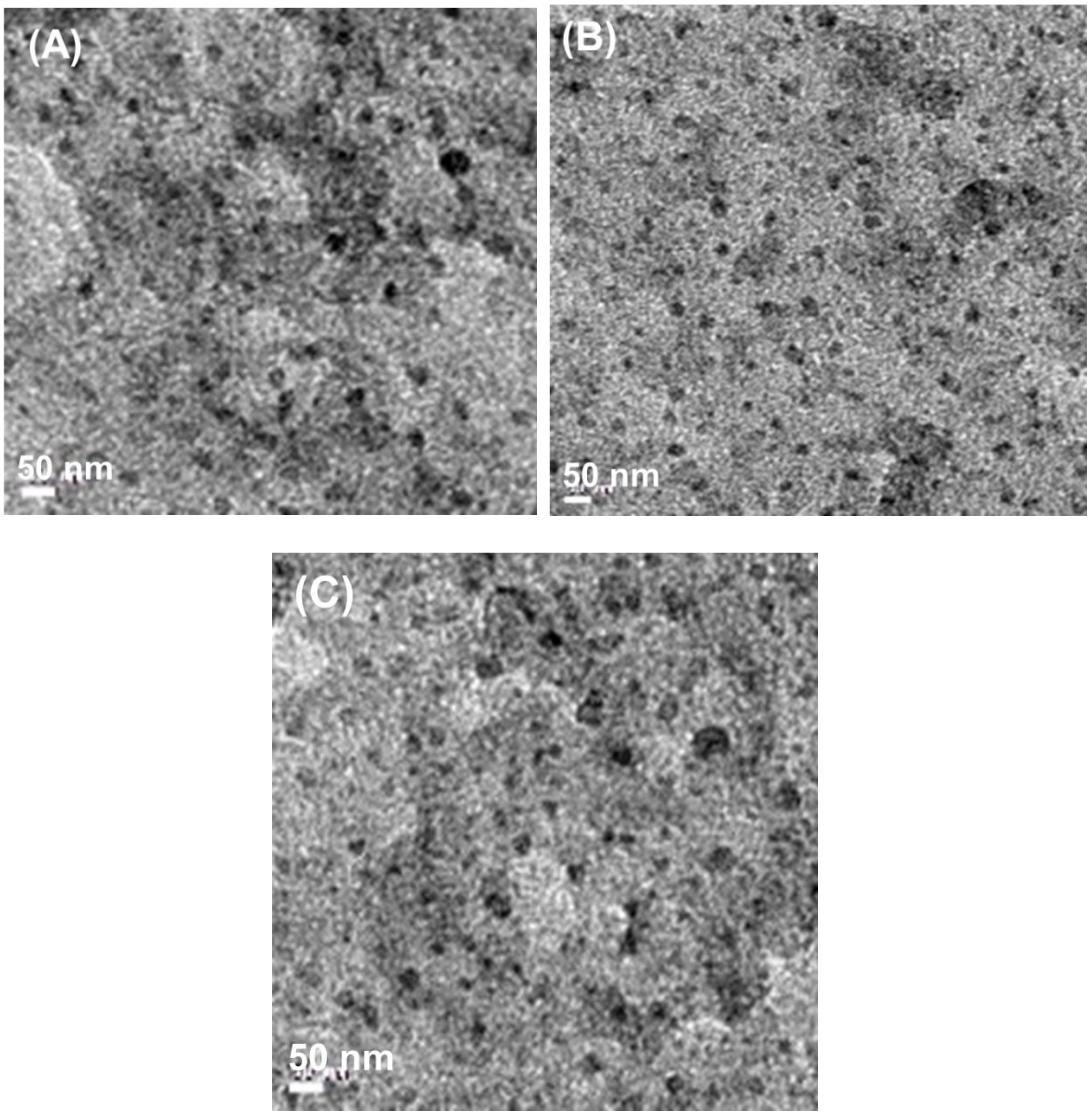


Figure 4.7: Representative TEM images [(A) - (C)] of the synthesised silica nanoparticles; scale bar 50 nm.

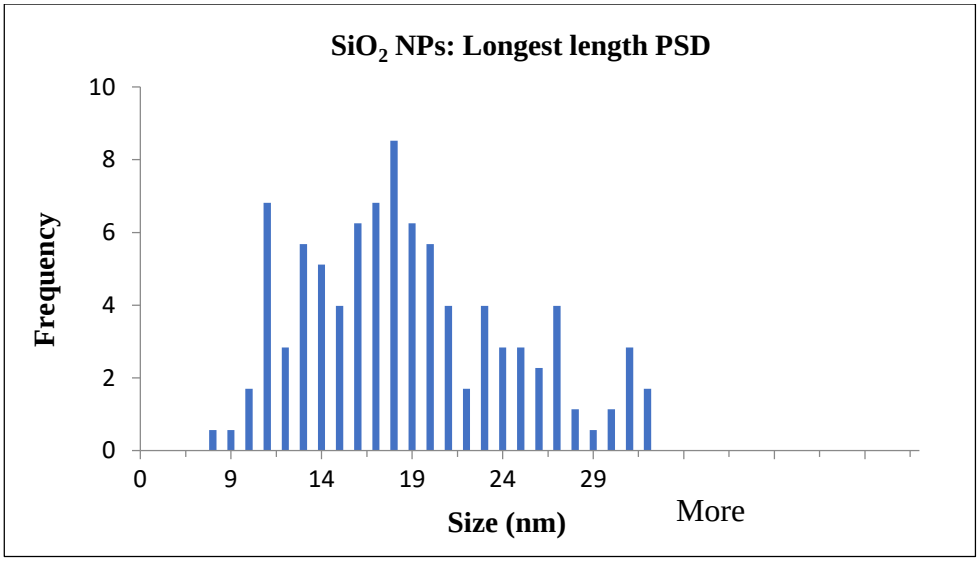


Figure 4.8: Histogram depicting size (nm) versus frequency for aSiNP suspension.

STEM

Size measurement of aSiNPs was also carried out by using a scanning transmission electron microscope (STEM). This technique has provided higher resolution and smaller error values than the previous techniques presented above. Notably, STEM resolution is much higher than TEM. STEM images (**Figure 4.9**) were collected on the sample grids that were used for TEM. **Figure 4. 10** shows the size distributions of aSiNPs and visualises the small and spherical shaped NPs. On some occasions, these particles can be seen to pack together. Average particle diameter by STEM was found to be 1.947±0.704 nm. The sizes obtained from STEM are smaller than sizes measured using DLS and TEM methods.

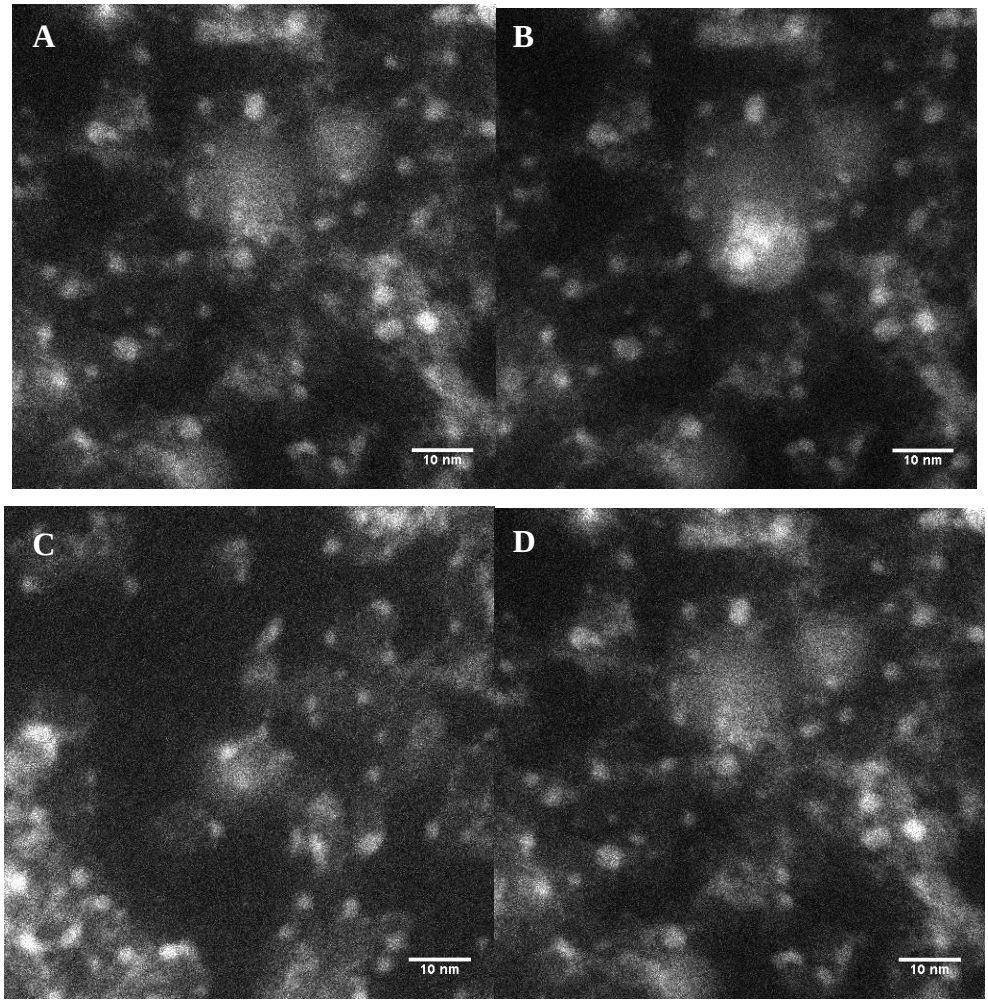


Figure 4.9: Examples of STEM micrographs [A-D] for SiNPs, scale bar 10 nm.

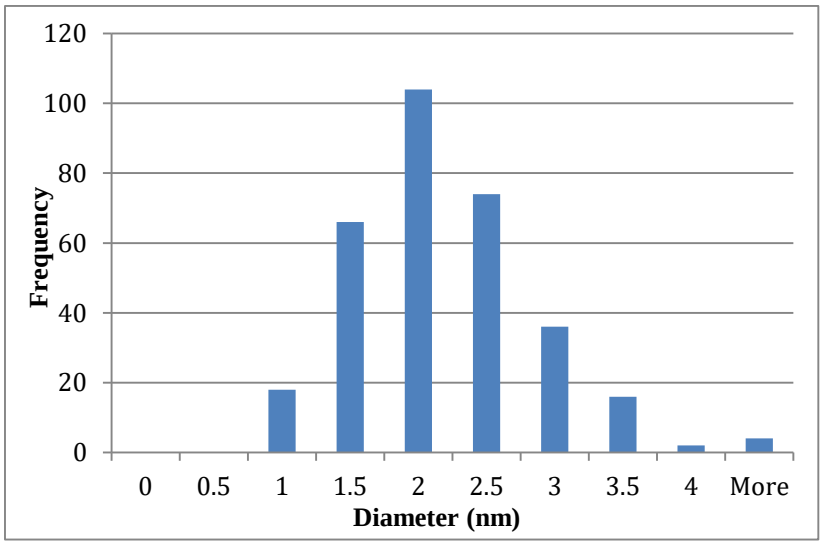


Figure 4.10: Histogram showing size distribution of 320 aSiNPs measured by STEM.

SAXS

The scattering patterns of multimodal distribution were fitted using Gaussian distribution as shown in equation **(4.2)**, which related the equation in section 2.2.6.1 for calculating particle radius and standard deviation. A subsample of the synthesised aSiNPs presented the measured radii of gyration that converted to particle sizes. The SAXS pattern of aSiNPs in **Figure 4.11** was shown in a log-log plot and displayed in two structural features. The structural feature in the Guinier region (smaller q region) provides the radius of gyration and size distribution for the hard-sphere model using the Guinier approximation (in section 2.2.6.1). This region is used to observe the inter-particle interaction. The form factor is given by calculating the slope in the higher q region where there is a high constant slope. The slope is around 4 which provides spherical shape and roughness surface.

Gaussian distribution

$$G_{gauss}(r, \mu, \sigma) = \frac{1}{\sqrt{2\pi\sigma}} exp\left[-\frac{[r-\mu]^2}{2\sigma^2}\right] \quad \textbf{(4.2)}$$

$$<R> = \mu$$

$$SD = \sigma$$

where: G_{gauss} (r_{e^-},μ,σ) =the Gaussian distribution function

r_{e^-} = electron density function (distribution)

<R> = is the mean particle radius that can be found from the first moment of the distribution

μ = mean (radius) and σ = standard deviation

Although the three batches of aSiNPs were prepared in various concentrations

as mentioned in section 2.2.6.1, the manipulation of SAXS patterns showed no size change (or distribution) in the bimodal particle from the same batch. The two size populations (as structural level 1 and 2) were fitted using Gaussian distribution and, shown in **Table 4.7**, the average size of one population was 1.6 nm and the second population was 7.2 nm. It was found that the best fit in the intermediate range in high q range with a slope of approximately -4 according to **Figure 4.11**. The primary particles were modelled with a spherical form factor (Guinier, André and Fournet, 1955; Schnablegger and Singh, 2013).

Table 4.7 SAXS data showing the two distinct populations of particle sizes from different batches of aSiNPs, measured at 10 mg/mL concentration.

Batch no.	Radius of gyration	Particle size [nm]	SD	Mean size [nm]
Structural Level 1				
1	3.702	7.405	0.5724	
2	3.512	7.024	0.5593	7.18±0.57
3	3.550	7.101	0.5833	
Structural Level 2				
1	0.77899	1.558	0.5484	
2	0.835377	1.671	0.5512	1.64±0.53
3	0.843176	1.686	0.5034	

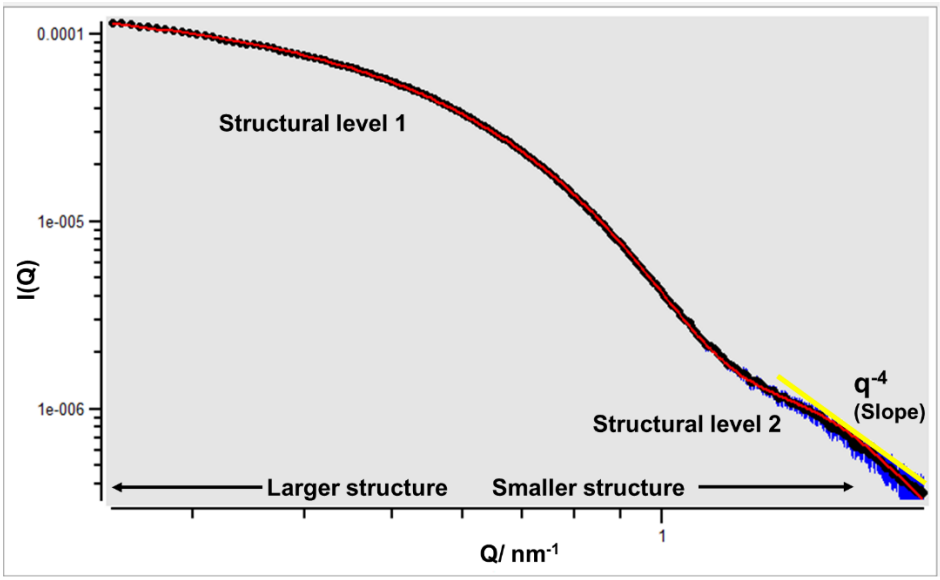


Figure 4.11: SAXS results of aSiNPs suspended in ultrapure water, the 1D pattern showed in the blue line. The fitted curve (red line) composed of two structural levels using SASFit software; the fit was based on a model of a sphere with the lognormal distribution regarding the slope of SAXS pattern (=3.538).

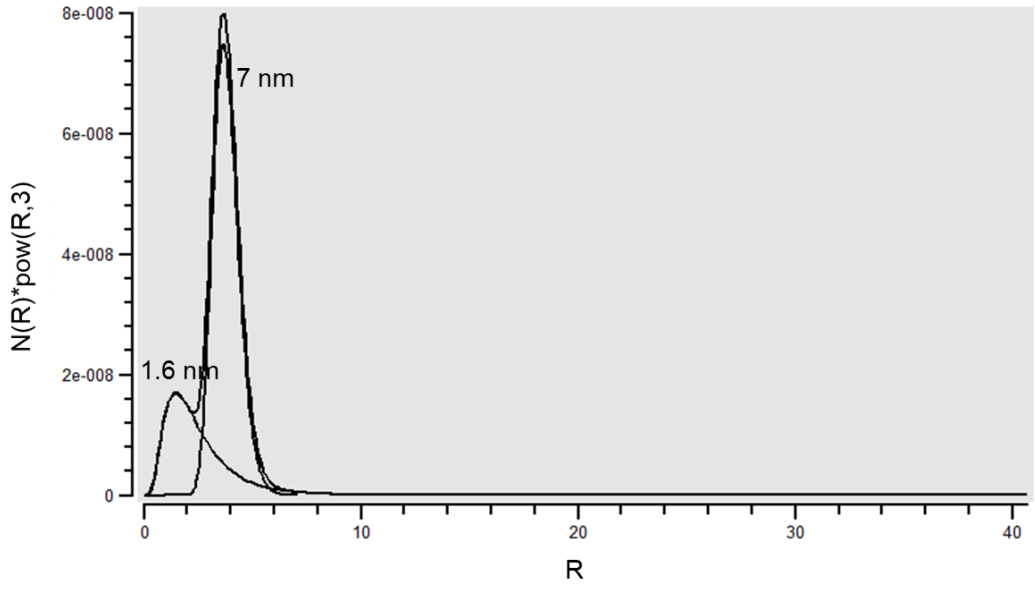


Figure 4.12: The fitted SAXS graph of aSiNPs shows the mean radii (X) are 1.64 and 7.18 nm, and the error ranges of the size distributions (s) are 0.53 and 0.57 respectively.

Furthermore, the aSiNP suspension was evaluated for particle size and size distribution 2 years post synthesis by the Federal Institute for Materials Research and Testing (BAM), Berlin, Germany (as shown in **Figure 4.13**) to confirm the presence of bimodal populations in the samples and to understand the changes in particle size due to storage. The SAXS patterns from BAM (radius 3.964 and 8 nm) showed two populations, similar to the results from the synchrotron analysis done in Thailand. The aged particles were slightly larger than the freshly synthesised particles, a result that was anticipated due to long term storage; this will be discussed more fully later.

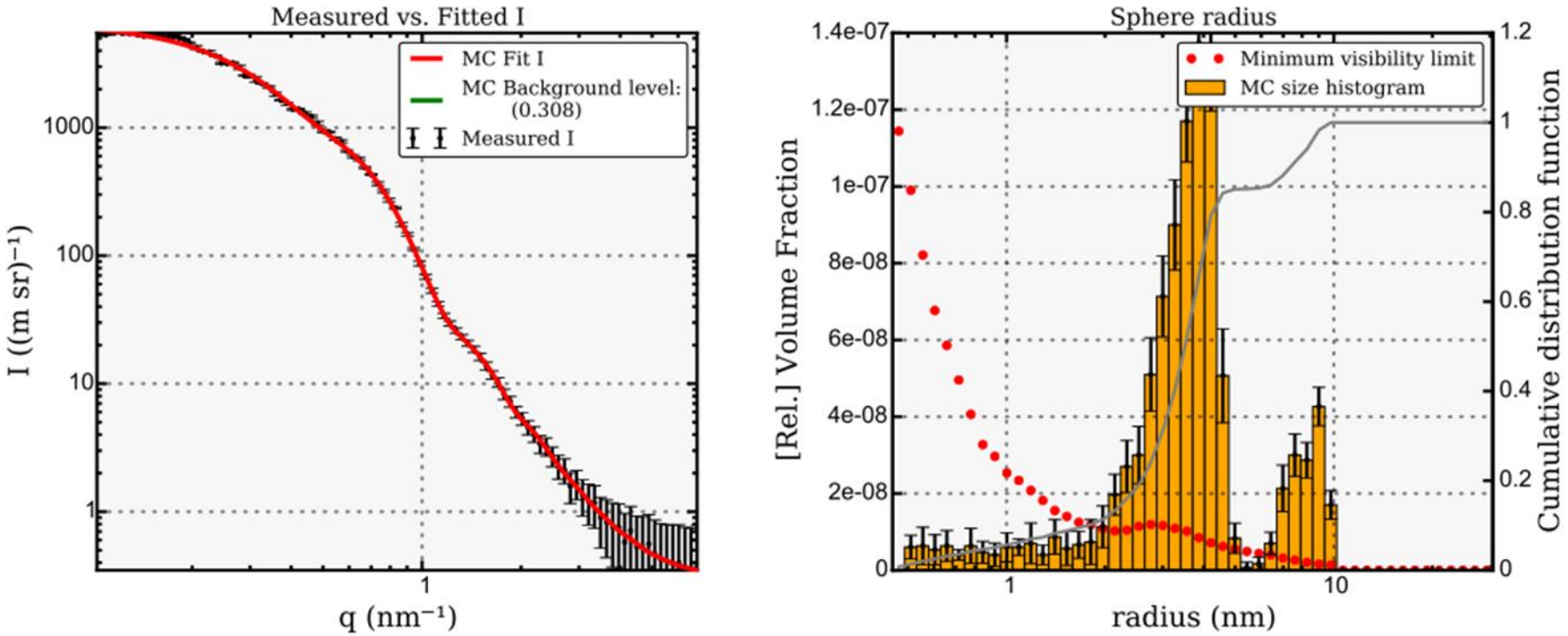


Figure 4.13: The SAXS scattering pattern and size distributions from BAM, Germany composed of two structural levels using McSAS 1.3.1; the fitted curve (red line) was a spherical model based on lognormal distribution. Histogram showed bimodal distribution of particles; radius size 3.964 and 8 nm.

Comparison of the particle sizes measured by multiple methods

The particle sizes obtained by multi- method characterisation approach is summarised in **Table 4.8**, which provide size, and standard deviation (SD) and the corresponding method.

Table 4.8 Particle size characterisation of aSiNPs

Method	Mean particle size (nm) ± SD
DLS	2.498±0.789
TEM	16.43±4.21
STEM	1.947±0.704
SAXS	7.18±0.57 (structure level 1)
	1.64±0.53 (structure level 2)

According to the results presented here, particle size measurements by DLS, STEM and SAXS are in general agreement. The size provided by TEM is greater than by other techniques, probably as a result of the relatively lower resolution of this technique. As DLS measurements describe the hydrodynamic diameter, the proximity between these values and those by STEM (2.2 and 1.947 nm respectively) suggest only a small difference between hydrodynamic diameter measured by DLS and particle size measured by STEM and SAXS, though in the case of the latter, two size populations were identified, at 1.6 and 7 nm respectively; the two size populations have been confirmed by the same SAXS technique in a different lab (BAM) and using different software (McSAS).

4.6.2 Shape

SEM

SEM analysis was performed to understand the morphology of the samples. **Figure 4.14** shows the SEM images of powdered aSiNPs produced by using low-temperature dehydration process, also known as lyophilisation. It was observed that the particles were spherical in shape. Densely packed aggregates were also seen and could be the result of the dehydration process during sample preparation.

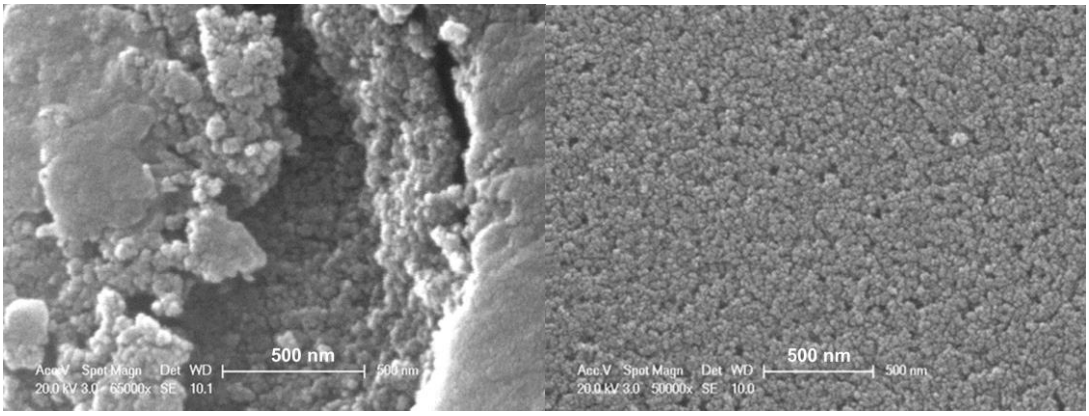


Figure 4.14: SEM images of amorphous silica nanoparticle powder that were synthesized by a sol-gel process, scale bar 500 nm.

SAXS

Shape was further investigated to get confirmative results by manipulating 2D scattering pattern (**Figure 4.15**) by using SAXSIT4p0. The resulting 2D SAXS profiles can be helpful to specify a shape of particles. It was found that the scattering patterns of aSiNP suspensions were similar to the sample of silica sphere (quartz) but not well-defined periodic nanostructure (or weak ordering arrangement) in the system.

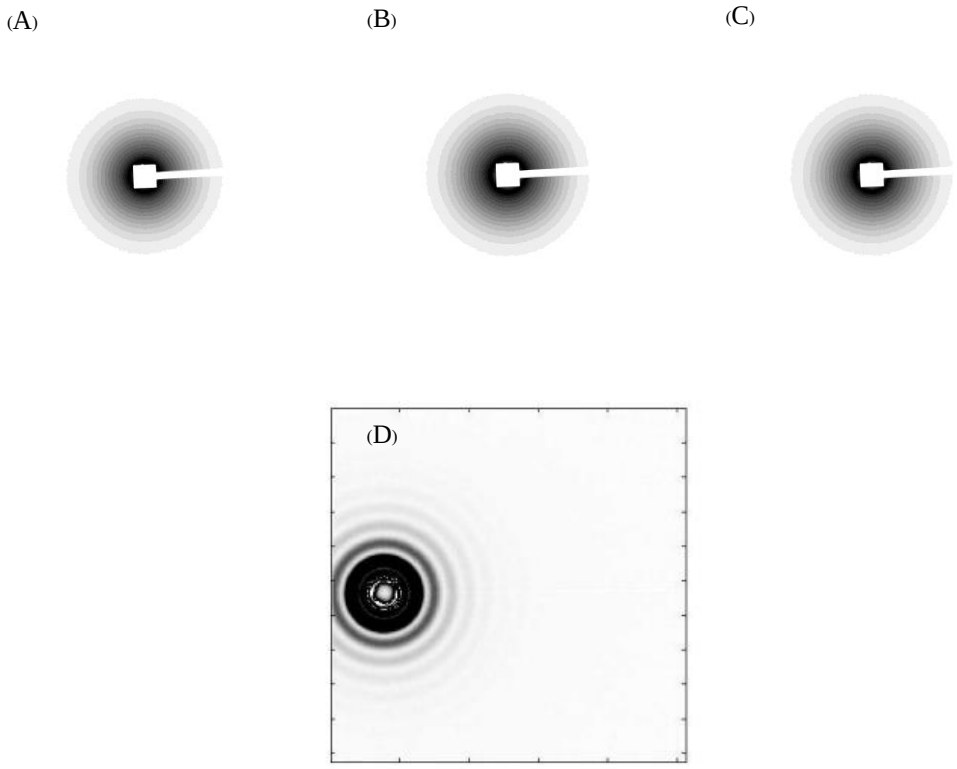


Figure 4.15: Scattering profiles of aSiNP suspension; (A) Batch 1, (B) Batch 2, (C) Batch 3 (D) Scattering pattern of Silica sphere (quartz). http://bigbro.biophys.cornell.edu/documents/SAX_Calibrants/kjejan3.png

4.6.3 Morphology (Crystallinity structure) Powder-XRD

The powdered aSiNPs were investigated to identify the elements and crystallinity with XRD in section 2.2.11. The XRD pattern (as seen in **Figure 4.16**) showed only a broad peak around 20º2∂, which confirms the amorphous form of SiNPs. The broadening of peak is large (intensity ~ 1000) owing to the smaller particle size effect. This finding is in agreement with the study from Rasmussen *et al.* (2013) and Nandawar, Singh and Fozia Z. Haque. (2015).

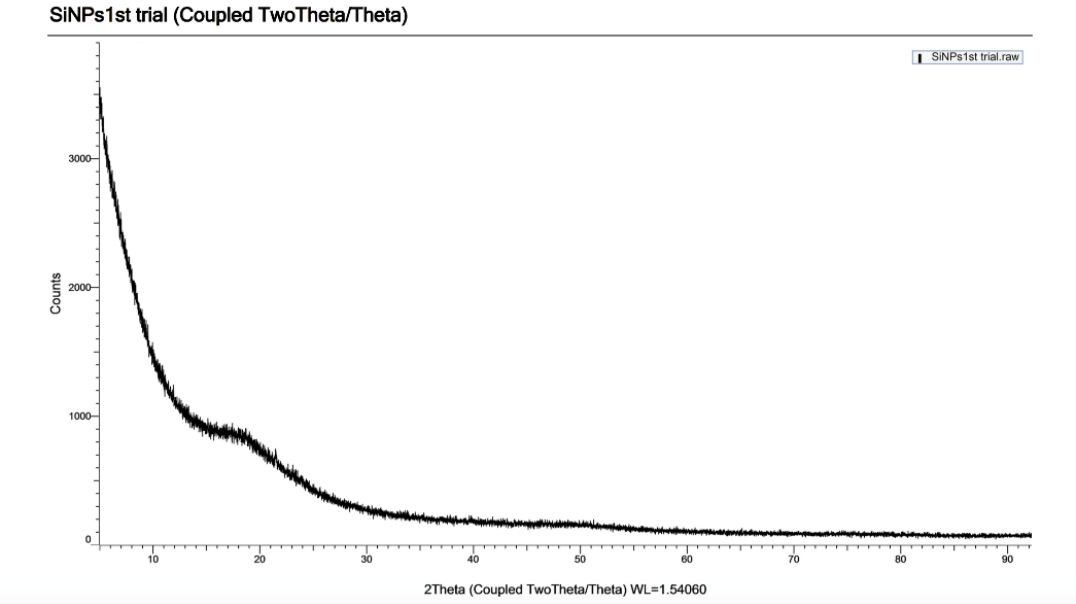


Figure 4.16: XRD diffractogram of the powdered aSiNPs.

4.6.4 Surface area

BET

The results of BET analysis, such as the surface area, C value, and correlation coefficient are shown in **Table 4.9**. aSiNPs have a very high surface area.

Table 4.9 The surface area of Synthesized Amorphous Silica Nanomaterials

Measurements	**Amorphous silica nanomaterials**		
	Batch 1	Batch 2	Batch 3
Surface area (m^2/g)	623.44	702.6	949.54
C value	124.819	65.120	61.045
Correlation coefficient	0.99997	0.9999	0.99872

4.6.5 Elemental composition

The aSiNPs were analysed for the concentration and the percentage yield for elemental composition using ICP-OES. XPS and XAS-EXAFS were additionally used to determine elemental composition FT-IR was implemented to determine the presence of functional bonding. The chemical composition of the synthesised aSiNPs can establish sample purity.

ICP-OES

The most commonly applied technique for analysis of elemental concentration is based on inductively coupled plasma (ICP). An analysis of silicon content in the suspension after removal of l-lysine and impurities was determined by ICP-OES. An average concentration of silicon content corresponding to three batches was obtained from ICP-OES was 15.5 mg/mL and 40.239 %yield (as shown in **Table 4.10**). The concentration of Si content is higher than the previous study (Thomassen *et al.*, 2010). In addition, the UPW in the filtration process was collected to investigate the amount of Si. The average of Si content in UPW, came out of the filtration system was 14.45 mg/mL (37.623%). Calibration graph (in **Figure 4.17**) was obtained from four different standard concentrations at 1, 10, 50 and 100 ppm. The correlation coefficient (r) of the standard curve was 0.998522. The coefficient of variation (CV) for the analysis of silicon was always less than 0.1%.

Table 4.10 Silicon concentration from synthesis as measured by ICP-OES.

Sample name	Concentration of Si content (mg/mL)	
	In	Out
SiNPs batch 1	16.5787±0.014	14.5887±0.052
SiNPs batch 2	15.3234±0.009	14.3703±0.049
SiNPs batch 3	14.4538±0.001	14.3848±0.052

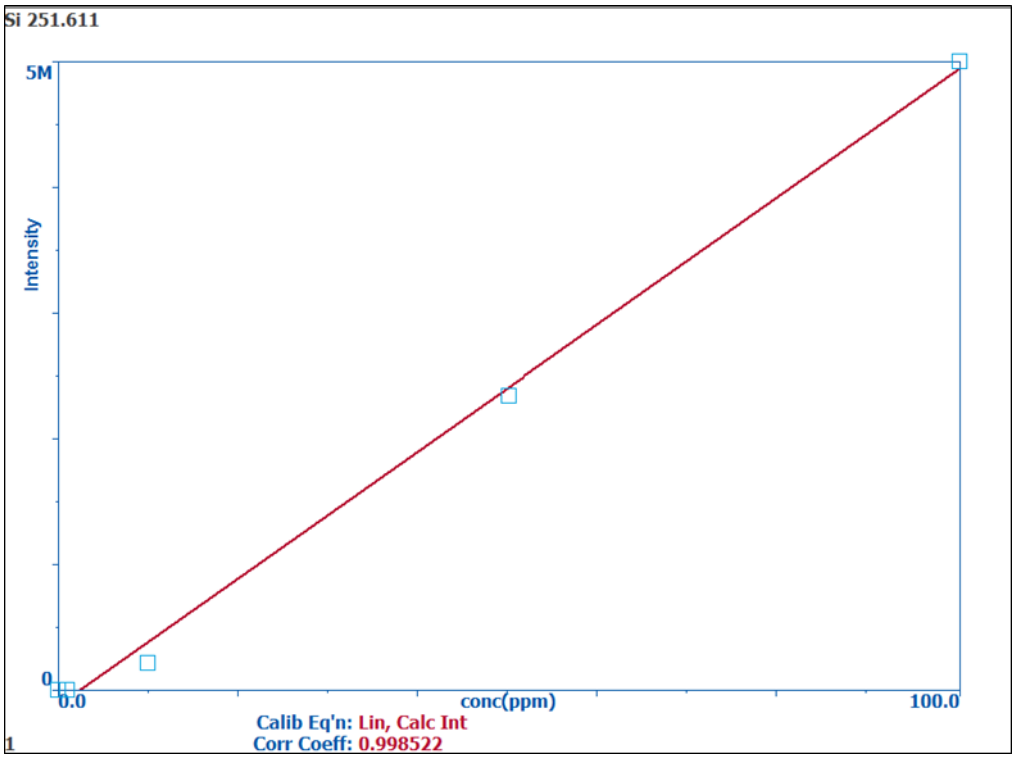


Figure 4.17: A calibration graph of standard Si.

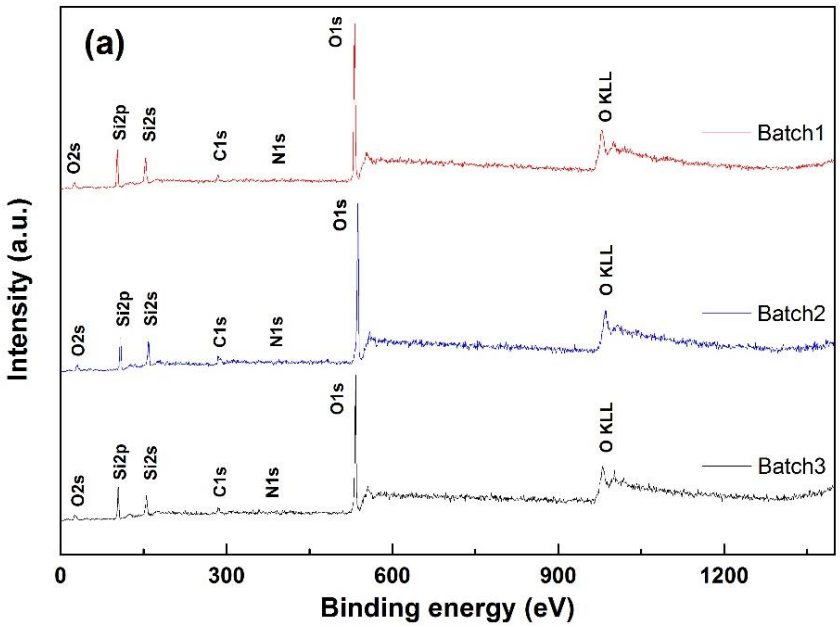
XPS

XPS analysis can be used to explore the surface chemistry of aSiNPs. The survey spectra in **Figure 4.18** (a) indicate the presence of Si, O, C and N in the samples. The presence of C in the samples is attributed to adventitious carbon contamination and N comes from the composition of l- lysine. The high resolution XPS scans in the Si2p and O1s regions are shown in **Figure 4.18** (b)

- (c). The binding energy of Si2p and O1s are observed at 103.0 eV and 532.2 eV, respectively, indicating the presence of SiO_2 (Thermo Scientific XPS, 2013). The percentages of atomic concentration are shown in **Table 4.11**. The average compositions of elements are silicon (24.75%), carbon (11.18%), nitrogen (1.15%), and oxygen (64.88%).

Table 4.11 Surface composition and atomic concentration (%) calculated from the spectra of elements.

Sample No. of aSiNPs	Atomic concentration (%)			
	%C	%O	%N	%Si
Batch 1	8.01	70.33	1.30	26.25
Batch 2	16.80	60.08	0.85	22.27
Batch 3	8.74	64.24	1.29	25.73



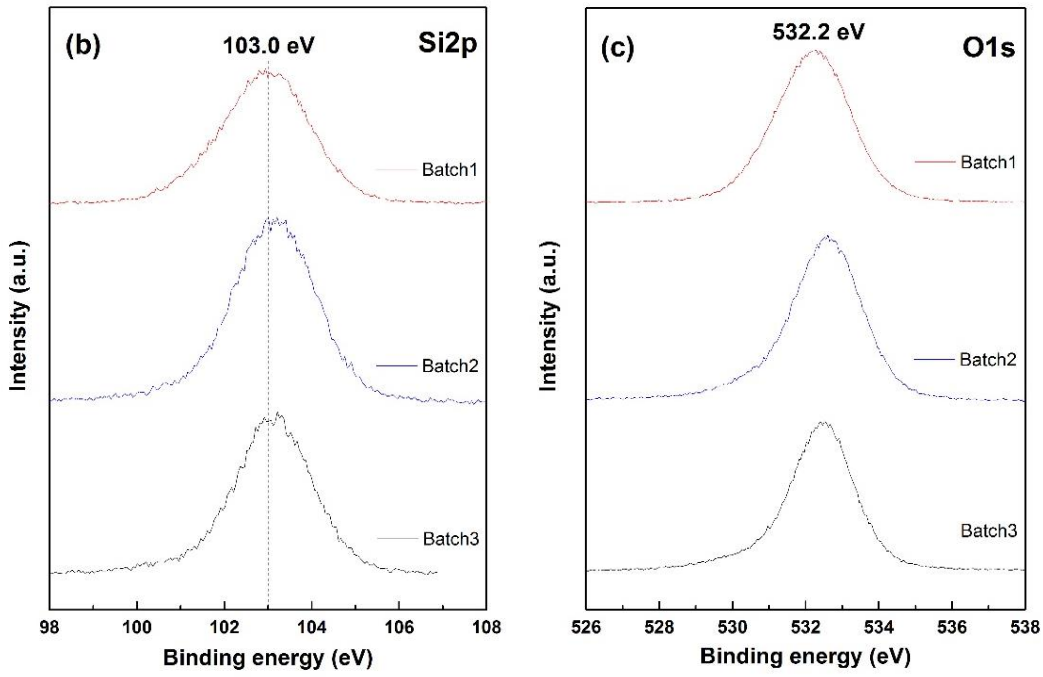


Figure 4.18: XPS survey spectra (a) and high resolution XPS spectra in the Si2p (b) and O1s (c) regions.

XAS-XANES

The element and oxidation state of the synthesised aSiNP suspensions were determined by using synchrotron radiation beamline 5.2 at SLRI, Thailand. The data were normalised using Athena software. **Figure 4.19** shows the Si*K*-edge XANES spectra of silica (quartz, SiO_2) and the samples of aSiNPs. The SiK-edge of aSiNPs spectra is similar in all cases and good agreement with the spectrum of SiO_2. It is apparent that the position of peak C at about 1846.8 eV, indicates the Si with O in the Si*K*-edge XANES with 4+ oxidation state (Bart *et al.*, 1995). It means that peak C in the Si*K*-edge spectrum is attributed to the dipole-allowed transition of Si $_{1s}$ electrons to the antibonding t_2 state of majority Si $_{3p}$ character ((Si $_{1s}$ t_2 (Si $_{3p-3s}$)). However, aSiNP batch no. 2 and 3 were found at peak D, became more intense and shift toward higher energy than amorphous silica (a-SiO_2) spectrum. Peak D and E are not present in both Si*K*-

and Si*L*-edge XANES of reference a-SiO_2 spectrum (Li *et al.*, 1994). The results of their peak positions may change the local structure showing SiNPs differ from quartz or a-SiO_2.

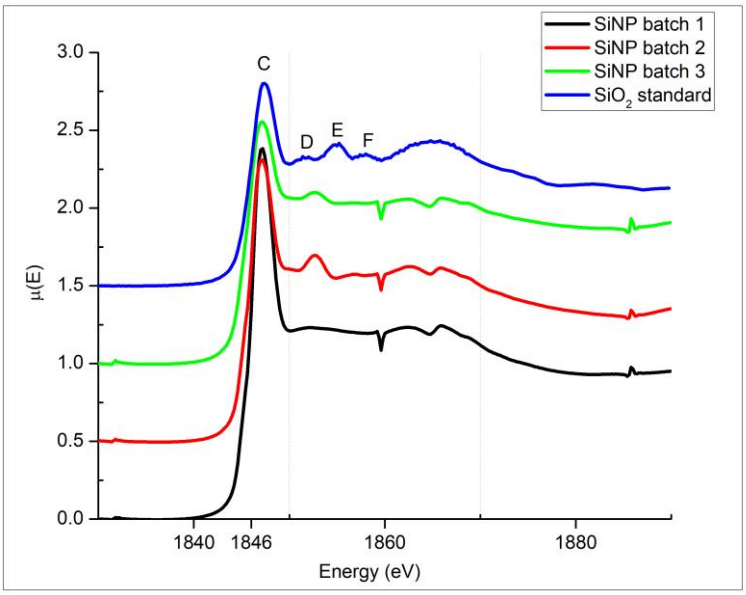


Figure 4.19: The Si*K*-edge XANES spectra of synthesised aSiNP are shown in black, red, and green lines and compared with silica (quartz) (blue line).

FTIR

The spectra were examined at wavenumber in the range of 400-4000 cm^{-1}, the number of scanning is 32 with a resolution of 4 cm^{-1}. A profile of the FT-IR spectrum of the powdered aSiNPs washed at once with UPW was shown in **Figure 4.20**. According to the FT-IR library (Merck, 2019), the bands were observed in the range 3400-2800 cm^{-1} that is attributed to the mode of N-H stretching peaks. N-H group is relevant to hydroxyl groups (OH), amine group (NR), and molecular water. Additionally, FT-IR spectra of Si-O presented at a wavenumber of around 1070 cm^{-1}, 950 cm^{-1}, 800 cm^{-1}, and 500 cm^{-1} (Spoiala *et al.*, 2014; Fijalkowski *et al.*, 2015).

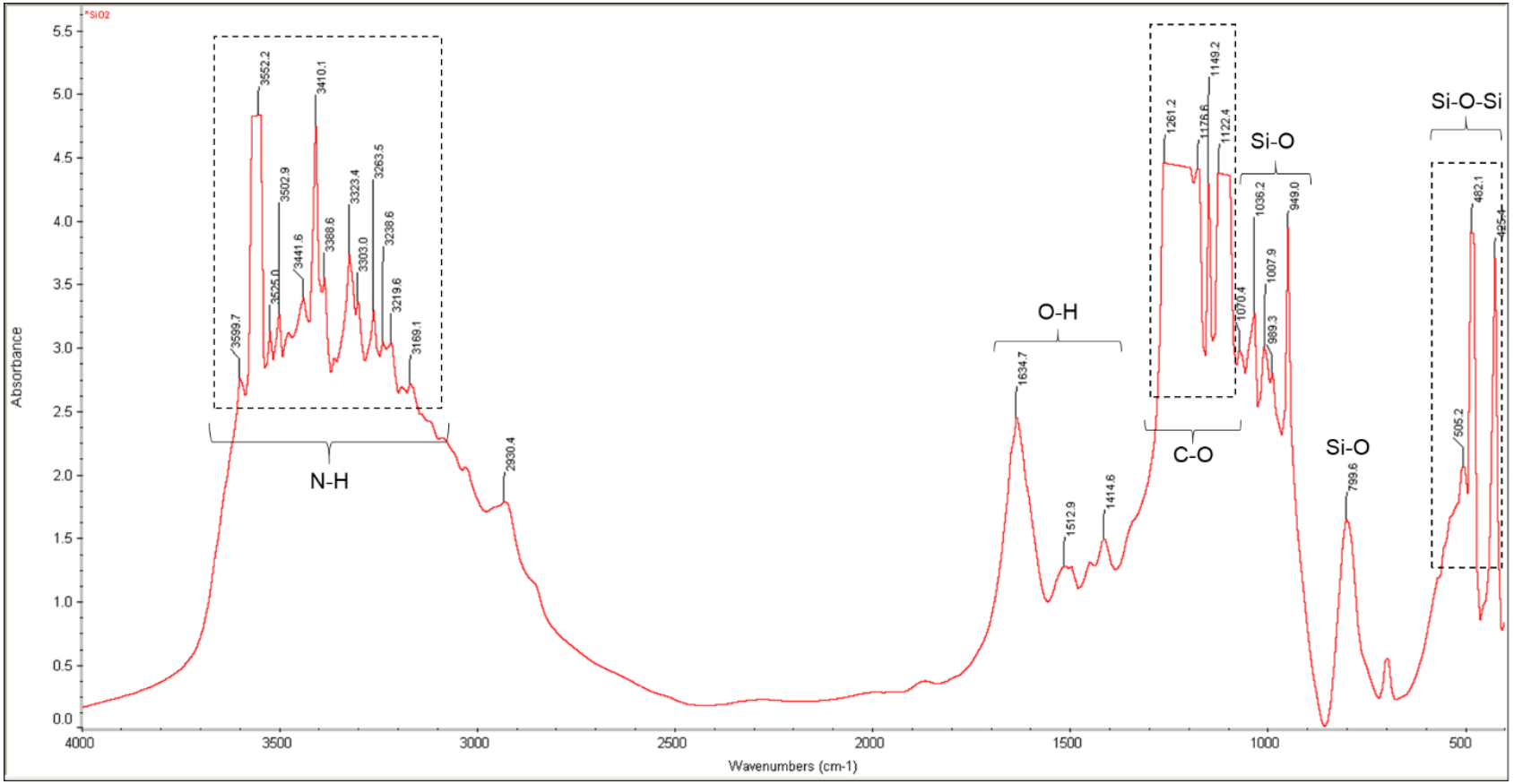


Figure 4.20: FTIR spectrum of synthesised amorphous silica NPs washed once in ultrapure water.

The FT-IR spectra described various peaks of SiO_2, with absorbance bands around 1097.6 cm^{-1} from the symmetric stretching vibration of the Si-O-Si bond and 1075.1 cm^{-1} from the asymmetric vibration of the Si-O bond, and finally an absorption band at 796.1 cm^{-1}, which can be assigned to the symmetric vibration of the Si-O bond (Santra *et al.*, 2001; Qasim *et al.*, 2014). The band at 469.9 cm^{-1} represents the bending mode of Si-O-Si bond. Overall, the FT-IR results show chemical structures related to the absorption and vibration of SiO_2 and L-lysine (N-H), as expected from the particle composition and in agreement with previous literature (Santra *et al.*, 2001; Snyder *et al.*, 2007; Qasim *et al.*, 2014; Spoiala *et al.*, 2014).

The ultrafiltration with UPW was carried on three times for each batch. The final of the washed aSiNP sample was obtained and subsequently identified the presence of functional group using FT-IR. **Figure 4.21** showed the spectrum of the washed aSiNPs sample. The presence of N-H group in the range 3400-2800 cm^{-1} is lower than in **Figure 4.20**. It seems that the wash process with UPW can remove l-lysine (amino group) and other impurities from the system. Various peaks of Si-O and Si-O-Si were assigned at a wavenumber of 1097.6 cm^{-1}, 1075.1 cm^{-1}, and 796.1 cm^{-1}. A more detailed discussion of the Si bonding environment will be presented next. All batches of the aSiNPs produced spectra in good agreement (as shown in **Figure 4.22**), indicating high reproducibility of aSiNP synthesis. The aSiNPs were calcined at 600˚C for 30 minutes; the spectra of the calcined aSiNPs showed some loss of the organic contents at the band of N-H stretching from 3400-2800 cm^{-1} to 3400 - 2900 cm^{-1} (as shown in **Figure 4.23**).

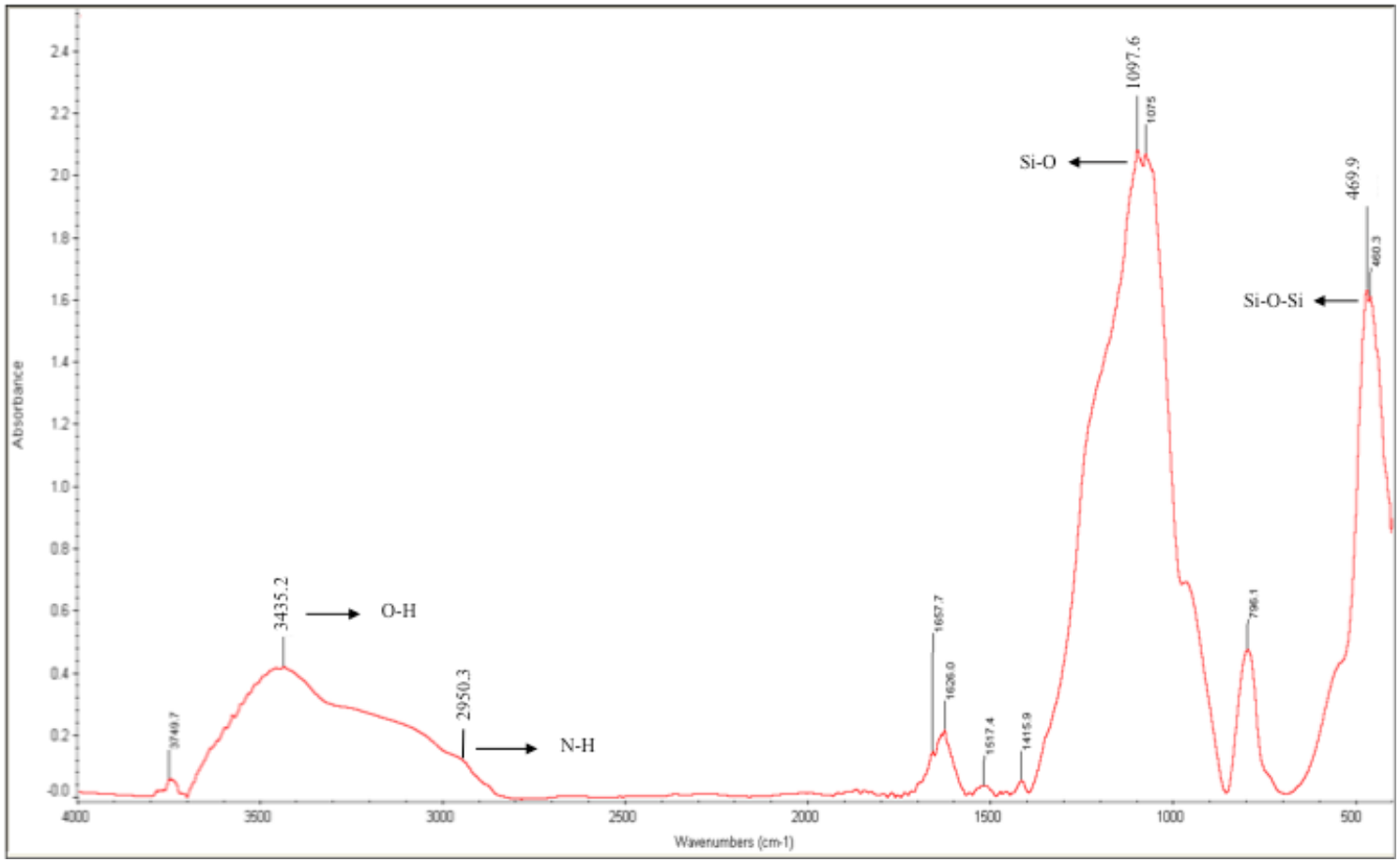


Figure 4.21: FT-IR spectrum of synthesised amorphous silica nanoparticles obtained from the sol-gel process, following repeated three times purification.

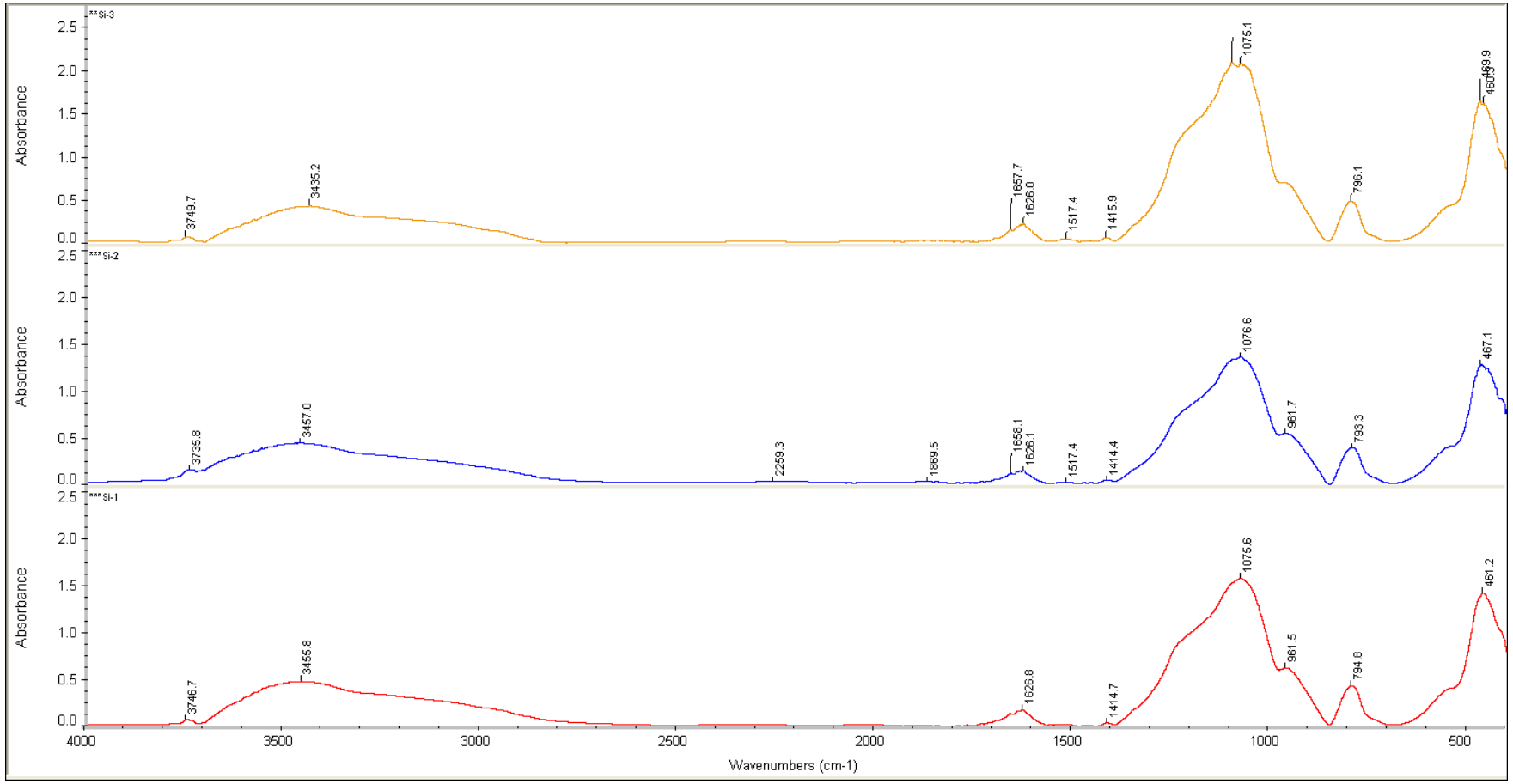


Figure 4.22: Comparison between FT-IR spectra of each of the three synthesised amorphous silica nanoparticle batches, which are in good agreement and their peaks corresponded to Figure 4.21.

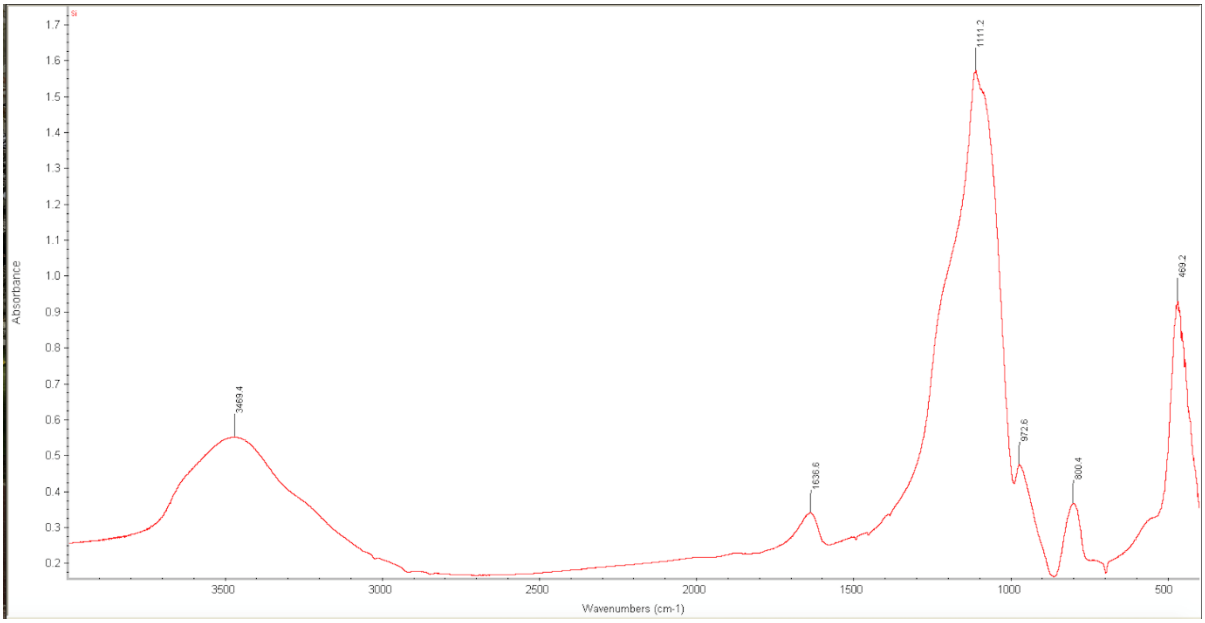


Figure 4.23: FT-IR spectra of synthesised amorphous silica nanoparticles obtained from the sol-gel process after calcination.

4.7 Discussion

The synthesis of amorphous silica nanoparticles (aSiNPs) by using an implemented sol-gel method (Thomassen *et al.*, 2010) has successfully been done. The purpose of the synthesis was to form as small particles as possible in the lower range of the nanoscale. A previous study using the same method as presented here, also reported aSiNP size around 2 nm with a single population present, based on DLS characterisation (Fijalkowski *et al.*, 2015).

The multi-method characterisation of aSiNPs has been carried out in order to determine size, zeta potential, shape, crystalline phase, surface area, elemental composition, oxidation state, and functional group.

As the NP sizes, SAXS reported the presence of bimodal particles in freshly synthesis and 2 years post synthesis of the suspensions. SAXS is a robust high-resolution method, able to characterise the structural components of particles in real space on a smaller scale from microns to Angstroms (as low as

0.1 nm) (Thomassen *et al.*, 2010). Whereas, DLS, STEM, and TEM presented here demonstrate the limitations of techniques; for example, DLS may only record an average size of two particle populations and fail to separate what is visible from fitting the SAXS data. It is unclear why the second population of particles, around size 7 nm identified by SAXS was not seen by STEM, and we hypothesise this might be the result of a weak agglomeration process picked up by SAXS in suspension that was lost during drying of samples for the STEM measurements.

The understanding of the synthesis mechanism of NP is useful to determine as much information as possible about NP properties. By applying this protocol, the hydrolysis reaction initiates by forming the primary particles as long as silicic acid is available. Growth occurs primarily through the addition of monomers to the more highly condensed particles rather than by particle aggregation. Particles 1-2 nm in diameter are formed in a few minutes above pH 7.

Above pH 7, the number of siloxane (Si-O-Si bonds) is increased, while hydroxyl groups from the silanol group (Si-OH) promote bond breakage and reverse restructuring of the growing polymer. All the condensed species are ionized and therefore, mutually repulsive. Due to the greater solubility of silica and the greater size dependence of solubility above pH 7, particles grow in size without aggregation or gelation and decrease in number as highly soluble small particles dissolve and reprecipitate on larger, less soluble particles. Growth stops when the difference in solubility between the smallest and largest particles becomes indistinguishable. This process is referred to as Ostwald ripening (ageing) (Alexander, Heston and Iler, 1954; Brinker and Scherer, 1990)

which supports the presence of the bimodal population in the aSiNP suspension.

TEM, STEM, SEM images were good agreement that the aSiNPs are spherical shape. Additionally, 1D SAXS graph can be used to identify the form factor of NP by using the slope at oscillating part, in Porod region. The slop of aSiNPs is around 3-4. It means that aSiNPs are sphere with a rough surface.

The higher concentration of Si content (at 15.5 mg/mL) was obtained from ICP-OES analysis, compared to a previous study (11.1 mg/mL) (Thomassen *et al.*, 2010). The % yield of aSiNPs was calculated based on the theoretical yield from the total silica input, here the results gave a moderate yield (40.239%). The presence of Si content (at 14.45 mg/mL, 37.623%) was observed in the UPW through the ultrafiltration, which possible affect the amount of aSiNPs in the suspension.

The elemental analysis of aSiNPs using XANES and XPS provided signification information, which highlighted the synthesised NPs containing silicon, oxygen, carbon and nitrogen. Using the Stöber method as similar as sol-gel have already reported the presence of carbon in the final aSiNP suspension (Van Helden, Jansen and Vrij, 1981). They assumed that the carbon content was assumed from unhydrolyzed ethoxy groups around 0.97%., whereas contained 91.5% weight silica and 5.25% water.

As the results of FT-IR, the washed aSiNPs using an ultrafiltration (repeatedly three times) has been achieved to remove L-lysine and impurities. The IR spectrum decreased greatly at the wavenumbers of OH stretching at 1626cm^{-1} due to scissor bending vibration of the water molecule (Snyder *et al.*, 2007; Spoiala *et al.*, 2014) and N-H stretching, and the peak of C-O stretching is

appeared in the spectrum. Following existing reports on silica particle formation from TEOS, carbon from the ethoxy groups is transformed into ethanol, which is easily dialyzed, and also lost by evaporation (Zeng *et al.*, 2012). Additionally, the effort of organic removal by using the calcination at 600 °C for the powdered aSiNPs seems to slightly remove the band of N-H stretching from 3400-2800 cm^{-1} to 3400 - 2900 cm^{-1}. Sufficient information concerning the physicochemical characterisation of aSiNPs is mentioned above and supplements with the evaluation of analytical methods is shown in **Table 4.12**

Table 4. 12 Evaluation of analytical methods for physicochemical characterisation of synthesized amorphous silica nanoparticles.

Method	Noted
Particle Size and Stability	
DLS	Uses as a screening method to obtain an initiative useful data approaching the equation that fits with SAXS scattering pattern of samples. NP dispersibility is relevant to point out individual particles and aggregation/agglomeration. In monodispersed samples, DLS can greatly estimate the representative quantity of particles in size range with test accurate. Zeta potential relates to electrical charge on the NPs, which controls the stability of a dispersion and proposes the NP behaviour in medium.
TEM	TEM imaging may not well define, which relates concentrations and sample preparation influence agglomeration on the grid. Provides an upscaled particle size and size distribution according to getting too closed particles and aggregation/agglomeration.

Method	Noted
STEM	STEM imaging allows for the determination of size and shape of nanoparticles and is noted aggregation/ agglomeration on occasions during sample preparation.
SAXS	Suitable for the mixture of ultrasmall particles that are sensitive to determining samples including sizes and size distribution offering sample stability. May not use as a stand-alone technique for size determination but uses to confirm results other techniques.
Morphology	
SEM	Provides 2D images for suitable defining nanoform and distinguishing the boundary of particles.
XRD	A suitable method to identify crystalline structure of nanomaterials.
SAXS	Provides shape, surface texture and structural information of nanoparticles according to distances of ordered materials, which uses to confirm crystalline phase.
Surface area	
BET	Recommends as a primary method to determine specific surface area and suitable for dry solid samples only.
Elemental composition and quantity	
FT-IR	Obtained information (e.g., functional group) uses to determine an impurity of NMs including residual materials or by-products and to develop the synthesis process (the purification for removing impurities).

Method	Noted
XPS	A suitable method to characterise elemental composition of nanomaterials' surfaces in percent atoms. Only dry solid samples could be identified the quantity of elements under ultrahigh vacuum, The binding energy of nanomaterials is possible identical the presence of SiO_2.
XAS (XANES-EXAFS)	Obtained information is used to further support XPS technique and the presence of SiO_2.
ICP-OES	A suitable technique to confirm the success of synthesis and gain number of quantities on nanomaterial.

4.8 Conclusion

The amorphous silica nanoparticles (aSiNPs) have successfully been synthesised within the size range of 1-10 nm by using sol-gel process and purified using conventional ultrafiltration to avoid aggregation and to remove impurities.

A multi-method characterisation approach was applied to determine the aSiNP properties. The particle size for three aSiNP batches obtained from DLS and STEM measurements, gave the diameter of 2.2 and 1.947 nm, respectively. In the case of SAXS analysis, two size populations were identified at 1.6 and 7 nm. The results from SAXS (Thailand) showed the presence of two size populations which was confirmed by SAXS at BAM (Berlin). The average size of TEM analysis is 16.43±4.21 nm, indicating the growth of particles in aqueous solution probably by aggregation during the sample preparation.

The aSNPs are quite stable for 2 months because of high zeta potential (-30 mV). BET results showed high surface area in the range of 623.44-949.54 m^2/g. The average zeta potential (ZP) from all aSiNP batches was found to be -36.1±6.43 mV, indicating the NPs are stable. Higher ZP could also be due to other factors, such as the pH value (7-9) and the presence of amine in the aqueous solution.

The elemental compositions using XPS, XAS- EXAFS/ XANES and FTIR showed main peaks at Si and O. There is a tiny peak of N or N-H in the samples after three repeated purification steps, however, this is advantageous because it prevents particle aggregation. ICP- OES further provided the silicon concentration to be 15.45 mg/mL.

This chapter provided the information from a range of characterisations of aSiNPs which would allow understanding the behaviour of NPs and to link these with potential mechanisms of toxicity. The available methods were evaluated for the physicochemical parameters of aSiNPs that there is quite a variety of methods suitable to identify nanomaterials as shown in **Table 4. 12**. In subsequent experiments, the synthesised aSiNPs would be applied in the studies of skin tests, such as skin penetration and skin irritation. In the context of the literature review of Chapter 1, it is notable that studies of aSiNPs with 1.6 and 7 nm size are still limited, therefore, the knowledge gained here is important. Penetration and cytotoxicity of aSiNPs through the reconstructed human skin models are detailed in Chapters 5 and 6 respectively.

Chapter 5 Penetration and Distribution Assessment of aSiNPs through a Skin Model

5.1 Introduction

There is a growing interest in the use of nanoparticles (NPs) in dermatology for topical applications in order to achieve photoprotection, hair treatment, facial (cosmetic) treatments and personal care products. Several uses of nanotechnology-based cosmeceutical performance have been enhanced deeper skin penetration, anti-aging effect, produced cosmetics with long lasting, and provided better UV protection. The presence of evidence about deeper skin penetration is insufficient detail that provided the previous agreements.

In all of these applications, NPs come directly to contact with human skin. Skin is the largest human organ and essential in protecting a human from external environmental threats, including biological hazards. Such hazards may, however, induce skin impairment or dysfunction. Consumers are increasingly exposed to nanomaterials, yet, to date, the understanding of potential toxicity to the skin, which is a primary concern in cosmetic applications, remains insufficient (Napierska *et al.*, 2010). Recent studies have suggested that there are limitations in knowledge of NPs passing through the skin barrier and subsequent effects (Nafisi, Schäfer-Korting and Maibach, 2015). These limitations, e.g. a detailed understanding of the controls on NPs penetration

through the skin and also underlying reactivity between skin cells (e. g. keratinocytes) and NPs need to be addressed. A major concern when NPs penetrate the skin is that they may potentially end up reaching internal organs or the bloodstream.

So far, only a few studies address NP dermal absorption, permeation and penetration. The work of Larese *et al.* (2009) revealed that 25 nm silver nanoparticles coated with polyvinylpyrrolidone can permeate the stratum corneum and the outermost surface of the epidermis in an *in vitro* skin damage study, detected by electron microscopy. A similar finding was reported in a study on gold nanoparticles (AuNPs) around 5-8 nm size with different surface functionalization and charges; the study was carried out on reconstructed human 3D Episkin™ model, and showed that AuNPs induce a phase change of lipid lamellae and pass through the epidermis. The positively charged AuNPs were most efficient in skin penetration through the paracellular and transcellular pathways, compared to the neutrally and negatively charged (Hao *et al.*, 2017). Furthermore, the drug delivery community have reported on how to optimise the efficiency in skin penetration and permeation of nanoparticles-containing formulations (Park, 2012). Previous results in the literature suggest that the level of NP penetration through the skin, depending on chemistry and experimental conditions, may influence skin penetration markedly. These may disrupt the skin barrier, the effectiveness of medical treatment and/or enhance transdermal penetration (Iannuccelli *et al.*, 2014; Bignon, Amigoni and Guittard, 2016).

Synthetic amorphous silica nanoparticles (aSiNPs) have been notable and vigorously studied in drug delivery as a multifunctional nanomedicine because

of their unique properties. (Pilloni *et al.*, 2013; Tang and Cheng, 2013; Zhao *et al.*, 2016; Chen *et al.*, 2018). However, aSiNPs may interact with biological matrices in different ways, as a function of their intrinsic properties, for instance, particle size, surface area, surface charge, and so on. The underlying interaction among nanoparticles, cells and bioactive reagents may enhance the efficiency of aSiNPs in medical treatments, but details of their interactions, including potential toxicity, are still limited. Therefore, a complete understanding of the skin penetration mechanism and aSiNP-tissue interactions are the purposes of this chapter. Focusing on the penetration of cosmetics through the skin, the use of human skin 3D models has become a useful tool for explaining the particle transformation in biological complexity and has been an easier method than using Franz diffusion cell[4]. There has been a rapid rise in the utilization of commercial reconstructed skin models for testing of cosmetics due to the European Union's complete ban on animal models for cosmetic testing in 2013 (European Union, 2009). Commercial reconstructed human epidermis (RhE) models are demonstrated to have reasonable similarity to the native human tissue in terms of morphology, lipid composition and biochemical markers (De Wever, Kurdykowski and Descargues, 2015). In this chapter, an independent human full-thickness skin models at Day 11 (D11) was used to evaluate the skin penetration of amorphous silica nanoparticles (aSiNPs) at various concentrations from 0.1-10 mg/mL. Appropriate analytical techniques were then carried out to produce quantitative data and physicochemical

[4] Franz diffusion cell: "an *in vitro* skin permeation assay, consists of two primary chambers separated by an animal skin layer, i.e. rabbit skin, rat skin or, pig skin. The test sample is applied to the skin membrane through the top chamber, whereas the bottom chamber contains the same media as the test sample but without the test substance."

properties, specifically: micro X-ray fluorescence (μ-XRF), X-ray absorption spectroscopy/X-ray Absorption Near Edge Spectroscopy (XAS/XANES), and small angle X-ray scattering. μ-XRF was used to track Si into skin layers which presented in the maps of nanoparticle distribution. Additionally, the oxidation number, chemical structure and particle size of Si after *in vitro* test were evaluated by using XAS/XANES, XPS and SAXS, respectively.

5.2 Materials and Methods

This section introduces the materials and analysis techniques including media preparation, fixation, sectioning, and sample quantification methods used for an *in vitro* skin penetration test. Details on the materials, such as a buffer solution, cell culture media, test samples, and human skin model were presented in the following section.

5.2.1 Reagents

Dulbeco's phosphate buffered saline (PBS) was purchased from Gibco and Hyclone. A fresh culture media (GDA3F^{+}) was purchased from Episkin^{TM} that contains nutrients to maintain viable cells. Optimal cutting temperature compound (OCT) solution was used as an embedding medium to keep the frozen tissue specimens and 70% ethanol was used to clean the working area at the beginning and the end of the experiment.

5.2.2 Colloidal Silica Nanoparticles

Details on the synthesised amorphous silica nanoparticles (aSiNPs) were presented in Chapter 4. Two different concentrations of aSiNPs were prepared

in ultrapure water at 0.1 mg/mL and 10 mg/mL and sonicated for 10 minutes prior to topical use.

5.2.3 Reconstructed Human Full Thickness Skin Model: T-skin™ at Day 11 Experiment and Media Preparation

The reconstructed human full thickness skin model: T-Skin at Day11 (D11) was purchased from Episkin™ (**Figure 5.1**). The main features of reconstructed human skin models were shown in section 1.8.2, Chapter 1. In summary, Episkin™ recommends two models of the full thickness skin to carry out an *in vitro* skin penetration, including skin model at Day 11 and at Day 17. The Day 17 model is cultured longer than the Day 11, approximately a week. Both models contain typically an upper and inner layer of human skin as well as epidermis and dermis, which placed on a polycarbonate filter as a supporter (see **Figure 5.2** and **Figure 5.3**). The outermost surface is stratum corneum that plays the role of skin barrier. The whole thickness of skin model is around 500 μm, excluding the filter. The thickness of epidermis and dermis is usually around 100 and 400 μm, respectively.

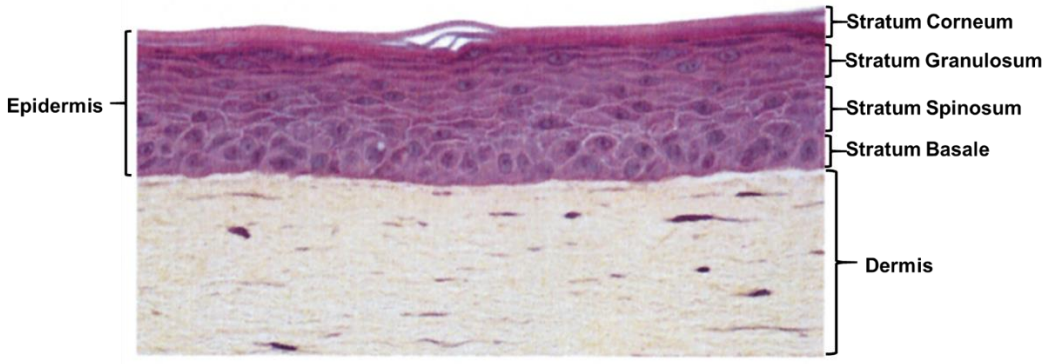


Figure 5.1: Morphology of the Full Thickness Human Skin Model-T skin Batch No: 18-SKIN-028; reprinted with permission of EpiSkin™.

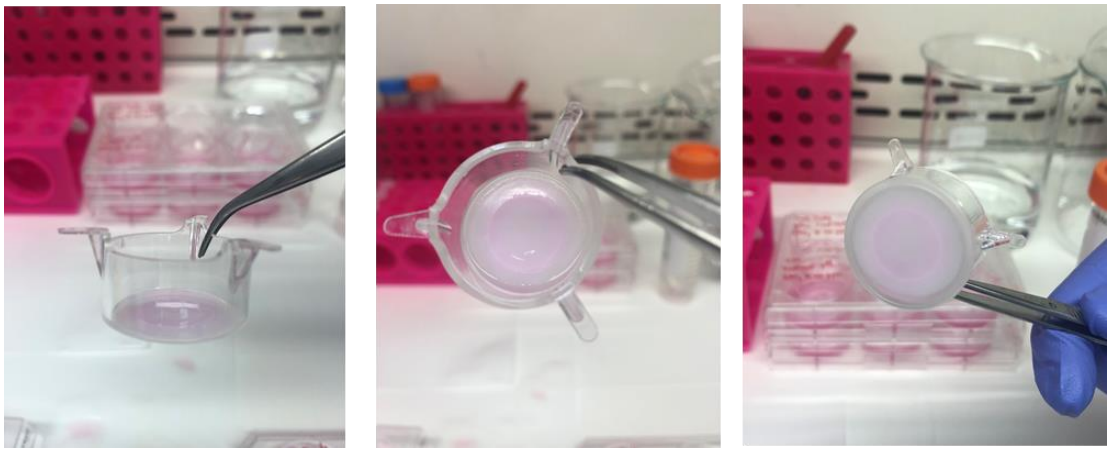


Figure 5.2: Representative photos of the reconstructed human full thickness skin model at Day 11 attaches in the insert, Batch No: 18-SKIN-028 EpiSkin™; presents a side view (left), a top view (middle), and a bottom view (right).

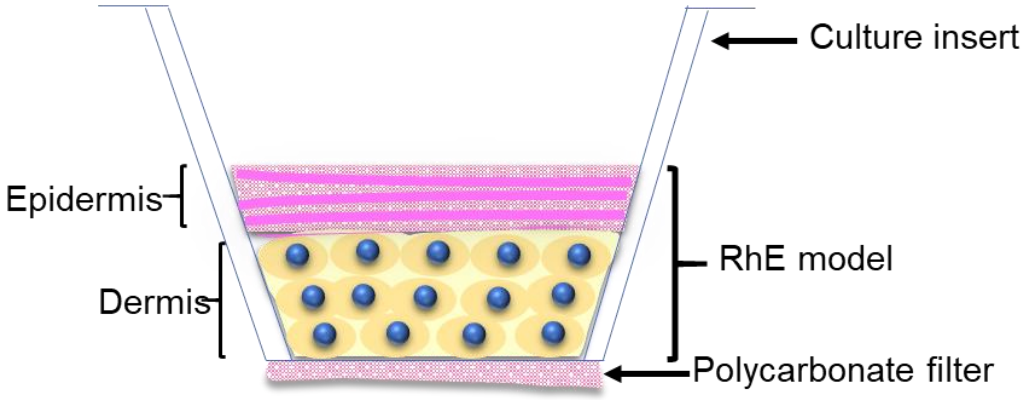


Figure 5.3: Schematic of different layers of the D11 model and its appendages.

5.2.4 *In Vitro* Skin Penetration

The application of nanomaterials in commercial personal care products and cosmetics may cause potential human exposure through skin contact**.** An understanding of how nanomaterials pass through the dermal route is currently limited, particularly for small particles, as is their potential toxicological effects, and this was the focus when performing the *in vitro* skin penetration test in this

study. The experimental procedures were adopted from Hao *et al.* (2017) and involved using a mechanism of natural absorption and diffusion through the human skin barrier and layers, i.e. stratum corneum, epidermis and dermis. The skin penetration test performed on an *in vitro* reconstructed human full thickness skin model at Day 11 (D11). The D11 model samples were treated according to the schematic of the protocol for skin penetration testing, as presented in **Figure 5.4** and **Figure 5.5.** An exposure experiment was set up and conducted under a biological fume hood at the University of Birmingham. The details of the procedures were divided into three steps and explained in the following sections.

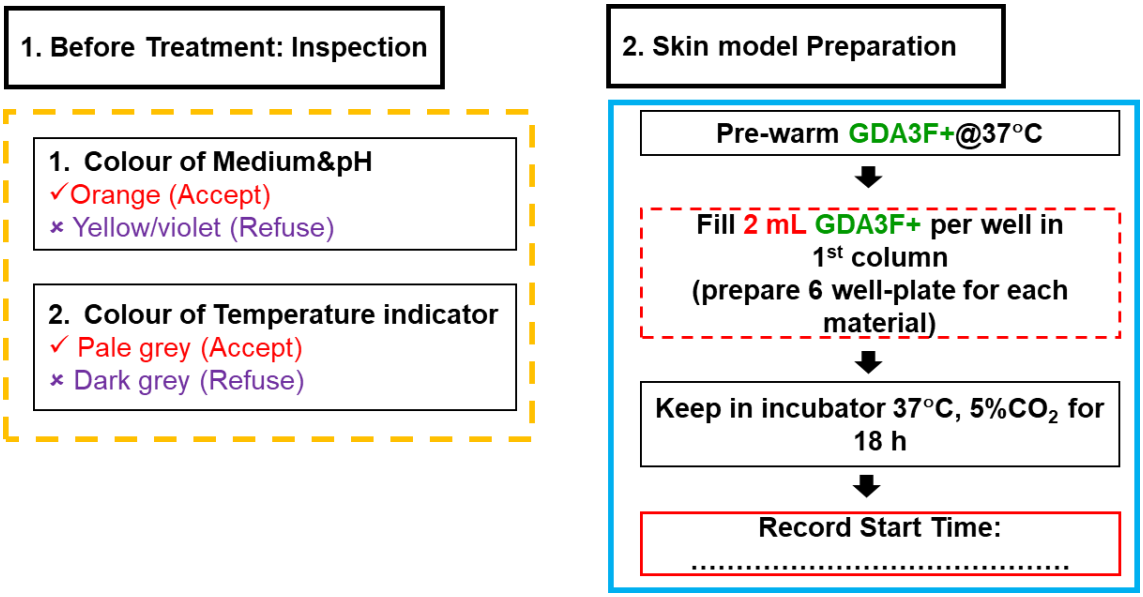


Figure 5.4: Schematic of protocol for skin penetration testing; Part 1: Inspection (Left) and Part 2: Skin model Preparation (Right).

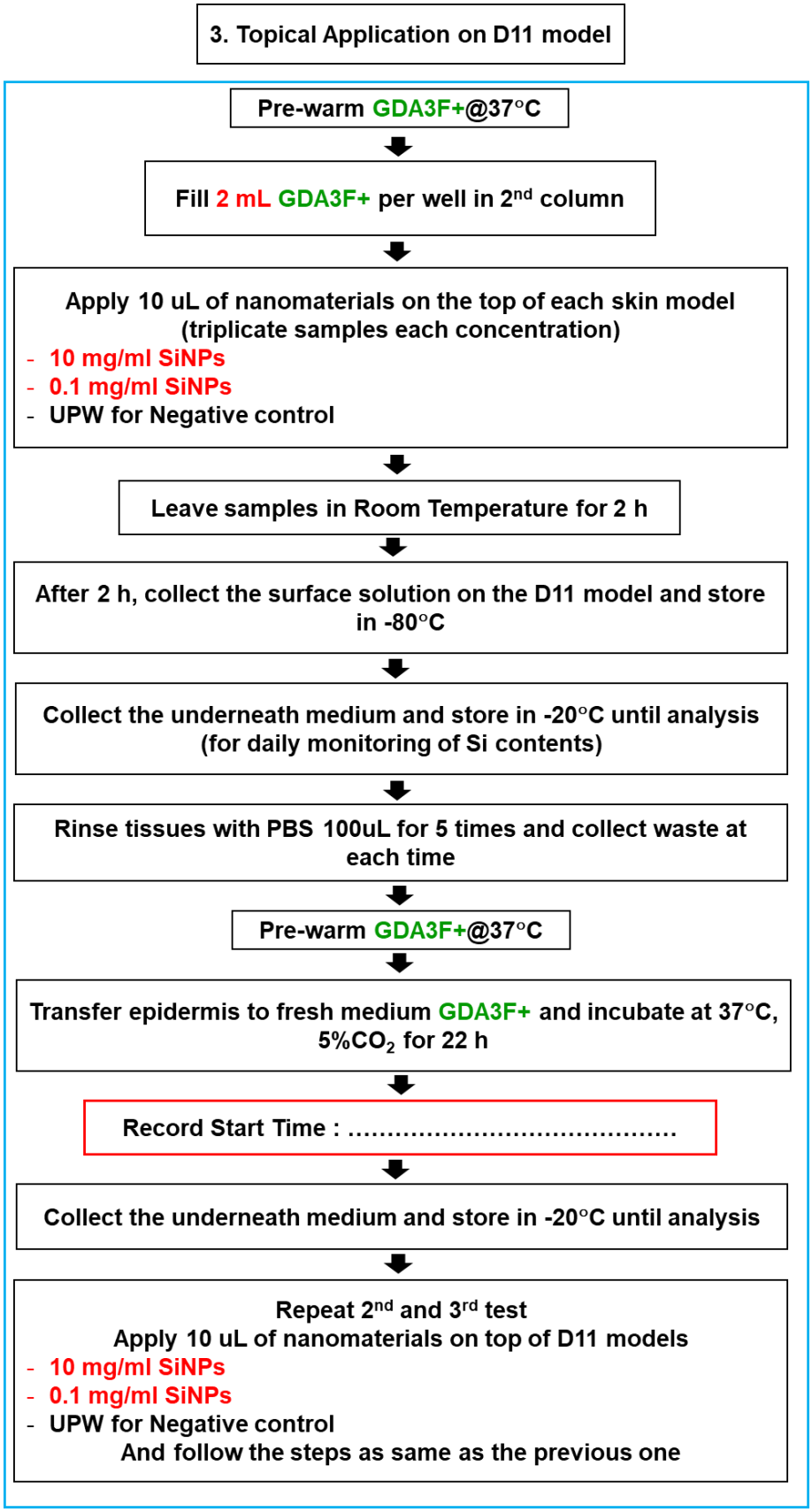


Figure 5.5: Schematic of protocol for skin penetration testing; Part 3: Topical Application on D11 models.

5.2.4.1 Pre-check

As the schematic of the protocol in **Figure 5. 4**, indicates, the pH and temperature were checked by using Thermax strip indicator (**Figure 5. 6**) and also checked the colour of the media before transferring D11 tissues in the fresh culture media (GDA3F^{+}). GDA3F^{+} was pre-warmed in a water bath at 37°C and filled into each well at 2 mL underneath the D11 tissues, which conducted this step under a biological fume hood at room temperature (≈ 22 - 25°C). The D11 tissues were incubated at 37°C, 5% CO_2 for 18 hours as shown in **Figure 5.4**. After incubation, the D11 models were ready to start the skin penetration test.



Figure 5.6: Thermax strip indicator is used to investigate an exposure of temperature during the skin model delivery.

5.2.4.2 *In vitro* Skin Penetration Test

10 µL of each the sonicated aSiNP concentration was topically applied evenly on the outermost epidermis and maintained in the room temperature for 2 hours, whereas 10 µL of Milli-Q water was used as a negative control and was along with the test samples. This step was repeated three times on three independent D11 models at each concentration. After aSiNP exposure, the top surface of D11 was extensively washed with 100 µL of PBS for five times in

order to remove any excessive aSiNPs remaining on the outermost of stratum corneum. Subsequently, the D11 models were transferred in a new 6 wells-plate where the fresh GDA3F^{+} media were filled into. These plates were stored in the incubator for 22 hours. At the end of the incubation, the GDA3F^{+} media underneath the D11 models (≈ 1 mL) was also collected daily in order to monitor the Si content across the polycarbonate filter. As the schematic in **Figure 5.5**, the exposure, sample collection, and subsequent culture were carried out in a similar way for a second and third time. The subsequent culture, i.e. GDA3F^{+} media, PBS were kept at -20 °C until it was analysed by ICP-OES.

The result from analysis of aSiNPs remaining in PBS (collected from washing process after aSiNP exposure), showed non-detectable concentration of silicon in the PBS, suggesting that aSiNPs had crossed through the stratum corneum readily.

5.2.4.3 Endpoint

At the final step of 22 hours incubation after triplicate aSiNP treatments, the exposure experiments were terminated, and the D11 samples were punched off and frozen in liquid nitrogen then stored at -80 °C for analysis.

5.2.5 XRF Analysis

5.2.5.1 Sample Preparation

At the end of the experiment, the D11 tissues were embedded in OCT solution and kept in -80˚C until hardened. The embedded tissues were vertically sectioned using a Leica cryostat CM 1950 at 70 µm thickness to obtain cross-sectional layers (such as those shown in **Figure 5.7** and **Figure 5.8**), in order to visualise a cross-section of the tissue by using a microscopy. XRF was

carried out to determine the translocation of aSiNPs on the upper layer of D11 tissues and into both skin layers. The XRF technique would allow detection at > 30 μm depth from the surface. These samples were continuously analysed by using other synchrotron techniques as well as XANES, XPS, and SAXS.

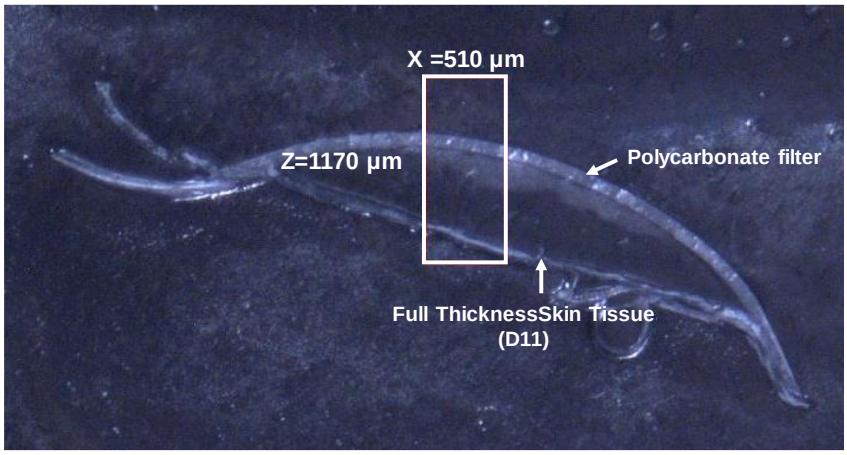


Figure 5.7: Representative photo of a cross-sectioned D11 tissue at 70 μm thickness exposure to colloidal aSiNPs at 0.1 mg/mL concentration. The white rectangular is the randomized area for XRF analysis. X axis and Z axis are the width and length, respectively.

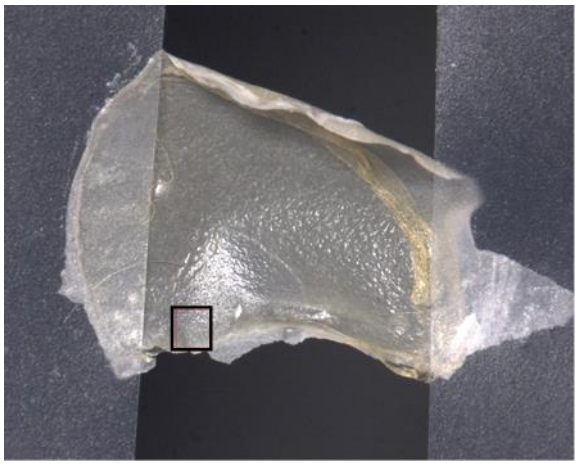


Figure 5.8: Representative photo of a biopsy punched-off D11 tissue exposure to colloidal aSiNPs at 10 mg/mL concentration.

5.2.5.2 Procedure

Microbeam X-ray Fluorescence (μ-XRF) spectroscopy at beamline 6b was carried out on the D11 tissues, at SLRI, Nakhon Ratchasima, Thailand. This technique uses a white X-ray beam from the bending magnet of the 1.2 GeV storage ring, which is directed through a chamber that consists of a fixed aperture made of an oxygen-free thermal conductivity copper wire with a 50 μm thickness Kapton® tape as the window onto the sample. The size of the focused white beam is set at 30 μm size steps scanning by the copper wire loaded with the sample in the vertical (X-axis) and horizontal (Z-axis) directions, whereas the Y-axis is the direction of the motor movement in forward and backward mode. The wire is scanned vertically while the intensity of Cu *K*α X-ray fluorescence is recorded. A random area of the D11 sample was chosen for analysis as shown in **Figure 5.7** and **Figure 5.8**, for example at X-axis position (1.6, 2.11) and Z-axis position (-0.85, 0.32), which produced a total number of 720 points. Data were processed and depicted as XRF images of NP distribution on D11 models using PyMCA software 5.4.1.

5.2.6 SAXS Analysis

5.2.6.1 Sample Preparation

The previously mentioned D11 samples, which were analysed by μ-XRF were then used to determine size change by SAXS. The D11 tissues were attached on the Kapton® tape, attached to a stainless-steel plate as shown in **Figure 5.9**. A blank tissue, which is the D11 tissue without any treatment was used as a background in order to subtract the scattering pattern from the tissue exposed to aSiNPs.

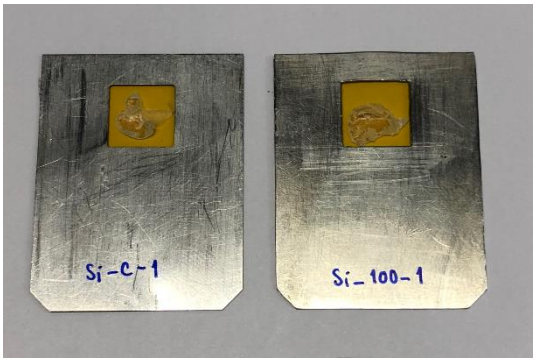


Figure 5.9: Samples of D11 tissues exposed to aSiNPs at 10 mg/mL (left) and 0.1 mg/mL (right) for analysing by SAXS.

5.2.6.2 Procedure

All SAXS data on the D11 samples were collected on beamline 1.3W at the SLRI, Nakhon Ratchasima, Thailand using a double multilayer monochromatic (W/B4C) X-ray beam at 9 keV, with Rayonix SX165 detector to collect the SAXS patterns as shown in the previous chapter. The 2D scattering patterns were reduced to 1D profile of intensity (I) and q by integrated beam intensity. For the simulation, the SAXSoPy version 1.8, which has been developed by SLRI was used to normalize and align data. For the fitting, the SAXS data were normalized with a spherical model, which is given by

$$I_{sphere}(q) = I_{0,sphere}\left[\int \left|F_{sphere}(x,q)\right|^2 f_R(x,m,\sigma)dx\right] S_{HS}(q,R_{HS},\eta) \quad \textbf{(5.1)}$$

Where $I_{0,\,sphere}$ is an arbitrary scaling factor. The sphere form factor is given by

$$F_{sphere}(x,q) = \frac{\sin qx \; - qx\cos qx}{(qx)^3} \quad \textbf{(5.2)}$$

The sphere radius has a Gaussian distribution

$$f_R(x,m,\sigma) = \frac{1}{\sigma\sqrt{2\pi}} exp\left\{-\frac{(x-m)^2}{2\sigma^2}\right\} \quad \textbf{(5.3)}$$

where m and σ are the mean radius (R_0) and standard deviation (SD), respectively.

5.2.7 XANES Analysis

5.2.7.1 Procedure

X-ray absorption spectroscopy on beamline 5.2 and 8 at SLRI, Nakhon Ratchasima, Thailand were used to investigate the atomic arrangement and elemental specification of the studied materials. XANES spectra were carried out to determine the oxidation state of silicon when passed through the skin layer. Athena software (updated version 2016) was used to analyse the data. XANES spectra were calibrated with a Ti foil and normalised using a linear pre-edge. The spectra were compared for the position of Si*K*-edge, and oxidation state with the reference spectra of silica (quartz; 4+) and silicon metal (Si; 0).

5.2.8 XPS Analysis

5.2.8.1 Procedure

The XPS measurement at beamline 3.2b was performed using PHI5000 Versa Probe II, ULVAC-PHI (Japan) with a monochromatized Al*K*α X-ray source (beam energy 1486.6 eV), at SLRI, Nakhon Ratchasima, Thailand. The samples were fixed on a carbon tape and connected to the stage as shown in **Figure 2.18**. The sample examination was carried out under ultrahigh vacuum with a base pressure below 10^{-8} mbar. For each sample, a general scan was repeated two times with area size 100*100 μm^2. The high-resolution scans of the XPS technique were performed for elements of interest such as calcium, silicon, oxygen, nitrogen, and carbon. The energies of photoelectrons were collected in term of binding energy from ejected electrons at depths greater

than 5-10 nm in the XPS spectra. Spectra were analysed via peak fitting by means of CasaXPS software. These provided detailed information about the chemical environment of the atoms at the surface and were compared with reference materials.

5.3 Results and Discussions

The aSiNP suspensions with two different concentrations were tested against reconstructed human full thickness skin model (D11) to determine the ability of aSiNPs to penetrate through skin layers, i.e. epidermis and dermis and also to assess if any changes in the particles, in terms of size, oxidation state, and surface elemental compositions, had taken place. The results and detailed discussion are described in the following sections.

5.3.1 In vitro skin penetration using XRF

Skin penetration of aSiNPs (at 0.1 mg/mL and 10 mg/mL) was investigated *in vitro* with D11 model using MilliQ water as the media as well as the negative control (**Figure 5.10**). The μ-XRF technique was applied to investigate aSiNPs remaining at the top interface and throughout the cross-section of D11 tissues, and additionally to generate distribution maps for aSiNPs across the skin model as shown in **Figure 5.11** and **Figure 5.12**.

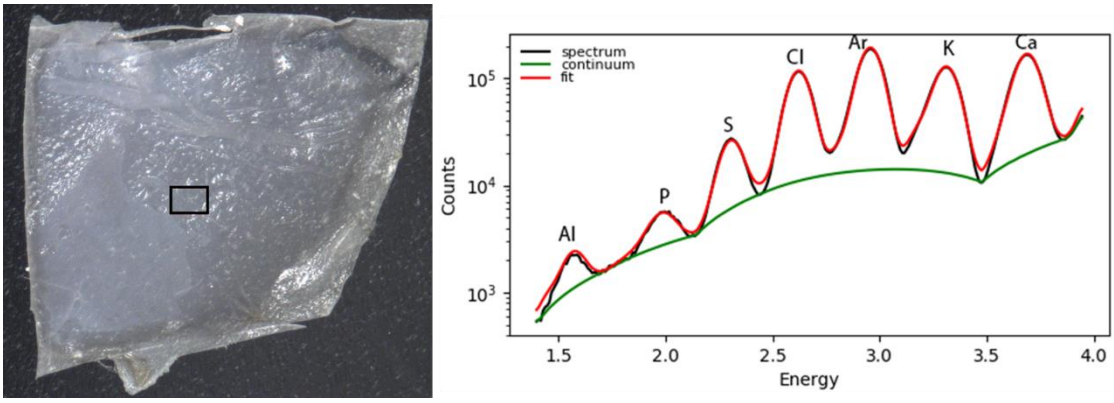


Figure 5.10: A punch biopsy of D11 tissue (left) exposed to MilliQ water. The rectangular box (black box) scanned, had an area size 0.252 mm^2. µ-XRF reference spectrum (right: black line) is correlated with the specific energy (eV) measured for each element (red line), so the range of elemental compositions found in the D11 tissue was identified.

As the fitted µ-XRF spectrum in **Figure 5.10** shows the D11 sample was exposed to Milli Q water as a negative control, and no XRF signal was detected at the energy position of Si in the D11 tissue biopsies. The other XRF signals of energy found in the µ-XRF spectrum were aligned with a number of other specific energies (eV), which allowed to identify the elements in the sample as calcium (Ca), potassium (K), argon (Ar), chlorine (Cl), sulphur (S), phosphorus (P), and aluminium (Al). In general, the elements present in the human skin tissue composed of Ca, Mg, K, P, S and sodium (Na) (Brown, 1927; V. Suntzeff and Carruthers, 1945; Vičanová *et al.*, 1998). The elements; Ca, K, S and P may also be presented in the D11 tissue. Ar comes from the chamber gas. Additionally, the presence of Al is caused by the escape peak which generated from photons leaving the detector. Cl is an element contained in PBS. Cross-sectioning of the D11 tissue is a delicate process and may occasionally allow such contamination.

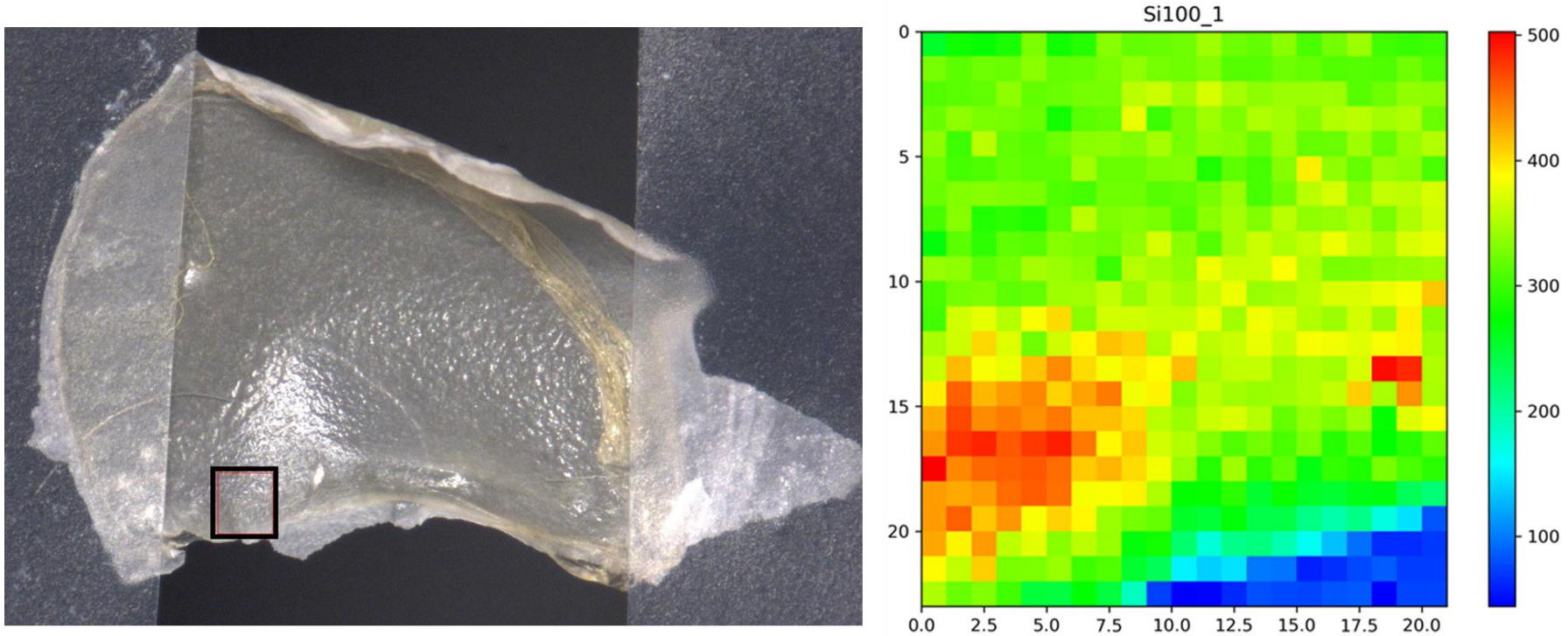


Figure 5.11: Representative image showing the surface area where μ-XRF scanned from the uppermost of D11 to 30 μm depth for the sample exposed to aSiNPs at 0.1 mg/mL concentration, size 0.396 mm^2 (left). The distribution map of Si (right), showing the accumulation amount of aSiNPs.

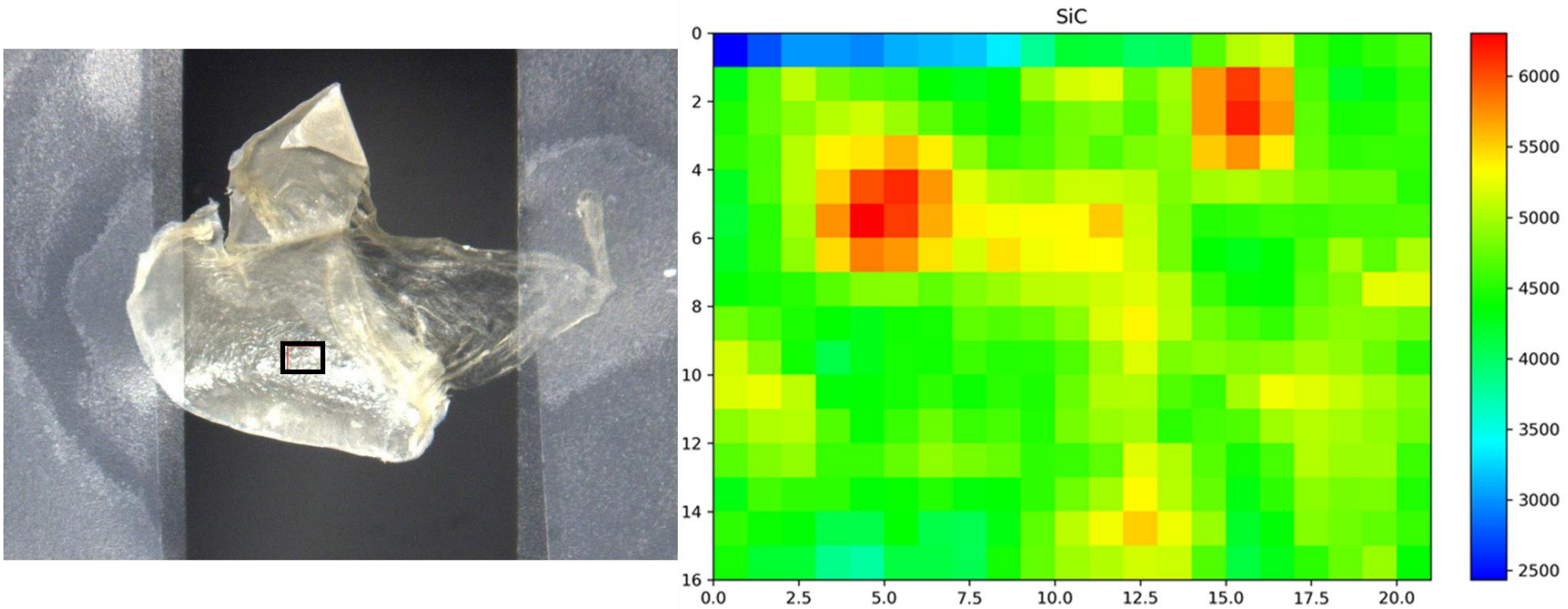


Figure 5.12: Representative image showing the surface area where μ-XRF scanned from the uppermost of skin to 30 μm depth for the sample exposed to aSiNPs at 10 mg/mL concentration, size 0.27 mm^2 (left). The surface distribution map of Si (right), showing the accumulation amount of aSiNPs.

Figure 5.11 and **Figure 5.12** show the D11 tissue biopsies that were used to investigate the distribution of Si across the skin surface. The surface distribution map of Si showed that Si content was found present extensively on the D11 tissue biopsies. It is therefore likely that the aSiNPs were able to penetrate the stratum corneum. Considering the results from zeta potential reported in Chapter 4, the synthesised aSiNPs showed a negative charge. It is therefore likely that the NPs had enhanced interaction with the cell membranes, due to their charge, and were internalised by the skin cells as proposed in relevant studies in the literature (Rancan *et al.*, 2012; Gupta and Rai, 2016). In those studies of gold (Hao *et al.*, 2017) and nano-TiO_2 (Peira *et al.*, 2014), it was proposed that due to the electrostatic interaction with a negatively charged cell membrane, positively charged gold NPs and nano-TiO_2 were capable of greater delivery through the skin. The recent result is not in agreement with the previous studies.

The finding in this study of substantial penetration may also be linked to the molecular weight of NPs which, when low (< 0.6 kDa), would allow them to be easily absorbed (Potts and Guy, 1992; Bos and Meinardi, 2000; Schäfer-Korting, Mehnert and Korting, 2007) through pores between cells (called that intercellular routes). The synthesised aSiNPs has a molecular weight of 0.0016 kDa that is likely to have led to an increase in their absorption. The main barrier function of human skin is attributed to stratum corneum (SC), the tight junctions of which play an essential role in restricting access to external substances. The mechanism by which SC acts as a barrier is through containing corneocytes and lipid-enriched regions, which impede loss of moisture and solutes. SC is composed of hydrophobic extracellular lipid components (with a long lamellar

structure) as well as lipophilic components; ceramides, free fatty acids, and cholesterol which maintain the barrier to the movement of water and electrolytes. Besides, the lipid matrix containing short lamellar structure is the hydrophilic part in SC (Hatta *et al.*, 2006), which could allow internalisation of the negatively charged aSiNPs through the SC.

Previous studies of the effect of NP surface charge on skin penetration involving negatively charged gold nanoparticles (Lee *et al.*, 2013) and silica nanoparticles (Lee *et al.*, 2016) showed higher flux of the negatively charged NPs in the skin than the positively charged particles, perhaps because of a greater diffusion coefficient for the negatively charged NP. In addition, both hydrophobic and hydrophilic parts are present in liposomes, as a vehicle to deliver the nutrients and drugs in the cell (Torchilin, 2005), and therefore may interact with either type of charged particles. The specific side of hydrophilic barrier can drive the substance passing through skin based on a hydration gradient. Moreover, the particle size of aSiNPs may influence the passive diffusion through the gaps between tight junctions (~ 6 nm) (Rancan *et al.*, 2012) and bypass the pore sizes within the stratum corneum (20 nm) (Haq *et al.*, 2018). In fact, different NP types and sizes, e.g. TiO_2-17 nm, FeO-10 nm, ZnO-26 nm can penetrate the stratum corneum after topical application (Larese *et al.*, 2009) and Au-15 nm can penetrate in dermis (Fernandes *et al.*, 2015). The penetration mechanism is likely to be related to both nanoparticle size and charge. Hence, the ability of aSiNPs for penetration may have been associated with the intrinsic properties of human skin which normally facilitate its function, but in this case inadvertently allowed aSiNPs to overcome the skin barrier.

Furthermore, the different concentrations used affected the amount of Si on the surface D11 biopsies. The higher concentration used, the higher amount of Si content was shown on the surface distribution map. The images showed that the proportion of skin exposed to aSiNPs at 10 mg/mL **(Figure 5.12)** is greater than that exposed to 0.1 mg/mL **(Figure 5.11).**

Due to the observations from µ-XRF showing high concentrations of aSiNPs on the skin surface, it is possible that aSiNPs could reach into the stratum corneum as discussed above. To further investigate the ability of aSiNPs to penetrate through deeper skin layers (i.e. epidermis and dermis), the cross-section of D11 tissue was examined in order to assess NP translocation and compare the outcome with the data presented earlier on Si coverage of the skin surface. The presence of Si from the different exposures is shown below in the distribution maps, in **Figure 5.13 - Figure 5.16.**

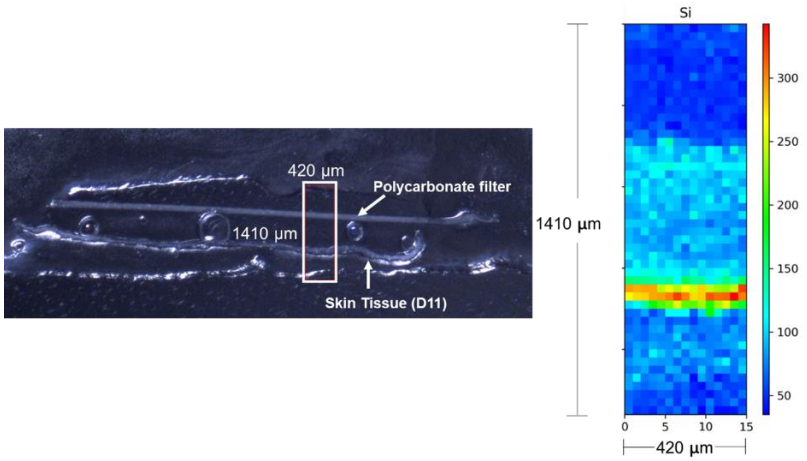


Figure 5.13: Representative image (sample no. 1 exposed to aSiNPs at 10 mg/mL) showing a cross-section of D11 tissue (left) and the presence of Si across the skin model represented by the white box. The colour scale bar is calibrated to show the relative concentration of Si found in the skin from no detection (blue) to high amount (red colour) (right).

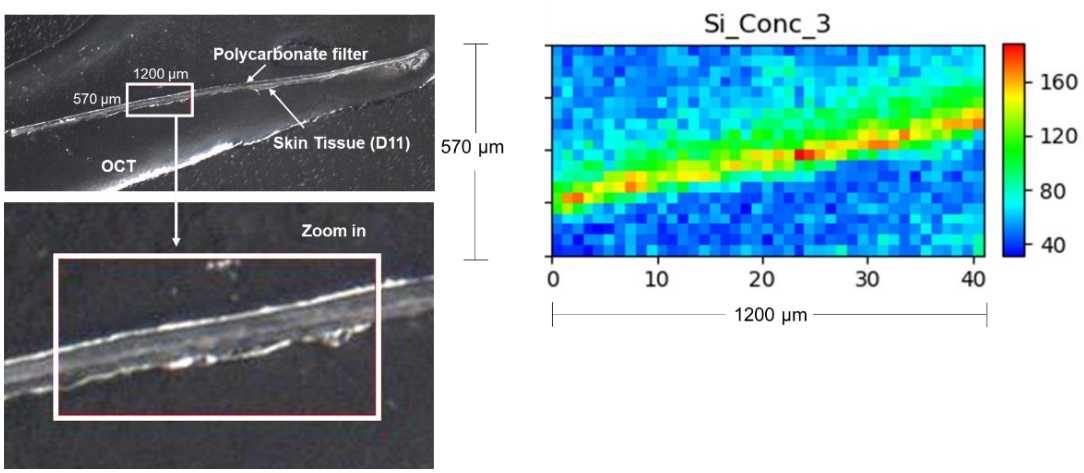


Figure 5.14: Representative image (sample no. 3 exposed to aSiNPs at 10 mg/mL) showing a cross-section of D11 tissue (left) and the presence of Si across the skin model, represented by the white box. The colour scale bar is calibrated to show the relative concentration of Si found in the skin from no detection (blue colour) to high amount (red colour) (right).

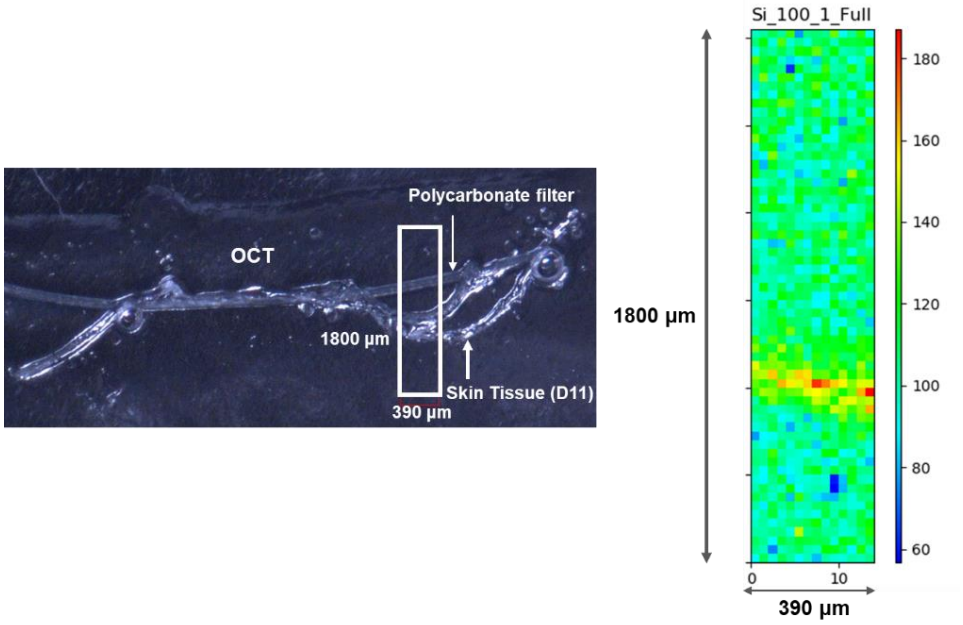


Figure 5.15: Representative image (sample no. 1 exposed to aSiNPs at 0.1 mg/mL) showing a cross-section of D11 tissue (left) and the presence of Si across the skin model, represented by the white box. The colour scale bar is

calibrated to show the relative concentration of Si found in the skin from no detection (blue colour) to high amount (red colour) (right).

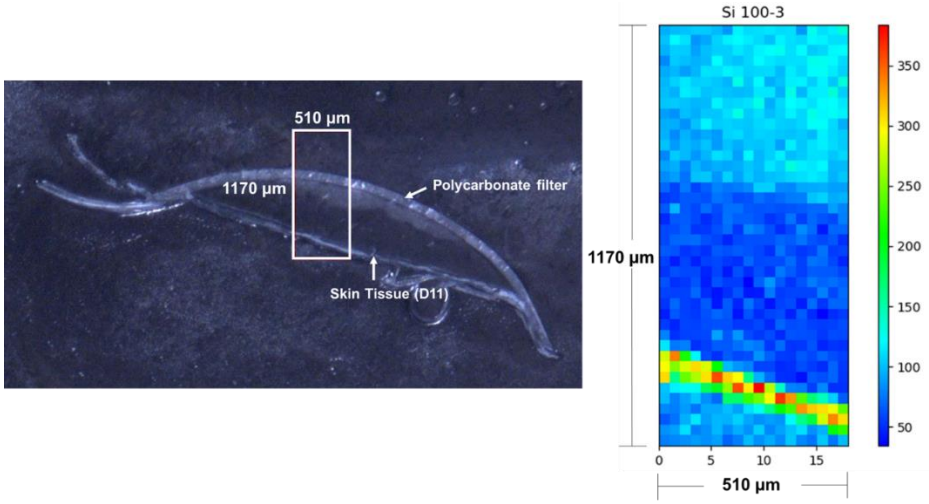


Figure 5.16: Representative image (sample no. 3@exposed to aSiNPs at 0.1 mg/mL) showing a cross-section of D11 tissue (left) and the presence of Si across the skin model, represented by the white box. The colour scale bar is calibrated to show the relative concentration of Si found in the skin from no detection (blue colour) to high amount (red colour) (right).

The D11 tissues were sectioned in the vertical direction at 70 µm thickness in order to keep the whole structure of full thickness human skin (i.e. epidermis and dermis), which were examined in each section. Here, the µ-XRF results (as shown in **Figure 5.13 - Figure 5.16**) were further verified by the D11 models which in fact demonstrated the amount of aSiNPs at low concentration (0.1 mg/mL) reached slightly greater than at high concentration (10 mg/mL), as may be seen based on the colour scale bar; however these differences may not be statistically significant. These results are in good agreement with the earlier observations of silica distribution over the skin surface. In **Figure 5.12,** the colour scale bar showed higher amount of Si on the surface of the skin at the

lower concentration, compared with the colour scale bar in **Figure 5.11**. It may be that the high concentration of NPs used in the higher exposure, can reduce the amount of absorption into the skin because of the saturation of loading as a physical skin barrier response (Wester, Noonan and Maibach, 1980; Labouta, El-Khordagui, *et al.*, 2011). It should also be noted that the exposure time seems to show a linear correlation with the amount of NP penetrating into the skin (Rougier, Lotte and Maibach, 1987; Labouta, El-Khordagui, *et al.*, 2011). The above findings are significant in the overall assessment of a link between the loading of aSiNPs onto the human skin surface and the penetration to greater depth across the epidermis layer.

5.3.2 SAXS

To enable an understanding of how the particle size of aSiNP changes during its penetration through the skin layers, the SAXS technique was used to characterise the size of particles remaining in the D11 tissue. The scattering patterns from the blank, the treated tissue, and only Kapton® tape were examined and manipulated using SAXSoPy, the detailed preparation was described in section 5.2.6. The 1D SAXS graph is shown in **Figure 5.17**

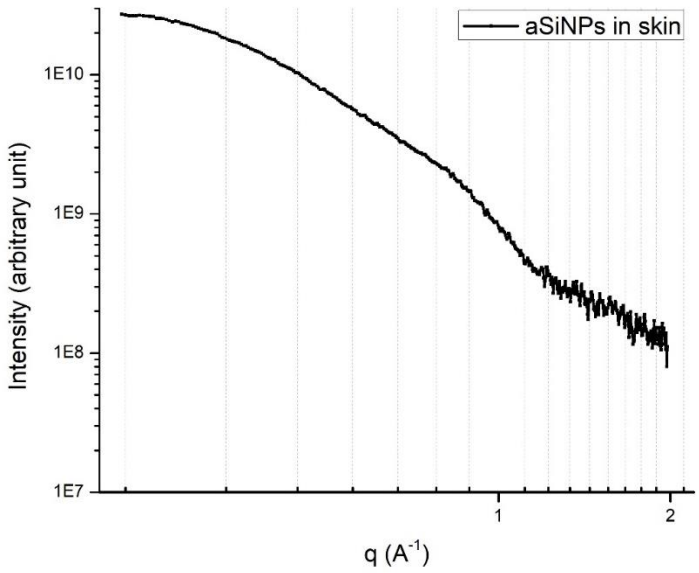


Figure 5.17: The SAXS scattering profile results for aSiNPs interspersed into the D11 tissue, fitted using SAXSsPy with a spherical model. The form factors and structure factor were present in the SAXS curve.

The form factor in Porod region uses to interpret shape and surface topography, while the structure factor in the Guinier region relates particle arrangement, i.e. agglomerate and aggregate. The spherical shape was obtained from the slope (P) of the SAXS graph in Porod region (P=4). The particle sizes of aSiNPs remaining in the D11 skin can be inferred from the SAXS data by fitting with the spherical model as shown in the equation **(5.1) - (5.3)**. The fitted SAXS graph showed the bimodal particles as same as the previous result of SAXS in section 4.6.4, Chapter 4, but aSiNPs after skin penetration increased in sizes. The results suggested that aSiNPs are approximately 6. 691±0. 617 and 11.811±1.270 nm in diameter, as shown in **Figure 5.18**. This findings are in agreement with two previous studies which showed the passive NPs permeation and described different NP size in *in vitro* skin penetration to form bigger agglomerates (Ryman-Rasmussen, Riviere and Monteiro-Riviere, 2006;

Zhang and Monteiro-Riviere, 2008; Moia, 2015). In addition, particle size is not necessarily a constant parameter as agglomeration of particles can occur over time and also in relation to experimental conditions (e.g. presence of surfactants within particle vehicle formulation). However, whilst this issue of agglomeration has been suggested as being important (as well as an important experiment variable), agglomeration state is often not reported within studies.

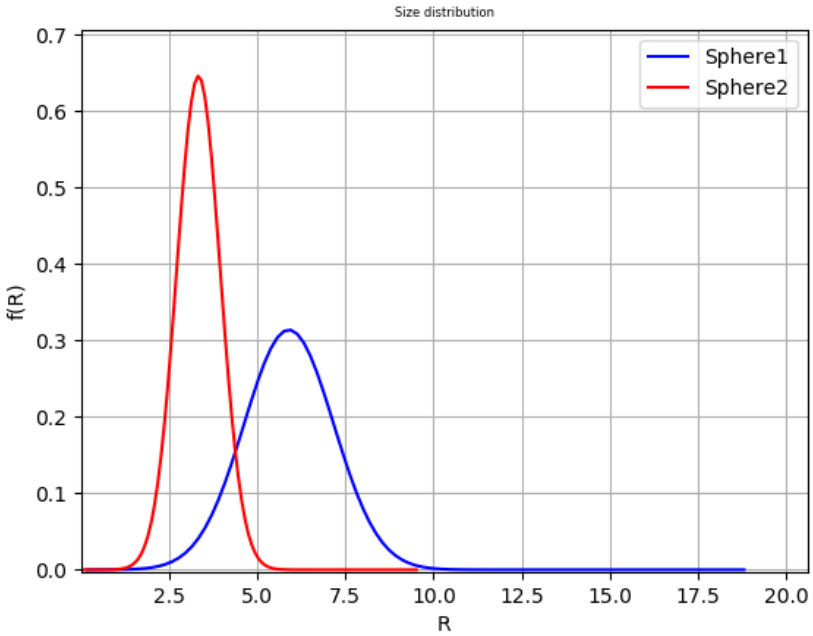


Figure 5.18: SAXS curve results for the particle sizes of aSiNPs interspersed into the D11 tissue.

5.3.3 XANES

XANES identified *K-edge* energy and the oxidation state of Si in both matrices; water and skin tissue. Only one main spectrum containing four peaks labelled A-D in **Figure 5.19** (pink line) was observed the Si*K-edge* from the standard material of amorphous silica. The pre-edge peak A occurs as a broadening at the base of the main edge feature, the main transition (Peak B), and a peak around 1847 eV (Peak C), which characterized the Si with O in the *SiK-edge*

XANES. The *SiK-edge* spectrum of colloidal aSiNPs is in agreement with the fingerprint results of Dien *et al.* (1994) (Li *et al.*, 1994). The Si*K-edge* spectra of aSiNPs in the skin tissue exposure to 0.1 and 10 mg/mL concentration are shown in **Figure 5.19**, and are quite different from the standard materials, i.e. amorphous silica (pink line) and silicon powder (black line). The apparent wide range of aSiNP compositions in the tissues, based on the numerous peaks, is intriguing and was further investigated to identify possible chemical structure including oxidation state. However, peak A (as well as the standard of aSiNP spectrum) of both D11 tissue samples is significantly more intense and shifts toward lower energy in the tissue samples corresponding to a reduced charge transfer. The shift for peak Si is related to the local structure of the Si atom that may represent different groups, such as silanol group (Si-OH) and alkyl group (Si-O-C) (Li *et al.*, 1994). A possible explanation for this chemical changed may be the large surface of NPs, which have high free surface energy and are therefore highly reactive. This may induce NP-biological environment (e.g. glycoproteins, lipoproteins, electrolytes, ions) surface interactions (Dobrovolskaia, Germolec and Weaver, 2009; Lynch, Salvati and Dawson, 2009) leading to chemical environment modifications. Both glycoproteins and lipoproteins often arrange around NPs (a process described as formation of a protein-corona). Moreover, electrolytes (or ions) found in the native human skin, such as Na^{+}, K^{+}, Mg^{2+}, Ca^{2+}, and P^{3+} may also react and modify the chemistry of Si (Brown, 1927; V. Suntzeff and Carruthers, 1945; Vičanová *et al.*, 1998). It is well established that SiNPs can trigger cells to release cytosolic Ca^{2+} overload (Guo *et al.*, 2018). It has been proposed that the interaction between silicon and excess Ca^{2+} can generate calcium silicide in the forms of

CaSi, Ca_2Si, $CaSi_2$ (Ropp, 2013). The oxidative state of Si in the form of calcium silicide is equivalent to -2 as shown in **Figure 5.19**. The data support for this observation is insufficient, hence, changes of NP structure after *in vitro* skin penetration needs to be studied further using EXAFS which may support the above observations and further indicate NP chemical modifications within the skin resulting from the penetration of NPs and potentially influencing their toxicity.

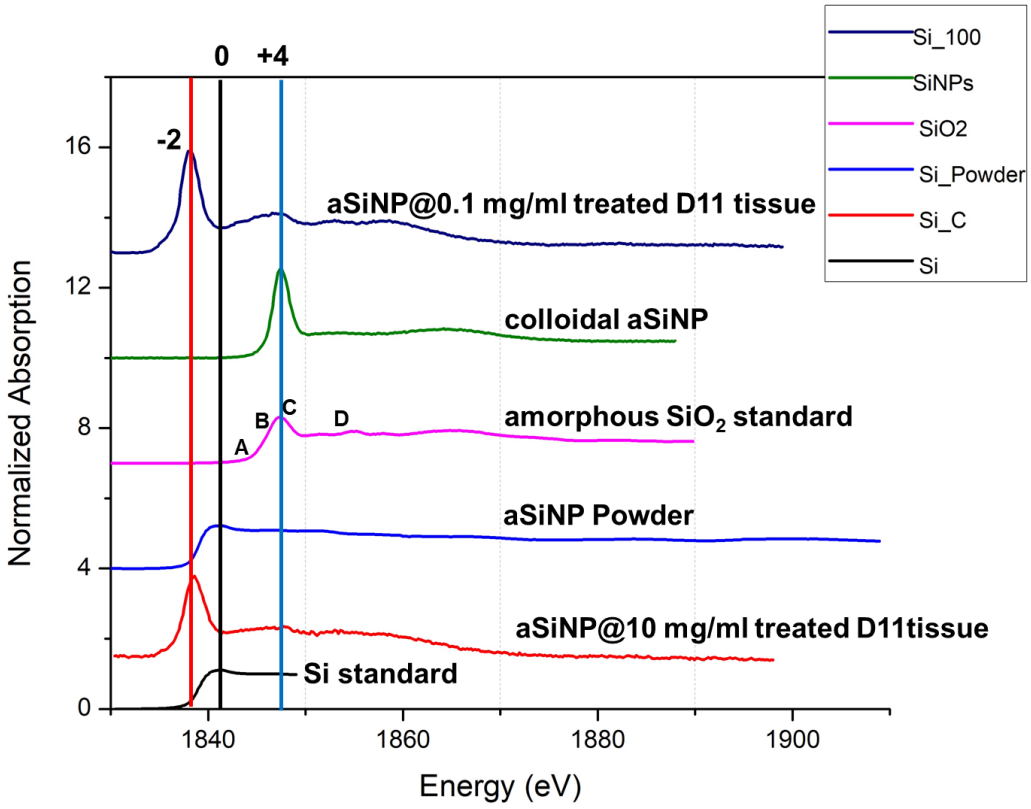


Figure 5.19: Representative Si*K-edge* XANES spectra of Si found in the skin tissue models. The spectra represent the starting suspension and powder compared to referenced standard materials: amorphous silica (SiO_2; 4+) and silicon powder (Si; 0).

5.3.4 XPS

Using XPS, wide scan spectra representing the kinetic energy of the peak positions at a sequence of energies were carried out to identify the elemental composition and surface chemical structure of the studied samples, while the peak intensities measure the quantity of material on the surface of the sample. The D11 tissues including an exposure to ultrapure water as a negative control, an exposure to aSiNPs at 0.1 mg/mL and one at 10 mg/mL were fixed onto holders with carbon tape. For each sample, the general scan was repeated two times with area size 100*100 μm^2. The high-resolution scans of XPS technique were carried out for the elements of interest such as calcium, silicon, oxygen, nitrogen, and carbon (shown in **Figure 5.20**).

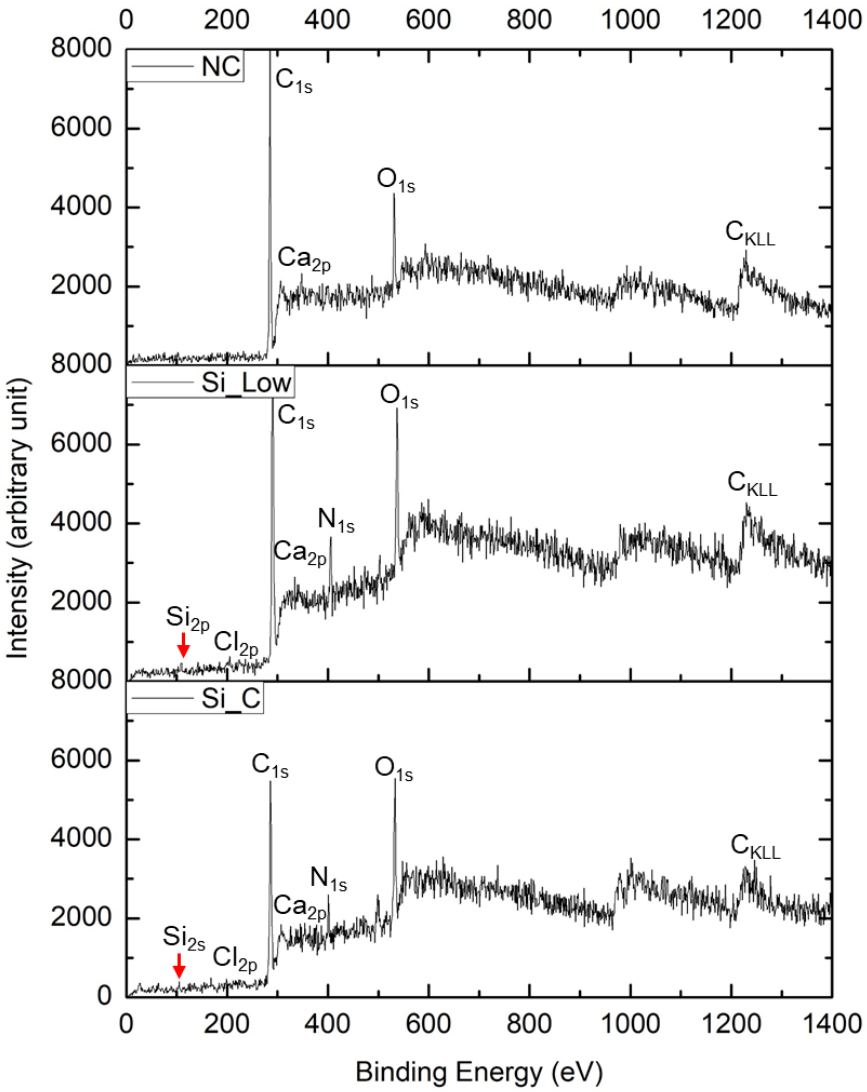


Figure 5.20: Wide Scan of Comparative Binding Energies from the samples of D11 tissues, Top: Negative Control-UPW (NC_{UPW}), Middle: Si-Low is the D11 skin exposure to 0.1 mg/mL of aSiNPs and Bottom: Si-H is the D11 skin exposure to 10 mg/mL using XPS.

The XPS spectrum of Si which was in the D11 skin exposure to aSiNPs at 0.1 mg/mL (Si@Low) is coincident with the Si-C showing the presence of elements, such as Ca_{2p}, Si_{2p}, Cl_{2p}, N_{1s}, O_{1s}, and C_{1s}. Even the intensity of XPS spectra is low signal and high noise in both samples, which may concern the small amount of aSiNPs used in the experiment.

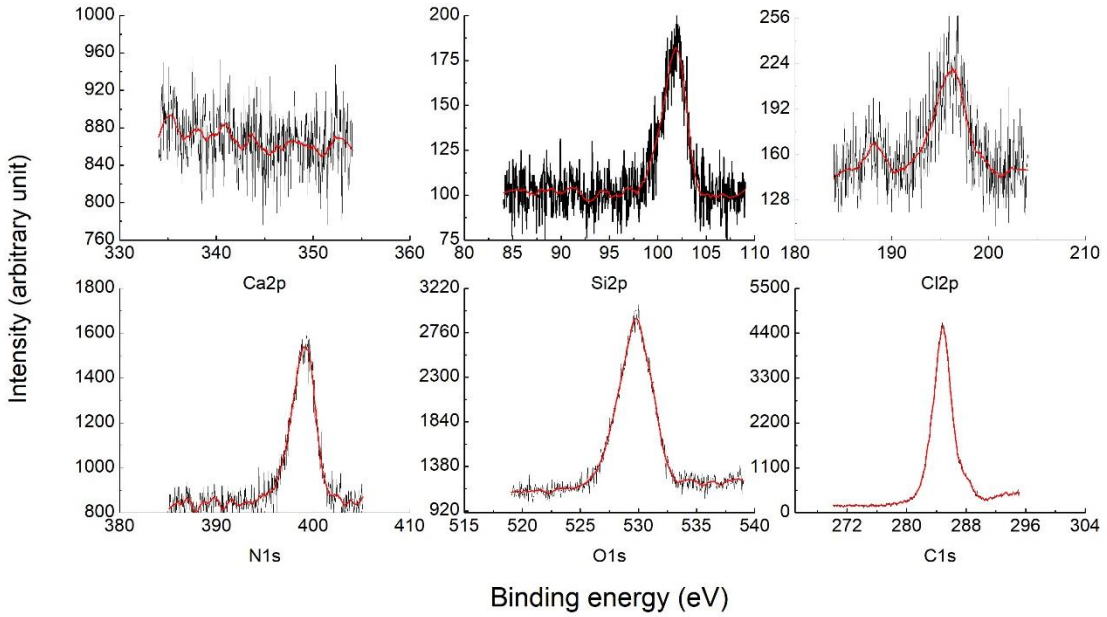


Figure 5.21: XPS spectra of the Ca2p, Si2p, Cl2p, N1s, O1s, and C1s signals acquired from the D11 tissue exposure to 0.1 mg/mL of aSiNPs. Black lines are the spectra collected, while the red lines are the result of peak fitting.

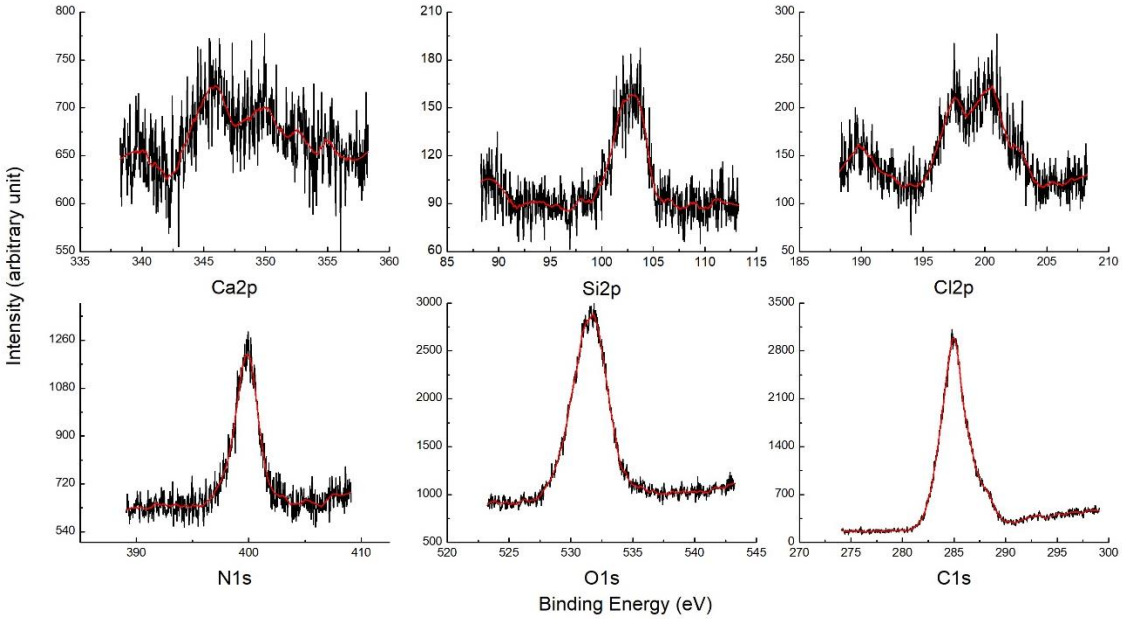


Figure 5.22: XPS spectra of the Ca2p, Si2p, Cl2p, N1s, O1s, and C1s signals acquired from the D11 tissue exposure to 0.1 mg/mL of aSiNPs. Black lines are the spectra collected, while the red lines are the result of peak fitting.

Regarding **Figure 5.20** - **Figure 5.22**, to determine the chemical structure of Si atom, binding energies of Ca2p, Si2p, Cl2p, N1s, O1s, and C1s were observed. The elemental peak positions of binding energies are presented in **Table 5.1.** Likewise, the peak positions of Ca, Si and O are coincident with the studies of Black *et al.*, 2002 and Rheinheimer and Casanova, 2016. The XPS results showed the binding energies of elements found in the skin and proposed to fit chemical structures by matching with the library reference of NIST X-ray Photoelectron Spectroscopy Database. These findings may fit a large number of chemical structural models (e.g. $CaSiO_3$ (calcium silicate), Ca_2SiO_4 (dicalcium silicate) and Ca_3SiO_5 (tricalcium silicate)) on aSiNP surface. The simulation of chemical structure correlated to NPs-biological interactions, therefore, need to be further clarified with a high resolution technique such EXAFS.

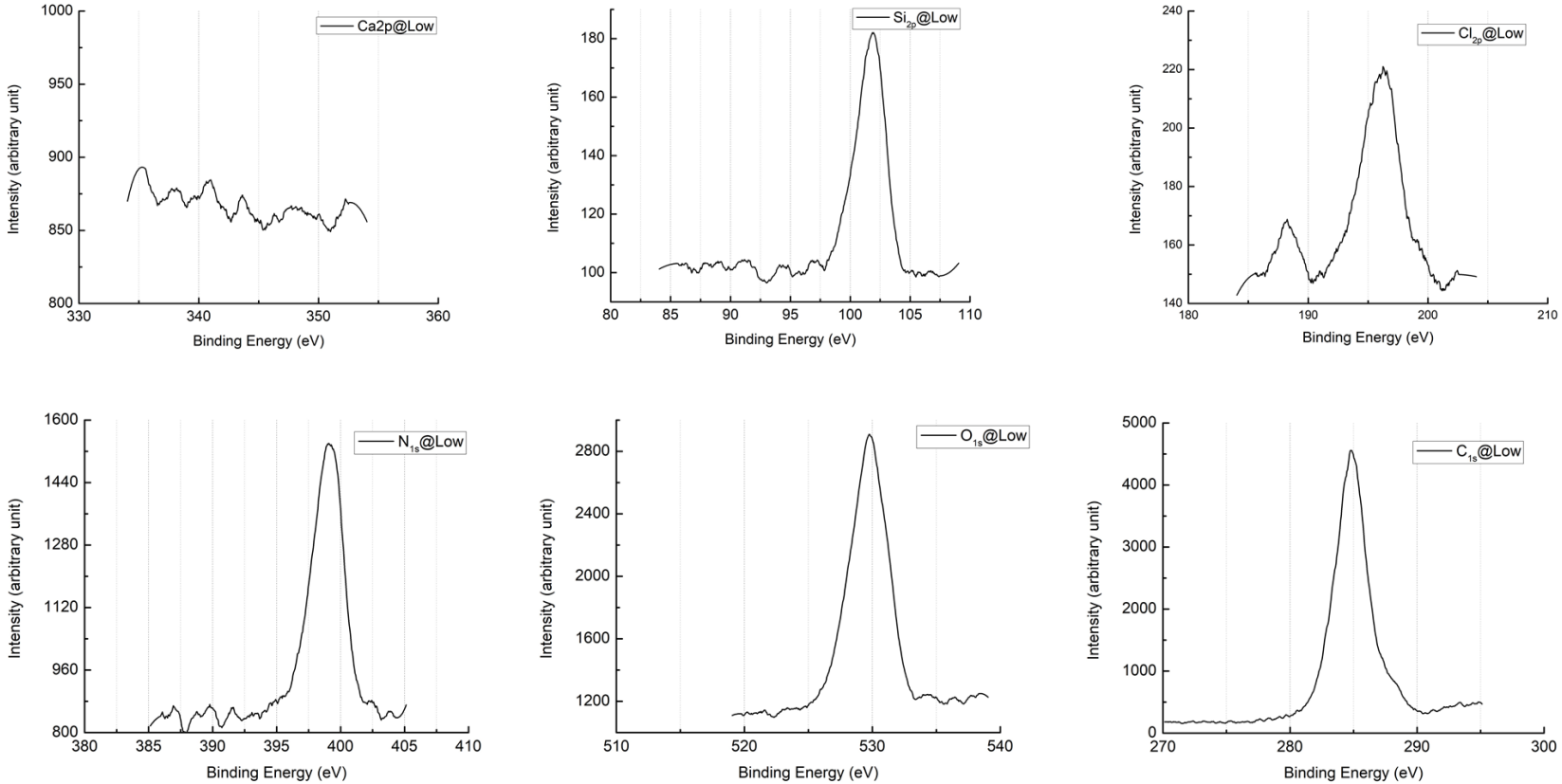


Figure 5.23: The peak fitting of the Ca2p, Si2p, Cl2p, N1s, O1s, and C1s signals acquired from the D11 tissue exposure to 0.1 mg/mL of aSiNPs.

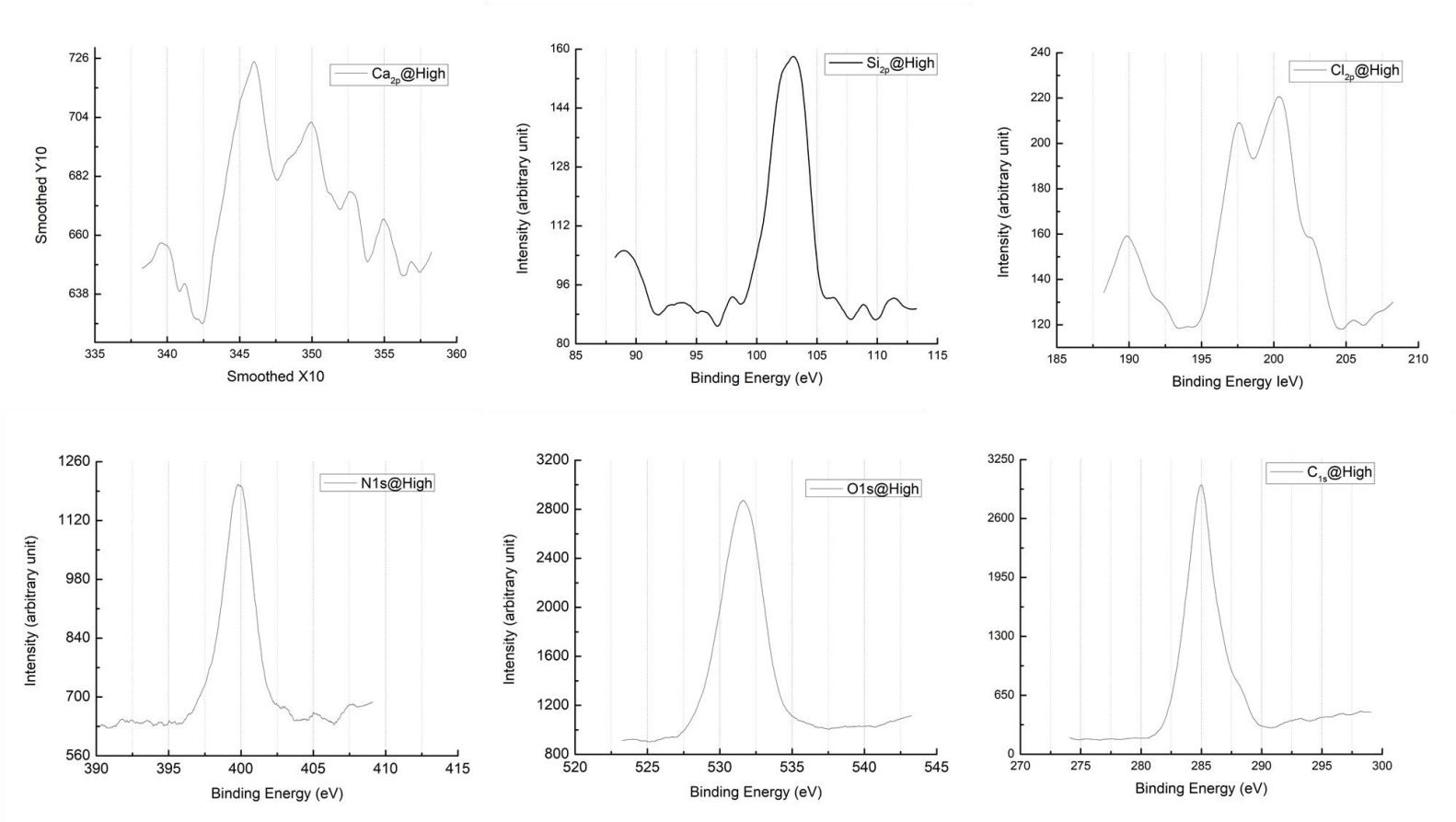


Figure 5.24: The peak fitting of the Ca2p, Si2p, Cl2p, N1s, O1s, and C1s signals acquired from the D11 tissue exposure to 10 mg/mL of aSiNPs.

Table 5.1 Peak Position for all samples.

Sample	**Peak Position (eV)**					
	$Ca_{2p\ (3/2)}$	**Si_{2p}**	**O_{1s}**	**Cl_{2p}**	**N_{1s}**	**C_{1s}**
NC_{UPW}	347.57	-	530.5	-	400.52	285.04
Si-Low	347.25	101.26	529	196	399.48	283.9
Si-C	346.25	102.87	531.25	200.12	400.11	284.67

Note: NC_{UPW} = Ultrapure water was topically applied on the D11 tissue

Si-Low = D11 tissue was exposed to colloidal aSiNPs at 0.1 mg/mL

Si-C = D11 tissue was exposed to colliodal aSiNPs at 10 mg/mL

5.4 Discussion

In the present study, the skin penetration of aSiNPs was investigated using a combination of synchrotron-based techniques in order to characterise changes in NP structure after *in vitro* skin penetration. Because the assessment of NPs in the tissue sample is not easy, the combination of technique could offer a better chance to provide a mechanistic understanding of the processes involved.

Regarding a topical application on skin at various concentrations, the distribution maps of Si on the skin surface from both exposures show steady increases in proportion. It is suggested that the aSiNPs with the sizes of 1.6 and 7 nm can invade the skin barrier along with the lipid matrices of stratum corneum and penetrate far within the epidermis layer, mostly likely through an intercellular route, i.e. gaps between tight junctions (Larese Filon *et al.*, 2015; Gubala *et al.*, 2018b). A molecule with a molecular weight lower than 500 Da can penetrate the skin (Williams and Barry, 2012; Nafisi and Maibach, 2018). The studied aSiNPs penetrated the skin model to some depth but did not pass through the polyvinylchloride filter of the model; this may imply that the barrier in dermal layers can limit NP penetration and may not allow them to invade the bloodstream. This, however, may mean that ultrasmall NPs may accumulate and (if insoluble) become a long-lasting feature within the skin layers. The detailed mechanism of such activity may depend on the specific circumstances and properties of both NPs and skin and may vary across different NPs-skin system.

The SAXS results, suggest that during interactions with the skin, the aSNP size increased from the original sizes to a larger bimodal size distribution of 6.69 and 11.8 nm in diameter. Size increases resulting from “ageing’ of the particles were also identified with no exposure to skin (as shown in section 3.6.2.4). This refers to as

Ostwald ripening effect (Alexander, Heston and Iler, 1954; Brinker and Scherer, 1990) which supports the presence of the bimodal population and the particle growth of aSiNPs in the skin models.

XANES results demonstrated the alteration of the oxidation state of silicon from 4+ to 2-, suggesting changes (reduction) in the chemical environment of Si. Additionally, the XPS results of exposure conditions (low and high concentrations) showed that the binding energy of silicon was shifted toward lower energy at 101.26 and 102.87 eV, respectively. The shift for the Si peak is related to the local structure of the Si atoms, perhaps as a result of the formation of silanol group (Si-OH) and alkyl group (Si-O-C) (Li *et al.*, 1994). The presence of silanol group. The presence of silanol group could be inducing membrane destabilization which contributes to NPs-biological environment (e.g. phospholipid, glycoproteins, lipoproteins, electrolytes, ions) interactions on NP surface (Dobrovolskaia, Germolec and Weaver, 2009; Lynch, Salvati and Dawson, 2009; Kettiger *et al.*, 2016; Contini *et al.*, 2018). Furthermore, SiNPs can trigger cells to release of cytosolic Ca^{2+} (Guo *et al.*, 2018). The possible interaction from the release of excessive Ca^{2+} can affect the chemical environment and oxidation state of Si by forming calcium silicide structure (i.e. CaSi, Ca_2Si, $CaSi_2$ (Ropp, 2013). However, the underlying mechanism of degradation of aSiNPs remains unknown. Therefore, this should be addressed in the further in-depth studies of this interaction. It is a critical need to carefully determine the underlying interaction of aSiNPs within the human skin to allow better assessment of the potential behaviour of NPs in human.

5.5 Conclusion

The combined knowledge gained from the work presented in Chapters 4 and 5, points to aSiNPs with a range of sizes 1.6 and 7 nm penetrating beyond the epidermis layer and potentially staying as a long-lasting toxicant within the skin tissue. It is currently available in the diffusion of NPs through the topical route, these result was proven to reach in deeper layer and successfully fulfilled the intended physicochemical properties (e.g. size and elemental structure) for the topical application.

As the result in this chapter, the cytotoxicity of aSiNPs on the human skin has to be addressed further and this is the topic of study in Chapter 6 which will begin with examining *in vitro* skin irritation using the reconstructed human epidermis model, observing the skin cell morphology, and quantifying the amount of cytokine response. Till now, only few studies investigated the skin irritation of aSiNPs and their inflammatory effects.

Chapter 6 Results of the effects of amorphous silica nanoparticles on Episkin™ small/reconstructed human epidermis (RhE) model

6.1 Introduction

The use of nanomaterials in cosmetics has been rapidly increasing in recent years, and this is reflected in their large-scale commercial production globally. One of the three most-produced nanomaterials for cosmetic applications in 2013 was silica nanoparticles (SiNPs) (Murugadoss *et al.*, 2017). It is expected that nano-silica will reach a global market size of 5 trillion USD by 2025 (Grandview Research, 2017). Amorphous SiNPs (aSiNPs) are being included in a range of cosmetic formulations (e.g. foundations, lipsticks, and blushers etc.) because of their simplicity of preparation, tunable morphology, easy surface modification, unique physicochemical properties, multifunctionality as well as their biocompatibility and biodegradability. For example, silica nanomaterials are mostly used as a mineral to enhance the effectiveness, texture and shelf-life of various commercial cosmetics and act as an anti-caking agent, and as an absorbent to release active compounds over time. However, the widespread use of cosmetics with aSiNPs increases human exposure and may result on effects to human health and the environment that are not yet known. An assessment of skin irritation is mostly required as a means of evaluating biological safety, as an alternative method to other commonly used *in vivo* and *in vitro* models (Eskes *et*

al., 2007; ISO, 2014; Corporation, 2017). Previous *in vitro* and *in vivo* studies have focused on the relationship between aSiNP size and toxicity, however, no consensus has been reached in part due to the variable properties of the silica nanomaterials (Napierska *et al.*, 2009). For example, *in vitro* skin toxicity of aSiNPs (at size 70, 300 and 1000 nm particles) using mouse epidermis with keratinocytes and Langerhans cells revealed an increase in cellular uptake and cytotoxicity associated with a reduction in particle size (Nabeshi *et al.*, 2010). Several investigations in mice have shown that exposure to smaller-sized aSiNPs (70 nm) leads to cellular damage in the skin and significant reactive oxygen species (ROS) formation in cells (Nabeshi, Yoshikawa, Matsuyama, Nakazato, Matsuo, *et al.*, 2011), possibly due to the larger surface area of smaller nanoparticles (Nel *et al.*, 2006). Moreover, aSiNPs in diameter of 50 nm induced significantly glutathione depletion and reactive oxygen species (ROS) generation, which correlated with reduction in cellular antioxidant level that affected cytotoxicity (Liang *et al.*, 2014).

More recently, Palmer *et al.* (2019) found that 20 nm aSiNPs reduced by nearly 50% the 2, 4-dinitrofluorobenzene (DNFB) induced skin swelling response in mouse ears, skin expression of cytokines (i.e. interleukin 6, interleukin 1beta, keratinocyte chemoattractant, interferon gamma and macrophage inflammatory protein 2), compared to ears treated with only DNFB, after 24 hours. This finding may concern the adaptive immune response corresponding to aSiNP exposure to a smaller size (20 nm), but a larger particle size (400 nm) is not (Palmer *et al.*, 2019). As in the aforementioned *in vitro* studies, the smaller particle frequently induces more toxicity, but the results of the study by Palmer et al. (2019) is

different. Therefore, skin exposure to aSiNPs needs to further consider in cytotoxicity and to extend to immune response tests.

A typical cytotoxicity for safety assessment normally involves identifying the potential for skin irritation performed using *in vivo* and *in vitro* models (Eskes *et al.*, 2007; ISO, 2014). *In vivo* experiments have been performed by testing in rabbit; Draize test (Park *et al.*, 2011) and mouse; local lymph node (Park *et al.*, 2013). *In vitro* experiments are performed on human keratinocyte cell line HaCaT and dendritic cells (Rancan *et al.*, 2012), mouse keratinocytes HEL-30 (Yu *et al.*, 2009), and the HaCaT cells and an immortal keratinocyte cell line (Palmer *et al.*, 2019). Once, the *in vitro* SkinEthic® Episkin™ was used to evaluate the potential corrosion of SiNPs (as followed the OECD guideline 431) in the range diameter of 10-20 nm (Tedesco *et al.*, 2015) and the *in vitro* 3D reconstructed skin micronucleus EpiDerm® for genetic toxicity assessment of BASF Levasil® SiNPs (16 and 85 nm) (Wills *et al.*, 2016). However, this specific model has not been tested on ultra-small (2 and 7 nm) synthetic amorphous silica nanomaterials before this work. In the present study, human skin irritation of aSiNPs at 10 mg/mL was carried out using the RhE *in vitro* model, following a typical OECD test protocol with modifications to adapt it to nanomaterials and with a number of additional techniques/methods, e.g. ELISA and histological assessment.

6.2 Chemicals

6.2.1 Reagents

Sodium dodecyl sulphate (SDS) and 3-(4,5-Dimethylthiazol-2-yl)-2,5-diphenyltetrazolium bromide (MTT powder) were purchased from Sigma-Aldrich. Dulbecco's phosphate buffered saline (D-PBS) was purchased from Gibco and Hyclone. SDS was prepared to 5% w/v of ultrapure water, both SDS and PBS were used as positive and negative controls, respectively. Acidic isopropanol was prepared by using 1.8 mL of 12 N HCl in 500 mL of isopropanol, the final concentration is 0.04N HCl.

Regarding the ELISA assay, the kit was purchased from Boster Biological Technology that contains Anti-Human IL-1α Pre-coated 96-well strip microplate, Human IL-1α standard, Human IL-1α Biotinylated antibody (100x), Avidin-Biotin-Peroxidase complex (100x), sample diluent, antibody diluent, Avidin-Biotin-Peroxidase diluent, colour developing reagent (TMB), stop solution 3,(4,5-dimethylthiazol-2-yl)-2,5-diphenyltetrazolium bromide.

6.2.2 Colloidal Silica Nanoparticles

A suspension of amorphous silica nanoparticles (aSiNPs) was synthesized following a published method using the lysine-silica process and detailed characterization reported previously (Davis *et al.*, 2006; Thomassen *et al.*, 2010; Musigapong *et al.*, 2019). Particle size in the suspension of the stock solution was assessed as bimodal, at 2 nm and 7 nm; particle concentration was 10

mg/mL with negative surface charge (-35 mV) as detailed in section 4.6.1 and 4.6.4, Chapter 4.

6.3 Reconstructed Human Epidermis (RhE) Model

Reconstructed human epidermis (RhE) models, small size (0.5 cm^2), day 17 (RhE/S/17) were purchased from EpiSkin™ (Lyon, France) and detailed information of quality controls for this batch was presented in **Table 6.1**. The commercial maintenance and assay media used in this study were used as cell culture media containing the necessary nutrients for skin cells. They were purchased from EpiSkin™ and their compositon is not made available by the manufacturers. To learn how to employ the model correctly a training course on how to apply the skin model and skin irritation test was taken at Episkin™, Lyon, France. Prior to use, the RhE models were inspected to ensure a good condition according to manufacturer instructions, i.e. colour of media, pH and temperature. Then, the culture insert containing epidermis and a collagen matrix (shown in **Figure 6.1**) were transferred to the maintenance media and incubated for 24 hours.

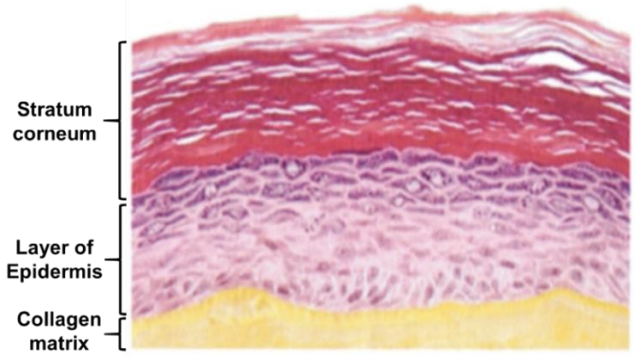


Figure 6.1: Morphology of the RhE/S/17 model, Batch No: 18-EKIN-015; reprinted with permission of EpiSkin™.

Table 6.1 Quality controls of RhE/E17 (Batch no. 18-EKIN-015) from EpiSkin™

Test	Specification	Result
Histology scoring (HES stained vertical paraffin sections)	≥ 19.5	23.1 ± 0.4 (CV = 1.6%)
	Well-differentiated epidermis consisting of a basal layer, several spinous and granular layers and a thick stratum corneum	Satisfactory
IC 50 determination (SDS concentration, MTT test)	1.5 mg/mL ≤ IC50 ≤ 3.0 mg/mL	2.2 mg/mL

6.4 MTT assay

The MTT assay is a method to determine mitochondrial activity in which the yellow tetrazolium salt MTT gets converted into purple formazan crystals when cell death occurs. The optical density (OD) of formazan concentration is obtained by using a microplate reader (Multiskan Sky spectrophotometric microplate reader; Thermo Fisher) at 540 nm.

6.4.1 Assessment of MTT Interference of the Test-Substance

To ensure that chemicals used in the test do not interfere with the MTT reagent, the following procedure is done before starting the experiment. 10 µL of aSiNPs were added into 2mL of 0.3 mg/mL MTT solution and incubated for 3 h at 37 °C. If blue or purple colour was observed, it is deduced that the chemicals tested can

likely interfere with the ability to stain tissues. As **Figure 6.2** shows, the aSiNP suspension did not show any colour and thus is not expected to interfere with the MTT assay.

In a case where the tested substance was interfering with the MTT assay by showing purple or blue colouration of the MTT solution, further steps would have been required to evaluate the non-specific reduction of MTT value (%NSMTT) and use for correcting the OD reading. Each tested substance including the negative control was applied on three killed epidermis samples, which is a living epidermis model cultured in a distilled water instead of a maintenance media and incubate for 48 hours. Three untreated killed epidermis are prepared as a negative control. The MTT solution would allow to react for 3 hours to enable any binding to take place. After that, the OD values of each sample are measured at 570 nm wavelength as the endpoint of the experiment using a microplate reader.

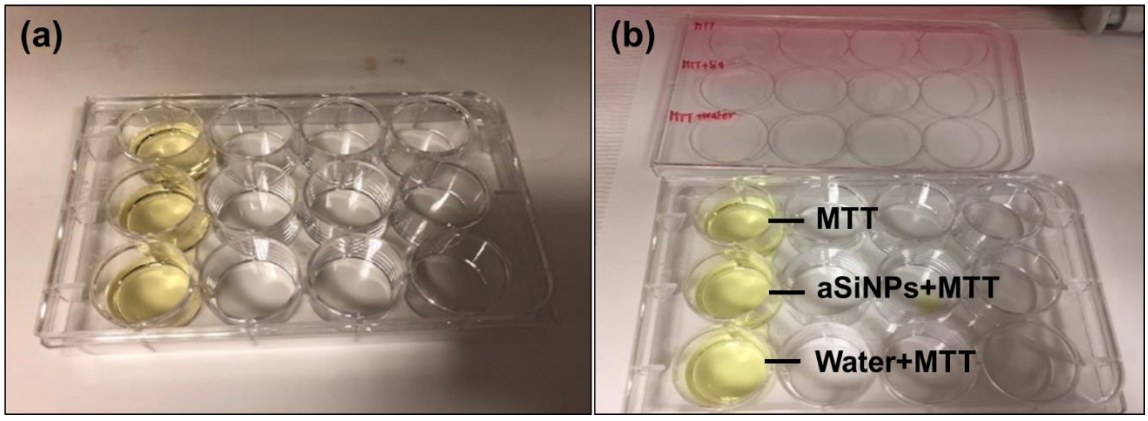


Figure 6.2: Images from experiments investigating potential reaction between the aSiNPs suspensions of this study and the MTT assay. Ultrapure water was used as a control (i.e. no interaction substance/no MTT-reducer); picture (a) shows the solutions' colour before and picture (b) after 3 h incubation.

6.4.2 Assessment of the Colour Potential of the Test-Substance

Prior to any treatment, the aSiNPs suspension was evaluated for the potential to induce colouration, when interacting with water, simulating a humid environment of the skin tissue. This change may interfere with the assay, which leads to a false estimate of viability. 10 µL of aSiNPs were added in 90 µL of water in an Eppendorf tube, and were shaken for 15 minutes. At the endpoint, the colour of the test-chemical was checked, the colour was detected by visualisation and measured OD value by microplate reader. As a result, aSiNPs suspension do not have the potential to interfere with the assay.

In case of the substance staining the tissues, a further inspection would be required to evaluate and estimate the non-specific colour value (%NSC_{living}) from the OD value of chemical substance and negative control (PBS). The staining ability of the substance will then be used to subtract the non-specific OD and thus obtain the true % viability.

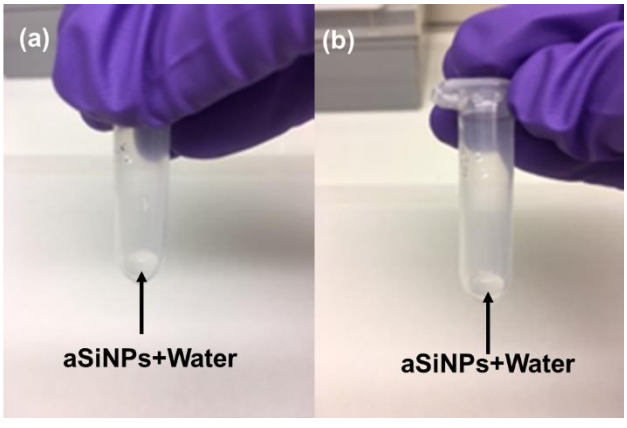


Figure 6.3: Examples of testing the colour potential of the aSiNP suspensions; (a) and (b) the colour of the suspension before and after shaking for 15 minutes.

In summary, both MTT interference and colour potential assessment of aSiNPs showed that no interference with the MTT assay and no colour potential was detected from the aSiNPs treatments.

6.4.3 Treatment

10 µL of each substance (aSiNPs at 10 mg/mL concentration, positive and negative controls) were pipetted on the top of the RhE in three independent experiments. The small sterile flat-ended forceps were used to spread the substances thorough the uppermost epidermis and then left in the room temperature for 15 minutes. Dulbecco's PBS with calcium and magnesium (Ca++ and Mg++) and 5% SDS were used as the negative (NC_{PBS}) and positive (PC_{SDS}) controls, respectively. Treatments were carried out in triplicate, using three different reconstructed human epidermis samples. 25 mL of PBS was used to rinse the treated tissues, which were then transferred to fresh medium and placed in the incubator for 42 h at 37 °C, 5% CO_2 and 95% humidity.

6.4.4 Endpoint

A cellular metabolic activity relates a mitochondrial respiration activity due to the cellular energy capacity of a cell. MTT assay assesses the enzymatic reduction of a tetrazolium component (MTT) to MTT-formazan that is catalysed by the mitochondria of viable cells. MTT assay is a colourimetric assay which was used as an indicator of cell viability and cytotoxicity (Mosmann, 2005). Tissues were washed with PBS and placed in a well where 2 mL of 0.3 mg/mL MTT solution filled in. The tissues were incubated for 3 hours at 37 °C, 5% CO_2 and 95% humidity. After 3 hours of incubation, the epidermis lying on the collagen matrix

were sectioned in a circle shape, and then collagen matrix was separated from the epidermis.

After that 500 µL of 0.04 N acidic isopropanol was added in each Eppendorf® where the epidermis tissues were placed into. The Eppendorf® were left overnight at room temperature in order to extract formazan crystal from the epidermis tissues. At the end of the formazan salt extraction, the 500 µL isopropanol solution (in each Eppendorf®) were aliquoted (at 200 µL) in two new wells using a 96 well plate as shown in **Figure 6.4**, and the OD value was quantified using a microplate reader at 570 nm. The dark purple colour represents the high activity of cellular enzymes from living keratinocytes. If the colour is light purple, this may indicate the reduction of living keratinocytes. The assay acceptance criteria for NC_{PBS} and PC_{SDS} are shown in **Table 6.2**. The mean of OD_{570} was taken from three independent tissues and compared to the negative control. The decision on classification of aSiNPs as an irritant for skin irritation was done as per the prediction model in section 3.2 according to the United Nations Globally Harmonised System (UN GHS, 2002) and Guidance to Regulation (EC) No 1272/2008 on classification, labelling and packaging (CLP) classification (**Table 6.3**) (European Chemicals Agency, 2017).

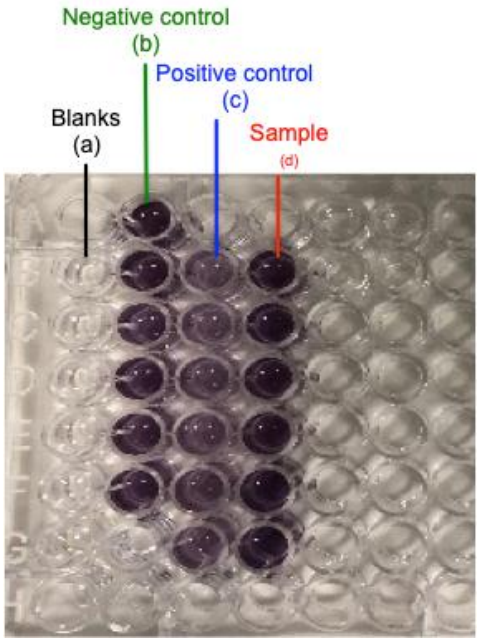


Figure 6.4: Three tissue exposures, each aliquoted in duplicate are shown here with the formazan added, leading to 6 wells per treatment. (a) Blank wells, (b) negative control (NC_{PBS}) wells, (c) positive control (PC_{SDS}) wells, (d) aSiNPs treated wells.

Table 6.2 Assay acceptance criteria for the Episkin™ Skin Irritation Test

Acceptance criteria	**Optical Density (OD, %)**
NC_{PBS}: OD value	OD > 0.6
PC_{SDS}: mean viability	≤40%
Tissue variability of all tests: % viability	SD ≤18

Table 6.3 The prediction model of skin irritation potential from the UN GHS and EU CLP classification to hazard communicate in the form of labelling for skin irritation.

***In vitro* results**	***In vivo* classification**
Mean tissue cell viability ≤50%	Category 2: Irritant
Mean tissue cell viability > 50%	No Category

6.5 Histology

6.5.1 Technique

Histology is the study of microanatomy of cells, tissues, and organs which involves visualising their structure using a microscope. It provides information between structure and function, correlating possible causes of cell differentiation, cell proliferation, and/or cell death and treatments. Haematoxylin and eosin (H&E) stains are commonly used to colour cells and tissues for histological study. The eosin stain is an acidic dye, which reacts with the basic components in cells, such as cytoplasmic proteins, intracellular membranes, extracellular fibres and epithelial keratinocytes in red or pink. The haematoxylin stain is a basic dye to colour acidic structures, i.e. nucleus, and parts of the cytoplasm containing RNA in a purplish-blue. Histological assessments were carried out at the Institute of Cardiovascular Sciences, the University of Birmingham.

6.5.2 Sample Preparation

6.5.2.1 Embedding

The treated epidermis (RhE tissue) from the *in vitro* skin irritation test (as shown in **Figure 6.5**) were preserved in the freezer at -20˚C before they were prepared for histological analysis. To preserve the skin structure and cross-section, RhE samples were embedded in a clear solution, namely Optimal Cutting Temperature (OCT) solution. A square sample block is used as a mould (about 1 cm^2 area) to contain OCT and fit the treated RhE tissues in each block. The prepared samples were frozen rapidly in liquid nitrogen until the tissue hardens around 30 seconds and then stored in the freezer at -80 ˚C.

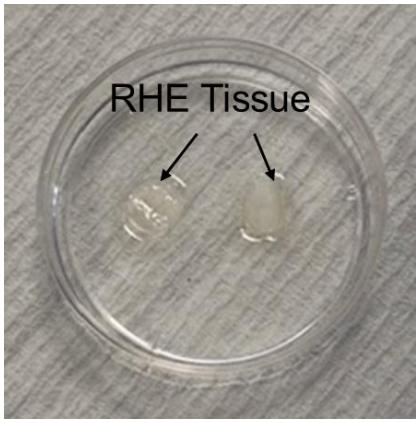


Figure 6.5: An example of preserved tissues from skin irritation testing.

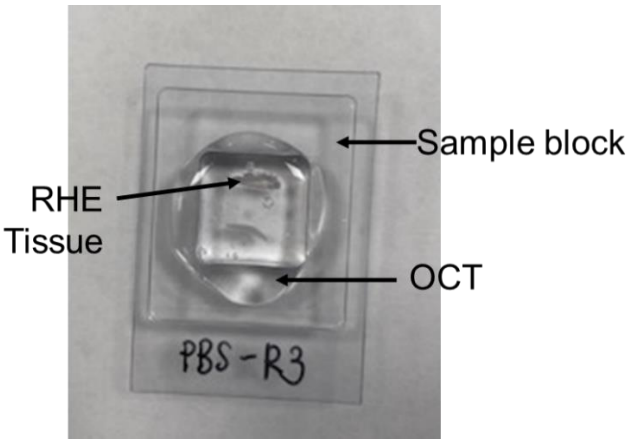


Figure 6.6: Embedded RhE tissue in OCT solution on a square sample block.

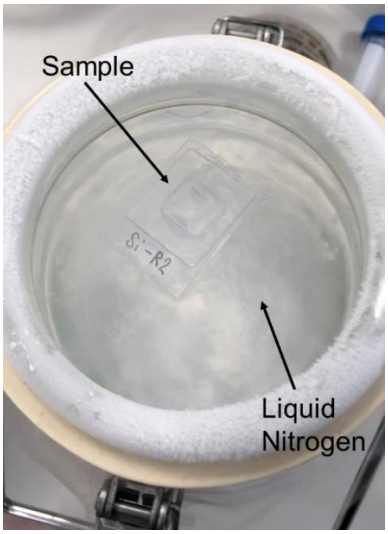


Figure 6.7: Embedded sample in liquid nitrogen until tissue and OCT harden.



Figure 6.8: Samples (frozen sections) ready for thin sectioning.

6.5.2.2 Sectioning

The sectioning procedure is a detailed information to prepare an appropriate RhE tissue for H&E staining. Firstly, the fixed RhE tissues in OCT were mounted on a stage of the cryostat and trimmed the OCT until seeing the edge of RhE tissue with a cold knife (keep in -30 ˚C). Each tissue sample was cross sectioned at 20 µm thick for three pieces, which were placed on an individual polystyrene slide for H&E staining and visualising the structure of tissue with a microscope.

6.5.2.3 H&E Staining

H&E staining is widely used for medical diagnosis and histological assessment in general. H&E staining is used to dye the tissue including cell membrane, nucleus, cytoplasmic parts of cell, etc. The step guide of H&E staining can be done quickly and in this study, the guide of Rolls and Sampias (2019) (Rolls and Sampias, 2019) was adopted as follows. As the section 6.5.2.2, the cross sectioned tissues on the slides were started with 4% paraformaldehyde and performed in the solution at room temperature for 10 minutes. Then the slides were immersed in 100% ethanol for 10 minutes, repeated in 90% ethanol for 5 minutes and in 50% and 30% ethanol for 1 minute each. The aforementioned procedures were used

to prepare the tissues properly and also provide a well balance of their properties before staining. After that, the tissues were rinsed with plenty of PBS for 5 minutes and subjected to haematoxylin stain for 5 minutes. The tissues were rinsed thoroughly with running tap water after placing them in 0.3% acid alcohol for 1 minute. The tissues were rinsed with plenty of Scott tap water (bluing agent) to remove any potential for inconsistency, i.e. alkaline causing uneven Eosin staining and dyed with Eosin for 30 seconds. The tissues were retreated with paraformaldehyde and absolute alcohol, two changes of 10 minutes each for dehydrating. These tissues were mounted with Xylene for 5 minutes for clearing and covered with the glass coverslips.

6.5.2.4 Histological Evaluation

Epidermal morphology was observed and imaged using a microscope. The images were used to evaluate the structure by comparing with the negative control treated tissue or normal human skin epidermis.

6.6 ELISA: Human Interleukin-1α (IL-1α) Immunoassay

6.6.1 ELISA Technique

Enzyme- linked immunosorbent assay (ELISA) is an immunoassay method allowing detection of secretory cytokines in the biological samples and quantification of peptide, protein, antibody and hormone levels (Boster Biological Technology, 2019). ELISA correlates the specific antibodies binding the target antigen using various techniques, i.e. direct, indirect, sandwich, and competitive ELISAs. In ELISA, antigen-antibody combination is used to indicate the presence of antigen binding and quantify colourimetric from enzyme activity. ELISA is

commonly performed in 96-well polystyrene plates, where specific antigen-antibody as a substrate has been previously passively immobilized on the wells. The substrate can interact with the interested enzyme as a subcategory of the cytokines, consequently forming the conjugation between a substrate and enzyme. The product of the interaction will be quantified the amount compared to the calibration curve of the standard product. In this study, the amount of Interleukin 1 alpha (IL-1α) is determined as followed.

6.6.2 Preparation of Reagents

Prior to use, all reagents, which were detailed in section 6.2.1 were brought to 37˚C for 15-20 minutes. The wash buffer powder was dissolved in 1000 mL of deionized water and stored at 4˚C for a week. 100 µL of human IL-1α Biotinylated antibody was mixed by adding 1 µL of Antibody diluent. 1 µL of Avidin-Biotin-Peroxidase diluent was added in 100 µL of Avidin-Biotin-Peroxidase complex. the diluents of Antibody. These solutions are recommended to use within 2 hours of preparation.

6.6.3 Calibration Human IL1A Standard Preparation

A calibration curve of Human interleukin - 1alpha (IL-1α) standard is prepared prior to quantifying the concentration (pg/mL) of IL-1α found in the samples as comparative references for analysis. The range of IL-1α concentrations was prepared at 0 pg/mL, 4.7 pg/mL, 9.4 pg/mL, 18.8 mL, 37.5 mL, 75 mL, 150 mL, 300 pg/mL using lyophilized human IL1A from Boster Biological Technology. The concentrations were measured using a microplate reader at 450 nm and presented in the value of optical density (OD) absorbance. The standard

calibration curve provides the fitting equation and the coefficient of determination (R^2) as shown in **Figure 6.9**.

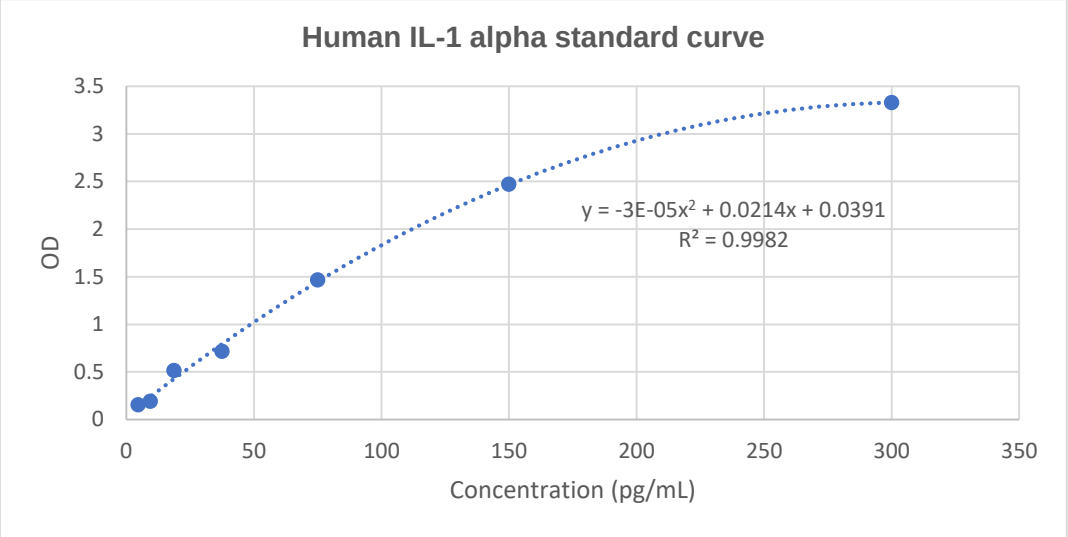


Figure 6.9: The calibration curve provides the relationship between the concentration of Human IL-1α (X-axis) and OD value (Y-axis), demonstrating in the quadratic equation.

6.6.4 Sample Preparation

Human IL-1α protein level was determined using ELISA PicoKine® Kit as per the manufacturer's instruction as an indicator for skin inflammation. At the end of the RhE exposure, the media underneath the chamber cell of each RhE exposure was collected and centrifuged at 7000 rpm at 4°C for 10 min. The supernatants were transferred to Eppendorf® tubes and diluted with sample diluent (so that the ratio of sample is within the range of the standard curve). 100 µL of the sample was added in duplicate into wells of a 96-well plate. The 96-well plate was sealed with a plate sealer and incubated at 37°C for 90 minutes to allow the secreted cytokines to react with the captured antibody. After the reaction, the liquid was discarded. Following that step, 100 µL of 1xBiotinylated Anti-Human were added

in each well, sealed, and then incubated at 37°C for 60 minutes to allow the proteins to conjugate to the enzymes. Then, the unbound protein was discarded through washing 3 times. The next step was to add 100 µL of 1xAvidin-Biotin-Peroxidase complex into each well and incubate at 37°C for 30 minutes. This resulted in the formation of a “sandwich” form between the immobilized antibody and the enzyme-labelled antibody. The wells were washed 5 times by using a washing buffer. After that, TMB colour-developing reagent was added to each well, kept in the dark at 37°C for 25 min. The top four standards acquired a blue shading as a result, seen in **Figure 6.10**. Then, 100 µL of TMB stop solution was added into each well, the solutions turned into yellow shading (see **Figure 6.11**) and were at this stage ready to be read for their optical density absorbance by a microplate reader at 450 nm.

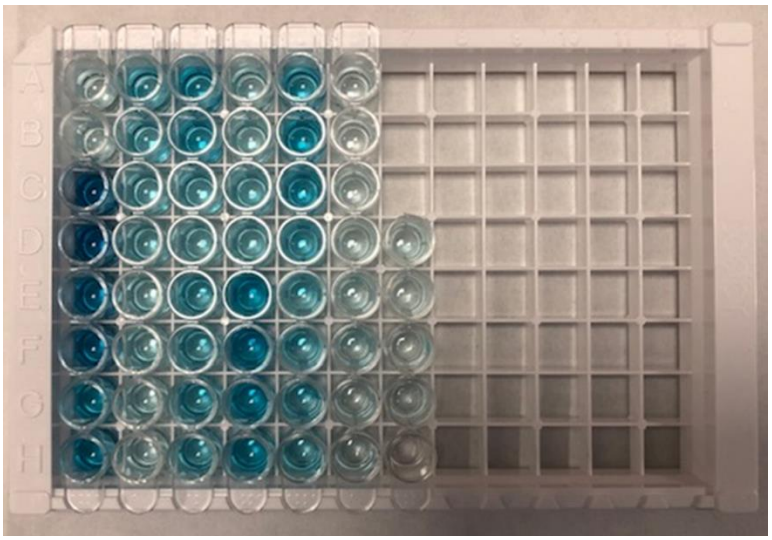


Figure 6.10: Human IL-1α Standard solutions having acquired blue shading by adding TMB colour-developing reagent

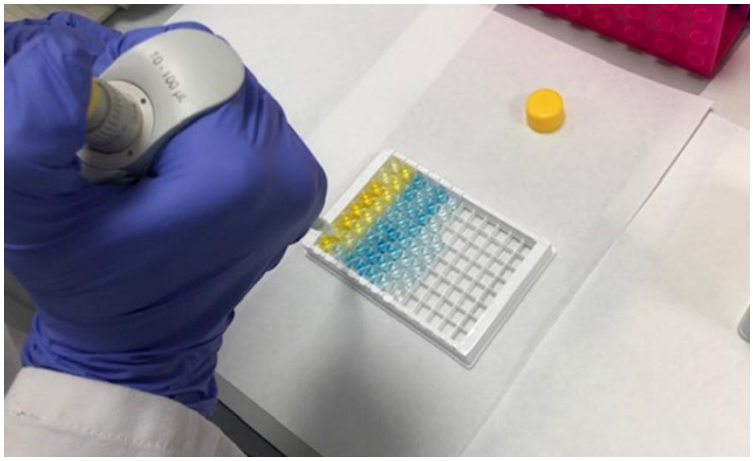


Figure 6.11: Human IL-1α Standard solutions having acquired yellow shading by adding TMB stop solution

6.6.5 Endpoint

Within 30 minutes of stopping the reaction, the OD absorbance should be read with a microplate reader at 450 nm. The percent viability of each sample was calculated to negative control using (**6.1).**

$$\%Viability_{Sample} = \left[\frac{OD_{Sample}}{MeanOD_{NC}}\right] x\ 100\% \qquad \textbf{(6.1)}$$

6.7 Statistical Analysis

Statistical analysis was performed using IBM SPSS Statistic version 26. The triplicate observed samples with MTT and ELISA tests are presented as mean values that were tested the normality by Shapiro-Wilk test (when n < 50 samples). Additionally, Levene Statistic was also used to compare a homogeneity of variance among a set of treatments (**Table 6.5**). If the sets of treatment meet both of criterion (e.g., normality and homogeneity of variance), parametric test (One-way ANOVA, followed by a post hoc Tukey's test) will apply to assess differences between groups defined by treatments. A

p value of < 0.05 was considered significant difference at 95% confidence level in all tests.

Table 6.4 Test of Normality of MTT and ELISA data of treatments (PBS, SDS and aSiNPs)

Variables		Shapiro-Wilk		
	Code	Statistic	df	Sig.
Optical density	PBS	0.911	3	0.421
	SDS	0.904	3	0.398
	SiNP	0.981	3	0.737
%Viability	PBS	0.911	3	0.420
	SDS	0.904	3	0.399
	SiNP	0.981	3	0.734
IL 1A	PBS	0.844	3	0.226
	SDS	0.971	3	0.672
	SiNP	0.976	3	0.705

The Shapiro-Wilk statistics in the tests of normality **Table 6.4** suggests that the data for optical density and %viability of MTT test, and IL-1A of ELISA test conform to normality with *p values* above 0.05.

Table 6.5 Test of Homogeneity of Variances

	Levene Statistic	***df1***	***df2***	***Sig.***
Optical Density	2.521	2	6	0.16
%Viability	2.525	2	6	0.16
IL-1A	2.717	2	6	0.144

Homogeneity of variances is used to indicate that groups have the same or similar variances. In the test of homogeneity of variances (Table 6.5), the *p value* of 0.16 in the Sig. column, which is larger than the critical value of 0.05, indicates that the variances of the treatment group are not significantly different from one another. The data for optical density, %viability, and IL-1A pass the criterion, parametric test (One-way ANOVA, followed by a post hoc Tukey's test) can be used to assess differences between the mean values of three treatments (i.e., aSiNP suspension, negative control (PBS), and positive control (SDS) at one time on cell to establish viability and pro-inflammatory cytokine release).

6.8 Results of *In Vitro* Skin Irritation Test

6.8.1 Tissue Viability Assessment (MTT assay)

The MTT assay is a general quantitative method for cell viability and works by normalizing OD values to a negative control set at 100%. The mean viability was taken from the triplicate experiments as shown in **Table 6.6**.

Table 6.6 The OD values and %Viability of the tissues used in the test conditions; PBS, SDS and aSiNPs

Sample	Mean of aliquots	%Viability	Mean OD (OD±SD)	Mean Viability (%±%SD)
PBS	0.5050	108.29	0.466±0.034	100±7.36
	0.4395	94.25		
	0.4545	97.46		
SDS	0.3710	79.56	0.385±0.018	82.56±3.89
	0.3785	81.17		
	0.4055	86.95		

Sample	Mean of aliquots	%Viability	Mean OD (OD±SD)	Mean Viability (%±%SD)
	0.4970	106.58		
aSiNPs	0.5065	108.61	0.509±0.013	109.04±2.71
	0.5220	111.94		

At the end of experiment, the OD of the solutions from the bottom of the exposure well was measured as %viability, which was derived from three individual rounds of testing for each sample. All samples tested showed higher mean % viability than the criterion of UN GHS&EU CLP after 15 minutes exposure (**Figure 6.12**). The overall average percent viability for aSiNPs was 109.04%. This finding indicates that aSiNPs can be classified as a non-irritant.

As the acceptance criteria for skin irritation (**Table 6.2**), the results of aSiNPs, NC_{PBS} were in a good agreement while PC_{SDS} was not. Conflicting tissue viability results for PC_{SDS} may concern the use of a lower concentration of SDS to prevent the excessive tissue damage often caused by 5% SDS and length of the exposure period for in vitro irritation test method. Mei Xiong *et al.* (2017) indicated 5%SDS as a skin irritation when applied on the reconstructed human skin model EPI-200 for 60-minute topical exposure. Histological assessment and IL-1α testing was carried out to clarify aSiNPs and conflicting tissue viability results for PC_{SDS}. However, cell viability following exposure to SDS was the lowest of all treatments with cell viability of 82.5% after 15 minutes of exposure, which was significantly decreased compared to NC_{PBS} and aSiNPs treatments. ANOVA was employed to determine the significance of different treatments. *F*-values and *p*-*values* showed the significance of each treatment which are listed in **Table 6.7**.

There was a statistically significant difference between the various exposure groups as determined by one-way ANOVA (F (2,6) = 21.307, p = 0.002).

Assumption 1:

Null hypothesis: There is no difference in mean % viability between groups defined by treatment.

Alternative hypothesis: There is difference in mean % viability between groups defined by treatment.

Table 6.7 Reporting results from a one-way *ANOVA*

MTT test		**Sum of Squares**	**df**	**Mean Saquare**	***F***	***Sig.***
Optical density	Between Group	.024	2	.012	21.288	.002
	Within Group	.003	6	.001		
	Total	.027	8			
%Viability	Between Group	1087.302	2	543.651	21.307	.002
	Within Group	153.089	6	25.515		
	Total	1240.391	8			

In this test, the *F* value, which is the between-group mean square divided by the within-group mean square, is large at 21.288 and 21.307 with significant at *p value* = 0.002. Therefore, the null hypothesis is rejected and the result can conclude that there is a significant difference in the mean OD and % viability values of the three treatments.

A post-hoc test, which requires equal group sizes and equal variance is used to identify subsets of means that differ significantly from each other, Post-hoc

Tukey's test revealed (**Table 6.8**) that the cell viability of SDS-treated tissues was statistically significantly lower than the other two treatments (aSiNPs -26.483±4.126, $p=0.002$ and PBS -17.441±4.126, $p=0.013$). There was no statistically significant difference between NC_{PBS} and SiNPs treatments ($p=0.151$). Thus, it was deduced that aSiNP is a non-irritant even at high concentration (~10 mg/mL).

Table 6.8 Pairwise comparisons by post-hoc Tukey's test.

%Viability		**Mean difference**	**Std. error**	**Sig.**	**95% confidence interval**	
(I) Treatment	**(J) Treatment**				**Lower bound**	**Upper bound**
SiNPs	PBS	9.043	4.124	0.151	-3.6112	21.697
	SDS	26.483*	4.124	0.002*	13.8288	39.137
SDS	PBS	-17.440	4.124	0.013*	-30.0945	-4.7855

*. The mean difference is significant at the 0.05 level.

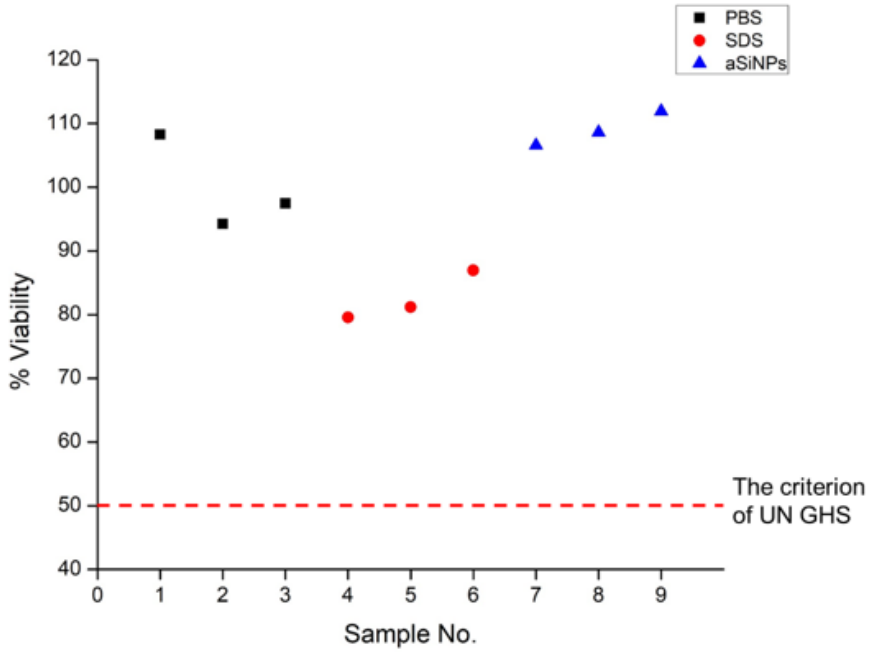


Figure 6.12: RhE models were exposed to PBS, SDS, and aSiNPs for 15 minutes and assessed %viability by MTT. Data are shown as the individual results for 3 tissue replicates tested over 3 independent experiments; 1. PBS (1-3), 2. SDS (4-6), and 3. aSiNPs (5-9).

6.8.2 Histology Assay

The use of histological assay using H&E staining is by far preferred for viewing cellular and tissue structure detail. In this case, the usefulness of H&E staining as an additional replicate of a sample in order to confirm results. The negative control tissue (NC_{PBS}) exhibited the gradual stratum corneum (SC) lamellar as well as the normal RhE model detachment from the collagen matrix in **Figure 6.1**. The positive control (PC_{SDS}) in **Figure 6. 13** showed sign of epidermal differentiation, such as the thickening of SC and epidermis, accompanied with loosely packed keratinocytes with decreasing the numbers of nucleus. However, the RhE model post aSiNP exposure showed only a slight change in the

epidermal barrier, i.e. differentiated layer and a keratinocyte without nucleus, compared to PC_{SDS}. Here, the previous finding indicates a beneficial effect from the aSiNPs that improves cell proliferation and cell migration moist environments promote cell proliferation (Öri *et al.*, 2017) and re-epithelialization (Junker *et al.*, 2013). As the aSiNPs contain 99% water they could have a similar effect. aSiNPs has been shown to support the growth of collagen in biological systems (Öri *et al.*, 2017), similar to the anti-inflammatory and antioxidation effects reported for gold NPs (Li *et al.*, 2015).

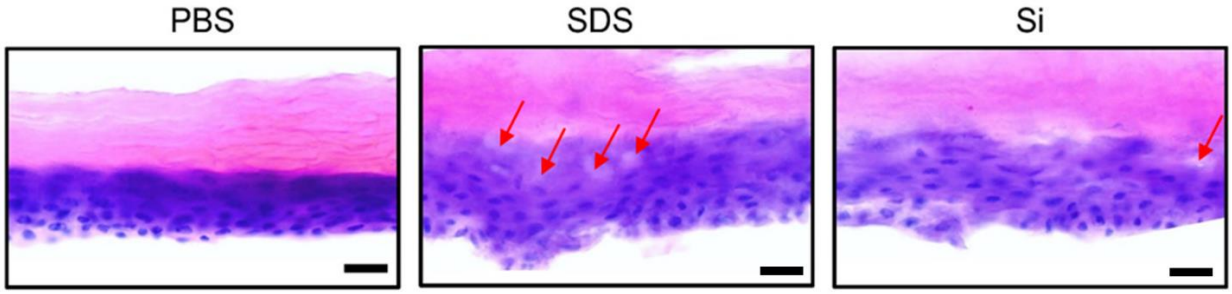


Figure 6.13: Histology of REH models stained with H&E following exposure to PBS, SDS and aSiNPs, scale bars 50 µm. SDS treated-tissues showed more keratinocytes without a nucleus than aSiNPs treated-tissues (red arrows).

6.8.3 ELISA: Human Interleukin-1α (IL-1A)

Human IL-1α release was detectable for all treatments (**Figure 6.14**) and a statistically found in term of inflammatory cytokine release ($F(2,6) = 13.369$, $p=0.006$). Therefore, the null hypothesis is rejected and the result can conclude that there is a significant difference in the mean IL-1A of the three treatments. A post-hoc test, which requires equal group sizes and equal variance is used to identify subsets of means that differ significantly from each other, There was no significant difference in the means of IL-1α concentration in PBS and SiNPs. The

concentration of IL-1α treated by SDS was significantly higher than PBS (260.727±56.763) and aSiNPs (247.107±56.763) at $p=0.009$ and 0.011, respectively.

Assumption 2:

Null hypothesis: There is no difference in mean IL-1A between groups defined by treatment.

Alternative hypothesis: There is difference in mean IL-1A between groups defined by treatment.

Table 6.9 Reporting results from a one-way *ANOVA*

ELISA test		**Sum of Squares**	**df**	**Mean Saquare**	***F***	***Sig.***
IL-1A	Between Group	129225.60	2	64612.80	13.369	.006
	Within Group	28998.450	6	4833.075		
	Total	158224.05	8			

Table 6.10 Pairwise comparisons by post-hoc Tukey's test.

IL-1A release		**Mean difference**	**Std. error**	**Sig.**	**95% confidence interval**	
(I) Treatment	**(J) Treatment**				**Lower bound**	**Upper bound**
SDS	PBS	260.727	56.763	0.009*	86.56	434.891
	SiNPs	247.107	56.763	0.011*	72.94	421.27
PBS	SiNPs	-13.620	56.763	0.969	-187.78	160.54

*. The mean difference is significant at the 0.05 level.

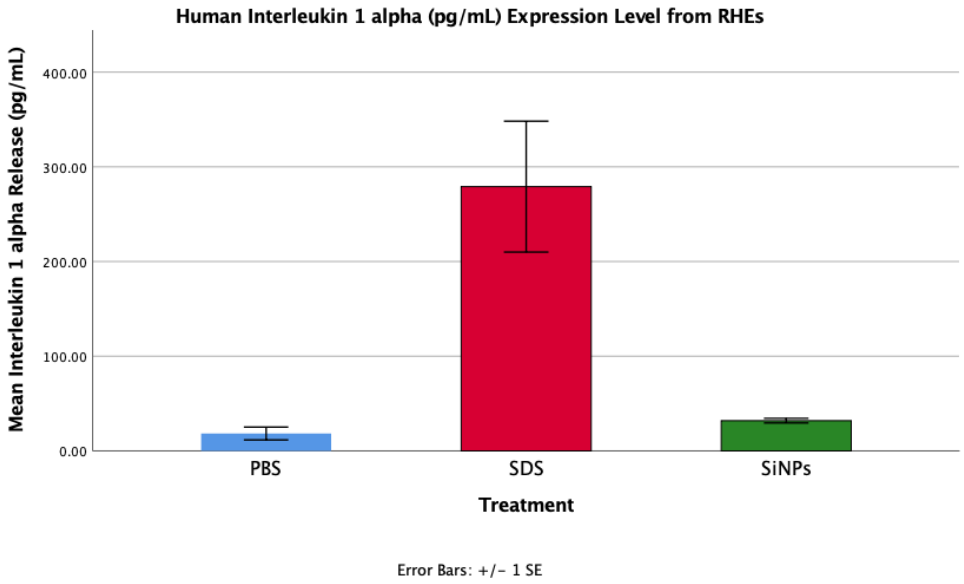


Figure 6.14: Immune response, measured as Human IL-1α released from RhE models after exposure to PBS, SDS and aSiNPs. The concentration of human IL-1α was assessed by ELISA, with results were presented in pg/mL. Data are expressed as mean±SE from three independent experiments. *(F(2,6)=13.369)*

6.9 Discussion

Based on previous studies, they have revealed that aSiNPs can induce cellular toxicity to a similar extent as crystalline silica (quartz) exposure (Lison *et al.*, 2016) and that the smaller size of aSiNPs, i.e. 15-nm, 20-nm and 30-nm was more toxic than the larger size as micro-size >100 nm (Yang *et al.*, 2010; Park *et al.*, 2013). However, in this study, we found that inflammatory cytokine (IL-1α) release of aSiNPs-treated tissue was not significantly different than the NC_{PBS} treated-tissue. Surprisingly, the 2 and 7 nm aSiNPs tested here show no inflammatory response as found in the most recent study of Palmer *et al.* (2019), suggesting the 20 nm aSiNPs applied *in vitro* keratinocytes which examined general inflammatory cytokines, namely IL-6 that led to the reduction of cytokine

release, is contrary to both previously literatures and the present study. This may have been caused by the presence of amines (N-H) in the aSiNPs suspension which may have reduced the effects of aSiNPs, i.e. a hemolytic effect (Kettiger, 2014). Furthermore, aSiNP based drug delivery and wound healing aspects have been shown to have tremendous potential (Press, 2012). Possibly, unique properties of aSiNPs such as their hydrophilic surface, large surface area and strongly negative surface charge may have interacted with the solutions e.g. PBS and cell medium or chemical gradients (Ca^{2+}, K^{+}, Na^{+}) in native skin barrier (Celli *et al.*, 2010) during the experiments presented here, causing a mechanism change, by which the aSiNPs reduced the keratinocyte response. Further work is thus required to increase confidence in aSiNPs cytotoxicity results. In particular, further work on keratinocytes should elucidate the mechanism of immune response.

6.10 Conclusion

Here, we investigated acute skin irritation of lab synthesized aSiNPs with a bimodal size of 2 and 7 nm when topically applied to a reconstructed human epidermis (RhE), following OECD test guideline No. 439 and additionally carried out histological observations of RhE and immune-mediated responses by ELISA-interleukin 1-alpha. In summary, the skin irritation test and cytotoxicity of the negatively charged 2 and 7 nm aSiNPs at the high dose indicated as a non-irritant Both techniques, MTT assay for cell viability and ELISA for interleukin 1-alpha, were in general agreement, whereas histological examination showed a tissue differentiation and proliferation, with a keratinocyte without a nucleus; however,

this was not as extensive as that observed in sodium dodecyl sulphate (SDS) treated - RhE tissues. However, additional research is needed, examining the potential chronic toxicity in human models, which would be required to ensure their suitability for cosmetic applications.

Chapter 7 Conclusions and Recommendations for Further Works

7.1 General Summary of Contents

Silica nanomaterials are widely used in cosmetics. Yet, very few studies exist (Guix *et al.*, 2008; Bernauer *et al.*, 2016) which have characterised silica nanomaterials in cosmetics using multi bulk and surface analytical and imaging techniques. Studies on potential toxicity of lab-synthesised amorphous silica nanoparticles on human skin are also sparse. The present work consists of characterisation of manufactured and lab-synthesised amorphous silica nanoparticles, the former in complex matrices, and their effect on the reconstructed human skin models. The recent application of reconstructed human skin models (full thickness skin model and epidermis model) have been used, for the first time, to identify the ability of aSiNPs (with very small particle sizes in the range of 1.6 and 7 nm) on penetration and the potential cytotoxicity on *in vitro* skin irritation. The key discovery of this study is that aSiNPs can penetrate significantly into the stratum corneum and epidermis layers.

It is hoped that this study, focusing on cosmetic characterisation, will contribute to a better understanding of NMs in commercial products and facilitate research on hazards of nanomaterials present is complex matrices in commercial applications and influence nanomaterials health and safety communication to the end-users and wider public.

As a brief overview of this thesis, Chapter 1 detailed the goal of the study, its scope, the relevant literature and the research objectives. Chapter 2 outlined the suit of analytical techniques and discussed the state-of-the-art methods in characterising silica nanomaterials and the toxicity studies related to human health. Chapter 3 presented a detailed characterisation of cosmetics and synthetic amorphous silica nanomaterials (SASs) using a multi-method approach. Chapter 4 presented the synthesis of amorphous silica nanoparticles using a sol-gel process and their characterisation, including synchrotron-based techniques to obtain a detailed set of properties. Chapter 5 observed *in vitro* skin penetration of aSiNPs, and applied the synchrotron based XRF, XAS and XPS to identify the translocation through the skin layers, and the interaction between aSiNPs and their biological environment. Chapter 6 further examined the effects of skin exposure to aSiNPs by quantifying cell viability, cytokine response, and cell morphology.

7.1.1 Aim to characterise their physicochemical of commercial cosmetics and synthetic amorphous silica nanomaterials (SASs) using a multi-method approach

One of the main objectives of the thesis was to do an extensive physicochemical characterisation of silica nanomaterials used in commercial cosmetics using a multi-method approach. Physicochemical characterisation of eight commercial cosmetics using multiple methods confirmed the presence of silicon-based materials and identified more than one component in the chemical structure. In addition, anatase and rutile titanium dioxide were found in some of the cosmetics

using EXAFS technique. Unfortunately, information on primary particle size of NMs was limited even by the use synchrotron based SAXS technique. This emphasizes the need for the development of special and more precise techniques for characterisation of nanomaterials in complex matrices to aid in regulatory decision-making. SAS characterisation results were in agreement with previous information from the JRC. In a few samples, XRD patterns showed broadened peaks of powdered SASs at 22˚2θ and a few sharp peaks which indicates the presence of a small amount of crystalline material in the amorphous SASs, this was not reported in the material description. The powdered SASs in UPW showed larger size and the particle networks as aggregates when dispersed in UPW, the primary particle of SASs is around 17 – 23 nm. A key recommendation here, therefore, is to always apply as many characterisation methods as possible for any material being characterised. A comparative of available characteristic methods for selected commercial cosmetics was described about the uses, advantage, and limitation in **Table 3.15**.

7.1.2 Aim to synthesise and characterise amorphous silica nanoparticles

In this study, amorphous silica nanoparticles (aSiNPs) were synthesised at a laboratory scale by using a sol-gel process based on the Stöber method (Stöber, Fink and Bohn, 1968). The focus of the synthesis was to produce ultra-small aSiNP particles, since the majority of existing literature addressed much larger size particles, with no evidence of any skin penetration. The main three parameters: (i) water, (ii) amino acid and (iii) TEOS used to synthesise amorphous silica played a role in determining the size and size distribution. aSiNPs were characterised using a suitable set of analytical techniques, specifically DLS, Zeta potential, TEM, STEM, SAXS, SEM, XRD, BET, XPS, XANES, FT-IR, and ICP-OES. The characterisation was also done after ageing the nanomaterials. DLS and STEM data showed smaller size values (~2-3 nm), compared to TEM (~16 nm). SAXS, on the other hand, provided primary particles of two size populations (~2 and 7 nm). The surface charge of all batches was found to be negative with high values (- 30 mV) and particles were found to be stable in suspension. The stability of the aSiNPs for a period of at least two months was monitored using DLS and for a year using SAXS. The aSiNPs showed slight increase in size over time, suggesting the possibility of Ostwald ripening (Brinker and Scherer, 1990). SEM images showed the spherical shape of aSiNPs in agreement with the SAXS data, as expressed by the slope of the relevant graph ($q^{-1} = 4$). XRD patterns showed broadened peaks of powdered aSiNPs at 22˚2θ which indicates the presence of amorphous form in the samples.

Furthermore, XPS and XANES showed all samples containing Si (4+). The results of FT-IR showed high purity of the samples following the used protocol of multiple washes with UPW. The % yield of synthesis was measured by ICP-OES and identified a higher yield (around 40%) than previously published work (Thomassen *et al.*, 2010). A comprehensive list of analytical and imaging techniques for assessing physicochemical descriptors can help to fully characterise synthesised aSiNPs enabling better understanding of their properties and enabling more precise prediction of their potential fate, transformations and behaviour in the environment. Using a suitable set of measurement techniques, it is possible to identify the structure of the nanomaterials in detail, enabling future use of this dataset in models involving structure- activity relationships to help identify potential hazards via various exposure routes. The evaluation of available analytical methods for aSiNPs characterisation was noted in **Table 4.12**.

7.1.3 Aim to study the skin penetration using reconstructed human full thickness skin model T-skin^{TM} at Day 11.

Chapter 5 presented the results of the investigation of aSiNPs passing through the skin layers and its physicochemical transformations. A comprehensive list of analytical and imaging techniques was used to fully characterise the synthesised aSiNP interaction with the reconstructed human full thickness skin model at Day 11. XRF technique was carried out to assess the aSiNP distribution and the location of aSiNPs in the skin after exposure. XANES results demonstrated the alteration of the oxidation state of silica from 4+ to 2-, these may induce the

differentiation in NPs by means of the loss of oxygen (i.e. reduction) at the particle surface. It was found that aSiNPs passed the stratum corneum through the dermis layer and interacted with components in reconstructed human full thickness skin models day 11 after exposure. Meanwhile, no NP was detected underneath the polycarbonate filter, this may imply that the barrier in dermal layers can limit NP penetration thereby preventing NPs translocation into the circulatory system. Using this skin model for broadness commercial products containing NMs may quantify the residue of NMs into the skin and evaluate advantages or drawbacks of NMs on skin cells for long-lasting exposure by using imaging techniques, i.e. histology.

Some changes, i. e. particle size distribution, oxidation state, and elemental composition at the surface may induce differences in behaviour in the biological environment. However, further studies on the degradation of NPs need to be performed, ideally using the EXAFS technique. High resolution of EXAFS data would allow to identify the local atoms and length of Si bonding by processing R-space and k-space; this will remove any uncertainty on the Si local environment and potential transformations by surface reactions with the skin.

7.1.4 Aim to investigate the effects of aSiNPs on Episkin™ small/reconstructed human epidermis (RhE) model

The OECD test guideline no. 439 was followed to understand potential effects, i. e. acute skin irritation and cell viability, and additionally using histology and inflammatory response to visualise the morphology of epidermis and to quantify the cytokines, respectively. No statistically significant difference was found

between negative control (NC_{PBS}) and aSiNPs treated RhE ($p = 0.151$) even for exposure at high concentration (~10 mg/mL). Thus, it was deduced that aSiNP is a non-irritant for the concentration tested in this study. In addition, the level of Interleukin-1α (an inflammatory marker) response to NPs exposure confirmed no effect of aSiNPs through RhE. It is interesting to note that the histological study revealed only a slight change in the epidermis, i.e. differentiated layer and a keratinocyte without nucleus, compared to negative control (NC_{PBS}). The morphological epidermis cells are proliferative in nature and differentiate into densely packed epidermis cells. However, further *in vitro* studies with different skin cells, models, damaged skin barrier, race and age, and chronic *in vivo* studies will help to establish potential effects, such as increased dermal uptake, translocation of NPs to other tissues and organs, pathological changes, of long-term use of cosmetics in such cases.

7.2 Future Work

The findings presented in this thesis suggest ways forward for further studies. The most prominent reason of use of NPs in various applications is the unique properties of materials at the nanoscale offering new opportunities for development of advanced materials. In particular, large surface area offers great advantage to combine with various materials, which extensively applies in the fields of biomedical, bioscience and bioengineering applications. The bioavailability stability of silica nanoparticle compounds is possible to enable an eco-friendly material to the environment and human health.

The results show the importance of comprehensive characterisation of NPs in various environments, and special use of advanced synchrotron-based techniques and high throughput approaches. For the future, further application of synchrotron-based techniques remains a powerful tool for advanced understanding of NM properties. However, working towards making lab-based techniques more diagnostic is a more broadly accessible line of research. A further recommendation is for future work on more efficient extraction of NMs from complex matrices as well as characterisation within complex matrices ideally by advancing existing techniques to become more tolerant of matrix complexity.

The reconstructed human skin model is an important practical standard for *in vitro* study. However, RhE model is a primary screening method which can be used to design more elaborate *in vivo* study for long-term exposure and *in vivo* experiments to understand chronic exposure effects (Hashempour *et al.*, 2019). In addition, using a range of different cell types, i.e. skin fibroblast and Langerhans cells can help to understand NP pathways and mechanisms in biological systems in a more comprehensive manner. Conducting skin penetration examination using labelled NPs can potentially determine the number of NPs remaining in the skin models.

A detailed study was performed an unravel interaction between nanomaterials and elements in the skin cells, which decreases an oxidative state of aSiNPs. These is more limited to explain their interactions. Thereby, the kinetic of NPs and mechanism of immune response are required to increase confidence aSiNPs cytotoxicity.

Recently, OECD prioritized silica nanoparticles in the list of nanomaterials needing toxicological evaluation (OECD, 2019). Previous studies reported that small size aSiNPs of Guo *et al.* (2018), Wu *et al.* (2019) and Lee *et al.* (2020) studies can induce the generation of reactive oxygen species (ROS), consequently leading to the enhanced cytotoxicity and cell apoptosis, in human pulmonary alveolar epithelial cells, endothelial cells, and skin cells (Guo *et al.*, 2018; Wu *et al.*, 2019) and cell death in neuronal cells (Lee *et al.*, 2020). Skin cell models are far less studies, but highly relevant to aSiNPs, given their extensive use in cosmetics. Therefore, formation of ROS species in RhE models and understanding the biochemical pathways of the formation of such ROS would be an interesting future research to understand the specific mechanisms of aSiNP toxicity in relevant to this thesis biological systems.

With the recent era of digital transformation, deriving from our ability to generate, store and reuse large data sets, much further work can be done on existing datasets containing NP characterisations and toxicity evaluations. Ultimately such data, from a variety of biological models should be pulled together and used toward modelling of toxicity predictions, possibly starting up in laboratory scale and eventually reaching to repeatable and more accurate predictions of full-scale environmental systems. It is hoped that both the data from this thesis, as well as the model materials (aSiNPs) developed will ultimately be used in such a manner.

Appendix

Oral Presentation

P. Musigapong, S. M. Briffa, I. Lynch, S. Soontaranon, N. Chanlek, E. Valsami-Jones, "Silica nanoparticle synthesis and multi-method characterization", the 7th International conference on nanostructures, nanomaterials and engineering 2018, Sapporo, Hokkaido, Japan, October 26-29, 2018.

P. Musigapong, I. Lynch, E. Valsami-Jones, *"Optimizing concentration of culture media at different temperatures and the amount of PEG for silica nanoparticle stability"*, SACC-TSAC 2019, London UK, February 15, 2019.

Poster Presentation

P. Musigapong, I. Lynch, E. Valsami-Jones, *"Optimizing concentration of biological media at different temperatures for silica nanoparticle stability"*, NanoSafety Forum for Young Scientists, Valletta, Malta, 10-11 September 2018.

References

Abd, E., Yousef, S. A., Pastore, M. N., Telaprolu, K., Mohammed, Y. H., Namjoshi, S., Grice, J. E. and Roberts, M. S. (2016) ‘Skin models for the testing of transdermal drugs’, *Clinical Pharmacology: Advances and Applications*, 8, pp. 163–176. doi: 10.2147/CPAA.S64788.

Adib, Z. M., Ghanbarzadeh, S., Kouhsoltani, M., Khosroshahi, A. Y. and Hamishehkar, H. (2016) ‘The effect of particle size on the deposition of solid lipid nanoparticles in different skin layers: A histological study’, *Advanced Pharmaceutical Bulletin*, 6(1), pp. 31–36. doi: 10.15171/apb.2016.006.

Al-Rawi, M., Diabaté, S. and Weiss, C. (2011) ‘Uptake and intracellular localization of submicron and nano-sized SiO 2 particles in HeLa cells’, *Archives of Toxicology*, 85(7), pp. 813–826. doi: 10.1007/s00204-010-0642-5.

Albanese, A., Tang, P. S. and Chan, W. C. W. (2012) ‘The Effect of Nanoparticle Size, Shape, and Surface Chemistry on Biological Systems’, *Annual Review of Biomedical Engineering*, 14(1), pp. 1–16. doi: 10.1146/annurev-bioeng-071811-150124.

Alexander, G. B., Heston, W. M. and Iler, R. K. (1954) ‘The Solubility of Amorphous Silica in Water’, *The Journal of Physical Chemistry*, 58(6), pp. 453–455. doi: 10.1021/j150516a002.

Ashtikar, M., Matthäus, C., Schmitt, M., Krafft, C., Fahr, A. and Popp, J. (2013) ‘Non-invasive depth profile imaging of the stratum corneum using confocal Raman microscopy: First insights into the method’, *European Journal of Pharmaceutical Sciences*. Elsevier B.V., 50(5), pp. 601–608. doi:

10.1016/j.ejps.2013.05.030.

Augustynski, J. (1993) ‘The role of the surface intermediates in the photoelectrochemical behaviour of anatase and rutile TiO2’, *Electrochimica Acta*, 38(1), pp. 43–46. doi: 10.1016/0013-4686(93)80008-N.

Axel, T. (2017) *Swelling and Microstructure of Nanoplatelet Systems*. Lund University.

Badawy, A. M. E. L., Silva, R. G., Morris, B., Scheckel, K. G. and Suidan, M. T. (2011) ‘Surface Charge-Dependent Toxicity of Silver Nanoparticles’, pp. 283–287.

Barbara L Dutrow, C. M. C. (2019) *X-ray Powder Diffraction (XRD)*. Available at: https://serc.carleton.edu/research_education/geochemsheets/techniques/XRD.html (Accessed: 5 January 2020).

Barillet, S., Simon-Deckers, A., Herlin-Boime, N., Mayne-L’Hermite, M., Reynaud, C., Cassio, D., Gouget, B. and Carrière, M. (2010) ‘Toxicological consequences of TiO2, SiC nanoparticles and multi-walled carbon nanotubes exposure in several mammalian cell types: An in vitro study’, *Journal of Nanoparticle Research*, 12(1), pp. 61–73. doi: 10.1007/s11051-009-9694-y.

Bart, F., Jollet, F., Duraud, J. P. and Douillard, L. (1995) ‘Electronic structure of a-Quartz’, *Physica Status Solidi (B)*, 176, pp. 163–176.

Beaucage, G. (1995) ‘Approximations Leading to a Unified Exponential/Power-Law Approach to Small-Angle Scattering’, *Journal of Applied Crystallography*. International Union of Crystallography, 28(6), pp. 717–728. doi: 10.1107/s0021889895005292.

Becheri, A., Dürr, M., Lo Nostro, P. and Baglioni, P. (2008) ‘Synthesis and

characterization of zinc oxide nanoparticles: Application to textiles as UV-absorbers', *Journal of Nanoparticle Research*, 10(4), pp. 679–689. doi: 10.1007/s11051-007-9318-3.

Berlier, G., Gastaldi, L., Sapino, S., Miletto, I., Bottinelli, E., Chirio, D. and Ugazio, E. (2013) 'MCM-41 as a useful vector for rutin topical formulations: Synthesis, characterization and testing', *International Journal of Pharmaceutics*. Elsevier B.V., 457(1), pp. 177–186. doi: 10.1016/j.ijpharm.2013.09.018.

Berlier, G., Gastaldi, L., Ugazio, E., Miletto, I., Iliade, P. and Sapino, S. (2013) 'Stabilization of quercetin flavonoid in MCM-41 mesoporous silica: Positive effect of surface functionalization', *Journal of Colloid and Interface Science*. Elsevier Inc., 393(1), pp. 109–118. doi: 10.1016/j.jcis.2012.10.073.

Bernauer, U., Chaudhry, Q., Dusinska, M., Lilienblum, W., Platzek, T., Rastogi, S. C., Rousselle, C., van Benthem, J., Hoet, P. H. M. and SCCS (2016) 'Opinion of the Scientific Committee on Consumer Safety (SCCS) - Revision of the opinion on the safety of the use of Silica, Hydrated Silica, and Silica Surface Modified with Alkyl Silylates (nano form) in cosmetic products', *Regulatory Toxicology and Pharmacology*. Elsevier Ltd, 74, pp. 79–80. doi: 10.1016/j.yrtph.2015.11.005.

Biesinger, M. C. (2009) *X-ray Photoelectron Spectroscopy (XPS) Reference Pages: XPS Description*, *2009*. Available at: http://www.xpsfitting.com/search/label/XPS Description (Accessed: 23 September 2019).

Bignon, C., Amigoni, S. and Guittard, F. (2016) 'Silica- and perfluoro-based nanoparticular polymeric network for the skin protection against

organophosphates Silica- and per fl uoro-based nanoparticular polymeric network for the skin protection against organophosphates', *Materials Research Express*. IOP Publishing, 3(065019), pp. 1–12.

Bijker, W. E., De Beaufort, I. D., Van Den Berg, A., Borm, P. J. A., Oyen, W. J. G., Robillard, G. T. and Van Dijk, H. F. G. (2007) 'A response to "Nanotechnology and the need for risk governance", O. Renn & M.C. Roco, 2006. J. Nanoparticle Research 8(2): 153-191', *Journal of Nanoparticle Research*, 9(6), pp. 1217–1220. doi: 10.1007/s11051-007-9261-3.

Black, L., Garbev, K., Stemmermann, P., Hallam, K. R. and Allen, G. C. (2002) 'X-ray Photoelectron Spectroscopy (XPS): A New Means of Studying C-S-H Structure and Chemistry', *Wasser-und Geotechnologie Nachrichten aus dem Institut fur Technische Chemie*, 2(January), pp. 37–44.

Bogush, G. H., Tracy, M. A. and Zukoski IV, C. F. (1988) 'Preparation of monodisperse silica particles: Control of size and mass fraction', *Journal of Non-Crystalline Solids*, 104(1), pp. 95–106. doi: 10.1016/0022-3093(88)90187-1.

Borm, P. J. A., Robbins, D., Haubold, S., Kuhlbusch, T., Fissan, H., Donaldson, K., Schins, R., Stone, V., Kreyling, W., Lademann, J., Krutmann, J., Warheit, D. and Oberdorster, E. (2006) *The potential risks of nanomaterials: a review carried out for ECETOC.*, *Particle and fibre toxicology*. doi: 10.1186/1743-8977-3-11.

Bos, J. D. and Meinardi, M. M. H. M. (2000) 'The 500 Dalton rule for the skin penetration of chemical compounds and drugs', *Experimental Dermatology*, 9(3), pp. 165–169. doi: 10.1034/j.1600-0625.2000.009003165.x.

Boster Biological Technology (2019) 'How to become an ELISA expert in 4

days', p. 46. Available at: https://www.bosterbio.com/elisa-troubleshooting-guide-download-page.

Bou-Dargham, M. J., Khamis, Z. I., Cognetta, A. B. and Sang, Q.-X. A. (2017) 'The role of interleukin-1 in inflammatory and malignant human skin diseases and the rationale for targeting interleukin-1 alpha', *Medicinal Research Reviews*, 37(1), pp. 180–216. doi: 10.1002/med.

Bowan, C. N. and Peppas, N. A. (1991) 'Sol-Gel processing: The physics and chemistry of sol-gel processing', *Journal of Controlled Release*, 15(2), p. 186. doi: 10.1016/0168-3659(91)90078-r.

Bragg, P. W. H. and Bragg, W. L. (1913) '428 Prof. W. H. Bragg and Mr. W. L. Bragg. [Apr. 7', 17, pp. 428–438.

Bras, W., Nikitenko, S., Portale, G., Beale, A., Van Der Eerden, A. and Detollenaere, D. (2010) 'Combined time-resolved SAXS and X-ray Spectroscopy methods', in *Journal of Physics: Conference Series*. Institute of Physics Publishing. doi: 10.1088/1742-6596/247/1/012047.

Briffa, S. M. (2017) 'Synthesis and ageing transformations of manufactured metal oxide nanomaterials', *PQDT - UK & Ireland*, (December). Available at: https://search.proquest.com/docview/2001153008?accountid=13607%0Ahttp://e-tidsskrifter.kb.dk/resolve??url_ver=Z39.88-2004&rft_val_fmt=info:ofi/fmt:kev:mtx:dissertation&genre=dissertations+%26+theses&sid=ProQ:ProQuest+Dissertations+%26+Theses+Global&atitle.

Brinker, C. J. J. and Scherer, G. W. (1990) *Sol-gel science : the physics and chemistry of sol-gel processing*. Academic Press. Available at: https://books.google.co.uk/books?id=V2vRvsTaCwMC&printsec=frontcover&source=gbs_ViewAPI&redir_esc=y#v=onepage&q&f=false (Accessed: 21

August 2019).

Brouwer, P. (2010) *Theory of XRF*, *Almelo: PANalytical BV*.

Brown, H. (1927) ‘Mineral content of skin’, *J. Biol. Chem.*, 75, pp. 789–794. doi: 10.1016/s0016-0032(27)92447-8.

Bruce Ravel (2009) *ATHENA: XAS Data Processing — Athena 0.9.26 documentation*. Available at: http://bruceravel.github.io/demeter/documents/Athena/index.html (Accessed: 5 January 2020).

Brust, M., Fink, J., Bethell, D., Schiffrin, D. J. and Kiely, C. (1995) ‘Synthesis and reactions of functionalised gold nanoparticles’, *Journal of the Chemical Society, Chemical Communications*, (16), pp. 1655–1656. doi: 10.1039/C39950001655.

Camacho-Flores, B. A., Martínez-Álvarez, O., Arenas-Arrocena, M. C., Garcia-Contreras, R., Argueta-Figueroa, L., De La Fuente-Hernández, J. and Acosta-Torres, L. S. (2015) ‘Copper: Synthesis techniques in nanoscale and powerful application as an antimicrobial agent’, *Journal of Nanomaterials*, pp. 1–10. doi: 10.1155/2015/415238.

Caputo, F. and Roesslein, M. (2015) ‘Measuring\tZeta\tPotential’, pp. 1–19. Available at: http://www.euncl.eu/about-us/assay-cascade/PDFs/Prescreening/EUNCL-PCC-002.pdf?m=1468937877 images.

Caruso, F., Mantellato, S., Palacios, M. and Flatt, R. J. (2017) ‘ICP-OES method for the characterization of cement pore solutions and their modification by polycarboxylate-based superplasticizers’, *Cement and Concrete Research*. doi: 10.1016/j.cemconres.2016.10.007.

Celli, A., Sanchez, S., Behne, M., Hazlett, T., Gratton, E. and Mauro, T.

(2010) ‘The epidermal Ca2+ gradient: Measurement using the phasor representation of fluorescent lifetime imaging’, *Biophysical Journal*. Biophysical Society, 98(5), pp. 911–921. doi: 10.1016/j.bpj.2009.10.055.

Chang, J. S., Chang, K. L. B., Hwang, D. F., Kong, Z. L. and Line, C. (2007) ‘In Vitro Cytotoxicitiy of Silica Nanoparticles at High Concentrations Strongly Depends on the Metabolic Activity Type of the’, *Environmental Science and Technology*, 41(6), pp. 2064–2068. doi: 10.1021/es062347t.

Chatterjee, R. (2008) ‘The challenge of regulating nanomaterials’, *Environmental Science and Technology*, 42(2), pp. 339–343. doi: 10.1021/es0870909.

Chen, F., Hableel, G., Zhao, E. R. and Jokerst, J. V. (2018) ‘Multifunctional nanomedicine with silica: Role of silica in nanoparticles for theranostic, imaging, and drug monitoring’, *Journal of Colloid and Interface Science*. Elsevier Inc., 521, pp. 261–279. doi: 10.1016/j.jcis.2018.02.053.

Chithrani, B. D., Ghazani, A. A. and Chan, W. C. W. (2006) ‘Determining the size and shape dependence of gold nanoparticle uptake into mammalian cells’, *Nano Letters*, 6(4), pp. 662–668. doi: 10.1021/nl052396o.

Chong, C. S. W., Cao, M., Wong, W. W., Fischer, K. P., Addison, W. R., Kwon, G. S., Tyrrell, D. L. and Samuel, J. (2005) ‘Enhancement of T helper type 1 immune responses against hepatitis B virus core antigen by PLGA nanoparticle vaccine delivery’, *Journal of Controlled Release*, 102(1), pp. 85–99. doi: 10.1016/j.jconrel.2004.09.014.

Contini, C., Schneemilch, M., Gaisford, S. and Quirke, N. (2018) ‘Nanoparticle–membrane interactions’, *Journal of Experimental Nanoscience*. Taylor & Francis, 13(1), pp. 62–81. doi: 10.1080/17458080.2017.1413253.

Corporation, M. (2017) *In Vitro EpiDerm™ Skin Irritation Test (EPI-200-SIT) For use with MatTek Corporation's Reconstructed Human Epidermal Model EpiDerm ™ (EPI-200-SIT)*. Available at: http://www.mattek.com/pages/abstracts/528.

Di Cristo, L., Movia, D., Bianchi, M. G., Allegri, M., Mohamed, B. M., Bell, A. P., Moore, C., Pinelli, S., Rasmussen, K., Riego-Sintes, J., Prina-Mello, A., Bussolati, O. and Bergamaschi, E. (2016) 'Proinflammatory effects of pyrogenic and precipitated amorphous silica nanoparticles in innate immunity cells', *Toxicological Sciences*, 150(1), pp. 40–53. doi: 10.1093/toxsci/kfv258.

Crosera, M., Prodi, A., Mauro, M., Pelin, M., Florio, C., Bellomo, F., Adami, G., Apostoli, P., De Palma, G., Bovenzi, M., Campanini, M. and Filon, F. L. (2015) 'Titanium dioxide nanoparticle penetration into the skin and effects on HaCaT cells', *International Journal of Environmental Research and Public Health*, 12(8), pp. 9282–9297. doi: 10.3390/ijerph120809282.

Cumberland, S. A. (2010) 'Synthesis and Environmental Chemistry', (March).

Davis, T. M. (2007) *Nanoparticle formation, evolution, and association in the presence of tetrapropylammonium cations and lysine*. University of Minnesota. Available at: https://books.google.fr/books?id=vgoGrIklNFAC&pg=PA1&lpg=PA1&redir_esc=y#v=onepage&q&f=falsedq=%22from+nanoparticles+to+ordered+materials%22&source=bl&ots=_oiBFgRG9K&sig=x0SPrpTN1nINaVU2leEVVaJB5RM&hl=fr&sa=X&ei=AZZMVcHECaOxygPN4oCwDQ&ved=0CBwQ6AEwAA#v=on.

Davis, T. M., Snyder, M. A., Krohn, J. E. and Tsapatsis, M. (2006) 'Nanoparticles in lysine-silica sols', *Chemistry of Materials*, 18(25), pp. 5814–5816. doi: 10.1021/cm061982v.

Dekkers, S., Bouwmeester, H., Bos, P. M. J., Peters, R. J. B., Rietveld, A. G. and Oomen, A. G. (2013) ‘Knowledge gaps in risk assessment of nanosilica in food: evaluation of the dissolution and toxicity of different forms of silica) Knowledge gaps in risk assessment of nanosilica in food: evaluation of the dissolution and toxicity of different forms of silica Knowledge gaps in risk assessment of nanosilica in food: evaluation of the dissolution and toxicity of different forms of silica’, *Nanotoxicology*, 7(4), pp. 367–377. doi: 10.3109/17435390.2012.662250.

Dey, D., Kumar, P. and Samantaray, S. (2017) ‘A review of nanofluid preparation, stability, and thermo-physical properties’, *Heat Transfer - Asian Research*, 46(8), pp. 1413–1442. doi: 10.1002/htj.21282.

Dhas, N. A., Raj, C. P. and Gedanken, A. (1998) ‘Synthesis, Characterization, and Properties of Metallic Copper Nanoparticles’, *Chemistry of Materials*, 10(5), pp. 1446–1452. doi: 10.1021/cm9708269.

Ding, Y. (2011) *Fundamental Theory of Transmission Electronic Microscopy*, *2011*. Available at: http://www.nanoscience.gatech.edu/zlwang/research/tem.html (Accessed: 14 September 2019).

Dixit, C. K., Bhakta, S., Kumar, A., Suib, S. L. and Rusling, J. F. (2016) ‘Fast nucleation for silica nanoparticle synthesis using a sol-gel method’, *Nanoscale*. Royal Society of Chemistry, 8(47), pp. 19662–19667. doi: 10.1039/c6nr07568a.

Dobrovolskaia, M. A., Germolec, D. R. and Weaver, J. L. (2009) ‘Evaluation of nanoparticle immunotoxicity’, *Nature Nanotechnology*, 4(7), pp. 411–414. doi: 10.1038/nnano.2009.175.

Dolez, P. I. (2015) *Nanomaterials Definitions, Classifications, and Applications*, *Nanoengineering: Global Approaches to Health and Safety Issues*. doi: 10.1016/B978-0-444-62747-6.00001-4.

Drescher, D., Orts-Gil, G., Laube, G., Natte, K., Veh, R. W., Österle, W. and Kneipp, J. (2011) 'Toxicity of amorphous silica nanoparticles on eukaryotic cell model is determined by particle agglomeration and serum protein adsorption effects', *Analytical and Bioanalytical Chemistry*, 400(5), pp. 1367–1373. doi: 10.1007/s00216-011-4893-7.

Ealias, A. M. and Saravanakumar, M. P. (2017) 'A review on the classification, characterisation, synthesis of nanoparticles and their application', *IOP Conference Series: Materials Science and Engineering*, 263(3). doi: 10.1088/1757-899X/263/3/032019.

ECETOC (2006) 'Synthetic Amorphous Silica (CAS No. 7631-86-9)', *JACC No. 51. Brussels*, (7631), p. 237. Available at: http://www.ecetoc.org/jacc-reports.

EcoMundo (2016) *Nanomaterials in cosmetic products | EcoMundo's blog*. Available at: https://www.ecomundo.eu/en/blog/nanomaterials-in-cosmetics (Accessed: 5 August 2019).

Eskes, C., Cole, T., Hoffmann, S., Worth, A., Cockshott, A., Gerner, I. and Zuang, V. (2007) 'The ECVAM international validation study on in vitro tests for acute skin irritation: Selection of test chemicals', *ATLA Alternatives to Laboratory Animals*, 35(6), pp. 603–619. doi: 10.1177/026119290703500608.

EU (2016) 'Commission Regulation (EU) 2016/1143 of 14.07.2016 amending Annex VI to Regulation (EC) No 1223/2009 of the European Parliament and of the Council on cosmetic (Titanium Dioxide)', 2016(July), pp. 25–28. doi:

http://eur-lex.europa.eu/pri/en/oj/dat/2003/l_285/l_28520031101en00330037.pdf.

European Centre for Ecotoxicology and Toxicology of Chemicals (2006) ‘Synthetic Amorphous Silica’, 2006, p. Available at: http://members.ecetoc.org/Documents/Document/JACC 051.pdf.

European Chemicals Agency (2017) *Guidance on the Application of the CLP Criteria Extracts of the document in this consultation :* Available at: https://echa.europa.eu/documents/10162/23036412/clp_en.pdf.

European Commission (2016) *Nanomaterials | Internal Market, Industry, Entrepreneurship and SMEs*. Available at: https://ec.europa.eu/growth/sectors/cosmetics/products/nanomaterials_en (Accessed: 5 August 2019).

European Parliament (2009) *Consolidated TEXT: 32009R1223 — EN — 16.04.2015*. Available at: https://eur-lex.europa.eu/legal-content/EN/TXT/HTML/?uri=CELEX:02009R1223-20150416&from=EN (Accessed: 22 August 2019).

European Union (2009) ‘Regulation (EC) nr 1223/2009 on cosmetic products’, (1223).

Fernandes, R., Smyth, N. R., Muskens, O. L., Nitti, S., Heuer-Jungemann, A., Ardern-Jones, M. R. and Kanaras, A. G. (2015) ‘Interactions of skin with gold nanoparticles of different surface charge, shape, and functionality’, *Small*, 11(6), pp. 713–721. doi: 10.1002/smll.201401913.

Fijalkowski, M., Adach, K., Marešová, H. and Kroisová, D. (2015) ‘Biogenic and synthetic amorphous silica - Compare and interaction with bacterial systems’, *NANOCON 2015 - 7th International Conference on Nanomaterials -*

Research and Application, Conference Proceedings, pp. 1–6.

Filipe, P., Silva, J. N., Silva, R., Cirne De Castro, J. L., Marques Gomes, M., Alves, L. C., Santus, R. and Pinheiro, T. (2009) 'Stratum corneum is an effective barrier to TiO2 and ZnO nanoparticle percutaneous absorption', *Skin Pharmacology and Physiology*, 22(5), pp. 266–275. doi: 10.1159/000235554.

Foss Hansen, S., Heggelund, L. R., Revilla Besora, P., Mackevica, A., Boldrin, A. and Baun, A. (2016) 'Nanoproducts - What is actually available to European consumers?', *Environmental Science: Nano*. Royal Society of Chemistry, 3(1), pp. 169–180. doi: 10.1039/c5en00182j.

Foss Hansen, S., Maynard, A., Baun, A. and Tickner, J. A. (2008) 'Late lessons from early warnings for nanotechnology', *Nature Nanotechnology*, 3(8), pp. 444–447. doi: 10.1038/nnano.2008.198.

Freese, C., Schreiner, D., Anspach, L., Bantz, C., Maskos, M., Unger, R. E. and Kirkpatrick, C. J. (2014) 'In vitro investigation of silica nanoparticle uptake into human endothelial cells under physiological cyclic stretch', *Particle and Fibre Toxicology*, 11(1). doi: 10.1186/s12989-014-0068-y.

Friends of the Earth Australia (2006) *Nanomaterials, sunscreens and cosmetics: Small Ingredients Big Rsks*, *http://nano.foe.org.au.* Available at: https://1bps6437gg8c169i0y1drtgz-wpengine.netdna-ssl.com/wp-content/uploads/2017/legacy/Nanomaterials_sunscreens_and_cosmetics.pdf.

Froggett, S. J., Clancy, S. F., Boverhof, D. R. and Canady, R. A. (2014) 'A review and perspective of existing research on the release of nanomaterials from solid nanocomposites', *Particle and Fibre Toxicology*, 11(1), pp. 1–28. doi: 10.1186/1743-8977-11-17.

Gamer, A. O., Leibold, E. and Van Ravenzwaay, B. (2006) 'The in vitro

absorption of microfine zinc oxide and titanium dioxide through porcine skin', *Toxicology in Vitro*, 20(3), pp. 301–307. doi: 10.1016/j.tiv.2005.08.008.

Gergely, A. and Coroyannakis, L. (2009) 'Nanotechnology in the EU cosmetics regulation The use of nanoTechnology in cosmeTic producTs', pp. 28–30.

El Ghandoor, H., Zidan, H. M., Khalil, M. M. H. and Ismail, M. I. M. (2012) 'Synthesis and some physical properties of magnetite (Fe <inf>3</inf>O <inf>4</inf>) nanoparticles', *International Journal of Electrochemical Science*, 7(6), pp. 5734–5745.

Goldstein, A., Soroka, Y., Frušić-Zlotkin, M., Popov, I. and Kohen, R. (2014) 'High resolution SEM imaging of gold nanoparticles in cells and tissues', *Journal of Microscopy*, 256(3), pp. 237–247. doi: 10.1111/jmi.12179.

Grandview Research (2017) *NanoSilica Market Analysis, By Product (P Type, S Type, and Type III), By Application (Rubber, Healthcare, Food, Coatings, Plastics, Concrete, Gypsum, Battery, Electronics, Cosmetics), And Segment Forecasts, 2018 - 2025*, *NanoSilica Market Size&Share, Global Industry Report*.

Gubala, V., Johnston, L. J., Liu, Z., Krug, H., Moore, C. J., Ober, C. K., Schwenk, M. and Vert, M. (2018a) 'Engineered nanomaterials and human health: Part 1. Preparation, functionalization and characterization (IUPAC Technical Report)', *Pure and Applied Chemistry*, 90(8), pp. 1283–1324. doi: 10.1515/pac-2017-0101.

Gubala, V., Johnston, L. J., Liu, Z., Krug, H., Moore, C. J., Ober, C. K., Schwenk, M. and Vert, M. (2018b) 'Engineered nanomaterials and human health: Part 2. Applications and nanotoxicology (IUPAC Technical Report)',

Pure and Applied Chemistry, 90(8), pp. 1283–1324. doi: 10.1515/pac-2017-0101.

Guinier, André and Fournet, G. (1955) 'Small-angle scattering of X-rays / André Guinier, Gerard Fournet ; translation by Christopher B. Walker, followed by a bibliography by Kenneth L. Yudowitch.', *New York : Wiley ; London : Chapman & Hall, 1955*. Available at: http://journals.iucr.org/q/issues/1956/10/00/a01829/a01829.pdf (Accessed: 28 August 2019).

Guix, M., Carbonell, C., Comenge, J., García-fernández, L. and Alarcón, A. (2008) 'Nanoparticles for cosmetics . How safe is safe ?', *Contribution to science*, 4(2), pp. 213–217. doi: 10.2436/20.7010.01.52.

Guo, C., Ma, R., Liu, X., Xia, Y., Niu, P., Ma, J., Zhou, X., Li, Y. and Sun, Z. (2018) 'Silica nanoparticles induced endothelial apoptosis via endoplasmic reticulum stress-mitochondrial apoptotic signaling pathway', *Chemosphere*, 210(10), pp. 183–192. doi: 10.1016/j.chemosphere.2018.06.170.

Gupta, R. and Rai, B. (2016) 'Penetration of Gold Nanoparticles through Human Skin: Unraveling Its Mechanisms at the Molecular Scale', *Journal of Physical Chemistry B*, 120(29), pp. 7133–7142. doi: 10.1021/acs.jpcb.6b03212.

Gysler, A., Kleuser, B., Sippl, W., Lange, K., Korting, H. C., Höltje, H. D. and Schäfer-Korting, M. (1999) 'Skin penetration and metabolism of topical glucocorticoids in reconstructed epidermis and in excised human skin', *Pharmaceutical Research*, pp. 1386–1391. doi: 10.1023/A:1018946924585.

Hao, F., Jin, X., Liu, Q. S., Zhou, Q. and Jiang, G. (2017) 'Epidermal Penetration of Gold Nanoparticles and Its Underlying Mechanism Based on

Human Reconstructed 3D Episkin Model', *ACS Applied Materials and Interfaces*, 9(49), pp. 42577–42588. doi: 10.1021/acsami.7b13700.

Haq, A., Dorrani, M., Goodyear, B., Joshi, V. and Michniak-Kohn, B. (2018) 'Membrane properties for permeability testing: Skin versus synthetic membranes', *International Journal of Pharmaceutics*. Elsevier, 539(1–2), pp. 58–64. doi: 10.1016/j.ijpharm.2018.01.029.

Hashempour, S., Ghanbarzadeh, S., Maibach, H. I., Ghorbani, M. and Hamishehkar, H. (2019) 'Skin toxicity of topically applied nanoparticles', *Therapeutic Delivery*, 10(6), pp. 383–396. doi: 10.4155/tde-2018-0060.

Hatta, I., Ohta, N., Inoue, K. and Yagi, N. (2006) 'Coexistence of two domains in intercellular lipid matrix of stratum corneum', *Biochimica et Biophysica Acta - Biomembranes*, 1758(11), pp. 1830–1836. doi: 10.1016/j.bbamem.2006.08.014.

He, Q., Zhang, Z., Gao, Y., Shi, J. and Li, Y. (2009) 'Intracellular localization and cytotoxicity of spherical mesoporous silica nano-and microparticles', *Small*, 5(23), pp. 2722–2729. doi: 10.1002/smll.200900923.

Heide, P. va. der (2011) 'John Wiley And Sons Inc 2011 Investor Conference - Final', *John Wiley And Sons Inc 2011*, pp. 1–37.

Van Helden, A. K., Jansen, J. W. and Vrij, A. (1981) 'Preparation and characterization of spherical monodisperse silica dispersions in nonaqueous solvents', *Journal of Colloid And Interface Science*, 81(2), pp. 354–368. doi: 10.1016/0021-9797(81)90417-3.

Hochella, M. F., Mogk, D. W., Ranville, J., Allen, I. C., Luther, G. W., Marr, L. C., McGrail, B. P., Murayama, M., Qafoku, N. P., Rosso, K. M., Sahai, N., Schroeder, P. A., Vikesland, P., Westerhoff, P. and Yang, Y. (2019) 'Natural,

incidental, and engineered nanomaterials and their impacts on the Earth system', *Science*, 363(6434). doi: 10.1126/science.aau8299.

Iannuccelli, V., Bertelli, D., Romagnoli, M., Scalia, S., Maretti, E., Sacchetti, F. and Leo, E. (2014) 'In vivo penetration of bare and lipid-coated silica nanoparticles across the human stratum corneum', *Colloids and Surfaces B: Biointerfaces*. Elsevier B.V., 122, pp. 653–661. doi: 10.1016/j.colsurfb.2014.07.046.

ISO (2014) 'ISO 10993-12:2012 Biological Evaluation ofMedical Devices-Part 10: Tests for irritation and skin sensitization.', *SMPTE Journal*, 95(5), pp. 601–602. doi: 10.5594/j17740.

Janssen, R. A. J. and Stouwdam, J. W. (2008) 'Red, green, and blue quantum dot LEDs with solution processable ZnO nanocrystal electron injection layers', *Journal of Materials Chemistry*, 18(16), pp. 1889–1894. doi: 10.1039/b800028j.

JRC (2010) *Considerations on a definition of nanomaterial for regulatory purposes*, *JRC Reference Reports*. doi: 10.2788/98686.

Ju-Nam, Y. and Lead, J. R. (2008) 'Manufactured nanoparticles: An overview of their chemistry, interactions and potential environmental implications', *Science of the Total Environment*. Elsevier B.V., 400(1–3), pp. 396–414. doi: 10.1016/j.scitotenv.2008.06.042.

Juliano, C. and Magrini, G. A. (2017) 'Cosmetic ingredients as emerging pollutants of environmental and health concern. A mini-review', *Cosmetics*, 4(2). doi: 10.3390/cosmetics4020011.

Junevičius, J., Žilinskas, J., Česaitis, K., Česaitienė, G., Gleiznys, D., Maželienė, Ž., Juozas Žilinskas, -D D S, Kęstutis Česaitis, -D D S, Gabrielė

Česaitienė 3 -Student, -D D S and Maželienė, -D D S Žaneta (2015) *Antimicrobial activity of silver and gold in toothpastes: A comparative analysis*, *Stomatologija Baltic Dental and Maxillofacial Journal*.

Junker, J. P. E., Kamel, R. A., Caterson, E. J. and Eriksson, E. (2013) 'Clinical Impact Upon Wound Healing and Inflammation in Moist, Wet, and Dry Environments', *Advances in Wound Care*, 2(7), pp. 348–356. doi: 10.1089/wound.2012.0412.

Kasper, J., Hermanns, M. I., Bantz, C., Maskos, M., Stauber, R., Pohl, C., Unger, R. E. and Kirkpatrick, J. C. (2011) 'Inflammatory and cytotoxic responses of an alveolar-capillary coculture model to silica nanoparticles: Comparison with conventional monocultures', *Particle and Fibre Toxicology*. BioMed Central Ltd, 8(1), p. 6. doi: 10.1186/1743-8977-8-6.

Kattan, P. I. (2016) *Ratio of Surface Area to Volume in Nanotechnology and Nanoscience*.

Keller, A. A. and Lazareva, A. (2013) 'Predicted Releases of Engineered Nanomaterials: From Global to Regional to Local', *Environmental Science and Technology Letters*, 1(1), pp. 65–70. doi: 10.1021/ez400106t.

Kettiger, H. E. (2014) *Silica nanoparticles and their interaction with cells: a multidisciplinary approach*. Basel University.

Kettiger, H., Québatte, G., Perrone, B. and Huwyler, J. (2016) 'Interactions between silica nanoparticles and phospholipid membranes', *Biochimica et Biophysica Acta - Biomembranes*. Elsevier B.V., 1858(9), pp. 2163–2170. doi: 10.1016/j.bbamem.2016.06.023.

Khan, Ibrahim, Saeed, K. and Khan, Idrees (2017) 'Nanoparticles: Properties, applications and toxicities', *Arabian Journal of Chemistry*. The Authors, 12(7),

pp. 908–931. doi: 10.1016/j.arabjc.2017.05.011.

Khezri, K., Saeedi, M. and Maleki Dizaj, S. (2018) ‘Application of nanoparticles in percutaneous delivery of active ingredients in cosmetic preparations’, *Biomedicine and Pharmacotherapy*, 106, pp. 1499–1505. doi: 10.1016/j.biopha.2018.07.084.

Krug, H. F. and Wick, P. (2011) ‘Nanotoxicology: An interdisciplinary challenge’, *Angewandte Chemie - International Edition*, 50(6), pp. 1260–1278. doi: 10.1002/anie.201001037.

Labouta, H. I., El-Khordagui, L. K., Kraus, T. and Schneider, M. (2011) ‘Mechanism and determinants of nanoparticle penetration through human skin’, *Nanoscale*, 3(12), p. 4989. doi: 10.1039/c1nr11109d.

Labouta, H. I., Liu, D. C., Lin, L. L., Butler, M. K., Grice, J. E., Raphael, A. P., Kraus, T., El-Khordagui, L. K., Soyer, H. P., Roberts, M. S., Schneider, M. and Prow, T. W. (2011) ‘Gold nanoparticle penetration and reduced metabolism in human skin by toluene’, *Pharmaceutical Research*, 28(11), pp. 2931–2944. doi: 10.1007/s11095-011-0561-z.

Lademann, J., Otberg, N., Richter, H., Weigmann, H. J., Lindemann, U., Schaefer, H. and Sterry, W. (2001) ‘Investigation of follicular penetration of topically applied substances’, *Skin Pharmacology and Applied Skin Physiology*, 14(SUPPL. 1), pp. 17–22. doi: 10.1159/000056385.

Lai, S. K., Wang, Y. and Hanes, J. (2010) ‘Mucus-penetrating nanoparticles for drug and gene delivery to mucosal tissues’, *Advanced Drug Delivery Reviews*, 61(2), pp. 158–171. doi: 10.1016/j.addr.2008.11.002.Mucus-penetrating.

Larese, F. F., D’Agostin, F., Crosera, M., Adami, G., Renzi, N., Bovenzi, M.

and Maina, G. (2009) ‘Human skin penetration of silver nanoparticles through intact and damaged skin’, *Toxicology*, 255(1–2), pp. 33–37. doi: 10.1016/j.tox.2008.09.025.

Larese Filon, F., Crosera, M., Adami, G., Bovenzi, M., Rossi, F. and Maina, G. (2011) ‘Human skin penetration of gold nanoparticles through intact and damaged skin’, *Nanotoxicology*, 5(4), pp. 493–501. doi: 10.3109/17435390.2010.551428.

Larese Filon, F., Mauro, M., Adami, G., Bovenzi, M. and Crosera, M. (2015) ‘Nanoparticles skin absorption: New aspects for a safety profile evaluation’, *Regulatory Toxicology and Pharmacology*. Elsevier Inc., 72(2), pp. 310–322. doi: 10.1016/j.yrtph.2015.05.005.

Lázaro García, A. (2014) *Nano-silica production at low temperatures from the dissolution of olivine, PhD Thesis,*. doi: 10.6100/IR774494.

Lee, K.-I., Lin, J.-W., Su, C.-C., Fang, K.-M., Yang, C.-Y., Kuo, C.-Y., Wu, C.-C., Wu, C.-T. and Chen, Y.-W. (2020) ‘Silica nanoparticles induce caspase-dependent apoptosis through reactive oxygen species-activated endoplasmic reticulum stress pathway in neuronal cells’, *Toxicology in Vitro*. Elsevier, 63(November 2019), p. 104739. doi: 10.1016/J.TIV.2019.104739.

Lee, O., Jeong, S. H., Shin, W. U., Lee, G., Oh, C. and Son, S. W. (2013) ‘Influence of surface charge of gold nanorods on skin penetration’, *Skin Research and Technology*, 19(1), pp. 390–396. doi: 10.1111/j.1600-0846.2012.00656.x.

Lee, O., Lee, S. H., Jeong, S. H., Kim, J., Ryu, H. J., Oh, C. and Son, S. W. (2016) ‘A quantitative study of nanoparticle skin penetration with interactive segmentation’, *Medical and Biological Engineering and Computing*, 54(10),

pp. 1469–1479. doi: 10.1007/s11517-015-1405-5.

Lee, W., Kang, S. H., Kim, J. Y., Kolekar, G. B., Sung, Y. E. and Han, S. H. (2009) ‘TiO2 nanotubes with a ZnO thin energy barrier for improved current efficiency of CdSe quantum-dot-sensitized solar cells’, *Nanotechnology*, 20(33), p. 7. doi: 10.1088/0957-4484/20/33/335706.

Lewicka, Z. A., Benedetto, A. F., Benoit, D. N., Yu, W. W., Fortner, J. D. and Colvin, V. L. (2011) ‘The structure, composition, and dimensions of TiO2 and ZnO nanomaterials in commercial sunscreens’, *Journal of Nanoparticle Research*, 13(9), pp. 3607–3617. doi: 10.1007/s11051-011-0438-4.

Li, D., Bancroft, G. M., Kasrai, M., Fleet, M. E., Secco, R. A., Feng, X. H., Tan, K. H. and Yang, B. X. (1994) ‘X-ray absorption spectroscopy of silicon dioxide (SiO2) polymorphs: the structural characterization of opal’, *American Mineralogist*, 79(7–8), pp. 622–632.

Li, X., Liu, Y., Fu, L., Cao, L., Wei, D. and Wang, Y. (2006) ‘Efficient synthesis of carbon nanotube-nanoparticle hybrids’, *Advanced Functional Materials*, 16(18), pp. 2431–2437. doi: 10.1002/adfm.200600339.

Li, X., Wang, H., Rong, H., Li, W., Luo, Y., Tian, K., Quan, D., Wang, Y. and Jiang, L. (2015) ‘Effect of composite SiO2@AuNPs on wound healing: In vitro and vivo studies’, *Journal of Colloid and Interface Science*. Elsevier Inc., 445, pp. 312–319. doi: 10.1016/j.jcis.2014.12.084.

Liang, H., Jin, C., Tang, Y., Wang, F., Ma, C. and Yang, Y. (2014) ‘Cytotoxicity of silica nanoparticles on HaCaT cells’, *Journal of Applied Toxicology*, 34(4), pp. 367–372. doi: 10.1002/jat.2953.

Lin, G. M., Shang, M. and Zhang, W. G. (2014) ‘Research on nanomaterials and its latest application’, *Advanced Materials Research*, 912–914, pp. 305–

308. doi: 10.4028/www.scientific.net/AMR.912-914.305.

Lin, W., Huang, Y.-W., Zhou, X.-D. and Ma, Y. (2006) 'In vitro toxicity of silica nanoparticles in human lung cancer cells', *Toxicology and Applied Pharmacology*, 217, pp. 252–259. doi: 10.1016/j.taap.2006.10.004.

Lin, Y.-S., Abadeer, N. and Haynes, C. L. (2011) 'Stability of small mesoporous silica nanoparticles in biological media.', *Chemical communications (Cambridge, England)*, 47(1), pp. 532–4. doi: 10.1039/c0cc02923h.

Lison, D., Garry, D., Leinardi, R., Pavan, C., Fubini, B., Tomatis, M., Pastero, L., Turci, F. and Anguissola, S. (2016) 'Revisiting the paradigm of silica pathogenicity with synthetic quartz crystals: the role of crystallinity and surface disorder', *Particle and Fibre Toxicology*, 13(1), pp. 1–12. doi: 10.1186/s12989-016-0136-6.

Lynch, I., Salvati, A. and Dawson, K. A. (2009) 'Protein-nanoparticle interactions: What does the cell see?', *Nature Nanotechnology*. Nature Publishing Group, 4(9), pp. 546–547. doi: 10.1038/nnano.2009.248.

Mahshid, Sara, Askari, Masoud, Ghamsari, M. S., Mahshid, S, Askari, M and Sasani Ghamsari, M. (2007) 'Synthesis of TiO2 Nanoparticles by Hydrolysis and Peptization of Titanium Isopropoxide Solution Application of Coal and Biomass in Direct Reduction of Magnetite Iron concentrate in cylindrical arrangement View project Polymer physics of confined DNA View ', *Journal of Materials Processing Technology*, 189(November 2017), pp. 296–300. doi: 10.1016/j.jmatprotec.2007.01.040.

Matsuo, K., Hirobe, S., Okada, N. and Nakagawa, S. (2016) 'Analysis of skin permeability and toxicological properties of amorphous silica particles',

Biological and Pharmaceutical Bulletin, 39(7), pp. 1201–1205. doi: 10.1248/bpb.b16-00258.

Mei Xiong, Z., O'Donovan, M., Sun, L., Young Choi, J., Ren, M. and Cao, K. (2017) 'Anti-Aging Potentials of Methylene Blue for Human Skin Longevity', *Scientific Reports*, 7(1), pp. 1–12. doi: 10.1038/s41598-017-02419-3.

Merck (2019) *IR Spectrum Table & Chart* | *Sigma-Aldrich*, *2019*. Available at: https://www.sigmaaldrich.com/technical-documents/articles/biology/ir-spectrum-table.html (Accessed: 10 September 2019).

Moia, C. (2015) *In vitro toxicological assessment of amorphous silica particles in relation to their characteristics and mode of action in human skin cells*. Available at: https://dspace.lib.cranfield.ac.uk/bitstream/1826/9760/1/Moia_C_2015.pdf.

Morishige, T., Yoshioka, Y., Inakura, H., Tanabe, A., Yao, X., Tsunoda, S., Tsutsumi, Y., Mukai, Y., Okada, N. and Nakagawa, S. (2010) 'Cytotoxicity of amorphous silica particles against macrophage-like THP-1 cells depends on particle-size and surface properties', *Pharmazie*, 65(8), pp. 596–599. doi: 10.1691/ph.2010.9408.

Mörtel, M., Witt, A., Heinemann, F. W., Bochmann, S., Bachmann, J. and Khusniyarov, M. M. (2017) 'Synthesis, Characterization, and Properties of Iron(II) Spin-Crossover Molecular Photoswitches Functioning at Room Temperature', *Inorganic Chemistry*, (Ii), p. acs.inorgchem.7b01952. doi: 10.1021/acs.inorgchem.7b01952.

Mosmann (2005) 'MTT-Assay: Cell Viability [Mosmann 1983, La Fontaine', p. 2004.

Münster, U., Nakamura, C., Haberland, A., Jores, K., Mehnert, W., Rummel, S., Schaller, M., Korting, H. C., Zouboulis, C. C., Blume-Peytavi, U. and Schäfer-Korting, M. (2005) 'RU 58841-myristate - Prodrug development for topical treatment of acne and androgenetic alopecia', *Pharmazie*, 60(1), pp. 8–12.

Murphy, D. P. (1967) 'The volume of the semen. A study of 3544 childless men.', *Fertility and sterility*, 18(1), pp. 124–126.

Murugadoss, S., Lison, D., Godderis, L., Van Den Brule, S., Mast, J., Brassinne, F., Sebaihi, N. and Hoet, P. H. (2017) 'Toxicology of silica nanoparticles: an update', *Archives of Toxicology*, pp. 2967–3010. doi: 10.1007/s00204-017-1993-y.

Musigapong, P., Briffa, S. M., Lynch, I., Soontaranon, S., Chanlek, N. and Valsami-Jones, E. (2019) 'Silica nanoparticle synthesis and multi-method characterisation', in *Materials Science Forum*. Trans Tech Publications (Materials Science Forum), pp. 82–90. doi: 10.4028/www.scientific.net/MSF.947.82.

Nabeshi, H., Yoshikawa, T., Matsuyama, K., Nakazato, Y., Arimori, A., Isobe, M., Tochigi, S., Kondoh, S., Hirai, T., Akase, T., Yamashita, T., Yamashita, K., Yoshida, T., Nagano, K., Abe, Y., Yoshioka, Y., Kamada, H., Imazawa, T., Itoh, N., Tsunoda, S. I. and Tsutsumi, Y. (2010) 'Size-dependent cytotoxic effects of amorphous silica nanoparticles on Langerhans cells', *Pharmazie*, 65(3), pp. 199–201. doi: 10.1691/ph.2010.9268.

Nabeshi, H., Yoshikawa, T., Matsuyama, K., Nakazato, Y., Matsuo, K., Arimori, A., Isobe, M., Tochigi, S., Kondoh, S., Hirai, T., Akase, T., Yamashita, T., Yamashita, K., Yoshida, T., Nagano, K., Abe, Y., Yoshioka, Y., Kamada,

H., Imazawa, T., Itoh, N., Nakagawa, S., Mayumi, T., Tsunoda, S. ichi and Tsutsumi, Y. (2011) ‘Systemic distribution, nuclear entry and cytotoxicity of amorphous nanosilica following topical application’, *Biomaterials*. Elsevier, 32(11), pp. 2713–2724. doi: 10.1016/j.biomaterials.2010.12.042.

Nabeshi, H., Yoshikawa, T., Matsuyama, K., Nakazato, Y., Tochigi, S., Kondoh, S., Hirai, T., Akase, T., Nagano, K., Abe, Y., Yoshioka, Y., Kamada, H., Itoh, N., Tsunoda, S. ichi and Tsutsumi, Y. (2011) ‘Amorphous nanosilica induce endocytosis-dependent ROS generation and DNA damage in human keratinocytes’, *Particle and Fibre Toxicology*. BioMed Central Ltd, 8(1), p. 1. doi: 10.1186/1743-8977-8-1.

Nafisi, S. and Maibach, H. I. (2018) *Skin penetration of nanoparticles*, *Emerging Nanotechnologies in Immunology*. Elsevier Inc. doi: 10.1016/b978-0-323-40016-9.00003-8.

Nafisi, S. and Maibach, M. . (2015) ‘Silica Nanoparticles for Increased Cosmetic Ingredient Efficacy *’, *Cosmetics & Toiletries*, (December), pp. 4–7.

Nafisi, S., Schäfer-Korting, M. and Maibach, H. I. (2015) ‘Perspectives on percutaneous penetration: Silica nanoparticles.’, *Nanotoxicology*, 9(5), pp. 643–57. doi: 10.3109/17435390.2014.958115.

Nandawar, R., Singh, P. and Fozia Z. Haque (2015) ‘Synthesis and characterization of SiO2 nanoparticles by sol-gel process’, *American Chemical Science Journal*, 5(1), pp. 1–10. doi: 10.9734/ACSj/2014/10875.

Nanocolors (2009) *Nano & the top 10 big cosmetics companies : L’Oréal, Procter & Gamble and Henkel on the podium for patents*. Available at: https://nanocolors.wordpress.com/2009/10/29/nano-the-top-10-big-cosmetics-companies-loreal-procter-gamble-and-henkel/ (Accessed: 12 December

2019).

Napierska, D., Thomassen, L. C. J., Lison, D., Martens, J. a and Hoet, P. H. (2010) ‘The nanosilica hazard: another variable entity.’, *Particle and fibre toxicology*, 7(1), p. 39. doi: 10.1186/1743-8977-7-39.

Napierska, D., Thomassen, L. C. J., Rabolli, V., Lison, D., Gonzalez, L., Kirsch-Volders, M., Martens, J. A. and Hoet, P. H. (2009) ‘Size-dependent cytotoxicity of monodisperse silica nanoparticles in human endothelial cells’, *Small*, 5(7), pp. 846–853. doi: 10.1002/smll.200800461.

Nel, A., Xia, T., Madler, L. and Li, N. (2006) ‘Toxic Potential of Materials at the Nanolevel’, *Science*, 311(5761), pp. 622–627. doi: 10.1126/science.1114397.

Nel, A., Xia, T., Meng, H., Wang, X., Lin, S., Ji, Z. and Zhang, H. (2013) ‘Nanomaterial toxicity testing in the 21st century: Use of a predictive toxicological approach and high-throughput screening’, *Accounts of Chemical Research*, 46(3), pp. 607–621. doi: 10.1021/ar300022h.

Nowack, B. and Bucheli, T. D. (2007) ‘Occurrence, behavior and effects of nanoparticles in the environment’, *Environmental Pollution*, 150(1), pp. 5–22. doi: 10.1016/j.envpol.2007.06.006.

Oberdörster, G., Oberdörster, E. and Oberdörster, J. (2005) ‘Nanotoxicology: An emerging discipline evolving from studies of ultrafine particles’, *Environmental Health Perspectives*, 113(7), pp. 823–839. doi: 10.1289/ehp.7339.

Ocean, I. and Program, D. (2013) ‘Xrd Diffraction Eva : Quick Start Guide’, *International Ocean Discovery Program*, pp. 1–8.

OECD (2010) ‘In Vitro Skin Irritation : Reconstructed Human Epidermis Test Method’, *Ocde*, 439(July), pp. 1–18. doi: 10.1787/9789264203822-en.

OECD (2015) ‘In Vitro Skin Irritation : Reconstructed Human Epidermis Test Method TG 439’, *Guideline for the testing of chemicals*, (July), pp. 1–21. doi: 1787/9789264242845-en.

OECD (2019) *Testing Programme of Manufactured Nanomaterials*. Available at: https://www.oecd.org/chemicalsafety/nanosafety/overview-testing-programme-manufactured-nanomaterials.htm (Accessed: 19 January 2020).

Orbis Research (2018) *Global Cosmetics Products Market expected to reach USD 805.61 billion by 2023 - Reuters*, *13 March 2018*. Available at: https://www.reuters.com/brandfeatures/venture-capital/article?id=30351 (Accessed: 17 June 2019).

Organolithiums, S. (2014) ‘List of Publications (Aiichiro Nagaki)’, 241(81), pp. 231–241. doi: 10.1007/12.

Öri, F., Dietrich, R., Ganz, C., Dau, M., Wolter, D., Kasten, A., Gerber, T. and Frerich, B. (2017) ‘Silicon-dioxide−polyvinylpyrrolidone as a wound dressing for skin defects in a murine model’, *Journal of Cranio-Maxillofacial Surgery*, 45(1), pp. 99–107. doi: 10.1016/j.jcms.2016.10.002.

Ovais, M., Raza, A., Naz, S., Islam, N. U., Khalil, A. T., Ali, S., Khan, M. A. and Shinwari, Z. K. (2017) ‘Current state and prospects of the phytosynthesized colloidal gold nanoparticles and their applications in cancer theranostics’, *Applied Microbiology and Biotechnology*. Applied Microbiology and Biotechnology, 101(9), pp. 3551–3565. doi: 10.1007/s00253-017-8250-4.

Palmer, B. C., Jatana, S., Phelan-Dickinson, S. J. and DeLouise, L. A. (2019) ‘Amorphous silicon dioxide nanoparticles modulate immune responses in a model of allergic contact dermatitis’, *Scientific Reports*, 9(1), pp. 1–11. doi: 10.1038/s41598-019-41493-7.

Pang, Y. X. and Bao, X. (2002) ‘Aluminium oxide nanoparticles prepared by water-in-oil microemulsions’, *Journal of Materials Chemistry*, 12(12), pp. 3699–3704. doi: 10.1039/b206501k.

Park, K. (2012) ‘No penetration of nanoparticles through intact skin’, *Journal of Controlled Release*. Elsevier B.V., 162(1), p. 258. doi: 10.1016/j.jconrel.2012.07.032.

Park, M., Verharen, H., Zwart, E., Hernandez, L., Van Benthem, J., Elsaesser, A., Barnes, C., Mckerr, G., Howard, V., Salvati, A., Lynch, I., Dawson, K. and De Jong, W. (2011) ‘Gennotoxicity evaluation of amorphous silica nanoparticles of different sizes using the micronucleus and the plasmid lacZ gene mutation assay’, *Nanotoxicology*, 5(2), pp. 168–181. doi: 10.3109/17435390.2010.506016.

Park, Y.-H., Bae, H. C., Jang, Y., Jeong, S. H., Lee, H. N., Ryu, W.-I., Yoo, M. G., Kim, Y.-R., Kim, M.-K., Lee, J. K., Jeong, J. and Son, S. W. (2013) ‘Effect of the size and surface charge of silica nanoparticles on cutaneous toxicity’, *Molecular & Cellular Toxicology*, 9(1), pp. 67–74. doi: 10.1007/s13273-013-0010-7.

Park, Y. H., Kim, J. N., Jeong, S. H., Choi, J. E., Lee, S. H., Choi, B. H., Lee, J. P., Sohn, K. H., Park, K. L., Kim, M. K. and Son, S. W. (2010) ‘Assessment of dermal toxicity of nanosilica using cultured keratinocytes, a human skin equivalent model and an in vivo model’, *Toxicology*, 267(1–3), pp. 178–181. doi: 10.1016/j.tox.2009.10.011.

Paskevicius, M., Webb, J., Pitt, M. P., Blach, T. P., Hauback, B. C., Gray, E. M. A. and Buckley, C. E. (2009) ‘Mechanochemical synthesis of aluminium nanoparticles and their deuterium sorption properties to 2 kbar’, *Journal of*

Alloys and Compounds, 481(1–2), pp. 595–599. doi: 10.1016/j.jallcom.2009.03.031.

Pedrosa, T. do N., Catarino, C. M., Pennacchi, P. C., Assis, S. R. de, Gimenes, F., Consolaro, M. E. L., Barros, S. B. de M. and Maria-Engler, S. S. (2017) 'A new reconstructed human epidermis for in vitro skin irritation testing', *Toxicology in Vitro*. Elsevier, 42(January), pp. 31–37. doi: 10.1016/j.tiv.2017.03.010.

Peira, E., Turci, F., Corazzari, I., Chirio, D., Battaglia, L., Fubini, B. and Gallarate, M. (2014) 'The influence of surface charge and photo-reactivity on skin-permeation enhancer property of nano-TiO2 in ex vivo pig skin model under indoor light', *International Journal of Pharmaceutics*. Elsevier B.V., 467(1–2), pp. 90–99. doi: 10.1016/j.ijpharm.2014.03.052.

Pennycook, S. J. and Nellist, P. D. (2011) *Scanning Transmission Electron Microscopy: Imaging and Analysis - Google Books*, *2011*. Available at: https://books.google.co.uk/books?id=N_98Hef0ZTYC&pg=PA1&lpg=PA1&dq=baron+manfred+von+ardenne+STEM&source=bl&ots=JOWfmvLVUs&sig=ACfU3U0mQfUJchAH5DAI7pOfo3lr414SJA&hl=en&sa=X&ved=2ahUKEwjto5OR8NLkAhXCQkEAHR2mDowQ6AEwE3oECAwQAQ#v=onepage&q&f=false (Accessed: 15 September 2019).

Pennycook, S. J., Varela, M., Chisholm, M. F., Borisevich, A. Y., Lupini, A. R., van Benthem, K., Oxley, M. P., Luo, W., McBride, J. R. and Rosenthal, S. J. (2010) 'Scanning transmission electron microscopy of nanostructures', *Oxford Handbook of Nanoscience and Technology: Volume 2: Materials: Structures, Properties and Characterization Techniques*, p. 205.

Perkins, M. A., Osterhues, M. A., Farage, M. A. and Robinson, M. K. (2001) 'A

noninvasive method to assess skin irritation and compromised skin conditions using simple tape adsorption of molecular markers of inflammation', *Skin Research and Technology*, 7(4), pp. 227–237. doi: 10.1034/j.1600-0846.2001.70405.x.

Pilloni, M., Ennas, G., Casu, M., Fadda, A. M., Frongia, F., Marongiu, F., Sanna, R., Scano, A., Valenti, D. and Sinico, C. (2013) 'Drug silica nanocomposite: preparation, characterization and skin permeation studies.', *Pharmaceutical development and technology*, 18(3), pp. 626–33. doi: 10.3109/10837450.2011.653821.

Poh, T. Y., Ali, N. A. T. B. M., Mac Aogáin, M., Kathawala, M. H., Setyawati, M. I., Ng, K. W. and Chotirmall, S. H. (2018) 'Inhaled nanomaterials and the respiratory microbiome: Clinical, immunological and toxicological perspectives', *Particle and Fibre Toxicology*. Particle and Fibre Toxicology, 15(1), pp. 1–16. doi: 10.1186/s12989-018-0282-0.

Potts, R. O. and Guy, R. H. (1992) 'Predicting Skin Permeability', *Pharmaceutical Research: An Official Journal of the American Association of Pharmaceutical Scientists*, 9(5), pp. 663–669. doi: 10.1023/A:1015810312465.

Powers, K. W., Brown, S. C., Krishna, V. B., Wasdo, S. C., Moudgil, B. M. and Roberts, S. M. (2006) 'Research strategies for safety evaluation of nanomaterials. Part VI. characterization of nanoscale particles for toxicological evaluation', *Toxicological Sciences*, 90(2), pp. 296–303. doi: 10.1093/toxsci/kfj099.

Press, D. (2012) 'IJN-28293-amorphous-silica-nanoparticles-aggregate---human-platelets--', pp. 631–639.

Prow, T. W., Grice, J. E., Lin, L. L., Faye, R., Butler, M., Becker, W., Wurm, E. M. T., Yoong, C., Robertson, T. A., Soyer, H. P. and Roberts, M. S. (2011) 'Nanoparticles and microparticles for skin drug delivery', *Advanced Drug Delivery Reviews*, 63(6), pp. 470–491. doi: 10.1016/j.addr.2011.01.012.

Qasim, M., Ananthaiah, J., Dhara, S., Paik, P. and Das, D. (2014) 'Synthesis and Characterization of Ultra-Fine Colloidal Silica Nanoparticles', *Advanced Science, Engineering and Medicine*, 6(9), pp. 965–973. doi: 10.1166/asem.2014.1578.

Quignard, S., Mosser, G., Boissière, M. and Coradin, T. (2012) 'Long-term fate of silica nanoparticles interacting with human dermal fibroblasts', *Biomaterials*. Elsevier Ltd, 33(17), pp. 4431–4442. doi: 10.1016/j.biomaterials.2012.03.004.

Rahman, I. A. and Padavettan, V. (2012) 'Synthesis of Silica nanoparticles by Sol-Gel: Size-dependent properties, surface modification, and applications in silica-polymer nanocompositesa review', *Journal of Nanomaterials*, 2012. doi: 10.1155/2012/132424.

Raj, S., Jose, S., Sumod, U. S. and Sabitha, M. (2012) 'Nanotechnology in cosmetics: Opportunities and challenges', *Journal of Pharmacy and Bioallied Sciences*. Wolters Kluwer -- Medknow Publications, 4(3), pp. 186–193. doi: 10.4103/0975-7406.99016.

Raju, G., Katiyar, N., Vadukumpully, S. and Shankarappa, S. A. (2018) 'Penetration of gold nanoparticles across the stratum corneum layer of thick-Skin', *Journal of Dermatological Science*. Japanese Society for Investigative Dermatology, 89(2), pp. 146–154. doi: 10.1016/j.jdermsci.2017.11.001.

Rancan, F., Gao, Q., Graf, C., Troppens, S., Hadam, S., Hackbarth, S.,

Kembuan, C., Blume-Peytavi, U., Rühl, E., Lademann, J. and Vogt, A. (2012) ‘Skin penetration and cellular uptake of amorphous silica nanoparticles with variable size, surface functionalization, and colloidal stability’, *ACS Nano*, 6(8), pp. 6829–6842. doi: 10.1021/nn301622h.

Rasmussen, K., Mech, A., Mast, J., de Temmerman, P.-J., Waegeneers, N., Steen, F. Van, Pizzolon, J. C., de Temmerman, L., van Doren, E., Jensen, A., Birkedal, R., Levin, M., Nielsen, H., Koponen, I. K., Axel, P., Kembouche, Y., Thieriet, N., Spalla, O., Giuot, C., Rousset, D., Bau, S., Bianchi, B., Gilliland, D., Pianella, F., Ceccone, G., Cotogno, G., Gibson, N. and Stamm, H. (2013) *Synthetic Amorphous Silicon Dioxide (NM-200, NM-201, NM-202, NM-203, NM-204): Characterisation and Physico-Chemical Properties*, *JRC Repository: NM-series of Representative Manufactured Nanomaterials*. doi: 10.2788/57989.

Rheinheimer, V. and Casanova, I. (2016) ‘Thin films as a tool for nanoscale studies of cement systems and building materials’, *Intech*, i(tourism), p. 13. doi: http://dx.doi.org/10.5772/57353.

Rolls, G. and Sampias, C. (2019) ‘H&E Staining Overview: A Guide to Best Practices’. Available at: https://www.leicabiosystems.com/knowledge-pathway/he-staining-overview-a-guide-to-best-practices/ (Accessed: 25 January 2020).

Ropp, R. C. (2013) *Group 14 (C, Si, Ge, Sn, and Pb) Alkaline Earth Compounds*, *Encyclopedia of the Alkaline Earth Compounds*. doi: 10.1016/b978-0-444-59550-8.00005-3.

Rougier, A., Lotte, C. and Maibach, H. I. (1987) ‘In vivo percutaneous penetration of some organic compounds related to anatomic site in humans:

Predictive assessment by the stripping method', *Journal of Pharmaceutical Sciences*, 76(6), pp. 451–454. doi: 10.1002/jps.2600760608.

Rouse, J. G., Yang, J., Ryman-Rasmussen, J. P., Barron, A. R. and Monteiro-Riviere, N. A. (2007) 'Effects of mechanical flexion on the penetration of fullerene amino acid-derivatized peptide nanoparticles through skin', *Nano Letters*, 7(1), pp. 155–160. doi: 10.1021/nl062464m.

Ryman-Rasmussen, J. P., Riviere, J. E. and Monteiro-Riviere, N. A. (2006) 'Penetration of intact skin by quantum dots with diverse physicochemical properties', *Toxicological Sciences*, 91(1), pp. 159–165. doi: 10.1093/toxsci/kfj122.

Ryu, H. J., Seong, N. W., So, B. J., Seo, H. S., Kim, J. H., Hong, J. S., Park, M. K., Kim, M. S., Kim, Y. R., Cho, K. B., Seo, M. Y., Kim, M. K., Maeng, E. H. and Son, S. W. (2014) 'Evaluation of silica nanoparticle toxicity after topical exposure for 90 days', *International Journal of Nanomedicine*, 9, pp. 127–136. doi: 10.2147/IJN.S57929.

Saallah, S. and Lenggoro, I. W. (2018) 'Nanoparticles carrying biological molecules: Recent advances and applications', *KONA Powder and Particle Journal*, 2018(35), pp. 89–111. doi: 10.14356/kona.2018015.

Salamanca, C. H., Barrera-Ocampo, A., Lasso, J. C., Camacho, N. and Yarce, C. J. (2018) 'Franz diffusion cell approach for pre-formulation characterisation of ketoprofen semi-solid dosage forms', *Pharmaceutics*, 10(3), pp. 1–10. doi: 10.3390/pharmaceutics10030148.

Santra, S., Zhang, P., Wang, K., Tapec, R. and Tan, W. (2001) 'Conjugation of biomolecules with luminophore-doped silica nanoparticles for photostable biomarkers', *Analytical Chemistry*, 73(20), pp. 4988–4993. doi:

10.1021/ac010406+.

Schäfer-Korting, M., Mehnert, W. and Korting, H. C. (2007) ‘Lipid nanoparticles for improved topical application of drugs for skin diseases’, *Advanced Drug Delivery Reviews*, 59, pp. 427–443. doi: 10.1016/B978-0-323-42868-2.00013-9.

Schnablegger, H. and Singh, Y. (2013) ‘The SAXS Guide’, *Anton Paar GmbH*, pp. 1–99. doi: 10.1006/aphy.1994.1055.

Scientific Committee on Consumer Safety (2012) ‘Guidance on the Safety Assessment of Nanomaterials in Cosmetics’, *European Commission*, (June), pp. 0–136. doi: 10.2773/ISBN.

Sharma, S. K., Vargas, J. M., Pirota, K. R., Kumar, S., Lee, C. G. and Knobel, M. (2011) ‘Synthesis and ageing effect in FeO nanoparticles: Transformation to core-shell FeO/Fe3O4 and their magnetic characterization’, *Journal of Alloys and Compounds*. Elsevier B.V., 509(22), pp. 6414–6417. doi: 10.1016/j.jallcom.2011.03.072.

Sharma, S., Mehta, S. K., Parmar, A. and Sachar, S. (2018) ‘Understanding Toxicity of Nanomaterials in the Environment: Crucial Tread for Controlling the Production, Processing, and Assessing the Risk’, in *Nanomaterials in Chromatography*, pp. 467–500. doi: 10.1016/b978-0-12-812792-6.00018-2.

Shelby, C. (2019) *Scanning Electron Microscope*, *2019*. Available at: https://www.purdue.edu/ehps/rem/laboratory/equipment safety/Research Equipment/sem.html (Accessed: 2 October 2019).

SLRI (2015) *What is Synchrotron Light*. Available at: https://www.slri.or.th/en/what-is-synchrotron-light.html (Accessed: 26 January 2020).

Snyder, M. A., Lee, J. A., Davis, T. M., Scriven, L. E. and Tsapatsis, M. (2007) ‘Silica nanoparticle crystals and ordered coatings using lys-sil and a novel coating device’, *Langmuir*, 23(20), pp. 9924–9928. doi: 10.1021/la701063v.

Solé, V. A., Papillon, E., Cotte, M., Walter, P. and Susini, J. (2007) ‘A multiplatform code for the analysis of energy-dispersive X-ray fluorescence spectra’, *Spectrochimica Acta - Part B Atomic Spectroscopy*, 62(1), pp. 63–68. doi: 10.1016/j.sab.2006.12.002.

Song, Y., Modrow, H., Henry, L. L., Saw, C. K., Doomes, E. E., Palshin, V., Hormes, J. and Kumar, C. S. S. R. (2006) ‘Microfluidic synthesis of cobalt nanoparticles’, *Chemistry of Materials*, 18(12), pp. 2817–2827. doi: 10.1021/cm052811d.

Spoiala, A., Albu, M. G., Ficai, A., Andronescu, E., Voicu, G. and Ungureanu, C. (2014) ‘THE SiO 2 /ZnO COMPOSITE MATERIALS FOR COSMETIC CREAMS’, *Digest Journal of Nanomaterials and Biostructures*, 9(4), pp. 1729–1737.

Stetefeld, J., McKenna, S. A. and Patel, T. R. (2016) ‘Dynamic light scattering: a practical guide and applications in biomedical sciences’, *Biophysical Reviews*. Biophysical Reviews, 8(4), pp. 409–427. doi: 10.1007/s12551-016-0218-6.

Stöber, W., Fink, A. and Bohn, E. (1968) ‘Controlled growth of monodisperse silica spheres in the micron size range’, *Journal of Colloid and Interface Science*, 26(1), pp. 62–69. doi: 10.1016/0021-9797(68)90272-5.

V. Suntzeff and Carruthers, C. (1945) ‘The Mineral Composition’, *J. Biol. Chem.*, 160, pp. 567–569.

Susan Swapp (2017) *Scanning Electron Microscopy (SEM)*, *May 26, 2017*.

Available at: https://serc.carleton.edu/research_education/geochemsheets/techniques/SEM.html (Accessed: 29 September 2019).

Tago, T., Tashiro, S., Hashimoto, Y., Wakabayashi, K. and Kishida, M. (2003) 'Synthesis and optical properties of SiO 2 -coated CeO 2 nanoparticles', (15), pp. 55–60.

Tang, L. and Cheng, J. (2013) 'Nonporous silica nanoparticles for nanomedicine application', *Nano Today*. Elsevier Ltd, 8(3), pp. 290–312. doi: 10.1016/j.nantod.2013.04.007.

Tedesco, E., Mičetić, I., Ciappellano, S. G., Micheletti, C., Venturini, M. and Benetti, F. (2015) 'Cytotoxicity and antibacterial activity of a new generation of nanoparticle-based consolidants for restoration and contribution to the safe-by-design implementation', *Toxicology in Vitro*, 29(7), pp. 1736–1744. doi: 10.1016/j.tiv.2015.07.002.

The British Standards Institute (2015) *PD ISO / TS 80004-6 : 2013 BSI Standards Publication Nanotechnologies — Vocabulary*.

The European Commission (2011) 'Commission recommendations', *Official journal of the European Union*, (275), pp. 38–39. doi: 10.7748/ns.24.26.6.s4.

The European Commission (2014) *Nanomaterials*, *https://ec.europa.eu/growth/sectors/chemicals/reach/nanomaterials_en*. Available at: https://ec.europa.eu/growth/sectors/chemicals/reach/nanomaterials_en (Accessed: 13 November 2019).

The International Organization for Standardization (2012) 'TECHNICAL REPORT ISO / TR13014 Nanotechnologies — Guidance on physico-chemical

characterization of engineered nanoscale materials for toxicologic assessment', 2012. Available at: http://www.tbtsps.cn/TbcxDownLoad?sysfname=Z:%5Cupload%5Cjwebsite%5Cspecialresearch/20141118/201411188778.pdf.

Thermo Scientific XPS (2013) *XPS Interpretation of Silicon*, *2013*. Available at: https://xpssimplified.com/elements/silicon.php (Accessed: 3 September 2019).

Thomassen, L. C. J., Aerts, A., Rabolli, V., Lison, D., Gonzalez, L., Kirsch-Volders, M., Napierska, D., Hoet, P. H., Kirschhock, C. E. A. and Martens, J. A. (2010) 'Synthesis and characterization of stable monodisperse silica nanoparticle sols for in vitro cytotoxicity testing', *Langmuir*, 26(1), pp. 328–335. doi: 10.1021/la902050k.

Tiwari, J. N., Tiwari, R. N. and Kim, K. S. (2012) 'Zero-dimensional, one-dimensional, two-dimensional and three-dimensional nanostructured materials for advanced electrochemical energy devices', *Progress in Materials Science*. Elsevier Ltd, 57(4), pp. 724–803. doi: 10.1016/j.pmatsci.2011.08.003.

Toll, R., Jacobi, U., Richter, H., Lademann, J., Schaefer, H. and Blume-Peytavi, U. (2004) 'Penetration profile of microspheres in follicular targeting of terminal hair follicles', *Journal of Investigative Dermatology*. Elsevier Masson SAS, 123(1), pp. 168–176. doi: 10.1111/j.0022-202X.2004.22717.x.

Torchilin, V. P. (2005) 'Recent advances with liposomes as pharmaceutical carriers', *Nature Reviews Drug Discovery*, 4(2), pp. 145–160. doi: 10.1038/nrd1632.

Toth, M. and Mathworks, T. (2017) 'Magnetic Properties of Sr2YRu1-xIrxO6 Compounds', (May 2013).

Truong, N. P., Whittaker, M. R., Mak, C. W. and Davis, T. P. (2015) 'The importance of nanoparticle shape in cancer drug delivery', *Expert Opinion on Drug Delivery*, 12(1), pp. 129–142. doi: 10.1517/17425247.2014.950564.

Tyner, K. M., Wokovich, A. M., Doub, W. H., Buhse, L. F., Sung, L. P., Watson, S. S. and Sadrieh, N. (2009) 'Comparing methods for detecting and characterizing metal oxide nanoparticles in unmodified commercial sunscreens', *Nanomedicine*, 4(2), pp. 145–159. doi: 10.2217/17435889.4.2.145.

Uboldi, C., Giudetti, G., Broggi, F., Gilliland, D., Ponti, J. and Rossi, F. (2012) 'Amorphous silica nanoparticles do not induce cytotoxicity, cell transformation or genotoxicity in Balb/3T3 mouse fibroblasts', *Mutation Research - Genetic Toxicology and Environmental Mutagenesis*, 745(1–2), pp. 11–20. doi: 10.1016/j.mrgentox.2011.10.010.

Ustinov, V. M., Zhukov, A. E., Kovsh, A. R., Mikhrin, S. S., Maleev, N. A., Volovik, B. V, Musikhin, Y. G., Shernyakov, Y. M., Kondat'eva, E. Y., Maximov, M. V, Tsatsul'nikov, A. F., Ledentsov, N. N., Alferov, Z. I., Lott, J. A. and Bimberg, D. (2000) 'substrates Long-wavelength quantum dot lasers on GaAs substrates', *Nanotechnology*, 11, pp. 397–400.

Vance, M. E., Kuiken, T., Vejerano, E. P., McGinnis, S. P., Hochella, M. F. and Hull, D. R. (2015) 'Nanotechnology in the real world: Redeveloping the nanomaterial consumer products inventory', *Beilstein Journal of Nanotechnology*, 6(1), pp. 1769–1780. doi: 10.3762/bjnano.6.181.

Vičanová, J., Boelsma, E., Mommaas, A. M., Kempenaar, J. A., Forslind, B., Pallon, J., Egelrud, T., Koerten, H. K. and Ponec, M. (1998) 'Normalization of epidermal calcium distribution profile in reconstructed human epidermis is

related to improvement of terminal differentiation and stratum corneum barrier formation', *Journal of Investigative Dermatology*, 111(1), pp. 97–106. doi: 10.1046/j.1523-1747.1998.00251.x.

Walock, M. (2012) 'Nanocomposite coatings based on quaternary metalnitrogen', p. 211.

Wester, R. C., Noonan, P. K. and Maibach, H. I. (1980) 'Variations in Percutaneous Absorption of Testosterone in the Rhesus Monkey Due to Anatomic Site of Application and Frequency of Application.', *Arch Dermatol Res.*, 235(267), pp. 229–235.

Wever, B. D. E., Petersohn, D. and Mewes, K. R. (2013) 'Overview of human 3D skin models used for dermal toxicity assessment Part 1', *Household and Personal Care Today*, 8(1), pp. 18–23.

De Wever, B., Kurdykowski, S. and Descargues, P. (2015) 'Human Skin Models for Research Applications in Pharmacology and Toxicology: Introducing NativeSkin ® , the "Missing Link" Bridging Cell Culture and/or Reconstructed Skin Models and Human Clinical Testing', *Applied In Vitro Toxicology*, 1(1), pp. 26–32. doi: 10.1089/aivt.2014.0010.

Wiesenthal, A., Hunter, L., Wang, S., Wickliffe, J. and Wilkerson, M. (2011) 'Nanoparticles: Small and mighty', *International Journal of Dermatology*, 50(3), pp. 247–254. doi: 10.1111/j.1365-4632.2010.04815.x.

Williams, A. C. and Barry, B. W. (2012) 'Penetration enhancers', *Advanced Drug Delivery Reviews*. Elsevier B.V., 64(SUPPL.), pp. 128–137. doi: 10.1016/j.addr.2012.09.032.

Wills, J. W., Hondow, N., Thomas, A. D., Chapman, K. E., Fish, D., Maffeis, T. G., Penny, M. W., Brown, R. A., Jenkins, G. J. S., Brown, A. P., White, P. A.

and Doak, S. H. (2016) ‘Genetic toxicity assessment of engineered nanoparticles using a 3D in vitro skin model (EpiDerm ™)’, *Particle and Fibre Toxicology*. Particle and Fibre Toxicology, 13(1), pp. 1–21. doi: 10.1186/s12989-016-0161-5.

Wu, T., Zhang, S., Liang, X., He, K., Wei, T., Wang, Y., Zou, L., Zhang, T., Xue, Y. and Tang, M. (2019) ‘The apoptosis induced by silica nanoparticle through endoplasmic reticulum stress response in human pulmonary alveolar epithelial cells’, *Toxicology in Vitro*. Elsevier, 56(October 2018), pp. 126–132. doi: 10.1016/j.tiv.2019.01.009.

Yang, X., Liu, J., He, H., Zhou, L., Gong, C., Wang, X., Yang, L., Yuan, J., Huang, H., He, L., Zhang, B. and Zhuang, Z. (2010) ‘SiO2nanoparticles induce cytotoxicity and protein expression alteration in HaCaT cells’, *Particle and Fibre Toxicology*, 7, pp. 1–12. doi: 10.1186/1743-8977-7-1.

Yin, Y., Xu, X., Ge, X., Xia, C. and Zhang, Z. (1998) ‘Synthesis of cadmium sulfide nanoparticles in situ using γ-radiation’, *Chemical Communications*, (16), pp. 1641–1642. doi: 10.1039/a802910e.

Yoon, S. Y. and Deng, Y. (2004) ‘Flocculation and reflocculation of clay suspension by different polymer systems under turbulent conditions’, *Journal of Colloid and Interface Science*, 278(1), pp. 139–145. doi: 10.1016/j.jcis.2004.05.011.

Yu, K. O., Grabinski, C. M., Schrand, A. M., Murdock, R. C., Wang, W., Gu, B., Schlager, J. J. and Hussain, S. M. (2009) ‘Toxicity of amorphous silica nanoparticles in mouse keratinocytes’, *Journal of Nanoparticle Research*, 11(1), pp. 15–24. doi: 10.1007/s11051-008-9417-9.

Zeng, J., Francia, C., Gerbaldi, C., Dumitrescu, M. A., Specchia, S. and

Spinelli, P. (2012) ‘Smart synthesis of hollow core mesoporous shell carbons (HCMSC) as effective catalyst supports for methanol oxidation and oxygen reduction reactions’, *Journal of Solid State Electrochemistry*, 16(9), pp. 3087–3096. doi: 10.1007/s10008-012-1750-3.

Zhai, H. and Maibach, H. I. (2004) *Dermatotoxicology*. CRC Press.

Zhang, L. W. and Monteiro-Riviere, N. A. (2008) ‘Assessment of quantum dot penetration into intact, tape-stripped, abraded and flexed rat skin’, *Skin Pharmacology and Physiology*, 21(3), pp. 166–180. doi: 10.1159/000131080.

Zhang, Y., Hu, L., Yu, D. and Gao, C. (2010) ‘Influence of silica particle internalization on adhesion and migration of human dermal fibroblasts’, *Biomaterials*, 31(32), pp. 8465–8474. doi: 10.1016/j.biomaterials.2010.07.060.

Zhao, Z., Gao, Y., Wu, C., Hao, Y., Zhao, Y. and Xu, J. (2016) ‘Development of novel core-shell dual-mesoporous silica nanoparticles for the production of high bioavailable controlled-release fenofibrate tablets’, *Drug Development and Industrial Pharmacy*, 42(2), pp. 199–208. doi: 10.3109/03639045.2015.1039018.

Zhong, J. Q., Wang, M., Hoffmann, W. H., Van Spronsen, M. A., Lu, D. and Boscoboinik, J. A. (2018) ‘Synchrotron-based ambient pressure X-ray photoelectron spectroscopy of hydrogen and helium’, *Applied Physics Letters*, 112(9). doi: 10.1063/1.5022479.

Zhu, Y., Choe, C.-S., Ahlberg, S., Meinke, M. C., Alexiev, U., Lademann, J. and Darvin, M. E. (2014) ‘ Penetration of silver nanoparticles into porcine skin ex vivo using fluorescence lifetime imaging microscopy, Raman microscopy, and surface-enhanced Raman scattering microscopy ’, *Journal of Biomedical Optics*, 20(5), p. 051006. doi: 10.1117/1.jbo.20.5.051006.

Zsikó, S., Csányi, E., Kovács, A., Budai-Szűcs, M., Gácsi, A. and Berkó, S. (2019) ‘Methods to evaluate skin penetration in vitro’, *Scientia Pharmaceutica*, 87(3), pp. 1–21. doi: 10.3390/scipharm87030019.